SIMULATION OF MAGNETOHYDRODYNAMICS TURBULENCE WITH APPLICATION TO PLASMA-ASSISTED SUPERSONIC COMBUSTION

A Thesis
Presented to
The Academic Faculty

by

Kenji Miki

In Partial Fulfillment
of the Requirements for the Degree
PhD in Aerospace Engineering in the
School of Aerospace Engineering

Georgia Institute of Technology
December 2008

SIMULATION OF MAGNETOHYDRODYNAMICS TURBULENCE WITH APPLICATION TO PLASMA-ASSISTED SUPERSONIC COMBUSTION

Approved by:

Professor Suresh Menon, Advisor
School of Aerospace Engineering
Georgia Institute of Technology

Professor Jeff Jagoda
School of Aerospace Engineering
Georgia Institute of Technology

Professor Stephen Ruffin
School of Aerospace Engineering
Georgia Institute of Technology

Assistant Professor Mitchell Walker
School of Aerospace Engineering
Georgia Institute of Technology

Assistant Professor Thorsten Stoesser
School of Civil and Environmental Engineering
Georgia Institute of Technology

Date Approved: 13 November 2008

To my family,

and

my uncle encouraging me from the heaven

ACKNOWLEDGEMENTS

I am sincerely grateful to my adviser, Dr. Suresh Menon, for his kind physical and mental support as well as academic advices. Without his suggestions and encouragements, I could not accomplish modeling MHD LES turbulence that required a lot of patience and a continuing process of trial and error. He also gave me a great opportunity to join the 32nd Combustion Symposium at Montreal, Canada. I will not forget the beautiful night view from the top of the Mount Royal. I want to extend my thanks to my Thesis Committee members: Dr. Jeff Jagoda, Dr. Stephen Ruffin, Dr. Mitchell Walker, and Dr. Thorsten Stoesser for their time, patience and valuable suggestions.

Also, I would like to thank for all friends at Computational Combustion Laboratory. When I came here five years ago without any knowledge of LES and codes, Franklin, Mathieu, Chris, and Natalie had kindly answered my endless questions and made my start at CCL go smooth. I cannot express my appreciation to my best friends, Ayse, Martin, Zazy, Jason, Brittyn, JP, and Joe who have always listened to my research and personal problem and cheered me up. Joey is such a brilliant graduate student I consider it a privilege to work and build up friendship with him. I also thank my other friends, Baris, Orchan, Hossam, Leandro, Choi, Kaushik, Srikanth, Nayan, Sumit, and Vaidya.

Lastly, but certainly not least, I give special thanks to my family and friends in Japan who always believe in my success and encourage me.

This research was sponsored by NASA/GRC and AFOSR through the University Research Engineering and Technology Institute for Aeropropulsion and Power. The author is grateful for being funded throughout his Ph.D. program.

TABLE OF CONTENTS

LIST OF TABLES

LIST OF FIGURES

LIST OF SYMBOLS

Roman Symbols

A	Magnetic potential
B_x, B_y, B_z, B_i	Cartesian magnetic vector components
C_{EBU}	model coefficient for the Eddy Break-Up model
C_ϵ	model coefficient for subgrid dissipation
$C_{\epsilon,b}$	model coefficient for subgrid MHD dissipation
C_λ	scalar diffusivity
C_ν	model coefficient for turbulent viscosity
$C_{p,b}$	model coefficient for subgrid MHD work
C_ν^T	model coefficient for MHD turbulent viscosity
c	speed of sound
c_p	specific heat at constant pressure per unit mass
c_v	specific heat at constant volume per unit mass
d	subgrid magnetic diffusive flux
D	mass diffusivity
D^{sgs}	dissipation of turbulent kinetic energy
Da	Damkohler number
E	Efficieny function in Thickened Flame model
E_a	activation energy
e	internal energy per unit mass
E_x, E_y, E_z, E_i	Cartesian electric field vector components
E_T^k	turbulent electromotive force
F	Flame thickening factor
$\mathbf{F}$	flux vector in x direction
$\mathbf{G}$	flux vector in y direction

$\mathbf{H}$	flux vector in z direction
H	total enthalpy per unit mass or subgrid total enthalpy flux
Ha	Hartman number
H_c	Cross helicity
H_i	enthalpy flux
H_m	Magnetic helicity
h	specific enthalpy per unit mass
i, j, k	computational grid indices
J	Jacobian of the coordinate system transformation
J_x, J_y, J_z, J_i	Cartesian current density vector components
k	turbulent kinetic energy or Boltzman constant
k^{sgs}	sub-grid turbulent kinetic energy
$k^{sgs,b}$	sub-grid turbulent magnetic energy
ℓ	characterlistic length scale
Le	Lewis number
M	rate of magnetic strain
Ma	Mach number
MW	molecular weight
N	total number of species or Interaction Parameter
P	production of turbulent kinetic energy
p	pressure
Pr	Prandtl number
$\mathbf{Q}$, $\mathbf{Q}'$	state vector
q	unit electric charge
q_i	heat flux
Re	Magnetic Reynolds number
Rm	Reynolds number
R_o	Rossby number
R_u	universal gas constant

r	spatial position
S	rate of strain and subgrid term
T	temperature or Maxwell stress
t	time
u, v, w, u_i	Cartesian velocity vector components
u'	rms velocity
V	volume or electric potential
$V_{i,m}$	diffusion velocity of species m
v_a	Alfvén wave-speed
x, y, z	Cartesian coordinate directions
X	mole fraction
Y	mass fraction
$Y_{i,m}$	flux of species m
Z_m	charge number of species m

Greek Symbols

α	coefficent of the α-effect
β	coefficent of the β-effect
γ	ratio of specific heats or coefficent of the γ-effect
$\overline{\Delta}$	grid size
δ_{ij}	Kronecker delta
$\Delta h'_f$	specific heat
Δh_f	enthalpy of formation per unit mass
ϵ_0	permitivity of free space
ϵ_{ijk}	alternative tensor
ϕ	equivalence ratio
$\Phi_{i,m}$	convective mass flux of species m
η	Kolmogorov length scale or magnetic resistivity

$\theta_{i,m}$	diffusive flux of species m
κ	thermal conductivity
λ	magnetic diffusivity
μ	dynamic viscosity
μ_0	magnetic permeability
ν	kinematic viscosity
ν_m	stoichiometric coefficient
ρ	density
τ_{ij}	viscous stress tensor
σ	electrical conductivity
σ_{ij}	viscous work
ξ, η, ζ	spatial directions in computational space
$\dot{\omega}$	reaction rate per unit volume

Subscripts

b	magnetic quantity
cgs	cm-gram-second measurement system
e	electron quantity
i, j, k	Cartesian tensor indices or species indices
k	species index
n	time step index
t, T	turbulent quantity

Superscripts

0	reference quantity
sgs	subgrid scale
$test$	test filter scale

Other Symbols

∂	partial derivative operator
∇	gradient operator
$\nabla\cdot$	divergence operator
$\sum$	summation operator
Δ	difference operator
$\mathscr{M}$	Mach number
$\tilde{}$	Favre spatial filter
$\hat{}$	test filter
$\bar{}$	space average
$'$, $''$	fluctuating quantity

Abbreviations

CFD	Computational Fluid Dynamics
CFL	Courant-Friedrichs-Lewy number
DARPA	Defense Advance Research Project Agency
DNS	Direct Numerical Simulation
DC	Direct current discharge
EBU	Eddy Break-Up model
GASL	General Applied Science Laboratories
LDKM	Localized Dynamic k-equation Model
LEM	Linear Eddy Mixing model
LES	Large Eddy Simulation
LTE	local thermodynamic equailibrium
MHD	Magnetohydrodynamics
MPI	Message Passing Interface

MUSCL	Monotone Upstream-centered Schemes for Conservation Laws
ODE	Ordinary Differential Equation
PAC	Plasma assisted combustion
PIBAL	Aerodynamics Laboratory of the Polytechnic Institute of Brooklyn
PDE	Partial Differential Equation
PDF	Probability Distribution Function
RANS	Reynolds Averaged Navier - Stokes
SSTO	Single-stage-to-orbit

SUMMARY

Plasma assisted combustion (PAC) is a promising alternative to hold or ignite a fuel and air mixture in a supersonic environment. The ability of supersonic combustion is of primary important for SCRAMJET technology. The advantages of PAC is the addition of large amounts of energy to specific regions of the SCRAMJET flow-field for short periods of time, and as a result accelerate the fuel/air kinetic rates to achieve a self-sustaining condition. Moreover, the promise of enhancement of fuel-air mixing by magnetohydrodynamics (MHD) flow control offers significant improvement of combustion performance. The development of a numerical tool for investigating high-temperature chemistry and plasma-dynamic effects of a discharge arc is desired to gain understanding of PAC technology and the potential improvement of the operational efficiency of SCRAMJET engines.

The main objective of this thesis is to develop a comprehensive model with the capability of modeling both a high Reynolds number and high magnetic Reynolds number turbulent flow for application to supersonic combustor. The development of this model can be divided into three categories: one, the development of a self-consistent MHD numerical model capable of modeling magnetic turbulence in high magnetic Reynolds number applications. Second, the development of a gas discharge model which models the interaction of externally applied fields in conductive medium. Third, the development of models necessary for studying supersonic combustion applications with plasma-assistance such the extension of chemical kinetics models to extremely high temperature and non-equilibrium phenomenon. The structure if this code will follow the development of the models necessary in these categories.

The first half of this thesis is devoted to the development of the Local Dynamic Kinetic Energy Model (LDKM) for a large-eddy simulation (LES) of MHD turbulence. The nonlinear coupling between the turbulent flow fields and magnetic fields is modeled by solving the Navier-Stokes equation and Maxwell equations. No assumptions about the magnetic

Reynolds number is made. Like the Reynolds stress, an unresolved stress term related to the Lorentz force (the turbulent residual-helicity effect (α-effect)) appears and must be closed. Based on a well-established closure of using the subgrid kinetic energy for closure of non-MHD turbulent terms, the subgrid magnetic energy is introduced and its governing equation is derived. Six model coefficients appearing in the closure of LES equation are calculated dynamically and locally using the scale similarities between grid and test filtered quantities. For validation, a high-Reynolds number isotropic decaying turbulence flow with and without mean magnetic field is studied. In addition, the effects of rotation are investigated. For the studies without rotation, it is observed that the energy spectrum follows a $k^{-5/3}$ law as shown in earlier DNS observations. With rotation, it is shown that two mechanisms are involved in the energy decay. Phase scrambling due to frame rotation and Joule dissipation compete as energy dissipation mechanisms. Two distinct regimes with respect to the rotation rate are observed. There is a critical rotation rate at which the energy decays predominately by Joule dissipation instead of phase scrambling. This MHD-LDKM model is shown to be applicable to wide variety of applications regardless of the magnetic Reynolds number.

Second, a three-dimensional free-burning argon (equilibrium plasma) arc in atmospheric pressure is investigated. The effect of an external field and cross flow on the free-burning arc is studied. The aforementioned general turbulent MHD model is used in this study, which partially serves as a demonstration of the code's capability and validity. The governing equations are solved in conservative form using a hybrid scheme that combines a high-order monotonic upwind scheme with a fourth-order predictor-corrector central scheme. An implicit scheme is used to compute the magnetic diffusion term appearing in the magnetic induction equation. This term imposes serious time-step constraint if computed in an explicit fashion. The inherent advantage of this model is its capability to be adapted to high Reynolds number flow applications. The validation of the model with experimental data at different current intensities shows generally good agreement. When an external field is applied, the overall shape of the free-burning arc drastically changes. The straightening of the arc indicates the potential for stabilization of a free-burning arc by magnetic forces.

Even though the turbulence is significantly attenuated as a result of the thermal expansion near the cathode, it adds an unsteady characteristic to the arc and, in general, has a negative impact on the stabilization of the electrical discharge.

Third, in order to investigate the effects of a plasma on supersonic combustion, the electron energy equation are solved in addition to the Navier-Stokes equations and the Maxwell's equations. For this purpose, a chemical kinetic model, which considers 16 species and 76 reactions, is used to simulate and understand how the ionized and radical species contribute to hydrogen-air flames. For validating this two temperature model, one-dimensional shock tube studies are performed. All observations obtained are qualitatively consistent with past observations.

Finally, these models are combined and utilized to model plasma assisted combustion in a SCRAMJET. Two types of plasmas are investigated: an equilibrium electrical discharge (arc) and a non-equilibrium plasma jet. It is shown that both plasmas significantly increase the concentration of radicals such as O, OH and H, and both have has a positive impact on combustion. For the equilibrium plasma case, a large gradient in gas temperature induces a large baroclinic torque which is related to turbulent production, and is expected to contribute to the enhancement of mixing. For non-equilibrium plasma jet case, the effect is limited in the vicinity of the jet, and further investigation to determine the most effective way to introduce the plasma jet is needed. In this case, the recirculation regions between the injection and the step and the wake region remains unburnt. MHD control plays a important role in the equilibrium plasma case, but not in the non-equilibrium case due to insufficient ionization fraction. All results are strongly dependent on collision rates.

CHAPTER I

INTRODUCTION AND OBJECTIVES

1.1 Introduction

About 100 years ago, French engineer Renè Lorin invented the ramjet for subsonic application and published the principle in the technical review *Aèrophile*. The idea of a ramjet is rather simple in terms of machinery compared to a turbojet, since a ramjet achieves compression of the air from the forward speed of the air using only a diffuser. The compressed air is mixed with fuel and combustion occurs, and the expanded through a nozzle. Unfortunately, at that time there was no vehicle to achieve the high speeds necessary (the necessary 'ram' pressure can only obtained above a certain speed typically about 485 $[m/s]$). Renè Lorin never reached the operational phase. The advantages of a ramjet in having no moving parts, a rather low cost induced by the manufacturing simplicity, and a low fuel consumption compared to the consumption of chemical rockets have attracted researchers for a long time. Forty years after the theory of a ramjet was discovered, Leduc's experimental aircraft made the first powered flight on April 21, 1949. The first historical supersonic flight by the North-Aviation company of France took place in 1953. At that time, the aeroplane, *Griffon II*, with the combination of a turbo-ramjet engine made a world record speed of 1640 $[km/h]$. This historical success marked the beginning of the supersonic flight era.

At higher Mach number flight operation, a ramjet is less efficient (147). The increase of stagnation temperature and pressure tends to limit the performance and to increase the thermal and mechanical loads on the combustion chamber walls. To bypass the inherent problem in a ramjet of slowing the intake air to subsonic speeds for fuel mixing and combustion, the flow is allowed to be supersonic throughout the engine. this supersonic ramjet removes the condition of subsonic combustion since the diffuser used in a ramjet is no longer used. The SCRAMJET though simple is aerodynamically challenging. To achieve the successful operational of a SCRAMJET is still a current research area. In the late 1980's and

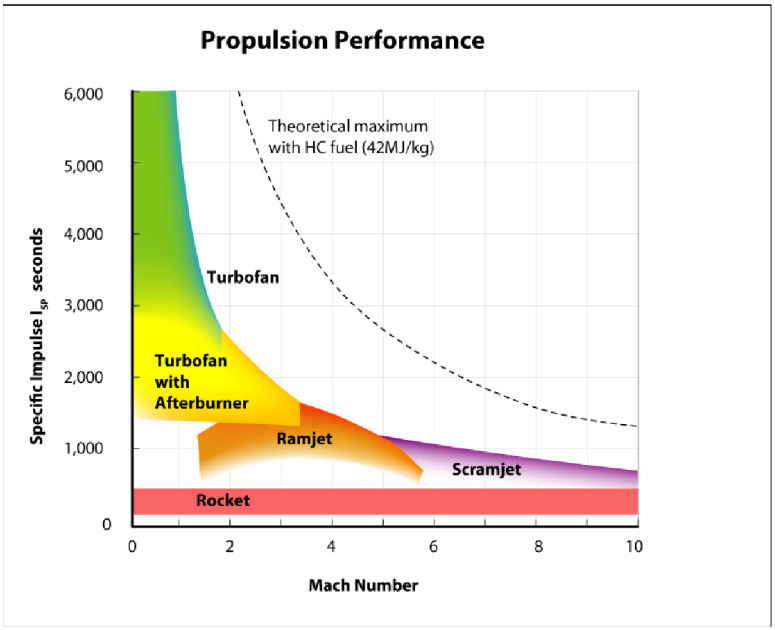

Figure 1: The specific impulse with the different Mach number (147)

early 1990's, the United States launched a large research effort (NASP program) aiming at the development of a single-state-orbit vehicle equipped with ramjet and SCRAMJET engines. This *2 billion* dollar project ended up revealing a number of technological difficulties.

1.1.1 General feature

The mechanism of a SCRAMJET is briefly explained. A more detailed explanation can be found somewhere else (24; 25; 39; 62; 135; 144). As mentioned above, the SCRAMJET is mechanically simple consisting of an inlet, a fuel injector, combustion chamber, and an exit nozzle. This mechanical simplicity is not a coincidence, but rather a requirement since, for a SCRAMJET, the kinetic energy of the supersonic inflow is significant and easily exceeds the amount of chemical energy released during combustion. For $Ma = 25$ flight, the heat released from combustion is only about 10% of the total enthalpy. This implies that it is essential to minimize aerodynamic drag such as shock wave generation. As the shock wave becomes stronger, the resultant drag drastically increases and exceeds the positive thrust produced. Moreover, the resulting compression causes the inflow to be overheated

reducing the overall combustion efficiency. Due to a high-speed flow, the residence time in the combustor is rather short. This prohibits the use of complex fuel such as kerosene and fuels such as hydrogen are typically preferred for these large flame speeds and used in most current experiments (117). Also, the combustion chamnber must be designed to make sure that fuel and oxidizer are mixed well and burn efficiently. Usually, we inject the fuel pressurized by a turbo pump (to a few hundred bar.) and expect the fuel to penetrate into the freestream flow creating turbulent motions which aid in the mixing.

There is another difficulty related to successful operation. Unlike a chemical rocket, it is rather difficult to keep the combustion rate (efficiency) constant since the compression of airflow is determined by airflow control and not by mechanical processes. Ideally, the pressure and temperature of the entering flow would be constant, but in reality, the flight occurs over a large range of altitude (pressure and temperature vary greatly) and has to be adjusted in order to avoid generating unwanted drag. Also, there is minimum and maximum Ma at which SCRAMJET can run efficiently. If the Mach number is too small, the flow is not compressed enough resulting in incomplete combustion due to a too cold flow temperature. Moreover, to keep the flow supersonic from the inlet and to the exit of the engine (at least $Ma \geq 1$), the flight vehicle speed should be high enough to keep from reducing the Mach number of the flow compression waves. Otherwise, the engine starts to "choke". It is also necessary to have a diverging combustor shape to avoid the limitations of heat addition in constant area duct causing "thermal choking" in which the higher temperature increases the sound speed and results in the reduction of Ma (67). Weber and MacKay (151) pointed out the potential superiority of the SCRAMJET engine at speeds in excess of $Ma = 7$. Therefore, to achieve such a high speed, additional propulsion systems such as ramjet, rockets and turbo engine have be combined with the SCRAMJET (113).

1.1.2 Experimental efforts

Since 1960's, there have been numerous experiments conducted in the united States. Ferri (39; 40; 41) working at RIBAL and at GASL, elucidated the chemistry of the hydrogen-air

system and investigated the effect of the turbulent mixing on the combustion efficiency. He concluded that the fixed geometry SCRAMJET engine limited the performance and suggested three-dimensional engine design. Another program at GASL during 1964-1968 designed a low-speed fixed geometry supersonic combustion ramjet designed to operate from $Ma = 3$ to 12. In addition, other SCRAMJET engines were developed under U.S.Air Force (149). NASA also started the Hypersonic Research Engine (HRE) in 1964 and built $X-15A-2$, and continued the Aerothermodynamic Integration Model (AIM) in 1970s (2). Surprisingly, AIM performance approached 70% of ideal performance and demonstrated the capability of a dual-mode engine over $Ma = 5-7$. In 1990's, DARPA started the NASP program to study SSTO vehicle concept and contributed substantially to the development of SCRAMJET engines. The program aimed to develop a hydrogen-fueled SCRAMJET to operate the wide speed range from $Ma = 4$ to 15. The detail achievement by NASP program can be found elsewhere (20). It concluded that hydrogen-fueled SCRAMJET engines have the potential for high performance at near-orbital speeds. On June 15, 2007 DARPA announced a successful SCRAMJET flight at $Ma = 10$ using rocket engines to boost the test vehicle to hypersonic speeds!

1.1.3 Scramjet performance

According to experimental observations, the main factors related to the thrust efficiency of SCRAMJETs are roughly categorized into the two parts: 1) aerodynamic drag control and 2) combustion enhancement. The former is strongly related to the geometrical changes of the SCRAMJET inlet configuration such as *a rectangular shape* (8), *a scope shape* (27) and *a jaws shape* (90). The combustion enhancement (studied in this thesis) has a significant impact on SCRAMJET performance. Combustion in high-speed environment is not efficient for the following reasons: (1) *short residence time to mix/burn* and (2) *difficulty of holding and stabilizing the flame*. Insufficient combustion cannot accelerate the flow faster than the inlet supersonic speed, and the SCRAMJET produces zero thrust.

To resolve the problem of short residence time for mixing/burning, a variety of mechanics

have been proposed seeking to shorten the ignition delay time such as (i) enhancing mixing of the fuel with air, (ii) increasing the temperature at the combustor inlet (but should be not too high!), (iii) introducing radicals, and (iv) changing the type of fuel/oxidizer. Usually hydrogen is preferable as SCRAMJET fuel since it has a high flame velocity due to its high molecular diffusivity resulting in a short ignition delay time. However, hydrocarbon-fueled SCRAMJETs for missile applications have also been investigated (HyTech program (38)). Sufficient increase of temperature and pressure is often achieved through the inlet shock waves. Enhancing mixing of fuel/air is a key factor in development of the successful supersonic combustion and is closely related to the flame holding process as mentioned below.

There are three flame stabilization techniques commonly proposed and applied in supersonic combustion. One of them is to use a bluff body such as a central injection concept (142) in which the bluff body (fuel injector) sits in the middle of freestream and acts as a flame-holder by geometric blockage of the flow, and the shedding vortices enhance mixing. The shape of the bluff body should have a minimal cross section (such as planar) in order to minimize the drag. A more complicated geometry like the ramped injector have also been proposed. It has been shown that the ramped injectors generate counter-rotating streamwise vortices to increase the mixing. A more comprehensive discussion about the bluff-body stabilization is given somewhere else (49; 50; 77; 108). Another method is to supersonically inject fuel in the normal direction. The advantage of this simple method is that bow shock produced in front of the injector causes boundary layer separation and thus the heated air and fuel mix subsonicly (a long residence time) (6; 93). The pressure losses associated with fuel injection can be controlled by changing the angle of the injections. (e.g., making the bow shock weaker) The third method is using a step or cavity. For both cases, the recirculation region formed inside the cavity or behind the step provides a location for the fuel and air to be mixed well at low velocities and where the hot products associated with the combustion process provide a continuous source of chemical radicals to stabilize the flame. A brief summary of the mechanisms of the step and the cavity related to the supersonic combustion is provided in the following section.

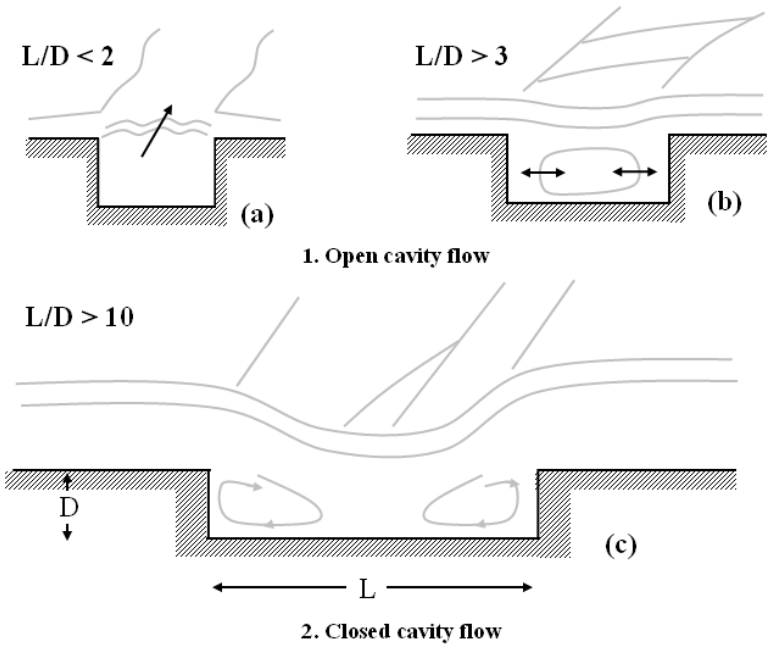

Figure 2: Schematic of cavity-driven oscillations(6)

1.1.3.1 Cavity flame holding

The distinguished character of cavities is that the cavity generates self-sustained oscillations which can introduce intense fluctuations in flow properties such as pressure, temperature and density. The cavity oscillation process is caused by the unsteady motion of the shear layer impinging on the rear wall. This causes the highly energetic freestream flow to enter the cavity resulting in the creation of compression waves (acoustic waves) that travel back and forth inside the cavity. These waves generate small vortices at the front wall, and the shear layer deflection angles increase or the spreading rate increases (6). Depending on the ratio between the cavity (D) depth and its width (L), either longitudinal oscillations or transverse oscillations are induced (see Fig. 2) (165). The transition from longitudinal oscillations to transverse oscillations is dependent on the Ma and L/D. (For example, $L/D = 2$ and $Ma = 1.5$.) When $L/D > 10$, the cavity is denoted as "closed", and the shear layer reattaches along the lower wall significantly increases drag. The cavity driven oscillations

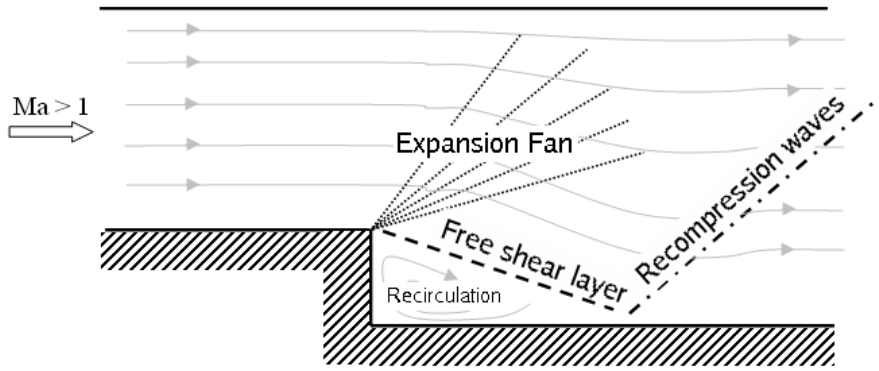

Figure 3: Schematic of the flow over the backward facing step.

can be used for the enhancement of mixing in the shear layer and have a positive impact on supersonic combustion. Sato *et al.* (125) revealed mixing was indeed enhanced by the acoustic disturbance and the efficiency of the enhancement was strongly dependent on the shape of the cavity. When oscillations with a certain frequency are introduced, large-scale coherent structures can be induced and cause the shear layer thickness to increase (163). The cavity also plays an important role of holding a flame by creating a recirculation region inside the cavity where hot products (radical pool) stay. Therefore, the cavity acts like a continuous pilot flame. The disadvantages of introducing the cavity is to have some pressure loss and that the mixing enhancement is limited to near the cavity. A more detailed discussion is given by elsewhere (6; 60; 64; 108; 125; 163; 165)

1.1.3.2 Step flame holding

Unlike the cavity, there is no rear wall in the step-wall configuration. Even though this is geometrically simple, the supersonic flow over the backward facing step is complicated and has been studied by many researchers (23; 28; 42; 79; 120; 134). The schematic of the typical flow over the backward facing step is shown in Fig. 3.

The supersonic flow expands at the step corner forming an expansion fan and a free shear layer directed toward the bottom wall. This free shear layer reattaches along the bottom wall and creates re-compression waves. There is a low pressure region behind the

expansion fan where the supersonic flow is accelerated further. Like the low speed flow seen inside the cavity, there exists the low speed flow between the shear layer and the bottom wall. This recirculation zone acts a flame holder in the exactly same manner as the cavity.

Experimental studies with downstream normal injection (28; 42; 79) show that the recirculation region increases as the fuel injection pressure increases. Mixing efficiency is more effective in this configuration than just normal injection along a flat plate. Moreover, the location of injection has a significant influence on the size of the recirculation zone between the injection and the backward facing step. Unlike the cavity case where the size of recirculation zone is fixed, the size of a recirculation zone in the step configuration can be adjustable which implies there is a potential to get better flame holding qualifies in this case. Besides, since the most effective way for stabilization of the flame is to apply turbulent processes for fuel/air mixing, the capability of the backward-facing step to generate turbulence is also considered as an effective tool. Therefore, the flow behind a backward-facing step is one of the most promising candidates for the SCRAMJET structure.

Considering the above discussion, it is easy to understand why cavity and step configuration have been preferably used for combustion enhancement and stabilization. This study considers a backward facing step with hydrogen/air combustion system.

1.1.4 Computational efforts

Due to the expensive experimental cost and the difficulty in creating realizable flow conditions (matching enthalpy and Reynolds number), numerical simulation of supersonic flows with recirculation zones have been attractive and show a lot of promise (21; 43; 44; 56; 120; 146; 154). Sahu computed $Ma = 2.46$ using two algebraic models and a two-equation $k - \epsilon$ turbulent model. The algebraic models were shown to be poor predictors of the mean velocity profiles inside the recirculation region, but the two-equation $k - \epsilon$ turbulent model did well. Chids and Caruso (21) examined the dependence of the $k - \epsilon$ turbulent model on Ma and got great agreement with the experimental data. Forsythe *et al.* used a Detached eddy simulation in which the advantages of the Large-eddy simulation (LES) and the Reynolds-averaged Navier-Stokes (RANS) are combined and applied it to an axisymmetric base flow.

In the model, RANS was used near the wall and LES was used everywhere else since LES requires fine grid resolution in the streamwise direction to resolve the small energy containing eddies. They also applied the compressibility corrections and succeeded in capturing the basic features of the complicated flow field. The results look physically reasonable. Yang (154) developed a locally implicit scheme with an anisotropic dissipation model by which the backstep corner vortex, expansion fan and oblique shock are distinctly resolved. Several researchers have studied this flow using turbulence models and investigated the turbulent effects.

Other researchers have studied supersonic flow over a step with fuel injection (29; 30; 31; 124; 146). Uenish *et al.* (146) developed a RANS model with the MacCormack's explicit method coupled with an eddy viscosity model and applied it to a realistic SCRAMJET combustor problem (H_2/Air) with a backward-facing step configuration. The results look physically reasonable. Sasse and Koschel (124) modified the k-ϵ turbulent model to include compressibility effect and validated the code with experimental data (58). Since the turbulent fluctuations play an important role in mixing (controlling the chemical reaction), they applied a statistical description by introducing a probability density function (PDF) of the thermo-chemical variable. As an application, they investigated the mixing layer (a supersonic flow air $Ma = 2.97$ and supersonic hydrogen flow $Ma_{fuel} = 1.3$ with a shear layer in the middle) and showed that the increase of temperature due to the shear stress caused ignition. Eklund *et al.* (31) numerically modeled an ethylene-fueled SCRAMJET combustor with aerodynamic ramp injector and a cavity for the $Ma = 1.8$ flow. Their model solved the Reynolds-averaged equations using an upwind scheme called Monotone Upstream-centered Schemes for Conservation Laws (MUSCL) with the Van Leer flux limiter (82) and evaluated the turbulent stresses with an eddy viscosity turbulent model. They showed a strong sensitivity of the Schmidt and Prandtl number on the turbulent modeling of the flow properties. The individual fuel jets of the ramp rapidly merged into a single plume resulting in poor fuel/air mixing. Ebrahimi *et al.* (29; 30) investigated the flow fields for SCRAMJET combustor for both rectangular and circular cross sections with ethylene-air-mixture and clarified the influence of the shape of the cross-section flow paths on the

combustion efficiency.

1.1.5 Plasma assisted combustion (PAC)

As mentioned above, a variety of approaches have been proposed to enhance or maintain combustion in supersonic flow. These geometrical changes, or passive methods such as cavities, rearward-facing steps, and bluff-bodies , do provide combustion enhancement through increased mixing, longer residence times, and flameholding. However, these devices are static in nature and may be difficult to optimize for the entire range of Mach numbers that are of interest.

A still more promising solution is the use of electrical discharges. A review about plasma assisted combustion is given by Starikovskaia (137). The plasma is expected to provide a local source of heat and radicals advancing the chemical kinetics, enhancing combustor performance, and possibly acting as a virtual flameholder to stabilize the flame during transients. Also, plasma location is easily moved as needed by the operating conditions. Moreover, the plasma may also significantly increase the baroclinic torque that is a result of non-aligned density and pressure gradients seen in the vorticity equation in the vector form (118):

$$\frac{\partial}{\partial t}\left(\frac{\rho}{\vec{\omega}}\right) + (\vec{v}\cdot\nabla)\left(\frac{\vec{\omega}}{\rho}\right) = \frac{1}{\rho}\vec{\omega}\cdot\nabla\vec{v} + \frac{1}{\rho^3}\nabla\rho\times\nabla p + \frac{1}{\rho}\nabla\times\left(\frac{1}{\rho}\nabla\cdot\tau\right) \tag{1}$$

Here, ρ, $\vec{v}$, p and τ are the density, the velocity fields, the pressure and the stress tensor, respectively. $\vec{w}$ is the vorticity field defined as $\vec{w} = \nabla\times\vec{v}$. Such torques are related to turbulent production and have been shown to be large in the plasma region (99; 129).

The types of electrical discharges can be classified as to how the plasma ionizes and dissociates the gas. Arc discharges, plasma torches, sustained radio frequency induced plasmas, and lasers supply large amounts of thermal energy (joule heating) typically resulting in high gas temperatures and highly favorable reaction rates. On the other hand, non-equilibrium plasmas including low-pressure glow, radio frequency, corona or barrier, microwave, and nano-second high-voltage discharges (3; 12; 15; 107; 150) rely on highly energetic electron collisions and radical generation to enhance combustion. These discharges

Table 1: Performance of various types of plasma-assisted combustion (84). (1) Arc, (2) DC, (3) Laser spark, (4) High-pressure glow, (5) Nano-second Pulse discharge, (6) Short-Pulse discharge and (7) corona.

Type	Power	Energy deposition	Mixing	Efficiency	Negative
1	$1-100\ kW$	◯	–	Low	Low speed region only
2	$1-100\ kW$	◯	◯	Low	Small volumetric effects
3	Wide range	◯	–	Low	Small volumetric effects
4	$1-100\ kW$	–	–	◯	High-level power
5	$0.01-1\ J/pulse$	–	–	◯	Low pressure only
6	$1-100\ J/pulse$	◯	◯	–	Complex system
7	$1\ W/cm^2$	–	–	◯	Low pressure only

result in extremely large electron temperatures ($\sim 10^4$ $[K]$) and only moderate mean flow temperature increases. Ideally, the plasma discharge should exist somewhere in between these two states in order to benefit from the high gas temperatures of the former and the high radical generation and more modest power requirements of the later (106).

Table 1 summarizes the performance of various types of the plasma assisted combustion. Generally speaking, the high energy deposition has a better mixing effect, and low efficiency because of heating the heavy particles. On the other hand, the low-energy deposition methods such as pulse discharge and corona discharge have a better efficiency in making radicals, and are limited to the low pressure applications or require complex systems.

From previous experimental observations about PAC, Calote (16) reported that the blowout limit of a premixed methane/air increased by a factor four when they applied the DC field. Also, it was reported that the burning velocity increased and the blowout limit expanded when AC was applied (89; 140). Compared with the increase of the burning velocity (blowout limit) with DC application, the improvement with AC is not sufficient. Won *et al.* investigated the influence of an electrical field on a laminar lifted propane/air flame and observed that the propagation speed of the propane edge flame increased by about 60% (153). The equilibrium plasma jet was also reported to increase flame speed and expand the flammability limit in the premixed flames (17). Other recent experimental work using the non-equilibrium plasma are also reported by many authors (22; 48; 84; 87; 138).

From recent experimental observation related to the SCRAMJET application, Leonov and Yarantsev (84) have noted that electrical discharges existing in an non-equilibrium

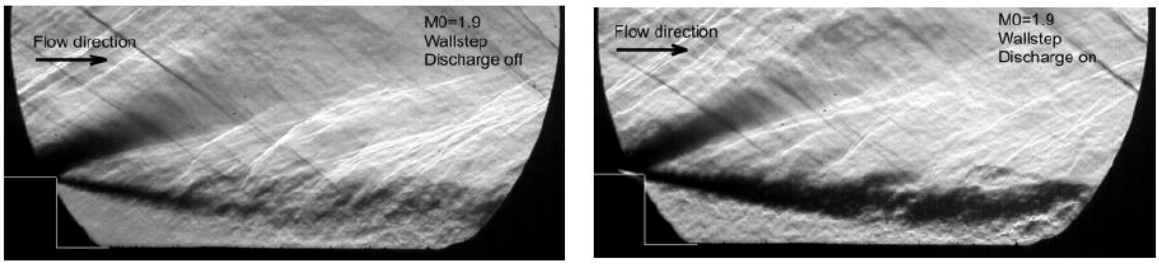

(a) Arc off

(b) Arc on

Figure 4: Schlieren photos of the discharge effects on the shear layer (84)

thermodynamic state and applied in a non-uniform manner offer the highest advantages in plasma-assisted combustion. In their experiment, $Ma = 2$ supersonic premixed (Air/H_2 or Air/C_2H_4) are introduced, and the anode and cathode are mounted at the top wall of the step and the bottom wall, respectively. Current input varies from $5A$ to $20A$. Due to the flow fluctuations inside the cavity, the S-type of the plasma cords are observed in a cavity case, resulting in the voltage vibration. On the other hand, the shape of plasmas become straight in the backward facing step case. Also, the detailed temperature measurement of the electron is about $T_e = 10,000K \sim 16,000K$ in which the plasma-chemical reaction surely occurs. However, the analysis of the N_2 spectra shows that the rotational temperature is about $T_{rot} = 2,800K \sim 3,200K$. It means that the strong non-equilibrium discharge (radicals are created.) is achieved even at the atmospheric pressure. Moreover, the flow structure is greatly influenced by the discharge. Figures 4 show the schlieren visualization with/without the discharge. It is clearly seen that the turbulence behind the step is intensified significantly and a much thicker shear layer is formed. These results show the positive impact of the electrical discharge on the SCRAMJET combustor performance by enhancement of mixing and generation of radicals. This innovative experimental work gives me an opportunity to develop the computational modeling for the supersonic plasma assisted combustion over the backward facing step.

1.2 Motivation and Objectives

The purpose of this thesis is to develop a comprehensive numerical model to simulate H_2/Air combustion in the SCRAMJET combustor configuration with the backward facing step. As a result of little computational and experimental data, there is no versatile solution to the design and application of PAC. Therefore, the computational model for this application has been desired and can be a powerful tool to give a deep insight into the next generation supersonic combustion system.

However, it is extremely difficult to model PAC from the numerical viewpoint. Complexity of modeling the PAC raises from the following reasons:

1. Complex interaction between flow fields and magnetic/electric fields
2. Large gradient of flow properties (gas temperature at plasma discharge: $\sim 10^4 K$ and the temperature of incoming flow: $\sim 300 K$)
3. Turbulent state of flow
4. Requirement of high temperature detail chemical kinetics
5. Chemically/thermally non-equilibrium state

In this study, the following tasks are defined in order to resolve these problems:

- **Task 1: Development of large-eddy simulation for MHD turbulence**

To develop and validate a new dynamic subgrid model for an electrically conducting fluid is the main part of this investigation. The proposed MHD turbulent solver should be applicable to numerous applications, including both MHD flows at high magnetic Reynolds number case in which the magnetic field and velocity field are highly coupled (for example, astrophysical/fusion plasma) and at low magnetic Reynolds number case in which the flow field does not effect the magnetic field significantly, but the magnetic field does (for example, localized plasma-arc). The detailed explanation of "magnetic Reynolds number" will

be discussed later. Moreover, the modeling procedure should be easily incorporated into a well-established compressible LES solver. Therefore, effort is made to reduce the introduction of unnecessary modeling coefficients, and the model coefficients are determined locally and dynamically instead of from experimental data. For a validation purpose, the proposed code will be tested for high-Re decaying isotropic decay turbulence with and without a mean magnetic field, and the effect of rotation is also studied.

- **Task 2: Development of equilibrium argon plasma-arc modeling**

Accurate modeling for the electrical discharge is necessary. A simple argon free-burning arc is modeled performed using empirical data for the thermal properties. The main purpose of these studies are to capture the external field effect on the flow field by solving the Poisson equation for the electrical and magnetic potentials. Moreover, the effect of the cross-flow and the constant external field on the arc column structure are also examined. Numerical difficulty related to the stiff systems of the diffusion equation for the magnetic field are addressed. A careful validation has been performed based on the published reference.

- **Task 3: Modeling of supersonic non-reacting (argon) / reacting (H_2/Air) flow over the backward facing step with MHD effect**

As an application of *Task 1* and *Task 2*, the electric discharge model is implemented in the realistic SCRAMJET combustor environment. First, the electrical discharge (continuous arc) is assumed to be in the local thermodynamic equilibrium (LTE). It is investigated how the electrical discharge influences on non-reacting argon flow fields with two different locations of the discharge. Second, reacting supersonic flow (H_2/Air) are performed using the turbulent chemistry closures (Eddy-Break-Up model) and high-temperature chemistry developed by Park (109). We investigate the enhancement of mixing fuel/air by supplying large amounts of thermal energy in the non premixed supersonic flow. Since the large current

density is induced near the step corner and finite electric conductivity exists, the flow may be controlled by the magnetic field. Therefore, we introduce the constant/oscillating magnetic field to see a potential of enhance mixing in the shear layer resulting the increase of the fuel penetration. Third, the effect of non-equilibrium plasma jet on the supersonic combustion is investigated. Since the input power required to sustain/initial the equilibrium plasma is significant and is not practical in an operational condition. Therefore, the application of cold plasma jet (non-equilibrium plasma jet) is considered and modeled. In the cold plasma, the electron temperature is $\sim 20,000K$, but the heavy particle temperature can be $1 \sim 2$ orders lower than the electron temperature. It implies that input power to generate the plasm efficiently enters into the chemical energy of the gas (generating radicals) instead of the thermal energy. Modeling for this type of plasma, the two-temperature model is developed, and newly the electron energy equation is also calculated. The SCRAMJET configuration with the cold plasma jet have been investigated, and the capability of cold plasma to hold the flame in the supersonic environment is evaluated.

1.3 Thesis Outline

The thesis is organized as follows:

1. Chapter 2 introduces the governing equations including Navier-Stokes equations and Maxwell's equations based on electrodynamics and hydrodynamics. We make some realistic assumptions for our system of interest and provide a detailed explanation for them.

2. Chapter 3 shows the formulation of the large eddy simulation equations based on the governing equations and the resulting subgrid terms related to MHD turbulence. The subgrid magnetic energy equation is derived. The method of calculating the six model coefficients using the local dynamic subgrid closure is discussed.

3. Chapter 4 explains the numerical implementations such as staggered-grid, the divergence-free condition of magnetic field, and the dual time step for the diffusion equations for the magnetic field.

4. Chapter 5 shows numerical results and validation of the newly developed MHD turbulent code. The decaying MHD isotropic turbulence is examined under the condition of imposing the external fields and the frame rotation. Energy spectra, dissipation spectra and the histories of the model coefficients are investigated.

5. Chapter 6 gives a validation of the electrical discharge model for the equilibrium argon arc. We compare our LES results with the experimental data with different input power. Moreover, the external field and laminar/turbulent cross flow effects on the arc column are examined.

6. Chapter 7 describes how the electrical discharge effects the non-reacting supersonic flow (argon) over the backward facing step. Three different locations of the electrodes are tested.

7. Chapter 8 extends the non-reacting flow discussed in Chapter 7 to reacting flow (H_2/Air) and shows the capability of the electrical discharge to hold the flame at $Ma = 3.5$ supersonic flow. Also, a constant/oscillating external magnetic field is introduced to investigate how MHD flow control may impact combustion performance.

8. Chapter 9 formulates the non-equilibrium plasma (two-temperature model), and we apply it to the supersonic combustion case. The configuration is the same as Leonov's experiment's setp-up (84). The capability of the cold plasma to produce radicals effectively is examined, and its ability to hold the flame is investigated.

9. Chapter 10 provides the conclusions and some suggestions for future research.

CHAPTER II

GOVERNING EQUATION

In this chapter, the governing equations describing the system of interest are introduced. In the derivation of them, we adapt some realistic assumptions for simplification and will explain them in detail. Since we consider the interaction between the fluid motion and the electromagnetic field, we divide the section into two parts: 1) Electromagnetics and 2) Hydrodynamics. The main linkage between these two is the nonlinear force called Lorentz force and corresponding work terms. This nonlinear force is mathematically similar to the viscous stress and will be discussed later.

2.1 Electromagnetics

Maxwell's equations are a set of four fundamental equations governing the behavior of electromagnetic fields and the interaction of the electric, magnetic, and charge density fields in a electrically charged medium. With the exception of a single term, Maxwell's equation were not new, but they did provide a concise mathematical framework for the study of electromagnetism. These equations along with the equation for charge conservation and the force law embody the basic principles of electrodynamics and are given in vector form as:

$$\nabla \times \vec{E} = -\frac{\partial \vec{B}}{\partial t} \qquad \text{Faraday's Law} \tag{2}$$

$$\nabla \times \vec{B} = \mu_0 \left(\vec{J} + \epsilon_0 \frac{\partial \vec{E}}{\partial t} \right) \qquad \text{Ampere-Maxwell equation} \tag{3}$$

$$\nabla \cdot \vec{E} = \frac{\rho_e}{\epsilon_0} \qquad \text{Gauss's law} \tag{4}$$

$$\nabla \cdot \vec{B} = 0 \qquad \text{Solenoidal nature of } \vec{B} \tag{5}$$

$$\nabla \cdot \vec{J} = -\frac{\partial \rho_e}{\partial t} \qquad \text{Charge conservation} \tag{6}$$

$$\vec{F} = q\vec{E} + \vec{J} \times \vec{B} \qquad \text{Electrostatic force plus Lorentz force} \tag{7}$$

Here, the constant q is the unit electric charge. The constant ϵ_0 is the permittivity of free space. Faraday's Law describes how an electric field (EMF) can be induced by time-varying magnetic flux. Note the Lorentz force ($\vec{J} \times \vec{B}$) is perpendicular to the velocity field, and the magnetic field does not explicitly provide the particle with energy. But through Faraday's Law, the induced electric field can accelerate the particles (the magnetic field implicitly accelerates it.). Ampere-Maxwell equation tells us that a magnetic field is created as a result of a moving charge. Two kinds of current are considered: the current density $\vec{J}$ related to the charged-particles "physical" motion and the displacement current, $\epsilon_0 \frac{\partial \vec{E}}{\partial t}$, which is not related to any physical motion of the electron. Gauss's law relates the spacial charge distribution to the electric potential V (the static electric field: $E_s = -\nabla V$). The resulting static electric field is irrotational. Therefore, $\vec{E}$ in Faraday's Law can be decomposed into the time-varying non-solenoidal E_i and the static solenoidal E_s. This results in : $\nabla \cdot \vec{E_i} = 0$ and $\nabla \times \vec{E_s} = 0$

Eq. (5) results from taking the derivative of Eq. (2), and it enables us to introduce the magnetic potential A. The charge conservation equation is obtained by taking the divergence of Ampere-Maxwell equation, Eq. (3), and modified by Gauss's law. It is not an independent equation. This simply says that the change of the net charge inside the box of interest is equal to the current density flowing through the surface. The last equation, Eq. (7), is the force per unit volume acting on the conductor with the charge density ρ_e. The first term represents the body force due to the electric field. The second one comes from the Lorentz force resulting from the relative motion in the magnetic field.

For the purposes of magnetohyrdodynamics (MHD), several assumptions are made to reduce Maxwell's equations. The charge density is assumed to be negligible (e.g., $\rho_e \approx 0$), which leads to result that both the electric (current) field and the magnetic field are solenoidal. This assumption is reasonable for plasmas, but not valid where the charge separation is appreciable (i.e. sheath regions) or in extremely low pressure systems. As a result both the electric and the magnetic fields can be described using potential functions. Also, the displacement current, $\epsilon_0 \frac{\partial \vec{E}}{\partial t}$, is assumed to be small compared to the current density $\vec{J}$. This is certainly valid for most MHD applications. In this sence, electromagnetic waves prapagating due to the exchange of energy between electric and magnetic forms with the speed of light is ignored. Further, the electrostatic force is assumed to be negligible compared to the Lorentz force.

The above electrodynamic equations are not complete. The magnetic and electric fields are uniquely determined since the divergence and circulation of both these fields are specified by Maxwell's equations. However, in terms of modeling, we need a way to relate the state of the electrically charged medium with Maxwell's equations. The way this is done is by use of $\vec{J}$ and the macroscopic property σ, the electrical conductivity. The current density is then related to the electrical field through Ohm's law. Ohm's law can be derived from the electron momentum equation

$$\rho_e \left[\frac{\partial \vec{u}_e}{\partial t} + (\vec{u}_e \cdot \nabla) \vec{u}_e \right] + \nabla p_e = -q n_e \vec{E} - \vec{J} \times \vec{B} + \sum_k m_e n_e \nu_{ek} (\vec{u}_k - \vec{u}_e) \tag{8}$$

Here, $\vec{u}_e$ and m_e is the electron velocity fields and mass, respectively. And, $\vec{u}_k$ is the k^{th} species velocity (the average of $\vec{u}_k$ should be equal to the bulk velocity of conducting flow.), and p_e is the electron pressure. On the right-hand side of the above equation, the first term is the electrostatic force, the second term accounts for the Lorentz force, and the last term accounts for the momentum exchanged in electron-k^{th} species (ion or neutral) collisions. To derive the above equation, we assume that the velocity distribution is close to Maxwell's distribution and the random motion is much larger than the mean velocity ($\vec{u}_e$).

Given that the electron inertial term is ignored and the relative velocity between ions and neutral ($\sim \vec{u}$) are zero and using $\vec{J} \sim q n_e (\vec{u} - \vec{u}_e)$ to eliminate $\vec{u}_e$ in Eq. (8), the

following equation for Ohm's law can be derived,

$$\vec{E}' = \vec{E} + \vec{u} \times \vec{B} = \frac{\vec{J}}{\sigma} + \frac{\vec{J} \times \vec{B} - \nabla p_e}{q n_e} \tag{9}$$

Here, the Hall current ($\vec{J} \times \vec{B}/qm_e$) and the current resulting in electron pressure gradients ($\nabla p_e/qn_e$) appear. If the Hall current and the electron pressure are assumed negligible, Ohm's law becomes a simple linear relationship with conductivity:

$$\vec{J} = \sigma \vec{E}' = \sigma(\vec{E} + \vec{u} \times \vec{B}) \tag{10}$$

From a modeling standpoint, Maxwell's equation are not convenient. A conservative form of the governing equation is preferred. Thus, with this perspective, a conservative equation for the magnetic field, called the magnetic induction equation is derived by rearranging and combining Maxwell's equations. In order to reduce the number of independent variables, Faraday's law, Ampere's law, and Ohm's law are combined to eliminate the electric field and the current density resulting in a transport equation for the magnetic field often called the magnetic induction equation:

$$\frac{\partial \vec{B}}{\partial t} = \nabla \times \left(\vec{u} \times \vec{B}\right) - \frac{1}{\mu_0} \nabla \times \left[\bar{\bar{\eta}} \cdot \left(\nabla \times \vec{B}\right)\right] \tag{11}$$

Where $\bar{\bar{\eta}}$ is resistivity tensor. If the gradient of the electron pressure and the Hall current are negligible when the flow density is high enough, then the resistivity tensor simplifies to a scalar equal to the inverse of the conductivity ($= \frac{1}{\sigma}$) as seen in Eq. (10). The first term on the right-hand side represents a convective transport of magnetic fields while the second term on the right-hand side represents the resistive dissipation or diffusion of magnetic fields (because of this finite diffusivity, the magnetic fields dissipates, and the corresponding magnetic energy s convected into the thermal energy.). It should be noted that this viewpoint of the magnetic field is preferable from a modeling standpoint, but physically the magnetic field is really not transported in the same way as a momentum flux. Regardless, we often think of the magnetic field in a similar way. The analogy between the induction equation and the vorticity equation gives us a insight about how the magnetic field

evolves. For example, the "stretching" effect is a key mechanism by which both vorticity and magnetic field are intensified or weakened. A detailed discussion is given by Shercliff (131).

The magnetic induction equation is greatly simplified using the solenoidal condition of the magnetic field. Thus, the equations governing the dynamics of electrically conducting flows simplify to the following,

$$\nabla \cdot \vec{B} = 0 \qquad \text{or} \qquad \nabla^2 \vec{A} = 0 \tag{12}$$

$$\nabla \cdot \vec{J} = 0 \qquad \text{or} \qquad \nabla^2 \phi = 0 \tag{13}$$

$$\frac{\partial \vec{B}}{\partial t} = \nabla \times \left(\vec{u} \times \vec{B} \right) + \nabla(\lambda \nabla \vec{B}) \tag{14}$$

where λ is the the magnetic diffusivity defined as $\lambda = (\mu_o \sigma)^{-1}$. Note the top two equations of above equations are only used for a calculation of the external field in this study.

2.2 Magnetohydrodynamics

In this subsection, we introduce the governing equations for magnetohydrodynamics in tensor notation. These equations are a combination of the electrodynamics equations and the equations of hydrodynamics. However, it is first important to mention when the effects of Maxwell's equations and the equations of electromagnetics are important in a conducting flow. The relative motion between the flow and magnetic field tends to be reduced by the induced current and relevant magnetic fields. In this sense, the conducting flow drags magnetic field line, and vise versa. This is the whole point of MHD. When are their effects significant? Like Reynolds number Re describing the relative importance of shear force and inertial force, there are three important non-dimensional parameters in the MHD system that determine this interaction: the parameter ($N = \sigma \mathbf{B}^2/\rho u$), Hartman number

($H_a = |\vec{B}|l(\sigma/\rho\nu)^{1/2}$), and magnetic Reynolds number ($R_m = \sigma\mu_o ul$). Here, σ, ν and μ_o are the electrical electrical conductivity, the kinematic viscosity, and the magnetic permeability, respectively. Physically, N shows the ratio of Lorentz forces to the inertia, and H_a does the ratio of Lorentz forces to the shear forces, and R_m does the ratio of the advection to the diffusion of the magnetic field. It is interesting to know that the characteristic length scale is important in MHD system (in R_m). To explain this, we introduce the concept of the magnetic diffusivity. When this diffusivity is large (R_m is small), the induced magnetic field quickly diffuses away and mutual interaction becomes less significant. On the other hand, when this diffusivity is small (R_m is large), the characteristic of magnetic diffusion becomes large and there is enough time for magnetic fields and flows to interact. In the former case, the induced magnetic fields are often ignored and only constant fields (external fields) are considered. This assumption is called *low magnetic Reynolds assumption* that is usually used for the various applications seen in the laboratory. With this in mind, th equation of MHD are introduced and will be simplified into a conservative form. We will discuss this assumption in next section.

An electrically conducting fluid is governed by the Navier-Stokes equations with the addition of a Lorentz force term in the momentum equation, and a corresponding work term in the energy equation. Those additional source terms are determined by Maxwell's equations (Eq. 12,13 and 14) In this study, we use the full compressible form that is similar to earlier model (54; 160), which can be used to study the high Mach number flows of future interests (e.g., (99)).

$$\frac{\partial \rho}{\partial t} + \frac{\partial \rho u_i}{\partial x_i} = 0 \tag{15}$$

$$\frac{\partial \rho u_i}{\partial t} + \frac{\partial}{\partial x_j}\left(\rho u_i u_j + p\delta_{ij} - \tau_{ij}\right) = F_{MHD,i} \tag{16}$$

$$\frac{\partial \rho E_g}{\partial t} + \frac{\partial}{\partial x_i}\left[\left(\rho E_g + p\right) u_i - \kappa \frac{\partial T}{\partial x_i} - u_j \tau_{ij}\right] = Q_{MHD} \tag{17}$$

$$\frac{\partial \rho Y_m}{\partial t} + \frac{\partial}{\partial x_i}\left[\rho Y_m \left(u_i + V_{i,m}\right)\right] = \dot{\omega}_m \tag{18}$$

$$p = \rho R T \tag{19}$$

The source terms, $F_{MHD,i}$ $(= \epsilon_{i,j,k} J_j B_i = \frac{\partial T_{ij}}{\partial x_j})$ and Q_{MHD} $(= J_k E_k)$ are equal to the electromagnetic force and the electrical power, respectively. The density, velocity components, thermodynamic pressure, gas constant, temperature, gasdynamic energy density per unit mass, species mass fraction, and the species mass reaction rate per unit volume are denoted as ρ, u_i, p, R, T, E_g, Y_m, and $\dot{\omega}$, respectively.

In momentum equation, Eq. (16), τ_{ij} is the viscous shear tensor defined as:

$$\tau_{ij} = \nu\left(\frac{\partial u_i}{\partial x_j} + \frac{\partial u_j}{\partial x_i}\right) - \frac{2}{3}\nu\frac{\partial u_k}{\partial x_k}\delta_{ij} \tag{20}$$

and T_{ij} seen in $F_{MHD,i}$ is Maxwell stress related to the Lorentz force $(\vec{J} \times \vec{B})$ defined as (5):

$$\frac{\partial T_{ij}}{\partial x_j} = \epsilon_{ijk} J_j B_k = \frac{\partial}{\partial x_j}\left\{\frac{B_i B_j}{\mu_0} - \frac{B_k B_k}{2\mu_0}\delta_{ij}\right\} \tag{21}$$

Here, J_k is the current density. The first term in Eq. (21) is similar to the viscous stress, and the second one is the magnetic pressure term. The magnetic pressure usually does not play an important role in the fluid system of interest. Since it is an irrotational force, it can be merged with the hydrodynamic pressure. The first part behaves like an elastic band that creates intrinsic MHD phenomena. (it is sometimes called "Faraday tensions".) This term becomes significantly important when R_m is large, since the magnetic field is frozen into the fluid and results in a strong mutual interaction. On the other hand, when R_m is small, we can simplify the system and will discuss this in the following subsection.

The significance of this expression is that we can replace the expression of the body force $(\epsilon_{ijk} J_j B_k)$ with a surface stress expression and treat it in a similar manner as the

viscous tensor. This means that we only need to specify the surface condition of the control volumes and do a surface integral.

When the electrical conductivity is zero, there is no current density. In such a case, the Lorentz force does not effect the hydrodynamic system. However, the last form of the Lorentz force in Eq. (21) may confuse us since it does not explicitly show the dependence of the electrical conductivity. In fact, when the electrical conductivity is zero, the first term and second term of T_{ij} does not necessary become zero. However, the derivatives of these term cancel each other. In this sense, T_{ij} is a fictitious stress!

In energy equation Eq. (17), q_i is the heat flux that is the sum of the thermal conduction and the enthalpy diffusion related to the species diffusion flux. It is defined as:

$$q_i = \kappa \frac{\partial T}{\partial x_i} + \rho \sum_m h_m Y_m V_{i,m} \tag{22}$$

Here, κ is the thermal conductivity and calculated as $\kappa = C_{p,mix}\mu/Pr$ where Cp_{mix} is the mass averaged specific heat, and Pr is the Prandtle number. h_m is the mth species enthalpy per unit mass and give by:

$$h_m = \Delta h^0_{h,m} + \int_{T_o}^{T} C_{p,m}(T')dT' \tag{23}$$

where $\Delta h^0_{h,m}$ is the formation enthalpy at the reference temperature (T_o). Using this expression, the temperature for the thermally perfect gas is calculated iteratively. $V_{i,m}$ is the species diffusion speed defined as

$$V_{i,m} = -\frac{D_m}{Y_m}\frac{\partial X_i}{\partial Y_m} \tag{24}$$

where D_m is the mass averaged molecular diffusion coefficient. There is no other diffusion mechanism related to temperature (Soret) nor pressure (Dufor) gradients. The detailed discussion related to the $V_{j,m}$ is given by Menon and Patel (97).

The electrical power per unit volume, $Q_{MHD} = J_k E_k$, can be rewritten to put the MHD

energy equation in a conservative form. Using a vector identity, $J_k E_k$ is expressed by B_k and E_k as :

$$J_k E_k = -\frac{1}{\mu_o}\epsilon_{kij}\frac{\partial \epsilon_{kij} B_i E_j}{\partial x_k} = B_i \epsilon_{ijk}\frac{\partial E_j}{\partial x_k} - E_j \epsilon_{jki}\frac{\partial B_i}{\partial x_k} \tag{25}$$

Then, utilizing Faraday's law, Ampere's law, and a vector identity in the above equation, the electrical power can be rewritten as:

$$J_k E_k = -\left[\frac{\partial}{\partial t}\left(\frac{B_k B_k}{2\mu_0}\right) + \frac{\partial}{\partial x_k}\left(\frac{\epsilon_{kij} E_i B_j}{\mu_0}\right)\right] \tag{26}$$

The first term is the rate of change of the magnetic energy density, and the second term is the Poynting flux of electromagnetic energy. The Poynting flux shows the net increase of the magnetic energy energy ($\frac{B_k B_k}{2\mu_0}$) and the electrical power ($E_k J_k$) in the control volume is equal to the surface integral of the Poynting flux. Furthermore, if the total energy density is redefined as the summation of the gasdynamic energy density plus the magnetic field energy density ($E = E_g + B^2/2\mu_0$), then the MHD energy and momentum conservation equation can be written in conservative form. Separating the conservation equations into inviscid and diffusive/resistive parts, the following equations combined with above equations are the governing equations for MHD:

$$\frac{\partial \rho u_i}{\partial t} + \frac{\partial}{\partial x_j}\left(\rho u_i u_j + p\delta_{ij} - T_{ij}\right) - \frac{\partial}{\partial x_j}\left(\tau_{ij}\right) = 0 \tag{27}$$

$$\frac{\partial \rho E}{\partial t} + \frac{\partial}{\partial x_i}\left[\left(\rho E + p\right) u_i - T_{ij} u_j\right] + \frac{\partial}{\partial x_i}\left(\epsilon_{i,j,k} E_j^{'} B_k - \kappa\frac{\partial T}{\partial x_i} - u_j \tau_{ij}\right) = 0 \tag{28}$$

$$\frac{\partial}{\partial x_i}\frac{\partial A_j}{\partial x_i} = 0 \tag{29}$$

$$\frac{\partial}{\partial x_i}\frac{\partial \phi}{\partial x_i} = 0 \tag{30}$$

$$\frac{\partial B_i}{\partial t} + \frac{\partial}{\partial x_j}\left(u_j B_i - B_j u_i - \lambda \frac{\partial B_i}{\partial x_j}\right) = 0 \tag{31}$$

In the state equation Eq. (19), the gas constant for the mixture is calculated by

$$R = \frac{R_u}{MW_{mix}} = R_u \sum_m \frac{Y_m}{MW_m} \tag{32}$$

where R_u is the universal gas constant.

2.3 Supplemental governing equations

In this section, some additional equations to be used for applications of interest in this study are introduced. They are simultaneously calculated with the above equations or replaced with some of them under specific assumptions.

2.3.1 External Fields Calculation.

For the purposes of MHD applications, external magnetic and electric fields are distinguished from the electromagnetic fields of the conducting flow. For example, a conducting flow over a solid surface feels the presence of a magnetic dipole inside the surface, but the magnetic field is not a property of the flow and thus is considered as a separate external field. Another example is the electric field created between two electrodes. These external fields are specified through boundary conditions and are considered separate from the magnetic and electric fields of the flow. From this point forward, the subscript "ex" is used to denote an external field, while no subscript implies that is a field quantity resulting from the conducting flow.

As imposing the external field which can be constant or a time-dependent variable, the additional terms have to be added into the magnetic field that is calculated in Eq. 14. As a result, B_i is replaced with $B_{T,i}$, which is the sum of the mean magnetic field ($B_{ex,i}$), the magnetic field induced by an external current (for example, arc current) ($J_{ex,i}$) and the fluctuation of the magnetic field (b_i). Similarly, $J_{T,i}$ ($= J_{ex,i} + \sigma \epsilon_{ijk} u_j B_{T,k}$) contains two parts of currents: mean current related to the imposed external current ($J_{ex,i}$) and

the fluctuation related to the interaction between the velocity and the magnetic field ($\sigma(\epsilon_{ijk}u_jB_{T,k})$).

Consequently, additional terms must appear in the governing equations of momentum Eq. (16) and energy conservation (Eq. 17). These terms are treated as additional source terms. For the momentum equation, the additional source term, $F_{ex,i}$ is given by:

$$F_{ex,i} = \epsilon_{i,j,k}J_{T,j}B_{T,i} - \epsilon_{i,j,k}J_jB_i = \epsilon_{i,j,k}J_jB_{ex,i} + \epsilon_{i,j,k}J_{ex,j}B_i + \epsilon_{i,j,k}J_{ex,j}B_{ex_i} \tag{33}$$

For the energy equation (Eq. 17), the additional source term, Q_{ex} similarly becomes

$$Q_{ex} = J_{T,k}E_{T,k} - J_kE_k = J_kE_{ex,k} + J_{ex,k}E_k + J_{ex,k}E_{ex,k} \tag{34}$$

In the magnetic induction equation, Eq. (14), the additional term, $M_{ex,k}$ is defined as

$$M_{ex,k} = \epsilon_{kij}\frac{\partial E_j}{\partial x_i} \tag{35}$$

These terms set simply to be zero when we does not impose any external field and no further modification is required.

2.3.2 Thermally Non-equilibrium Model.

When the heavy particle's translational-rotational temperature and vibration-electron temperature are not same, thermodynamic non-equilibrium occurs. At high pressure (e.g., atmospheric pressure), the number of collisions between particles are significant, and they quickly start to have the "common" temperature (e.g., equilibrium temperature). On the other hand, in the low pressure environment, there is a finite time for them to collide and do not transfer their energies significantly and equilibrium is approached in a finite time scale. For example, behind shock waves, the translational energy is immediately transfered into the thermal energy due to effective energy transfer mechanism, but vibration-electron temperature is still low due to the shortage of collisions. This non-equilibrium thermochemical relaxation can not be captured by a single temperature model mentioned above. In this study, we develop a "simple" two-temperature model. "Simple" implies that the model

does not consider turbulent effects on the corresponding additional governing equations and is mathematically similar to the laminar chemistry approach.

Chul Park did a pioneering work about the study of radiation, chemically/thermodynamic non-equilibrium air kinetics and developed a two-temperature model (109; 110). The necessity of introducing a two-temperature model is a result of the disparity between the experimental observations and predictions from conventional chemical kinetics (one temperature model). Using a one temperature model, the peak intensity of radiation occurs right after the shock where the temperature peaks. However, this was not observed from experiments, and there was some distance between the temperature peak and the radiation peak. This disparity has successfully been resolved by the multi-temperature model in which the vibrational temperature (T_v) is included as being different from the translational temperature (T). Park assumed that the electron temperature (T_e) is the same as T_v, and T is the same as the rotational temperature (T_r). Considering the influence of the T_v (T_e) on the chemical reaction, he newly introduced T_a defined as:

$$T_a = T^s T_v^{1-s} = T^s T_e^{1-s} \tag{36}$$

where s is between $0.5 - 0.7$. He named it as "Two-temperature model" that we use for our thermally non-equilibrium model developed here.

Considering this non-equilibrium effect and using this well-known model, there is a necessity to calculate the vibration-electron temperature separately. In this model, we use the free electron temperature in Park's two-temperature model. Thus, we do not consider vibrational energy. By introducing the electron energy equation, we calculate the electron temperature associated with its translation. The electron energy equation is given by (59; 83):

$$\frac{\partial \rho_e E_e}{\partial t} = -\frac{\partial E_e u_i}{\partial x_i} - p_e \frac{\partial u_i}{\partial x_i} + \frac{J_k J_k}{\sigma} + -\Delta \dot{\epsilon}_{e,h} + \frac{\partial}{\partial x_j}\left(k_e \frac{\partial T_e}{\partial x_i}\right) - \sum \omega_{k+1} \chi_{k \to k+1} \tag{37}$$

where E_e is the electron energy per mass defined as :

$$E_e = \frac{3}{2} n_e k_B T_e \tag{38}$$

Here, k_B is the Boltzman constant and n_e is the electron number density. Assuming the quasi-neutrality, n_e can be calculated as:

$$n_e = \sum_{m=1}^{6} Z_m n_m = \frac{\rho_e}{m_e} \tag{39}$$

where Z_m is charge number. using this quasi-neutrality assumption, it is not necessary to solve the momentum equation of electron (Eq.8). This is valid under the assumption that the characteristic system of the interest is larger than the Debye distance, λ_d defined as:

$$\lambda_d = \sqrt{\frac{\epsilon_0 k_B T_e}{n_e q^2}} \tag{40}$$

Inside the Debye distance, the electric field is uniformly distributed, but outside it, the electric field rapidly decreases. For the high pressure environment of our interest, λ_d is small (For $n_e \sim 10^{18}\ m^{-3}$ and $T_e \sim 10^4\ K$, λ_d is about $\sim 10^{-6}\ m$). Therefore, it is reasonable for us to use the quasi-neutrality assumption.

The first term in the right-hand side is the convective term, and the second one is the pressure work term. Here, the electron pressure is defined as:

$$P_e = n_e k_B T_e \tag{41}$$

The third term is the ohmic heating. Note for the non-equilibrium system, the ohmic heating term only appears in the electron energy equation not in the heavy particle equation, Eq. (17). The important physics to be noticed here is that energy is cascaded from the input power into the electron (from the surrounding plasma) to heavy particle by thermal energy dissipation. Therefore, there is no Joule heating term in energy equation of heavy particle.

The electric conductivity, σ, is a function of the electron density and collision frequency ($= \Gamma_{e,h}$):

$$\sigma = \frac{q^2 n_e^2}{2 m_e \Gamma_{e,h}} \tag{42}$$

When there is a strong magnetic field, σ becomes a tensor since the electron movement that is perpendicular to the magnetic field is reduced (electron are trapped by the fields), and the electric conductivity can be expressed by (55):

$$\sigma_\perp = \frac{\sigma_\parallel}{1 + \Omega^2} \tag{43}$$

where Ω is the Hall parameter that is large when the magnetic field is large and the pressure is small. But in our system, these effects are small, and Eq. 42 is used for the rest of studies. $\Gamma_{e,h}$ is given by:

$$\nu_{e,h} = \frac{\Gamma_{e,h}}{n_e} = \frac{1}{2} C_e n_h \sum Q_e, h \tag{44}$$

Here, $\nu_{e,h}$ is the collision frequency of an electron per unit volume and time, and C_e is the average speed of electron given by:

$$C_e = \sqrt{\frac{8 k_B T_e}{\pi m_e}} \tag{45}$$

Also, n_h is the heavy particle (neutral and ion species) mass density, and $Q_{e,h}$ is the collisional cross section that is usually found at a literature.

The energy cascade is denoted as the forth term $\Delta\dot{\epsilon}$ defined as:

$$\triangle \dot{\epsilon}_{e,h} = \frac{3 \rho_e \nu_{e,h}}{M_h} k_B (T_e - T) \tag{46}$$

This describes the heat transfer between heavy particle and electron due to the binary collision (83). This is a strong function of pressure since ρ_e and $\nu_{e,h}$ increases rapidly with the increase of pressure. Therefore, for the high pressure environment, T_e and T equilibrate immediately resulting in the thermal equilibrium state.

The last term is the energy loss of electron due to inelastic electron-impact process such as ionization, dissociation and recombination. Here, ω is the reaction rate and $\chi_{k\to k+1}$ is the difference of the formation enthalpy at that temperature between the products and the reactants. When the electron recombines with the positive ions, we subtract the total electron energy by the thermal energy of electrons. On the other hand, we assume that the electron created by the ionization process has the same temperature as one of the heavy particle.

Equation (28) is still the same even though E is the total energy defined as:

$$E = E_{g,h} + E_e + B^2/2\mu_0 \tag{47}$$

For equilibrium case, E_e merges into the internal energy of gas and does not explicitly appear. However, for non-equilibrium case, in order to calculate the electron temperature, we decouple these energy and solve Eq. (37) for E_e and the heavy particle energy equation ($E_h = E_{g,h} + B^2/2\mu_0$) (83):

$$\frac{\partial \rho E_h}{\partial t} + \frac{\partial}{\partial x_i}\left[(\rho E + p)\, u_i - T_{ij} u_j\right] - \frac{\partial}{\partial x_i}\left(\kappa \frac{\partial T}{\partial x_i} + u_j \tau_{ij}\right) = \triangle \dot{\epsilon}_{e,h} \tag{48}$$

The heat transfer due to binary collision appears in the right hand side as the source term. This term disappears when we combine Eq. (37) and Eq. (48). Also, as mentioned above, the ohmic heating is only considered in Eq. (37).

In this simple model, we do not consider the electronic excitation energy as a part of internal energy, and the model has a tendency to overestimate the electron temperature since the whole energy given from the surrounding plasma is into the translational energy of the electron. Now, our code uses experimental data for the specific heat which is based on the equilibrium state. Therefore, our electronic excitation energy is partially considered at the heavy particle temperature instead of the electron temperature. Strictly speaking, this is not accurate. In order to improve the model accuracy, the partition functions of all species of system have to be introduced, instead of using empirical curve-fits to determine the specific heat. This is a part of future work.

2.3.3 Low Magnetic Reynolds Number Assumption.

Is it always necessary to solve Maxwell equations with Navier-Stokes equations? From the engineering aspect, we try to avoid solving Maxwell equations as much as we can since it is an intricate nonlinear system, and it brings in an additional computational burden. Also, from our intuition, the electrical conductivity of the gas at the moderate temperature (below $5,000K$) is not large so that the induced current must be negligible. In order to estimate the relative importance of the MHD effect with the hydrodynamics, the aforesaid magnetic Reynold number R_m is useful. It is easy to estimate the R_m. For example, a supersonic flow case, $u \sim 10^3$, $\mu_0 \sim 10^{-6}$ and the characteristic length is ~ 1. The electrical conductivity, σ is the strong function of temperature and varies from zero to $\sim 10^3$ (for $T > 10,000K$). For supersonic combustion without a plasma source, R_m is 10^{-3}, and the flow does not disturb the magnetic field at all. However,with a plasma or seeded flow, the electrical conductivity can be above $\sim 10^3$ and R_m becomes close to unity where it is not always valid to neglect MHD effects.

Now, we consider the extreme case where $R_m << 1$. In such a case, the magnetic field (external field) has influence on flow fields through the Lorentz force, but there is no reverse effect from the flow field on the magnetic fields. In other words, there is no induced current that influences the magnetic field.

The main observation for $Rm << 1$ is given by (26):

1. The induced current is negligible.

2. The imposed magnetic field is approximately steady. Therefore, electric field ($\vec{E}_0$), magnetic field ($\vec{B}_0$) and current field ($\vec{J}_0$) remain same as the case of $\vec{u} = 0$.

3. $\vec{E}_0$ is irrotational and Ohm's law becomes:

$$\vec{J} = \sigma(- \bigtriangledown \phi + \vec{u} \times \vec{B}_0) \tag{49}$$

4. The Lorentz force is expressed by $\vec{F} = \vec{J}_0 \times \vec{B}_0$.

5. Not necessary to solve the induction equation!

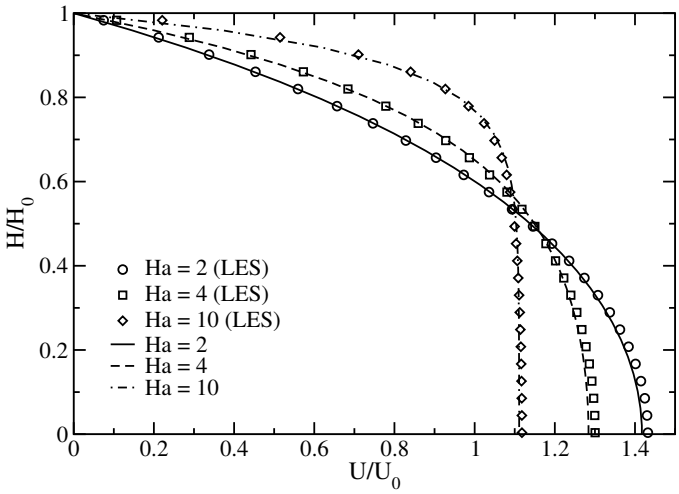

Figure 5: Normalized velocity profiles for laminar Hartman flow done by Schulz (100). Here, H_0 and U_0 denote the half-channel height and velocity averaged in the transverse direction, respectively. The lines indicate the analytical solution for the different Hartman numbers.

As an example of this assumption, the Hartman boundary layer problem is solved, and compared to the analytical solution numerically.

The problem is a channel flow with a fully developed electrically charged flow flowing with a constant applied field. The boundary layer is significantly influenced by the Lorentz force, and the boundary layer thickness varies greatly.

The flow direction is set in x-direction, $\vec{u} = (u_x, 0, 0)$, and the imposed magnetic field has only a y component, $\vec{B}_0 = (0, B_{y,ex}, 0)$. According to Eq. (21), the only non-zero component of Lorentz force is the x component and is expressed by:

$$F_x = -\sigma B_{y,ex}^2 u_x \tag{50}$$

Therefore, this force has to be balanced with the pressure gradient and the viscous stresses. The analytical solution for this simple system is given by:

$$u_x = u_o[1 - exp(-\frac{y}{\delta_h})] \tag{51}$$

where δ_h is $\sqrt{\frac{\rho\nu}{\sigma B_{y,ex}^2}}$. Since the Lorentz force acts to damp the mean flow, the boundary layer thickness becomes thinner as $B_{y,ex}$ increases. For validation of our code (100), we

performed the modeling of the Hartman flow between two plates and imposed a magnetic field (y-direction) and the electric field (z-direction). The results are shown in Fig. 5 with the analytical solution given by:

$$u_x(y) = u_o \left[1 - \frac{cosh(Ha)y/h_{1/2}}{cosh(Ha)} \right] \tag{52}$$

where $h_{1/2}$ is the half hight of the channel, and Ha is the Hartman number defined as:

$$Ha = B_{y,ex} h_{1/2} \sqrt{\frac{\sigma}{\rho\nu}} \tag{53}$$

As seen in the Fig. 5, the boundary layer thickness decreases with the increase of Ha. Because of the simplicity of Hartman flow problem and availability of the analytical solution, this problem has often used for the validation of MHD flow solver.

CHAPTER III

MHD LES EQUATIONS

This section is devoted to the explanation of the methodology of Local Dynamic Kinetic Energy Model (LDKM) for large-eddy simulation (LES) of MHD turbulence. This is one of main parts of my research.

3.1 Non-MHD turbulence modeling background

There are three widely used turbulent models *Direct Numerical Simulations (DNS)*, *the Reynolds Averaged Navier Stokes (RANS)* and *Large-Eddy Simulation (LES)*. In DNS approaches, the aim is to capture the smallest scale of motion in the system related to dissipation processes (e.g., Komogorov scale length). The computational cost is often prohibitively demanding, and it is reported that the grid resolution for 3D homogeneous turbulence is $\sim Re^{9/4}$ (115). This computational expensive nature of DNS prohibits it use in high Reynolds number application which are of real interest. However, many available DNS data for a low Reynolds number flows have been used for the validation of other turbulent modeling. Instead of exactly resolving as scales of turbulence, "approximate methods" (e.g., "MODEL") are adequate for many engineering application purposes. One of these models is RANS in which the governing equations are the time-averaged Navier-Stokes equations with the unclosed Reynolds stresses. In order to close the unclosed Reynolds stresses, the $k-\epsilon$ model is commonly used with the Boussinesq gradient diffusion approximation. This model can be a powerful tool to predict the mean flow, but does a poor job for unsteady flows such as swirl, flow with separation, or vortex shedding. Also due to the drawback of the gradient diffusion approximation, systems with multi-scales can not be accurately modeled by RANS (115). Another well-known "approximation" model is LES. In this model, the governing equations are spatially filtered and decomposed into a resolved part and unresolved part. Therefore, the large scale motion (resolved part) is exactly calculated by the filtered governing equation, and only the unresolved parts are modeled. The methodology

of LES is plausible in the sense that most part of turbulent kinetic energy is in large scales. Also, in the small-scales, the motion is considered universal so that it is more manageable in term of modeling. Unlike RANS, LES can accurately capture time-dependent nature and shows a great capability to resolve complex flows including separation. However, it is still necessary to model the effect of the unresolved parts and this requires the solving of a "closure problem' since the number of model coefficients is more than the number of governing equations. The accuracy of resolving the "closure problem" has a direct impact on the final answer of LES, and many efforts have been done for this (34; 51; 72; 73; 96; 102; 133).

3.1.1 Non-MHD Localized dynamic Kinetic-equation model (LDKM)

To model the subgrid stresses, there are several method to be proposed. The simplest model, proposed in the 60s, is the Smagorinsky model which is a simple eddy viscosity model for incompressible turbulent flows (133). In his model, the subgrid stresses are described by the mean rate of strain and a model constant. The drawback of his model is that a model constant has to be adjusted for the type of flow being model. In more recent models, this model constant is calculated "dynamically" so that the model constant is no longer constant anymore in "space" and "time" level, and rather is evaluated locally. About 15 years ago, a one-equation model using the sub-grid kinetic energy (LDKM) was proposed by Menon (96) and has been widely validated for compressible turbulence and developed further later (71). The essential idea of LDKM is following. The model coefficient for the expression of the subgrid stress is calculated using the assumption of scale similarity that the similarity exists between the largest unresolved scale and the smallest resolved scales. Then, the test filter which is smaller than the LES cut off scale is applied and is used to evaluate the model coefficient. The detailed explanation and formulation of LDKM is given in the next Section.

3.2 MHD turbulence modeling background

Like non-MHD turbulence, numerical simulations are a highly desirable tool to understand the fundamental aspects of MHD turbulence. However, for MHD turbulence, the linear and nonlinear coupling of the fluid motion with the magnetic field complicates the development

of an accurate model. To evaluate this nonlinear effect on the mean feature, the magnetic Reynolds number is introduced in the previous Section. When R_m is small, the induced field is assumed to be negligible and there is no necessary to model MHD-Turbulence. This is often observed in many experimental setup. On the other hand, when R_m is large, $\vec{u}$ and $\vec{B}$ interacts significantly, resulting in an increase in the complexity of the physics involved. In conventional LES turbulence modeling, this nonlinear coupling term gives rise to an additional unresolved magnetic stress similar to the sub-grid Reynolds stress. This unresolved term has been extensively studied in the past, and many approaches for closure of this term have been proposed (53; 74; 94; 132; 159; 167). A detailed discussion of the linkage between this term and the α-effect has also been reported elsewhere (26; 130; 162; 157). The physical significance of the α-effect is that it generates a mean electromotive force (emf) along the large-scale magnetic field through the interaction between turbulent fluctuation of velocity and magnetic field at the small scale. This is the central part of dynamo theory (78; 101; 162). A relevant example of the dynamo effect is the maintenance of long-lasting earth's magnetic field. Rotating turbulence model is also a good example of the dynamo, in which rotating motion and small-scale motion interact to generate the α-effect. Besides, the structure of fluid is also affected through a Coriolis force so that successfully modeling rotating MHD turbulence can be considered an acceptable benchmark to evaluate the performance of numerical schemes (as we do in this studies).

In three-dimensional MHD turbulence, there are three invariants that play a critical role in the behavior of MHD turbulence (46):

$$E^t = \frac{1}{2}\int (\rho u_k u_k + B_k B_k/\mu_0) dV = E^k + E^m \qquad \text{Total energy} \tag{54}$$

$$H_m = \int A_k B_k dV \qquad \text{Magnetic helicity} \tag{55}$$

$$H_c = \int u_k B_k dV \qquad \text{Cross helicity} \tag{56}$$

where A_k is the vector potential defined as $\epsilon_{kij}\partial A_j/\partial x_i = B_k$. Physically, H_m shows the topological linkage of magnetic field and is strongly related to the back-scatter mechanism by which the magnetic energy E^m is accumulated in the large scales (139). This is the so-called selective decay process (103). In most real applications, a finite value of H_m is expected, which results in a slower decay of magnetic energy. There are two important mechanisms related to the cross helicity H_c: the dynamic alignment process (91), which forces the plasma flow velocity and the magnetic field to align, and the back-transfer of kinetic energy (139). If these phenomena can be simulated, then it is another way to validate the numerical scheme, as we discuss later.

3.2.1 MHD turbulence modeling

LES subgrid models for MHD turbulence have been addressed in the past. Yoshizawa (158) constructed a subgrid Smagorinsky type model for incompressible MHD flow by using the dissipation rate of subgrid MHD turbulent energy. Later, using the two-scale direct interaction approximation (TSDIA), Yoshizawa and Hamba (161) upgraded this model to a more elaborate one in which, in addition to the turbulent energy, the cross helicity and the residual helicity were used to close the unresolved term. Yoshizawa also developed a compressible model (160). Numerical work using Yoshizawa′s model by Yokoi (157) showed that the turbulent cross helicity effect leads to a mean current parallel or antiparallel to the mean vorticity. Since Yoshizawas model closed the subgrid terms with the turbulent energy, the turbulent residual helicity, and the turbulent cross helicity, the governing equations for these terms are rather complicated and required nine model constants to be estimated based on DNS data. Recently Kobayashi (75; 76) developed a series of subgrid Smagorinsky type model and applied it to a MHD turbulent channel flow.

On the other hand, Theobald *et al.* (141) proposed a much simpler model for compressible flow where all the unresolved terms were summed up and combined with the diffusion term. They assumed that there was an equipartition between magnetic and kinetic energies in the inertial range wave number space to estimate the model constants. Apparently, the α-effect is not considered in their model, and the accuracy of this omission is questionable.

Another subgrid model for incompressible MHD turbulence was developed by M*ü*ller and Carati (94). They compared the performance of three types of closure for the model and showed that a cross-helicity model agrees perfectly with the reference data. This implies that turbulent electromotive force is strongly correlated with the resolved cross-helicity. This observation is also consistent with the Yoshizawa′s model.

3.3 MHD LES equations

MHD LES equations for single temperature case can be obtained by applying a spatial Favre filter (35) to the above equations (Eqs. (16)-(19)), the flow variables can be decomposed into the resolved and the unresolved parts, and then the LES governing equations are obtained. Here, the box filter appropriate for the finite volume scheme is used. The spatial filter is based on the local grid width $\overline{\Delta}$, and any filtered quantity is defined as $\widetilde{f} = \overline{\rho f}/\overline{\rho}$ where $\overline{\star}$ implies spatial filtering. More details on the LES filtering technique can be found elsewhere (115).

The resulting LES equations are:

$$\frac{\partial \bar{\rho}}{\partial t} + \frac{\partial}{\partial x_j}(\bar{\rho}\tilde{u}_j) = 0 \tag{57}$$

$$\frac{\partial \bar{\rho}\tilde{u}_i}{\partial t} + \frac{\partial}{\partial x_j}\left(\bar{\rho}\tilde{u}_i\tilde{u}_j + \bar{p}\delta_{ij} - \bar{\tau}_{ij} - \bar{T}_{ij} + \tau_{ij}^{sgs} + T_{ij}^{sgs}\right) = 0 \tag{58}$$

$$\frac{\partial \bar{\rho}\tilde{E}}{\partial t} + \frac{\partial}{\partial x_i}\left[\left(\bar{\rho}\tilde{E} + \bar{p}\right)\tilde{u}_i - \kappa\frac{\partial \bar{T}}{\partial x_i} - \tilde{u}_j\bar{\tau}_{ij} - H_i^{sgs} - \sigma_i^{sgs,v}\right] = \bar{J}_k\bar{E}_k + S^{sgs,b} \tag{59}$$

$$\frac{\partial \bar{B}_i}{\partial t} + \frac{\partial}{\partial x_j}\left(\tilde{u}_j\bar{B}_i - \bar{B}_j\tilde{u}_i + \tau_{ij}^{sgs,b} - \bar{\lambda}\frac{\partial \bar{B}_i}{\partial x_j} - d_{ij}^{sgs,b}\right) = 0 \tag{60}$$

$$\bar{p} = \bar{\rho}R\bar{T} \tag{61}$$

All terms with superscript "sgs" indicate subgrid scale term that need to be closed. Here, the filtered total energy per unit mass is defined as $\tilde{E} = \tilde{e} + \frac{1}{2}\tilde{u}_k\tilde{u}_k + k^{sgs}$, where k^{sgs} is defined as :

$$k^{sgs} = \frac{1}{2}(\widetilde{u_k u_k} - \tilde{u}_k\tilde{u}_k) \qquad \text{subgrid kinetic energy} \tag{62}$$

The subgrid terms appearing in the above LES equations are the subgrid Reynold stress, τ_{ij}^{sgs}, the subgrid Maxwell stress, T_{ij}^{sgs}, the subgrid total enthalpy flux, H_i^{sgs}, the subgrid viscous work, $\sigma_i^{sgs,v}$, the subgrid MHD work, $S^{sgs,b}$, the subgrid MHD stress, $\tau_{ij}^{sgs,b}$, and the subgrid magnetic diffusive flux, $d_{ij}^{sgs,b}$. These terms are formally defined as:

$$\begin{aligned}
\tau_{ij}^{sgs} &= (\bar{\rho}\widetilde{u_i u_j} - \bar{\rho}\tilde{u}_i\tilde{u}_j) \\
T_{ij}^{sgs} &= \frac{\overline{B_i B_j} - \bar{B}_i\bar{B}_j}{\mu_0} - \left(\frac{\overline{B_k B_k} - \bar{B}_k\bar{B}_k}{2\mu_0}\right)\delta_{ij} \\
H_i^{sgs} &= (\bar{\rho}\widetilde{E u_i} - \bar{\rho}\tilde{E}\tilde{u}_i) + (\overline{p u_i} - \bar{p}\tilde{u}_i) \\
\sigma_i^{sgs,v} &= (\widetilde{u_j\tau_{ij}} - \tilde{u}_j\bar{\tau}_{ij}) \\
S^{sgs,b} &= \overline{J_k E_k} - \bar{J}_k\bar{E}_k \\
\tau_{ij}^{sgs,b} &= (\overline{u_j B_i} - \overline{u_i B_j}) - (\tilde{u}_j\bar{B}_i - \tilde{u}_i\bar{B}_j) \\
d_{ij}^{sgs,b} &= \overline{\lambda\frac{\partial B_i}{\partial x_j}} - \bar{\lambda}\frac{\partial\bar{B}_i}{\partial x_j}
\end{aligned} \tag{63}$$

All these terms require closure. Note that the terms, τ_{ij}^{sgs},H_i^{sgs}, and $\sigma_i^{sgs,v}$ appear even in non-MHD flows, and closures are already available for them (97).

3.3.1 Closure of LES equation

The LES momentum equation contains two subgrid stresses that must be modeled: τ_{ij}^{sgs} and T_{ij}^{sgs}. Gradient diffusion assumption and dimensional analysis are used to close these terms, based on earlier effort (162). Thus,

$$\tau_{ij}^{sgs} = -2\bar{\rho}\nu_t(\tilde{S}_{ij} - \frac{1}{3}\tilde{S}_{kk}\delta_{ij}) + \frac{2}{3}\bar{\rho}k^{sgs}\delta_{ij} \tag{64}$$

$$T_{ij}^{sgs} = -2\nu_T(\bar{M}_{ij} - \frac{1}{3}\bar{M}_{kk}\delta_{ij}) - \frac{1}{3}k^{sgs,b}\delta_{ij} \tag{65}$$

Here, ν_t is the eddy-viscosity, and ν_T is the magnetic eddy diffusivity. $k^{sgs,b}$ is defined as:

$$k^{sgs,b} = \frac{1}{2\mu_0}(\overline{B_k B_k} - \bar{B}_k \bar{B}_k) \qquad \text{subgrid magnetic energy} \tag{66}$$

Also $\tilde{S}_{ij}$ and $\bar{M}_{ij}$ are the resolved rate of strain tensors defined as:

$$\tilde{S}_{ij} = \frac{1}{2}\left(\frac{\partial \tilde{u}_i}{\partial x_j} + \frac{\partial \tilde{u}_j}{\partial x_i}\right) \qquad \text{and} \qquad \bar{M}_{ij} = \tfrac{1}{2}\left(\tfrac{\partial \bar{B}_i}{\partial x_j} + \tfrac{\partial \bar{B}_j}{\partial x_i}\right) \tag{67}$$

The slight different constant ($+2/3$ for τ_{ij}^{sgs} and $-1/3$ for T_{ij}^{sgs}) occurs since T_{ij}^{sgs} contains the magnetic pressure term $[(\bar{B}_k \bar{B}_k/2\mu_0)\delta_{ij}]$, and this choice of constant ensures that the stress becomes zero when $i = j$. In previous models (1; 94), τ_{ij}^{sgs} and T_{ij}^{sgs} were combined and modeled by using only $\tilde{S}_{ij}$ since the velocity field and magnetic field have a strong correlation. However, this ignores the physical difference between subgrid velocity shear and magnetic shear. Here, we explicitly use $\bar{M}_{ij}$ to close T_{ij}^{sgs} and, this approach to model each part separately is a generalization that has a wider application. As noted later, ν_T can be used for the closure of $\tau_{ij}^{sgs,b}$ as well (159). The two model eddy viscosities, ν_t, ν_T are modeled, respectively as:

$$\nu_t = C_\nu \sqrt{k^{sgs}}\bar{\triangle} \qquad \text{and} \qquad \nu_T = C_\nu^T \sqrt{\tfrac{k^{sgs,b}}{\mu_0}}\bar{\triangle} \tag{68}$$

Here, $\bar{\triangle} = (\triangle x \triangle y \triangle z)^{1/3}$ is the local filter width, and C_ν and C_ν^T are model coefficients that are locally determined. In the incompressible model, it is convenient to express the magnetic field in Alfven units $[B_k' = B_k/\sqrt{\rho\mu_0}]$ since u_k and B_k' have the same unit, and equations become simpler. However, for the compressible case, B_k' does not simplify the equations and is not used. Thus, it is seen that μ_0 often appears in the equations for compressible MHD turbulence (160).

The unclosed term in the magnetic induction equation, $\tau_{ij}^{sgs,b}$ just as the subgrid Reynolds stress τ_{ij}^{sgs} plays a crucial role in sustaining the mean magnetic field. The closure of $\tau_{ij}^{sgs,b}$ is one of the primary challenges in the MHD turbulence model. Physically, it is known

that the eddy viscosity is reduced due to the cancellation of the Reynolds stress by the Maxwell stress (70). This negative contribution of the magnetic field to the eddy viscosity is a dominating effect. An extension of the Smagorinsky model was proposed by Shimomura (132), but he simply introduced a negative eddy viscosity to account for the MHD effect. Shimomura closed the model by using a dimensional analysis of the mean magnetic field. In contrast, the MHD-LDKM model developed in this paper is more elaborate. In order to understand the nature of $\tau_{ij}^{sgs,b}$ and its proposed closure, we introduce the concept of turbulent electromotive force E_T^k that approximately is linearly dependent on $\bar{B}_i$ (101; 78). Then, as the simplest model, E_T^k can be modeled as $E_T^k \approx \alpha \bar{B}_k$, and then used to close $\tau_{ij}^{sgs,b} = -2\epsilon_{kij} E_T^k$. This is called the α-effect. Yoshizawa analyzed this effect using TSDIA (159) and investigated the relationship among τ_{ij}^{sgs}, T_{ij}^{sgs}, and $\tau_{ij}^{sgs,b}$ through ν_t and ν_T. He obtained the following relations:

$$E_T^k = \alpha \bar{B}_k - \beta \bar{J}_k + \gamma \tilde{\Omega}_k \tag{69}$$

where,

$$\beta = \frac{5}{7}(\nu_t \mu_0) \qquad \text{and} \qquad \gamma = \tfrac{5}{7}(\nu_T \mu_0) \tag{70}$$

α is modeled as: $\alpha' \sqrt{k^{sgs}}$ here, and α' is dynamically calculated.

We see that E_T^k is dependent on $\bar{B}_k$, the mean current $\bar{J}_k$ [$= \epsilon_{kij} \partial \bar{B}_i / \partial x_j$] and the mean vorticity $\tilde{\Omega}_k$ [$= \epsilon_{kij} \partial \tilde{u}_i / \partial x_j$]. The two model coefficients β, γ are closed (once ν_t and ν_T are defined), but α' is not. This new model coefficient will be discussed in the next section. The interpretation of α, β and γ are as follows. The α-effect is critical in MHD turbulence where the small scale motion leads to the generation of the poloidal field from the azimuthal field and contributes to the large scale magnetic field. As a result, the induced magnetic field approaches the configuration in which $\bar{J}_k$ is parallel to the $\bar{B}_k$ as the Lorentz force vanishes. Physically, β can be understood easily by noticing that the $\beta \bar{J}_k$ term can be merged into the diffusion term, and thus, β enhances the magnetic diffusivity [$\lambda \rightarrow \lambda + \beta$]. This is called the anomalous resistivity effect (β-effect), and is intrinsically the same mechanism as the

eddy viscosity effect in the hydrodynamic system. Finally, γ is related to the cross-helicity effect by the fact that $\bar{J}_k$ is aligned with $\tilde{\Omega}_k$ ($\bar{B}_k \parallel \tilde{u}_k$). A detailed discussion of each of the mechanisms related to these coefficients is given by Yokoi (157).

Other subgrid terms appear in the LES filtered energy have to be closed as well. The subgrid total enthalpy flux H_i^{sgs} is modeled using the eddy viscosity and a gradient assumption as $H_i^{sgs} \approx -\bar{\rho}\frac{\nu_e}{Pr_t}\frac{\partial \tilde{H}}{\partial x_i}$. Pr_t is the subgrid Prandtle number that can also be computed using a dynamic procedure but is currently assumed to be unity. The subgrid viscous work, σ_i^{sgs}, is often neglected in conventional LES approaches (47). At present, $S^{sgs,b}$ and $d_{ij}^{sgs,b}$ are neglected but will be revisited in the near future.

With the closure term as defined the LES magnetic induction equation (Eq. (60)) becomes:

$$\frac{\partial \bar{B}_i}{\partial t} + \frac{\partial}{\partial x_j}\left(\tilde{u}_j\bar{B}_i - \bar{B}_j\tilde{u}_i - 2\epsilon_{kij}E_T^k - \bar{\lambda}\frac{\partial \bar{B}_i}{\partial x_j}\right) = 0 \tag{71}$$

3.4 The subgrid kinetic and magnetic energy equations

The MHD-LDKM model developed in this study uses *the subgrid kinetic energy* and *the subgrid magnetic energy* to close the SGS equations. The LES governing equations for k^{sgs} and $k^{sgs,b}$ are derived in the following section.

3.4.1 Derivation of k^{sgs} and $k^{sgs,b}$ equations

In order to derive the $k^{sgs,b}$ LES equation, the first step is to multiply the magnetic induction equation (Eq. 60) by B_i/μ_0 and apply a spatial filtering:

$$\frac{\partial}{\partial t}\left(\frac{\overline{B_kB_k}}{2\mu_0}\right) + \overline{\frac{B_i}{\mu_0}\frac{\partial}{\partial x_j}\left\{(u_jB_i - u_iB_j) - \lambda\frac{\partial B_i}{\partial x_j}\right\}} = 0 \tag{72}$$

The resolved part of the magnetic energy equation is obtained by multiplying the LES magnetic induction equation by $\bar{B}_i/\mu_0$:

$$\frac{\partial}{\partial t}\left(\frac{\bar{B}_k\bar{B}_k}{2\mu_0}\right) + \frac{\bar{B}_i}{\mu_0}\frac{\partial}{\partial x_j}\left\{(\tilde{u}_j\bar{B}_i - \tilde{u}_i\bar{B}_j) - \bar{\lambda}\frac{\partial \bar{B}_i}{\partial x_j} + \tau_{ij}^{sgs,b}\right\} = 0 \tag{73}$$

Subtracting Eq. (74) from Eq. (72), we get the $k^{sgs,b}$ LES equation:

$$\frac{\partial k^{sgs,b}}{\partial t} + \left[\overline{\frac{B_i}{\mu_0}\frac{\partial}{\partial x_j}(u_j B_i - u_i B_j)} - \frac{\bar{B}_i}{\mu_0}\frac{\partial}{\partial x_j}\left\{(\tilde{u}_j\bar{B}_i - \tilde{u}_i\bar{B}_j) - \bar{\lambda}\frac{\partial \bar{B}_i}{\partial x_j} + \tau_{ij}^{sgs,b}\right\}\right] = \overline{\frac{B_i}{\mu_b}\frac{\partial}{\partial x_j}\left(\lambda\frac{\partial B_i}{\partial x_j}\right)} - \frac{\bar{B}_i}{\mu_0}\frac{\partial}{\partial x_j}\left(\bar{\lambda}\frac{\partial \bar{B}_i}{\partial x_j}\right) \tag{74}$$

In the above equation, the right-hand side can be decomposed into the two parts: subgrid transport term ($\Gamma_{1,m}$) and dissipation term (D_m):

$$\overline{\frac{B_i}{\mu_0}\frac{\partial}{\partial x_j}\left(\lambda\frac{\partial B_i}{\partial x_j}\right)} - \frac{\bar{B}_i}{\mu_0}\frac{\partial}{\partial x_j}\left(\bar{\lambda}\frac{\partial \bar{B}_i}{\partial x_j}\right) = \Gamma_{1,m} - D_m \tag{75}$$

where

$$\begin{aligned}
\Gamma_{1,m} &= \left[\frac{\partial}{\partial x_j}\left\{\overline{\lambda\frac{\partial}{\partial x_j}\left(\frac{B_k B_k}{2\mu_0}\right)}\right\} - \frac{\partial}{\partial x_j}\left\{\bar{\lambda}\frac{\partial}{\partial x_j}\left(\frac{\bar{B}_k\bar{B}_k}{2\mu_0}\right)\right\}\right] \\
D_m &= \left[\overline{\frac{\partial B_i}{\partial x_j}\left\{\frac{\lambda}{\mu_0}\frac{\partial B_i}{\partial x_j}\right\}} - \frac{\partial \bar{B}_i}{\partial x_j}\left\{\frac{\bar{\lambda}}{\mu_0}\frac{\partial \bar{B}_i}{\partial x_j}\right\}\right]
\end{aligned} \tag{76}$$

The second term in left-hand side is divided into five terms: (a) convection term (A_m), (b) transport term ($\Gamma_{2,m}$), (c) rate of subgrid production term ($P_{1,m}$), (d) rate of production related to the subgrid stress term ($P_{2,m}$), and (e) the compressibility ($C_{o,m}$):

$$\left[\overline{\frac{B_i}{\mu_0}\frac{\partial}{\partial x_j}(u_j B_i - u_i B_j)} - \frac{\bar{B}_i}{\mu_0}\frac{\partial}{\partial x_j}\left\{(\tilde{u}_j\bar{B}_i - \tilde{u}_i\bar{B}_j) + \tau_{ij}^{sgs,b}\right\}\right] = A_m - \Gamma_{2,m} - P_{1,m} - P_{2,m} - C_{o,m} \tag{77}$$

where

$$\begin{aligned}
A_m &= \overline{\frac{\partial}{\partial x_j}\left(u_j\frac{B_k B_k}{2\mu_0}\right)} - \frac{\partial}{\partial x_j}\left(\tilde{u}_j\frac{\bar{B}_k\bar{B}_k}{2\mu_0}\right) = \sigma_{A_m}\frac{\partial}{\partial x_j}(\tilde{u}_j k^{sgs,b}) \\
\Gamma_{2,m} &= \frac{1}{\mu_0}\frac{\partial \tau_{ij}^{sgs,b}\bar{B}_i}{\partial x_j} \\
P_{1,m} &= -\left(\overline{\frac{B_i B_j}{\mu_0}\frac{\partial u_i}{\partial x_j}} - \frac{\bar{B}_i\bar{B}_j}{\mu_0}\frac{\partial \tilde{u}_i}{\partial x_j}\right) \\
P_{2,m} &= -\left(\frac{\tau_{ij}^{sgs,b}}{\mu_0}\frac{\partial \bar{B}_i}{\partial x_j}\right) \\
C_{o,m} &= -\left(\overline{\frac{B_k B_k}{2\mu_0}\frac{\partial u_j}{\partial x_j}} - \frac{\bar{B}_k\bar{B}_k}{2\mu_0}\frac{\partial \tilde{u}_j}{\partial x_j}\right)
\end{aligned} \tag{78}$$

Here, σ_{A_m} is set unity in this study for simplicity but will be revisited in the future.

Finally, the $k^{sgs,b}$ LES equation is expressed in the following form:

$$\frac{\partial k^{sgs,b}}{\partial t} + \frac{\partial}{\partial x_j}(\tilde{u}_j k^{sgs,b}) = \Gamma_m - D_m + P_m + C_{o,m} \tag{79}$$

where $P_m = P_{1,m} + P_{2,m}$ and $\Gamma_m = \Gamma_{1,m} + \Gamma_{2,m}$

The k^{sgs} LES equation for MHD flow is based on the non-MHD k^{sgs} LES equation derived and validated earlier (1; 72; 73; 112), except that there are additional MHD related contributions. In addition to the subgrid Reynolds stress τ_{ij}^{sgs}, there is another resolved shear stress tensor related to the Maxwell stress (T_{ij}) and the subgrid stress tensor (T_{ij}^{sgs}). Therefore, the modified k^{sgs} LES equation for MHD case can be written as:

$$\begin{aligned}
\frac{\partial \bar{\rho} k^{sgs}}{\partial t} + \frac{\partial}{\partial x_j}(\bar{\rho} k^{sgs} \tilde{u}_j) = & -\left(\overline{\frac{\partial p}{\partial x_j} u_j} - \frac{\partial \bar{p}}{\partial x_j}\tilde{u}_j\right) - \frac{\partial}{\partial x_j}(\widetilde{\rho k u_j} - \bar{\rho}\tilde{k}\tilde{u}_j) \\
& - \left(\frac{\partial \widetilde{\tau_{ij} u_i}}{\partial x_j} - \frac{\partial \tilde{\tau}_{ij}\tilde{u}_i}{\partial x_j}\right) + \left(\frac{\partial \widetilde{u_i}}{\partial x_j}\tau_{ij} - \frac{\partial \tilde{u}_i}{\partial x_j}\tilde{\tau}_{ij}\right) \\
& - \frac{\partial \tau_{ij}^{sgs}\tilde{u}_i}{\partial x_j} - \tau_{ij}^{sgs}\frac{\partial \tilde{u}_i}{\partial x_j} - \left(\frac{\partial \widetilde{T_{ij} u_i}}{\partial x_j} - \frac{\partial \bar{T}_{ij}\tilde{u}_i}{\partial x_j}\right) \\
& + \left(\frac{\partial \widetilde{u_i}}{\partial x_j}T_{ij} - \frac{\partial \tilde{u}_i}{\partial x_j}\bar{T}_{ij}\right) - \frac{\partial T_{ij}^{sgs}\tilde{u}_i}{\partial x_j} - T_{ij}^{sgs}\frac{\partial \tilde{u}_i}{\partial x_j}
\end{aligned} \tag{80}$$

We can rewrite this equation in a form similar to Eq. (79):

$$\frac{\partial \bar{\rho} k^{sgs}}{\partial t} + \frac{\partial}{\partial x_j}(\bar{\rho} k^{sgs} \tilde{u}_j) = \Gamma_k - D_k + P_k + (\Gamma_{k,b} + P_{k,b})_{MHD} \tag{81}$$

where

$$\begin{aligned}
\Gamma_k &= -\tfrac{\partial}{\partial x_j}(\widetilde{\rho k u_j} - \bar{\rho}\tilde{k}\tilde{u}_j) - \left(\overline{\tfrac{\partial p}{\partial x_j} u_j} - \tfrac{\partial \bar{p}}{\partial x_j}\tilde{u}_j\right) - \tfrac{\partial \tau_{ij}^{sgs}\tilde{u}_i}{\partial x_j} \\
D_k &= -\left(\tfrac{\partial \widetilde{\tau_{ij}}}{\partial x_j} u_i - \tfrac{\partial \tilde{\tau}_{ij}}{\partial x_j}\tilde{u}_i\right) \\
P_k &= -\tau_{ij}^{sgs}\tfrac{\partial \tilde{u}_i}{\partial x_j} \\
\Gamma_{k,b} &= -\tfrac{\partial T_{ij}^{sgs}\tilde{u}_i}{\partial x_j} \\
P_{k,b} &= -T_{ij}^{sgs}\tfrac{\partial \tilde{u}_i}{\partial x_j} - \left(\tfrac{\partial \widetilde{T_{ij}}}{\partial x_j} u_i - \tfrac{\partial \bar{T}_{ij}}{\partial x_j}\tilde{u}_i\right)
\end{aligned} \tag{82}$$

3.4.2 Closure of k^{sgs} and $k^{sgs,b}$ equations

In the k^{sgs} LES equation (Eq. (79)), the left-hand side is calculated exactly, and no closure is required. The right-hand side is modeled as the combination of the three physical mechanism: the subgrid transport, the production and the dissipation. Here (as earlier, (97; 73)), all the subgrid transport terms (Γ_k and $\Gamma_{k,b}$) are combined and modeled as "transport" $= \frac{\partial}{\partial x_j}\left(\bar{\rho}\frac{\nu_e}{Pr_t}\frac{\partial k^{sgs}}{\partial x_j}\right)$, where Pr_t is assumed to be unity in this model and ν_e is the effective viscosity defined as $\nu_e = \nu + \nu_t - \sqrt{\mu_0\bar{\rho}}\nu_T$. Here, we consider the negative contribution of MHD effects on the total viscosity. Since the concept of the negative viscosity remains uncertain, and it numerically happens in practice, ν_e is constrained to be positive in our model. The rate of production (P_k and $P_{k,b}$) does not need explicit closure (although it contains modeled subgrid stresses). Thus, "production" $= -\tau_{ij}^{sgs}\frac{\partial \tilde{u}_j}{\partial x_i} - T_{ij}^{sgs}\frac{\partial \tilde{u}_j}{\partial x_i}$. The dissipation term ($D_k$) follows the earlier closures (73) approach and is modeled as "dissipation" $= -\frac{\bar{\rho}C_\epsilon}{\bar{\triangle}}(k^{sgs})^{\frac{3}{2}}$. Here, C_ϵ is determined dynamically as are C^ν, C_ν^T, and $C_{p,b}$. Combining the above equations results in the following equation for k^{sgs}.

$$\frac{\partial \bar{\rho}k^{sgs}}{\partial t} + \frac{\partial}{\partial x_j}\bar{\rho}k^{sgs}\tilde{u}_j = \frac{\partial}{\partial x_j}\left(\bar{\rho}\frac{\nu_e}{Pr_t}\frac{\partial k^{sgs}}{\partial x_j}\right) - \frac{\bar{\rho}C_\epsilon}{\bar{\triangle}}(k^{sgs})^{\frac{3}{2}} - \tau_{ij}^{sgs}\frac{\partial \tilde{u}_j}{\partial x_i} - T_{ij}^{sgs}\frac{\partial \tilde{u}_j}{\partial x_i} - \frac{C_{p,b}}{\bar{\triangle}}\sqrt{k^{sgs}}k^{sgs,b} \tag{83}$$

In the $k^{sgs,b}$ LES equation, all terms need closure. As in the closure of the k^{sgs} model equation, we model the MHD right-hand side components using similar approaches. The terms needing closure are the convection A_m, the subgrid transport Γ_m, the dissipation D_m, the production P_m, and the term related to the compressibility $C_{o,m}$. They are modeled as:

$$\begin{aligned}
\Gamma_m &= \frac{\partial}{\partial x_j}\left(\bar{\lambda}\frac{\partial k^{sgs,b}}{\partial x_j}\right) \\
D_m &= \frac{C_{\epsilon,b}k^{sgs,b}\sqrt{k^{sgs,b}/\bar{\rho}}}{\bar{\triangle}} \\
P_m &= -\frac{\tau_{ij}^{sgs,b}}{\mu_0}\frac{\partial \bar{B}_i}{\partial x_j} \\
C_{o,m} &= -k^{sgs,b}\frac{\partial \tilde{u}_j}{\partial x_j}
\end{aligned} \tag{84}$$

Here, $C_{\epsilon,b}$ is another model coefficient that is also obtained dynamically. Finally, the modeled subgrid magnetic energy equation becomes:

$$\frac{\partial k^{sgs,b}}{\partial t} + \frac{\partial}{\partial x_j}(\tilde{u}_j k^{sgs,b}) = \frac{\partial}{\partial x_j}\left(\bar{\lambda}\frac{\partial k^{sgs,b}}{\partial x_j}\right) - \frac{C_{\epsilon,b}k^{sgs,b}\sqrt{k^{sgs,b}/\bar{\rho}}}{\bar{\triangle}} - \frac{1}{\mu_0}\tau_{ij}^{sgs,b}\frac{\partial \bar{B}_i}{\partial x_j} - k^{sgs,b}\frac{\partial \tilde{u}_j}{\partial x_j} \quad (85)$$

where $C_{\epsilon,b}$ is a model coefficient. In Eq. 83, the two production terms $T_{ij}^{sgs}\frac{\partial \tilde{u}_j}{\partial x_i}$ and $\frac{C_{p,b}}{\bar{\triangle}}\sqrt{k^{sgs}}k^{sgs,b}$ are related to the energy budget with the resolved part of kinetic energy and the subgrid magnetic energy, respectively. On the other hand, in Eq. 85, the corresponding term is P_m that is the sume of $P_{1,m}$ and $P_{2,m}$.

In summary, the SGS closure of the MHD LES equation is achieved by solving transport equations for k^{sgs} and $k^{sgs,b}$. There are six coefficients that are all obtained locally and dynamically.

3.4.3 Dynamic calculation of model coefficients

The above equations for MHD turbulence are still not closed since there are the six model coefficients (C_ν, C_ν^T, C_ϵ, $C_{\epsilon,b}$, $C_{p,b}$ and $\alpha^{'}$) that need to be determined. Hamba (57) closed his model constants by comparing the numerical results with results from other simulations. In our approach, all coefficients are computed locally and dynamically to give them more general appilicability. The details of the formulation of the LDKM approach can be found elsewhere (72; 73) but some critical ones are repeated here for completeness. The key step is to evaluate the relevant quantities at the test filter level ($\hat{\triangle} = 2\bar{\triangle}$) with the assumption that there is scale similarity between the properties at $\hat{\triangle}$ and $\bar{\triangle}$ (which is observed in some experimental data (86) at least for non-MHD flows.). The specific procedure to compute these terms are given below since some are new procedures for MHD flow.

3.4.3.1 The $\alpha^{'}$ coefficient

The procedure for computing $\alpha^{'}$ starts with the exact expression for $\tau_{ij}^{sgs,b}$ to the model equation:

$$\alpha^{'}\sqrt{k^{sgs}}\bar{B}_k - \beta\bar{J}_k + \gamma\tilde{\Omega}_k = E_T^k \approx 1/2\epsilon_{kij}\left\{(\overline{u_j B_i} - \overline{u_i B_j}) - (\tilde{u}_j\bar{B}_i - \tilde{u}_i\bar{B}_j)\right\} \quad (86)$$

If all terms on the right-hand side were known, $\alpha^{'}$ could be directly computed. However, in LES, the right-hand is the unresolved terms, and are unknown. Here (and as in the earlier non-MHD approach), we assume that the subgrid MHD stress at the grid filter level and at the test filter level are similar. Therefore, we can evaluate the right-hand directly by test filtering the quantities that are resolved at the grid filter level and related to modeled terms at the same test filter level. Thus, an expression similar to the above equation can be written at the test filter grid level as:

$$\alpha^{'}\sqrt{\hat{k}^{sgs}}\hat{\bar{B}}_k - \beta\hat{\bar{J}}_k + \gamma\hat{\bar{\Omega}}_k = E_T^k \approx \frac{1}{2}\epsilon_{kij}((\widehat{\tilde{u}_j\bar{B}_i} - \widehat{\tilde{u}_i\bar{B}_j}) - (\hat{\tilde{u}}_j\hat{\bar{B}}_i - \hat{\tilde{u}}_i\hat{\bar{B}}_j)) \tag{87}$$

Here, $\hat{k}^{sgs}$ is the subgrid kinetic energy at the test filter level defined as

$$\hat{k}^{sgs} = \frac{1}{2}\left(\frac{\widehat{\bar{\rho}\tilde{u}_k^2}}{\hat{\bar{\rho}}} - \frac{\widehat{\bar{\rho}\tilde{u}_k}^2}{\hat{\bar{\rho}}^2}\right) \tag{88}$$

In the above equation, all terms except $\alpha^{'}$ are known, and so $\alpha^{'}$ can be extracted by algebraic rearrangement. However, the condition is over-specified (*i.e.,* three equations, one unknown). Based on the idea proposed by Lilly (85), the model error Er^k is defined by:

$$Er^k = L^k - \alpha^{'}\sqrt{\hat{k}^{sgs}}\hat{\bar{B}}_k \tag{89}$$

where,

$$L^k = 1/2\epsilon_{kij}\left\{(\widehat{\tilde{u}_j\bar{B}_i} - \widehat{\tilde{u}_i\bar{B}_j})) - (\hat{\tilde{u}}_j\hat{\bar{B}}_i - \hat{\tilde{u}}_i\hat{\bar{B}}_j)\right\} + \beta\hat{\bar{J}}_k - \gamma\hat{\bar{\Omega}}_k \tag{90}$$

Er^k could be a positive or a negative number, therefore minimizing the RMS of the error. The derivative with respect to the model coefficient should be zero. That is,

$$\frac{\partial Er^k Er^k}{\partial\alpha^{'}} = 0 = -2\sqrt{\hat{k}^{sgs}}L_k\hat{\bar{B}}_k + 2\alpha^{'}\hat{k}^{sgs}\hat{\bar{B}}_k\hat{\bar{B}}_k \tag{91}$$

From this, $\alpha^{'}$ is computed as:

$$\alpha^{'} = \frac{L_k \hat{\bar{B}}_k}{\sqrt{\hat{k}^{sgs}} \hat{\bar{B}}_k \hat{\bar{B}}_k} \tag{92}$$

This simple expression for $\alpha^{'}$ is reasonable, since it is intrinsically identical to the exact definition of α: $\alpha \stackrel{\text{def}}{=} \frac{E_T^k \cdot \bar{B}_k}{\bar{B}_k^2}$ except for the fact that L_k represents only the portion of the turbulent electromotive force after subtracting the β-effect and the cross-helicity effect. It is known that E_T^k becomes zero when there are no partial alignment of the small-scale eddies, since the cumulative influence of many small-scale activities can give rise to a large-scale magnetic field. Also, the finite current helicity is required for $E_T^k \neq 0$ (66). These inherent characteristics of E_T^k make it rather difficult to estimate $\alpha^{'}$ by using a conventional scheme. In the current approach, however, L_k has all the information of small-scale motion, and thus enables the model to imitate the physical significance of α $(= \sqrt{k^{sgs}}\alpha^{'})$. Moreover, the evaluation of $\alpha^{'}$ using Eq. (92) is also stable since the denominator is well defined and non-zero in the flow field. This is an important requirement for dynamic models when applied in complex flows.

3.4.3.2 The MHD dissipation model coefficient, $C_{\epsilon,b}$

Using the same dynamic approach used earlier (73), the dissipation at the test filter level can be used to obtain a closure for $C_{\epsilon,b}$. Thus, at the test filter level, the dissipation is obtained as:

$$\frac{\bar{\lambda}}{\mu_0}\left(\frac{\partial \widehat{\bar{B}_j}}{\partial x_i}\frac{\partial \bar{B}_j}{\partial x_i} - \frac{\partial \hat{\bar{B}}_j}{\partial x_i}\frac{\partial \hat{\bar{B}}_j}{\partial x_i}\right) \approx \frac{C_{\epsilon,b}\hat{k}^{sgs,b}\sqrt{\hat{k}^{sgs,b}/\hat{\rho}}}{\hat{\triangle}} \tag{93}$$

where $\hat{k}^{sgs,b}$ is the subgrid magnetic energy at the test filter level:

$$\hat{k}^{sgs,b} = \frac{1}{2\mu_0}(\widehat{\bar{B}_k \bar{B}_k} - \hat{\bar{B}}_k \hat{\bar{B}}_k) \tag{94}$$

All terms, except $C_{\epsilon,b}$ are known and therefore, an expression for $C_{\epsilon,b}$ is obtained as:

$$C_{\epsilon,b} = \frac{\hat{\triangle}\bar{\lambda}}{\mu_0 \hat{k}^{sgs,b}\sqrt{\hat{k}^{sgs,b}/\hat{\bar{\rho}}}}\left(\frac{\partial \widehat{\bar{B}_j}}{\partial x_i}\frac{\partial \bar{B}_j}{\partial x_i} - \frac{\partial \hat{\bar{B}}_j}{\partial x_i}\frac{\partial \hat{\bar{B}}_j}{\partial x_i}\right) \tag{95}$$

3.4.3.3 The MHD subgrid stress model coefficient, C_ν^T

The same procedure is used for computing C_ν^T. An analogous test field expression is written as:

$$\left(\frac{\widehat{\bar{B}_i\bar{B}_j}}{\mu_0} - \frac{\widehat{\bar{B}_k\bar{B}_k}}{2\mu_0}\delta_{ij}\right) - \left(\frac{\hat{\bar{B}}_i\hat{\bar{B}}_j}{\mu_0} - \frac{\hat{\bar{B}}_k\hat{\bar{B}}_k}{2\mu_0}\delta_{ij}\right) + \frac{1}{3}\hat{k}^{sgs,b}\delta_{ij}$$
$$\approx -2C_\nu^T\sqrt{\frac{\hat{k}^{sgs,b}}{\mu_0}}\hat{\triangle}(\hat{\bar{M}}_{ij} - \frac{1}{3}\hat{\bar{M}}_{kk}\delta_{ij}) \tag{96}$$

and the coefficient C_ν^T is determined by the least-square method. The result is:

$$C_\nu^T = -\frac{L_{ij}^b D_{ij}^b}{2D_{ij}^b D_{ij}^b} \tag{97}$$

where,

$$\begin{aligned} L_{ij}^b &= (\widehat{\bar{B}_i\bar{B}_j}/\mu_0 - \widehat{\bar{B}_k\bar{B}_k}/2\mu_0\delta_{ij}) - (\hat{\bar{B}}_i\hat{\bar{B}}_j/\mu_0 - \hat{\bar{B}}_k\hat{\bar{B}}_k/2\mu_0\delta_{ij}) + \tfrac{1}{3}\hat{k}^{sgs,b}\delta_{ij} \\ D_{ij}^b &= \sqrt{\tfrac{\hat{k}^{sgs,b}}{\mu_0}}\hat{\triangle}(\hat{\bar{M}}_{ij} - \tfrac{1}{3}\hat{\bar{M}}_{kk}\delta_{ij}) \end{aligned} \tag{98}$$

3.4.3.4 The MHD subgrid product model coefficient, $C_{p,b}$

The method for dynamically computing $C_{p,b}$ is similar to that described above. The test field expression for this product term related to the Lorentz work propelling the fluid is written as:

$$\widehat{\tilde{u}_i\frac{\partial\bar{T}_{ij}}{\partial x_j}} - \left(\frac{\widehat{\bar{\rho}\tilde{u}_j}}{\hat{\bar{\rho}}}\right)\frac{\partial\hat{\bar{T}}_{ij}}{\partial x_j} \approx C_{p,b}\frac{\hat{k}^{sgs,b}\sqrt{\hat{k}^{sgs}}}{\hat{\triangle}} \tag{99}$$

From this expression, $C_{p,b}$ can be computed as:

$$C_{p,b} = \frac{\hat{\triangle}}{\hat{k}^{sgs,b}\sqrt{\hat{k}^{sgs}}}\left\{\widehat{\tilde{u}_i\frac{\partial\bar{T}_{ij}}{\partial x_j}} - \left(\frac{\widehat{\bar{\rho}\tilde{u}_j}}{\hat{\bar{\rho}}}\right)\frac{\partial\hat{\bar{T}}_{ij}}{\partial x_j}\right\} \tag{100}$$

3.4.3.5 The non-MHD subgrid stress and dissipation model coefficients, C_ν, C_ϵ

No new modification is needed since the MHD term effects only C_ν^T. The expression of C_ν is given by (72; 73; 112):

$$C_\nu = -\frac{L_{ij}D_{ij}}{2D_{ij}D_{ij}} \tag{101}$$

where,

$$\begin{aligned} L_{ij} &= \bar{\rho}\widehat{\tilde{u}_i\tilde{u}_j} - \frac{\widehat{\bar{\rho}\tilde{u}_j}\widehat{\bar{\rho}\tilde{u}_j}}{\hat{\bar{\rho}}} - \frac{1}{3}\left\{\bar{\rho}\widehat{\tilde{u}_k\tilde{u}_k} - \frac{\widehat{\bar{\rho}\tilde{u}_k}\widehat{\bar{\rho}\tilde{u}_k}}{\hat{\bar{\rho}}}\right\}\delta_{ij} \\ D_{ij} &= \hat{\triangle}\hat{\bar{\rho}}\sqrt{\hat{k}^{sgs}}\left\{\hat{\tilde{S}}_{ij} - \frac{1}{3}\hat{\tilde{S}}_{kk}\delta_{ij}\right\} \end{aligned} \tag{102}$$

Similarly, no modification is needed for evaluating C_ϵ, and C_ϵ for non-MHD turbulence is given by (72; 73; 112):

$$C_\epsilon = \frac{(\bar{\mu}+\mu_t)\left\{\widehat{\tilde{s}_{ij}\frac{\partial\tilde{u}_j}{\partial x_i}} - \hat{\tilde{s}}_{ij}\frac{\partial\widehat{\tilde{u}_j}}{\partial x_i}\right\}\hat{\triangle}}{\hat{\bar{\rho}}(\hat{k}^{sgs})^{\frac{3}{2}}} \tag{103}$$

where $\mu_t = \bar{\rho}\nu_t$, the tensor $\tilde{s}_{ij}$ is $\frac{\partial\tilde{u}_i}{\partial x_j} + \frac{\partial\tilde{u}_j}{\partial x_i} - \frac{2}{3}\frac{\partial\tilde{u}_k}{\partial x_k}\delta_{ij}$, and $\hat{\tilde{s}}_{ij}$ is the tensor at the test filter level.

In summary, the proposed LES model for MHD flows employs a two-equation formulation based on the subgrid kinetic energy (k^{sgs}), and the subgrid magnetic energy ($k^{sgs,b}$). The six coefficients (two for non-MHD and four for MHD effects) are all obtained locally (in space and time) as a part of the solution. The applicability and stability of this dynamic approach is demonstrated in Result Section .

CHAPTER IV

NUMERICAL METHODS

In this chapter, the numerical methods to solve the governing equations are introduced. All equations will be expressed in the conservative form and integrated within the control volume. The flux of the conservative variables are defined at the each surface of the volume of the interest. Advantages of this kind of integration is that it is necessary to do only surface integration in order to get the volume-averaged variables for the conservative variables from which we get the primitive variables to describe the system completely. Another advantage is that the finite-volume method guarantees that the variables to be solved are automatically conserved unlike the finite-difference method. Also, there are no restrictions in the choice of grid. As a result, the finite-volume method has been widely used in CFD communities. In this method, we assume that the volume-averaged variables are determined at the cell center. However, for MHD turbulence, a staggered grid is more useful due to the $\partial B_k/\partial x_k = 0$ constraint. This constraint is one of the big difficulties to be dealt with. Our numerically obtained magnetic field has to satisfy this constraint, since Maxwell's equation are mathematically derived based on this. However, numerically, due to the nature of the discretized variables, the error can easily accumulate resulting in obtaining the non-physical answers. The advantages and limitation of using the staggered grid will be also discussed. Another numerical difficulty to solve the system comes from the fact that system of our interest is really stiff, therefore it is natural to introduce the dual time step for solving some equations or implicit schemes in which the CFD constraint for minimum time step can be relaxed. Finally, the boundary conditions are discussed. The magnetic /electric field's boundary conditions are always problematic and require careful treatment.

4.1 Finite-Volume Scheme

The full set of conservation equations solved in the Cartesian co-ordinates are expressed in divergence form:

$$\frac{\partial \vec{U}}{\partial t} + \frac{\partial \vec{F}_x}{\partial x} + \frac{\partial \vec{F}_y}{\partial y} + \frac{\partial \vec{F}_z}{\partial z} = \vec{\Phi} \tag{104}$$

where $\vec{U}$, $\vec{F}_i$ and $\vec{\Phi}$ are the conservative variables, the flux vectors, and the vector of source terms, respectively. The volume-integration of the above equation gives the final forms of equation that we numerically solve:

$$\int_V \frac{\partial \vec{U}}{\partial t} dV + \int_V \left\{ \frac{\partial \vec{F}_x}{\partial x} + \frac{\partial \vec{F}_y}{\partial y} + \frac{\partial \vec{F}_z}{\partial z} \right\} dV = \int_V \vec{\Phi} dV \tag{105}$$

and, using the Green's theorem, the second term can be expressed in the surface integration as:

$$\frac{\partial}{\partial t} \int_V \vec{U} dV + \int_S (\vec{F}_x dS_x + \vec{F}_y dS_y + \vec{F}_z dS_z) dV = \int_V \vec{\Phi} dV \tag{106}$$

where dS_i is the area segment that is normal to i-direction. Note the volume-integration can be put inside the time-differentiation operator due to stationary grids. Equation 106 tells that that the change of $\vec{U}$ unit time is equal to the summation of all fluxes crossing the surface of the control volume. Therefore, it is required to accurately evaluate each flux at the surface.

The vectors of $\vec{U}$, $\vec{F}_x$, $\vec{F}_y$, $\vec{F}_z$, and $\vec{\Phi}$ for the MHD non-equilibrium reacting flow are defined as:

$$\vec{U} = (\bar{\rho},\ \bar{\rho}\tilde{u},\ \bar{\rho}\tilde{v},\ \bar{\rho}\tilde{w},\ \bar{\rho}\tilde{E}_h,\ \bar{\rho}k^{sgs},\ \bar{\rho}\tilde{Y}_k,\ \bar{\rho}_e\tilde{E}_e,\ \bar{B}_x,\ \bar{B}_y,\ \bar{B}_z, k^{sgs,b})^T \tag{107}$$

where $\tilde{E}$ is defined as $E_h = E_{g,h} + B^2/2\mu_0$, and $P\vec{h}i$ is given by:

$$\vec{\Phi} = (0,\ 0,\ 0,\ 0, -\Delta\dot{\epsilon}_{e,h} - R, S_{k^{sgs}},\ \omega_k,\ S_{E_e},\ 0,\ 0,\ 0, S_{k^{sgs,b}})^T \tag{108}$$

where, $-R$ is the radiation recombination loss. The terms $S_{k^{sgs}}$, S_{E_e}, and $S_{k^{sgs,b}}$ are given by:

$$S_{k^{sgs}} = -\frac{\bar{\rho}C_\epsilon}{\triangle}(k^{sgs})^{\frac{3}{2}} - \tau_{ij}^{sgs}\frac{\partial \tilde{u}_j}{\partial x_i} - T_{ij}^{sgs}\frac{\partial \tilde{u}_j}{\partial x_i} - \frac{C_{p,b}}{\triangle}\sqrt{k^{sgs}}k^{sgs,b}$$
$$S_{E_e} = -p_e\frac{\partial u_i}{\partial x_i} + \frac{J_k J_k}{\sigma} + -\Delta\dot{\epsilon}_{e,h} - \sum \omega_{k+1}\chi_{k\to k+1}$$
$$S_{k^{sgs,b}} = -\frac{C_{\epsilon,b}k^{sgs,b}\sqrt{k^{sgs,b}/\bar{\rho}}}{\triangle} - \frac{1}{\mu_0}\tau_{ij}^{sgs,b}\frac{\partial \bar{B}_i}{\partial x_j} - k^{sgs,b}\frac{\partial \tilde{u}_j}{\partial x_j}$$

And, $\vec{F}_x$, $\vec{F}_y$, and $\vec{F}_z$ are defined as:

$$F_x = \begin{pmatrix} \bar{\rho}\tilde{u} \\ \bar{\rho}\tilde{u}\tilde{u} + \bar{p} \\ \bar{\rho}\tilde{u}\tilde{v} \\ \bar{\rho}\tilde{u}\tilde{w} \\ \bar{\rho}\tilde{u}(\tilde{E}_h + \bar{p}) \\ \bar{\rho}\tilde{u}k^{sgs} \\ \bar{\rho}\tilde{u}\tilde{Y}_k \\ \bar{\rho}_e\tilde{u}E_e \\ 0 \\ 0 \\ 0 \\ \tilde{u}k^{sgs,b} \end{pmatrix} + \begin{pmatrix} 0 \\ -\bar{\tau}_{xx} - \bar{T}_{xx} + \tau_{xx}^{sgs} + T_{xx}^{sgs} \\ -\bar{\tau}_{xy} - \bar{T}_{xy} + \tau_{xy}^{sgs} + T_{xy}^{sgs} \\ -\bar{\tau}_{xz} - \bar{T}_{xz} + \tau_{xz}^{sgs} + T_{xz}^{sgs} \\ \tilde{u}\bar{\tau}_{xx} + \tilde{v}\bar{\tau}_{xy} + \tilde{w}\bar{\tau}_{xz} - \bar{q}_x - H_x^{sgs} - \sigma_x^{sgs} \\ \frac{\bar{\rho}\nu_e}{Pr_t}\frac{\partial k^{sgs}}{\partial x} \\ -\bar{\rho}\tilde{Y}_k\tilde{V}_{x,k} - Y_{x,k}^{sgs} - \theta_{x,k}^{sgs} \\ k_e\frac{\partial \bar{T}_e}{\partial x} \\ \lambda(-\frac{\partial}{\partial x}\bar{B}_x) + \tau_{xx}^{sgs,b} \\ \tilde{u}\bar{B}_y - \bar{B}_x\tilde{v} - \lambda\frac{\partial}{\partial x}\bar{B}_y + \tau_{xy}^{sgs,b} \\ \tilde{u}\bar{B}_z - \bar{B}_x\tilde{w} - \lambda\frac{\partial}{\partial x}\bar{B}_z + \tau_{xz}^{sgs,b} \\ \lambda\frac{\partial}{\partial x}k^{sgs,b} \end{pmatrix} \tag{109}$$

$$F_y = \begin{pmatrix} \bar{\rho}\tilde{v} \\ \bar{\rho}\tilde{v}\tilde{u} \\ \bar{\rho}\tilde{v}\tilde{v} + \bar{p} \\ \bar{\rho}\tilde{v}\tilde{w} \\ \bar{\rho}\tilde{v}(\tilde{E}_h + \bar{p}) \\ \bar{\rho}\tilde{v}k^{sgs} \\ \bar{\rho}\tilde{v}\tilde{Y}_k \\ \bar{\rho}_e\tilde{v}\bar{E}_e \\ 0 \\ 0 \\ 0 \\ \tilde{v}k^{sgs,b} \end{pmatrix} + \begin{pmatrix} 0 \\ -\bar{\tau}_{yx} - \bar{T}_{yx} + \tau_{yx}^{sgs} + T_{yx}^{sgs} \\ -\bar{\tau}_{yy} - \bar{T}_{yy} + \tau_{yy}^{sgs} + T_{yy}^{sgs} \\ -\bar{\tau}_{yz} - \bar{T}_{yz} + \tau_{yz}^{sgs} + T_{yz}^{sgs} \\ \tilde{u}\bar{\tau}_{yx} + \tilde{v}\bar{\tau}_{yy} + \tilde{w}\bar{\tau}_{yz} - \bar{q}_y - H_y^{sgs} - \sigma_y^{sgs} \\ \frac{\bar{\rho}\nu_e}{Pr_t}\frac{\partial k^{sgs}}{\partial y} \\ -\bar{\rho}\tilde{Y}_k\tilde{V}_{y,k} - Y_{y,k}^{sgs} - \theta_{y,k}^{sgs} \\ k_e\frac{\partial \bar{T}_e}{\partial y} \\ \tilde{v}\bar{B}_x - \bar{B}_y\tilde{u} - \lambda\frac{\partial}{\partial y}\bar{B}_x + \tau_{yx}^{sgs,b} \\ \lambda\frac{\partial}{\partial y}\bar{B}_y + \tau_{yy}^{sgs,b} \\ \tilde{v}\bar{B}_z - \bar{B}_y\tilde{w} - \lambda\frac{\partial}{\partial y}\bar{B}_z + \tau_{yz}^{sgs,b} \\ \lambda\frac{\partial}{\partial y}k^{sgs,b} \end{pmatrix} \tag{110}$$

$$F_z = \begin{pmatrix} \bar{\rho}\tilde{w} \\ \bar{\rho}\tilde{w}\tilde{u} \\ \bar{\rho}\tilde{w}\tilde{v} \\ \bar{\rho}\tilde{w}\tilde{w} + \bar{p} \\ \bar{\rho}\tilde{w}(\tilde{E}_h + \bar{p}) \\ \bar{\rho}\tilde{w}k^{sgs} \\ \bar{\rho}\tilde{w}\tilde{Y}_k \\ \bar{\rho}_e\tilde{w}E_e \\ 0 \\ 0 \\ 0 \\ \tilde{w}k^{sgs,b} \end{pmatrix} + \begin{pmatrix} 0 \\ -\bar{\tau}_{zx} - \bar{T}_{zx} + \tau_{zx}^{sgs} + T_{zx}^{sgs} \\ -\bar{\tau}_{zy} - \bar{T}_{zy} + \tau_{zx}^{sgs} + T_{zx}^{sgs} \\ -\bar{\tau}_{zz} - \bar{T}_{zz} + \tau_{zx}^{sgs} + T_{zx}^{sgs} \\ \tilde{u}\bar{\tau}_{zx} + \tilde{v}\bar{\tau}_{zy} + \tilde{w}\bar{\tau}_{zz} - \bar{q}_z - H_z^{sgs} - \sigma_z^{sgs} \\ \frac{\bar{\rho}\nu_e}{Pr_t}\frac{\partial k^{sgs}}{\partial z} \\ -\bar{\rho}\tilde{Y}_k\tilde{V}_{z,k} - Y_{z,k}^{sgs} - \theta_{z,k}^{sgs} \\ k_e\frac{\partial \bar{T}_e}{\partial z} \\ \tilde{w}\bar{B}_x - \bar{B}_z\tilde{u} - \lambda\frac{\partial}{\partial z}\bar{B}_x + \tau_{zx}^{sgs,b} \\ \tilde{w}\bar{B}_y - \bar{B}_z\tilde{v} - \lambda\frac{\partial}{\partial z}\bar{B}_y + \tau_{zy}^{sgs,b} \\ \lambda\frac{\partial}{\partial z}\bar{B}_z + \tau_{zz}^{sgs,b} \\ \lambda\frac{\partial}{\partial z}k^{sgs,b} \end{pmatrix} \tag{111}$$

4.2 The $\partial B_k/\partial x_k = 0$ constraint

In the previous section, we formulated the closed LES equations to solve MHD turbulence under the condition $\partial B_i/\partial x_i = 0$. These equations are valid from the theoretical viewpoint. However, from the numerical viewpoint, this is not always true, especially when using finite-difference or finite-volume codes with limited numerical accuracy. Ideally, $\partial B_i/\partial x_i$ converges to zero as the grid resolution $\triangle x$ and $\triangle t$ approach zero. Unfortunately, this negates the purpose of LES and increases computational time unnecessarily. Thus, a numerical scheme is necessary to force the $\partial B_i/\partial x_i$ to become zero or at least a small enough (acceptable) value. A comprehensive discussion is given by Gabor (143). In this paper, several schemes are evaluated, such as *the eight-wave formulation* (116) that enforces the truncation error to be zero, *the projection scheme* (13) that enforces the constraint in some discretization by projection of the magnetic field and *the constrained transport scheme*(36) that conserves $\partial B_i/\partial x_i$ to machine accuracy in some discretization for every grid cell. In the current implementation, when we introduce the magnetic field that has some non-zero values of $\partial B_k/\partial x_k$, we eliminate it initially by using *the projection scheme*. Afterward, during the simulation, we adopt *the constrained transport scheme*(119) to avoid accumulation of the truncation error.

4.2.1 Projection scheme

In *the projection scheme* proposed by Brackbill and Barnes (13), the vector field B_k is decomposed into the two parts: a curl and a gradient so that:

$$B_k = \epsilon_{kij}\frac{\partial A_i}{\partial x_j} + \frac{\partial \phi}{\partial x_k} \tag{112}$$

Here A is the vector potential and has a physical meaning like a streamline. The variable ϕ does not have any significant meaning. A nonzero of ϕ results from numerical error. Taking the divergence of the above equation, a Poisson equation is obtained:

$$\frac{\partial^2 \phi}{\partial x_k^2} = \epsilon_{kij}\frac{\partial B_i}{\partial x_j} \tag{113}$$

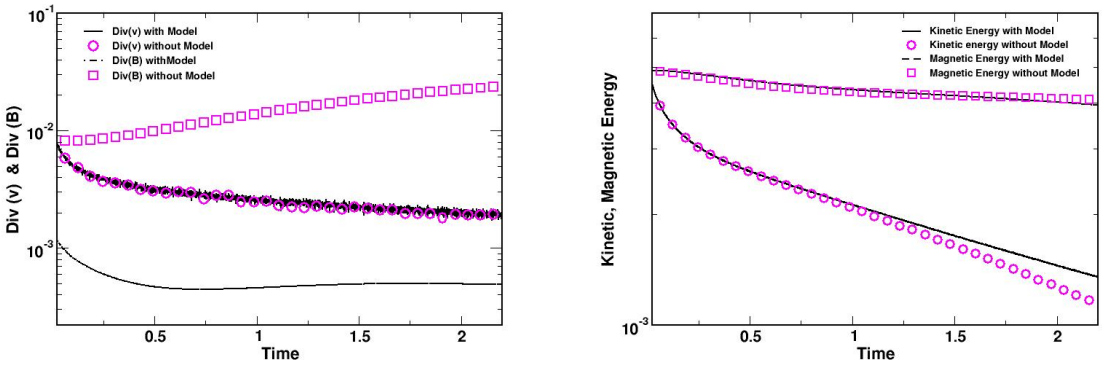

(a) (b)

Figure 6: History of (a) $\partial u_i/\partial x_i$ and $\partial B_i/\partial x_i$ and (b) the kinetic and magnetic energy with/without the projection scheme.

If we successfully solve this equation for ϕ, we can modify B such that we calculate numerically

$$B_i' = B_i - \frac{\partial \phi}{\partial x_i} \tag{114}$$

If the Poisson equation can be accurately solved, $\partial B_i'/\partial x_i$ must be zero. In practice, $\partial B_i'/\partial x_i$ is not zero, but much less than $\partial B_i/\partial x_i$. In order to achieve the criteria of accuracy, we need to iterate this operation. In many respects, this requirement is similar to the $\partial u_i/\partial x_i = 0$ requirement in incompressible flow. However, to solve a Poisson equation inside the complicated geometry by single machine is computationally expensive. Therefore, a parallelisation for solving a Poisson equation have been implemented.

In order to investigate the effect of the *the projection scheme*, the simple isotropic turbulence (the resolution is 64^3) was studied with/without modification. Due to the computational cost, the Poisson equation was solved every five steps. In Fig. 6 (a)-(b), the histories of $\partial u_i/\partial x_i$ and $\partial B_i/\partial x_i$ and kinetic energy and magnetic energy are shown for two cases: with/without projection scheme. At $t = 0.01$, the magnetic field is initiated. Without modification, th magnitude of $\partial B_i/\partial x_i$ is about five times larger than the $\partial u_i/\partial x_i$. The initial increase of $\partial B_i/\partial x_i$ is caused by the incorrect initialization of magnetic field.

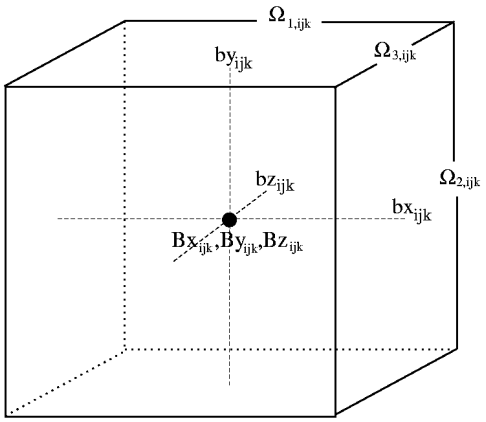

Figure 7: A schematic of the staggered grid. Bx, By, Bz are defined in the cell center, and bx, by, bz are defined on grid interfaces. The advective fluxes Ω_i are at grid edge.

The slow decrease is related to the reduction of magnetic turbulence, therefore, the relative importance of a nonzero effect on the numerical result in significant. On the other hand, with modification, $\partial B_i/\partial x_i$ become about one fifth of $\partial u_i/\partial x_i$ and does not have an initial peak. This means that the *the projection scheme* successfully eliminates the unphysical part of the magnetic field and keep $\partial B_i/\partial x_i$ relatively small. The unphysical non-zero effect can be seen in the gradient of kinetic energy and magnetic energy variation with time (see Fig. 6 (b)). The case without modification has a steeper in kinetic energy, but is slightly less steep in th magnetic field. This can be explained by considering the magnetic and kinetic energy equations in which the unphysical non-zero effect is considered.

$$\frac{\partial}{\partial t}\left(\frac{\bar{B}_k\bar{B}_k}{2\mu_0}\right)+\frac{\bar{B}_i}{\mu_0}\frac{\partial}{\partial x_j}\left\{(\tilde{u}_j\bar{B}_i-\tilde{u}_i\bar{B}_j)-\bar{\lambda}\frac{\partial\bar{B}_i}{\partial x_j}+\tau_{ij}^{sgs,b}\right\}=\frac{\bar{B}_i\tilde{u}_i}{2\mu_0}\frac{\partial\bar{B}_j}{\partial x_j} \tag{115}$$

In Eq. 115, the additional term that disappears under the condition $\partial B_i/\partial x_i = 0$ appears. The counterpart of this term also appears in the kinetic energy equation. It shows that the unphysical non-zero effect plays an additional role in transferring the energy between the magnetic energy and kinetic energy. Moreover, this effect is acceleration of the plasma parallel to the field line because $\frac{\bar{B}_i}{\mu_0}\partial\bar{B}_k/\partial x_k$ has to be added in Lorentz force term.

4.2.2 Constrained transport scheme

In *the constrained transport scheme*, the components of magnetic field (bx, by, bz) are defined at the grid interface, and the advective fluxes $(\Omega_1, \Omega_2, \Omega_3)$ are calculated at the grid edges (see Fig. 7). The cell-centered values of magnetic field (Bx, By, Bz) are then calculated by interpolating the values at grid interfaces as: $Bx_{i,j,k} = \frac{1}{2}(bx_{i,j,k} + bx_{i-1,j,k})$, $By_{i,j,k} = \frac{1}{2}(by_{i,j,k} + by_{i,j-1,k})$, and $Bz_{i,j,k} = \frac{1}{2}(bz_{i,j,k} + bz_{i,j,k-1})$.

These terms are then used to be evaluate the Lorentz force term in the momentum equation. The unique positioning of values associated with the magnetic field ensures that numerical error due to discretization and integration is zero, and $\partial B_k/\partial x_k$ is restricted from increasing. The accuracy obtained here is as good as what has been reported in literature (119).

Here is a brief discussion about how it works in two dimensional case. The magnetic field are updated as

$$bx^{n+1}_{x,i,j} = bx^{n}_{x,i,j} - \frac{\Delta t}{\Delta y}(\Omega_{i,j} - \Omega_{i,j-1}) \tag{116}$$

and

$$by^{n+1}_{y,i,j} = by^{n}_{y,i,j} + \frac{\Delta t}{\Delta x}(\Omega_{i,j} - \Omega_{i-1,j}) \tag{117}$$

Therefore, the divergence of b^n_i is given by:

$$\begin{aligned} \partial b^{n+1}_i/\partial x_i &= \frac{bx^{n+1}_{x,i,j} - bx^{n+1}_{x,i-1,j}}{\Delta x} + \frac{by^{n+1}_{y,i,j} - by^{n+1}_{y,i,j-1}}{\Delta y} \\ &= \frac{bx^{n}_{x,i,j} - bx^{n}_{x,i-1,j}}{\Delta x} + \frac{by^{n}_{y,i,j} - by^{n}_{y,i,j-1}}{\Delta y} + 0 \\ &= \frac{bx^{0}_{x,i,j} - bx^{n}_{x,i-1,j}}{\Delta x} + \frac{by^{0}_{y,i,j} - by^{n}_{y,i,j-1}}{\Delta y} \end{aligned} \tag{118}$$

The sum of contribution of advective fluxes are exactly cancelled each other and does not contribute to the the divergence of b^n_i. Therefore, if the it is zero at first, it ensures that it is always zero. Therefore, it is necessary to generate the divergence-free initialization for the

magnetic fields. This requirement becomes critical when the non-ideal MHD (diffusion term is involved) is calculated. Since, the diffusion term is obtained based on the divergence-free condition. For example, the second derivative of b_x is calculated as:

$$\frac{\partial^2 b_x}{\partial x^2} + \frac{\partial^2 b_x}{\partial y^2} + \frac{\partial^2 b_x}{\partial z^2} = -\left\{ \frac{\partial}{\partial y}\left(\frac{\partial b_y}{\partial x}\right) + \frac{\partial}{\partial z}\left(\frac{\partial b_z}{\partial x}\right)\right\} + \frac{\partial^2 b_x}{\partial y^2} + \frac{\partial^2 b_x}{\partial z^2} \tag{119}$$

An incorrect estimation of Ω brings in the problem of the diffusion of magnetic field in the parallel to the fields itself.

4.3 Dual Time Step.

The numerical solver is an explicit time-integration, finite-volume method that is nominally second-order accurate in space and time. The time-step is chosen to satisfy Courant-Friedrichs-Lewy (CFL) condition (19):

$$\Delta t \leq \Delta t_c = \frac{\Delta x}{|u| + c_s + v_a} \tag{120}$$

Here, c_s is the sound speed and v_a is the Alfvén wave-speed. For the numerical stability, we take $\Delta t = C_{CFL}\Delta t_c$ where a safety factor C_{CFL} is set 0.5. The time-step is also limited by diffusional processes,

$$\begin{aligned} \Delta t \leq \Delta t_d &= min(\Delta t_{d,\lambda}, \Delta t_{d,\mu_e}, \Delta t_{d,\bar{\sigma}}, \Delta t_{d,\kappa}) \\ &= min\left(\frac{\Delta x^2}{max(\bar{\lambda}, \nu_e, \bar{\sigma})}, \frac{\Delta x^2 \bar{\rho} Pr_t}{2\mu\gamma}\right) \end{aligned} \tag{121}$$

Here, γ is the ratio of specific heat. The fluid diffusion time-scale and magnetic field diffusion time-scale are of the same order when the magnetic Prandtl number is set to unity. For cold air/plasma coexisting problem, however, the range of magnetic Prandtl number varies greatly from the cold air region to the plasma region. The diffusion of electrical potential requires very small time steps at the plasma. These diffusion process limit the choice of time-step. The typical characteristic time scales of the different physical mechanism are given as:

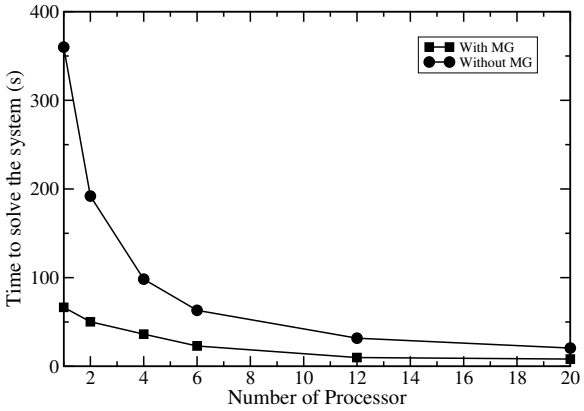

Figure 8: Comparison of computational time to solve the system between the MG model and no model.

$$
\begin{aligned}
&Viscous\ diffusion: && \Delta t_{d,\mu_e} \approx 10^{-5}s \\
&Convection: && \Delta t_c \approx 10^{-8}s \\
&Thermal\ diffusion: && \Delta t_{d,\kappa} \approx 10^{-9}s \\
&Electric\ diffusion: && \Delta t_{d,\bar{\sigma}} \approx 10^{-9}s \sim 10^{-12}s \\
&Magnetic\ diffusion: && \Delta t_{d,\bar{\lambda}} \approx 10^{-12}s \sim 10^{-15}s
\end{aligned}
\quad . \tag{122}
$$

If the time-step is chosen to satisfy the CFL, the required time step should be based on $\Delta t_{d,\bar{\lambda}} \approx 10^{-15}s$, and practically this is sever constraints on the feasibility of such a calculation. For this reason, we use a dual time step in which the diffusion flux is calculated $N_{\bar{\sigma}}$ times during a single flow time step. $N_{\bar{\sigma}}$ is determined by $N_{\bar{\sigma}} = \Delta t_c / \Delta t_{d,\bar{\sigma}}$. The convergence of the electrical potential is checked and stopped as soon as it reaches a steady value. Typical values of $N_{\bar{\sigma}}$ in this work $N_{\bar{\sigma}} \simeq 100 \sim 1000$. This dual-time-stepping scheme is not advantageous for the magnetic diffusion flux, since the time scales of Δt_c and $\Delta t_{d,\bar{\lambda}}$ are more than six orders of magnitude apart. Thus, an implicit three dimensional parallel multigrid method (MG) scheme of $O(\Delta t)$ (For higher time-space accuracy, Crank-Nicolson method is recommended as a future work.) is used for solving the diffusive part of the magnetic induction equation (14):

$$
\frac{\partial \bar{B}_i}{\partial t} = \frac{\partial}{\partial x_j}\left(\bar{\lambda}\frac{\partial \bar{B}_i}{\partial x_j}\right) \tag{123}
$$

To simplify the parallel programming, an alternating-direction implicit (ADI) method is used (114). The advantage of ADI for parallel programing is that it is not necessary to communicate data between neighboring processors during implicit iterations. The computational domain of each processor knows the boundary conditions in the same direction as the diffusive direction. The method is tested on a cubic domain of size $61 \times 61 \times 61$ with different number of processors. The results are shown in Fig. 8. The MG method drastically reduces the computational time especially when small number of processors are used. When a large number of processors are used, the time for communication becomes comparable with the time for iterative calculations and the reduction of computational time is less significant. The minimum computational time needed to solve the system (7.14 s) is achieved when 20 processors are used compared to 360 s which is required for a single processor without MG.

CHAPTER V

VALIDATION OF MHD LKDM MODEL

To test the validity of the MHD-LDKM closure for LES derived in the previous section, three types of simulation are conducted. In the first case, the effect of an externally applied magnetic field on an initially isotropic MHD turbulent flow is investigated. In the second case, homogeneous MHD turbulence is initially introduced in the computational domain so that turbulent decay can be investigated. No external field, forces or frame rotation are applied. In the last case, initially isotropic MHD turbulent subject to frame rotation is studied. Validation of this model is performed qualitatively and quantitatively.

The initial conditions used for the validation are listed in Table 1. Here, N represents the grid resolution. For the test condition used here, grid resolution of 64^3 and 32^3 are used for LES, and 128^3 for DNS. The magnetic helicity (H_m) and the cross helicity (H_c) (that are normalized with the total energy (E^t)) are tabulated in the last two columns. For all the cases, the ratio of kinetic energy and magnetic energy is unity, and the magnetic helicity is the same. On the other hand, the cross helicity has the maximum values for *Case 2* where the magnetic field and velocity field initially have the same profiles (called Alfvenic state). *Case 0* represents a baseline case at low magnetic Reynolds number, and *Case 1* initially has small magnetic helicity and cross helicity. However, *Case 2* has the maximum value for the cross helicity, but still has small magnetic helicity. Both these cases (1,2) are for moderate magnetic Reynolds number. Finally, *Case 3* and *Case 4* are at strong magnetic Reynolds number but with the different values of the magnetic diffusivity.

The numerical solver is an explicit time-integration, finite-volume method that is nominally fourth-order accurate in space and second-order time that has been extensively validated and applied to many flows (33; 112; 123) Explicit time accuracy requires using a time step that is the smallest of relevant time step.

Here, there are two time steps: the convective time step $\Delta t_c = \Delta x/(|u| + c_s + v_a)$,

Table 2: Summary of the system parameters of the decaying isotropic turbulence. We introduced isotropic turbulent flow field for a large range of $R_m = 0.01 \sim 10000$, and randomly initialize the magnetic field except in *Case 2* where the magnetic field and velocity field initially have the same profiles. Rm_λ is defined by $Rm_\lambda = \frac{2}{3}\sqrt{15E^kE^t/\epsilon\lambda}$.

	$\mathbf{N}$	$\mathbf{Rm_\lambda}$	$\mathbf{R_m}$	ρ	$\mathbf{E^k/E^m}$	$\mathbf{H_m/E^t}$	$\mathbf{H_c/E^t}$
Case 0-a	32	15	$0.01 - 0.05$	0.04	1.0	≈ 0.01	≈ 0.01
Case 0-b	64	15	~ 0.05	0.04	1.0	≈ 0.01	≈ 0.01
Case 0-c	128	15	~ 0.05	0.04	1.0	≈ 0.01	≈ 0.01
Case 0-d	64	75	~ 0.1	0.04	1.0	≈ 0.01	≈ 0.01
Case 0-e	128	75	~ 0.1	0.04	1.0	≈ 0.01	≈ 0.01
Case 1	32	51	5	0.04	1.0	≈ 0.01	≈ 0.01
Case 2	32	51	5	0.04	1.0	≈ 0.01	≈ 1
Case 3	32	40	5000	0.04	1.0	≈ 0.01	≈ 0.01
Case 4	32	40	500-10000	0.04	1.0	≈ 0.01	≈ 0.01

where c_s is the sound speed and v_a is the Alfvén speed, and the diffusion time step $\Delta t_d = \Delta x^2/max(\bar{\lambda}, \nu_e)$ (Note that the diffusion of flow and magnetic field has the same order.) Additionally, in the presence of the frame rotation, an additional time limitation due to the Coriolis appears: $\Delta t_r = 2.83/(2\omega)$ (104). Here, ω is the rotation rate.

5.1 Anisotropic turbulence

We use the initially isotropic turbulent case (*Case 0-b*) with an external applied field from the bottom to the upper surface. Figures 9 (a)-(c) show the contours of the kinetic energy at different time instants. Note that since turbulence is rapidly decaying, the energy scale are rescaled at each time step to enable qualitative visualization. These figures show that the diffusion of angular momentum along the field lines cause the vortex to elongate into a cylindrical shape. It is seen that the small-scale turbulent structure is significantly damped by MHD effect. These results qualitatively agree with previous observations of the effect of magnetic field obtained by Knaepen (74) using the dynamic Smagorinsky model and a low magnetic Reynolds number assumption.

To understand how the turbulent feature become two-dimensional in the presence of the external field, consider the definition of the Lorentz force and rewrite it as:

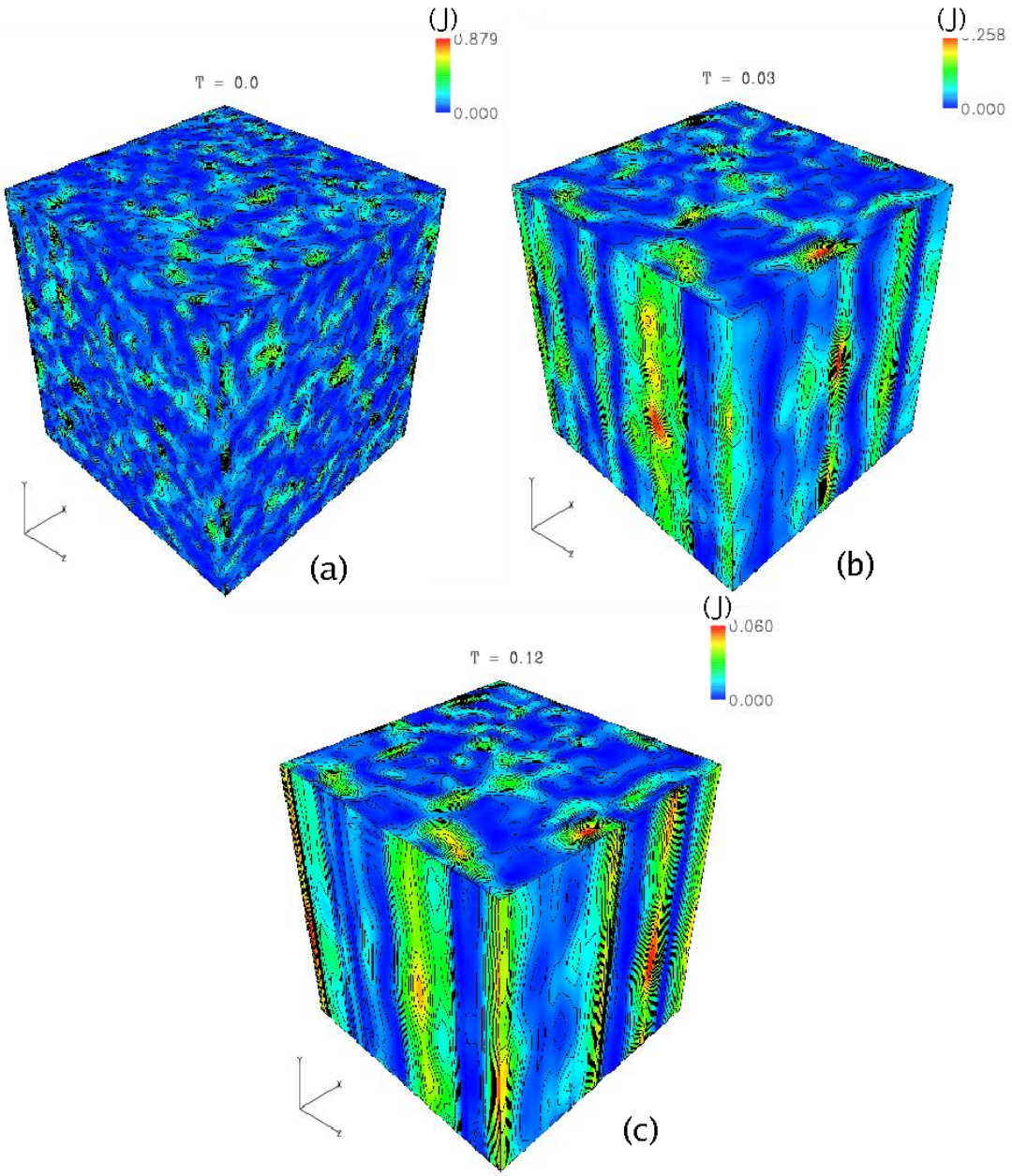

Figure 9: Contours of the kinetic energy obtained from the LES model for *Case 0-b* with $R_m = 0.01$. The times at which the contours are (a) $T = 0.0\ s$, (b) $T = 0.03\ s$, and (c) $T = 0.12\ s$.

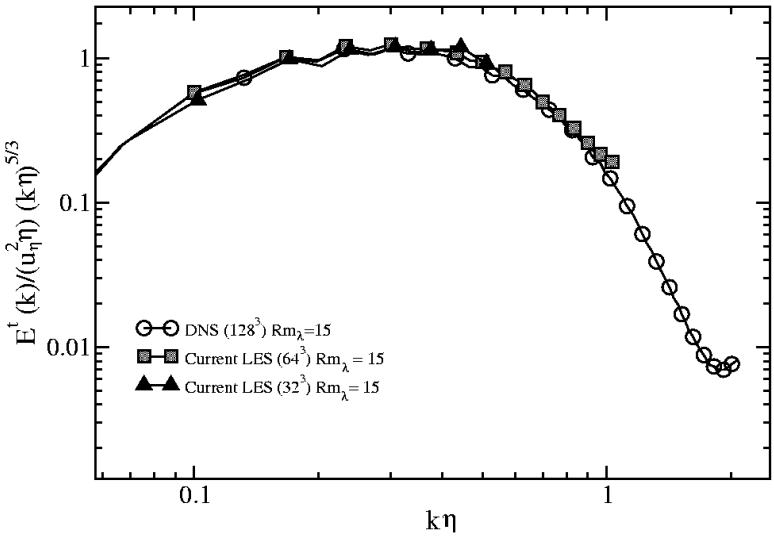

Figure 10: The normalized total energy spectra from DNS (128^3), LES (64^3), and LES (32^3) for *Case 0-a,b,c.*

$$\epsilon_{ijk}\bar{J}_j\bar{B}_k = \frac{\bar{B}_j}{\mu_0}\frac{\partial \bar{B}_i}{\partial x_j} - \frac{\partial}{\partial x_j}(P_{mag}\delta_{ij}) \tag{124}$$

The second term is irrotational and does not contribute to turbulent scale deformation. However, the first term is rotational and a strong anisotropic stress, since the large uniform field (By_0) appears only in the y component ($\left(\frac{\bar{B}x}{\mu_0}\frac{\partial \bar{B}x}{\partial x}, \frac{By_0+\bar{B}y}{\mu_0}\frac{\partial \bar{B}y}{\partial y}, \frac{\bar{B}z}{\mu_0}\frac{\partial \bar{B}z}{\partial z}\right)$). This stretches the turbulent flow in y-direction until this force is balanced by the hydrodynamic force.

5.2 Isotropic turbulence

5.2.1 Non-rotational case

We study freely decaying MHD turbulence without an external magnetic field in this section. The instantaneous contours of the components of the velocity field and magnetic field for DNS (128^3) and LES (64^3) were compared (not shown for brevity). Overall, flow is good qualitative agreement, especially in the large-scale motions. For more quantitative comparison (as done in the past by many researchers) we evaluate and compare the distribution of kinetic energy and dissipation rate in the spectral space.

Figure 10 shows the comparison of the normalized total energy spectra for $Rm_\lambda = 15$ from DNS, and our LES. All results collapses well, and all obtaine Kolmogorov constant of

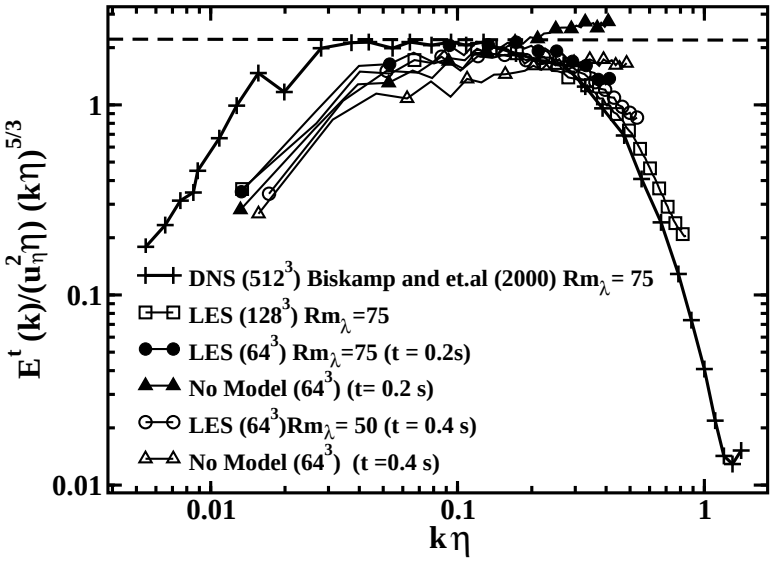

Figure 11: The normalized total energy spectra from DNS (512^3, Biskamp *et al.* (10)), LES (128^3), LES (64^3), and no subgrid model (64^3) for *Case 0-d,e.* The dashed line indicates the Kolomogorov spectrum with $C_K = 2.3$.

about $C_K \sim 1.4$ for this low Rm_λ turbulence case. In such a small Rm_λ case, the turbulent motion is insensible so that this test is important to evaluate a robustness of the turbulent model which should have a capability to handle the laminar flow (k^{sgs} and $k^{sgs,b}$ become zero).

For higher Rm_λ turbulence case, Fig. 11 compares our LES prediction of the Kolmogorov scaled energy spectrum with the DNS data (512^3) done by Biskamp (10). Also, the spectra obtained by non-model case are overlaid. In this high Rm_λ, the poor resolution is no longer able to capture the turbulent motion in the small-scale, and the ability to evaluate such a unresolved motion is essential.

For both spectra with different $Rm_\lambda = 50, 75$, the LES results follow the DNS data ($Rm_\lambda = 75$), and the predicted Kolmogorov constant roughly agrees with the DNS data ($C_K = 2.3$). However, for the case without the subgrid model it is seen that the spectra does not follow the DNS data in the high wave number clearly showing that the energy dissipation is not sufficient, and unphysical energy accumulation occurs at the small scales.

Figure 12 shows the time evolution of the normalized kinetic and magnetic energy spectra for $Rm_\lambda = 45 \sim 40$, respectively. It is seen that the spectra collapse on each other in the

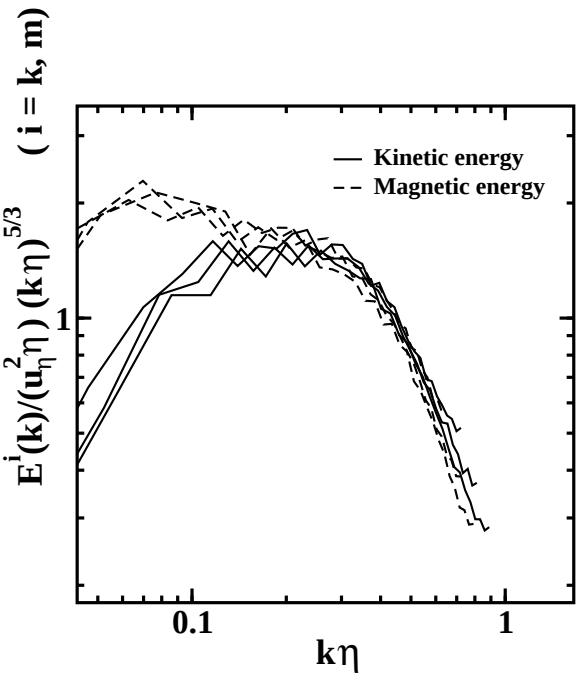

Figure 12: Comparison of time evolution ($Rm_\lambda = 40 \sim 45$) of the normalized magnetic and kinetic energy spectra calculated by LES (64^3) for *Case 0-d*.

high wave number. Since the magnetic energy decays much slower than the kinetic energy, the magnetic energy spectra in the low wave number where the most part of the energy contains is higher than the kinetic energy spectra. On the other hand, in the higher wave number, both collapse and behave like $E^k \sim E^m$. These results mirror those observed in DNS data (10). The difference between the turbulence kinetic energy and magnetic energy is caused by "a selective decay". The reason why it happens is that in MHD turbulence, there are several invariants as mentioned above out of which the magnetic helicity and cross helicity decay much slowly than does the turbulence energy. Therefore, these conservation laws put more constraints on MHD turbulence and are relaxed only by the dissipative effects. The different decay rate based on the initial magnetic helicity and cross helicity will be talked below. Both normalized spectra have flat profiles at the inertial range so that both follow a $k^{-5/3}$ law.

Figures 13 (a)-(c) show the time history of the spatially averaged α', C_ϵ, $C_{\epsilon,b}$, $C_{p,b}$, C_ν, and C_ν^T, respectively. After turbulence develops, these coefficients are relatively stable and

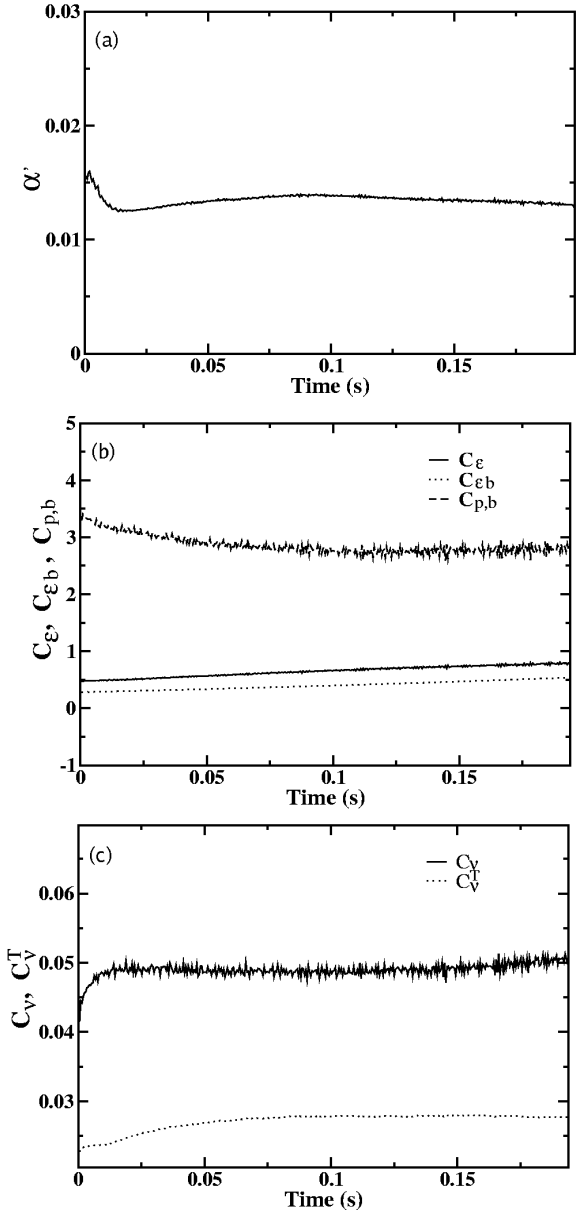

Figure 13: Time history of the model coefficients (a) α', (b) C_ϵ, $C_{\epsilon,b}$, and $C_{p,b}$, and (c) C_ν and C_ν^T for *Case 0-d*.

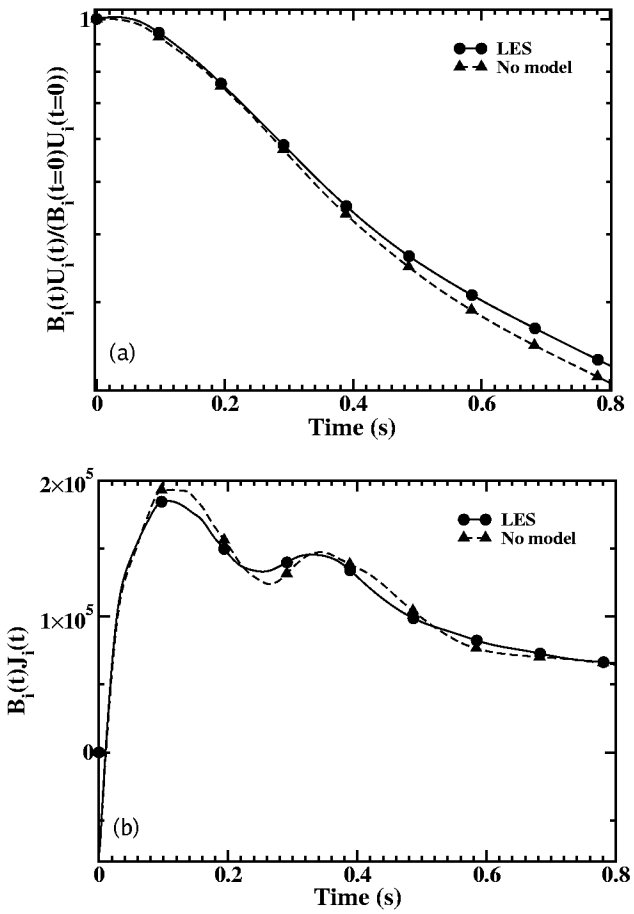

Figure 14: Time histories of (a) $\bar{B}_k\tilde{u}_k$ and (b) $\bar{B}_k\bar{J}_k$ for *Case 0-d*.

asymptotically approach $\alpha' \approx 10^{-2}$, $C_\epsilon, C_{\epsilon,b} \approx 1.0$, $C_{p,b} \approx 3$, $C_\nu \approx 0.05$, and $C_\nu^T \approx 0.03$. Note for non-MHD turbulence, $C_\nu \approx 0.067$ and $C_\epsilon \approx 0.916$ are typically observed (73).

Figures 14 (a) and (b) show the time history of $\bar{B}_k\tilde{u}_k$ and $\bar{B}_k\bar{J}_k$, respectively. These quantities are related to the cross-helicity effect and the α-effect, which are modeled in $\tau_{ij}^{sgs,b}$. The value of $\bar{B}_k\tilde{u}_k$ obtained by the current LES approach is larger than no model case due to the cross-helicity effect that aligns the magnetic field parallel to the flow field. This is important since the small-scale motion effects the large scale motion, and as a result the interaction between the magnetic fields and velocity fields are attenuated since $\vec{u}\times\vec{B}$ vanishes in the induction equation. As time passes, this effect results in a significant difference between the result with model and without model. With the model, the correlation between

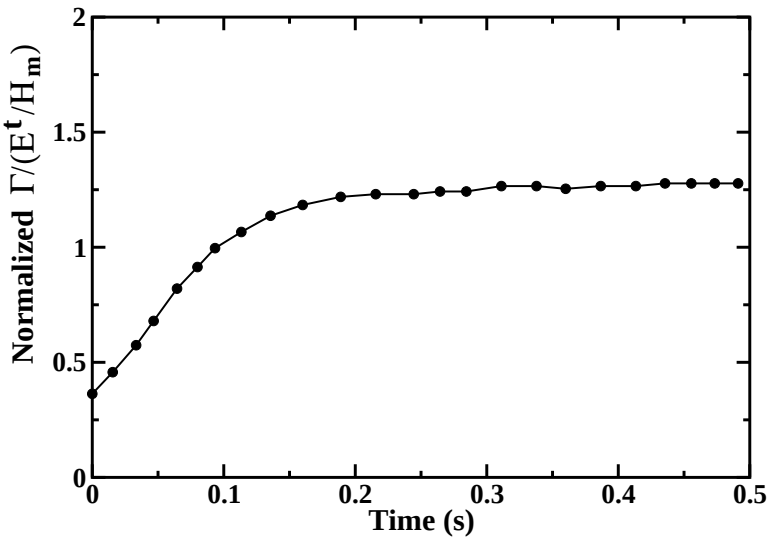

Figure 15: Time history of normalized $\Gamma/(E^t/H_m)$ for *Case 0-d*. After the MHD turbulence is fully developed ($t = 0.22s$), the ratio $\Gamma/(E^t/H_m)$ becomes constant as Biskamp pointed out with his DNS (512^3) result (10).

$\bar{B}_k$ and $\bar{u}_k$ is much higher so that the energy decay should be slower than one without the model.

In Fig. 14 (b), since the α-effect induces the magnetic field parallel to the electric current density, the higher value of $\bar{B}_k\bar{J}_k$ is expected. In fact, it is seen that the local minimum of $\bar{B}_k\bar{J}_k$ is slightly larger than the case without considering the α-effect. This implies that the α-effect works on aligning two fields. Note the oscillating profiles are due to the initial condition. These effects can play an important role in when R_m is significantly large. It is interesting that like the cross-helicity effect, the α-effect also attenuate the Lorentz force and results in the less interaction between velocity fields and magnetic fields.

From these observation, it is concluded that the accurate model of $\tau_{ij}^{sgs,b}$ is essential to predict the energy decay rate since the mutual dependence relation in the large-scale is greatly influenced by unresolved small-scale motions.

For another validation, we check the time variation of the energy ratio, $\Gamma = E^k/E^m$, E^t, and H_m. Biskamp (10) noted that Γ decays in 3D, whereas, it is a constant in 2D, and numerically showed that the ratio $\Gamma/(E^t/H_m)$ remains a constant. A similar result is observed in our study, after the MHD turbulence is fully developed ($t \geq 0.22\ s$) in Fig. 15.

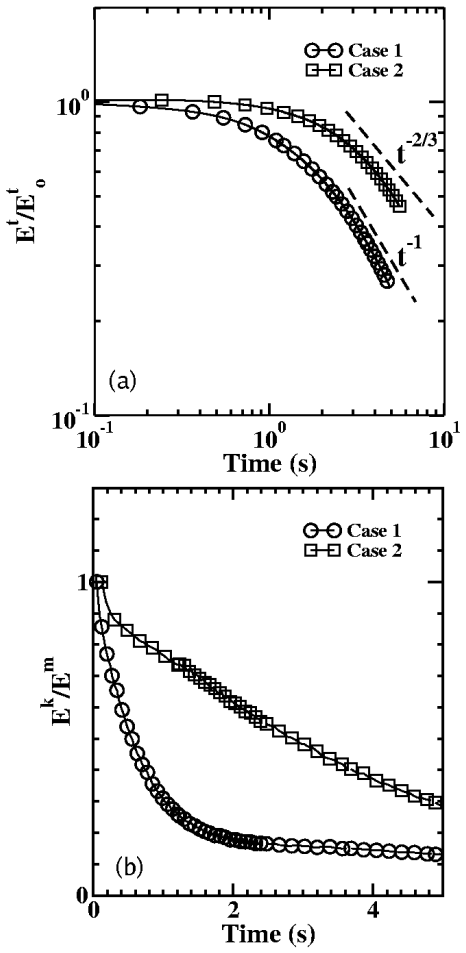

Figure 16: Time histories of (a) E^t and (b) E^k/E^m for *Case 1* and *Case 2*.

This result is consistent with Biskamp's high resolution DNS at (512^3) and gives confidence in the current strategy for LES.

Figures 16 (a)-(b) show the long-time behavior of total energy and energy ratio of E^k/E^m for *Case 1* and *Case 2*, respectively. These are moderate $R_m = 5$ cases, and the exchange of energy between flow field and magnetic field is initiated. For *Case 1*, H_c and H_m are very small. Thus, no back-scatter of magnetic and kinetic energy occurs, and the energy transfer occurs from the large-scale eddies to the small-scale eddies. In contrast, *Case 2* has finite H_c and back-scatter of kinetic energy is expected. Figure 16 (a) shows that E^t follows the asymptotic decay law for both cases, however, the decay rate is different. Without back-scatter, *Case 1* has a steeper gradient ($E^t \sim t^{-1}$) when compared to *Case 2*

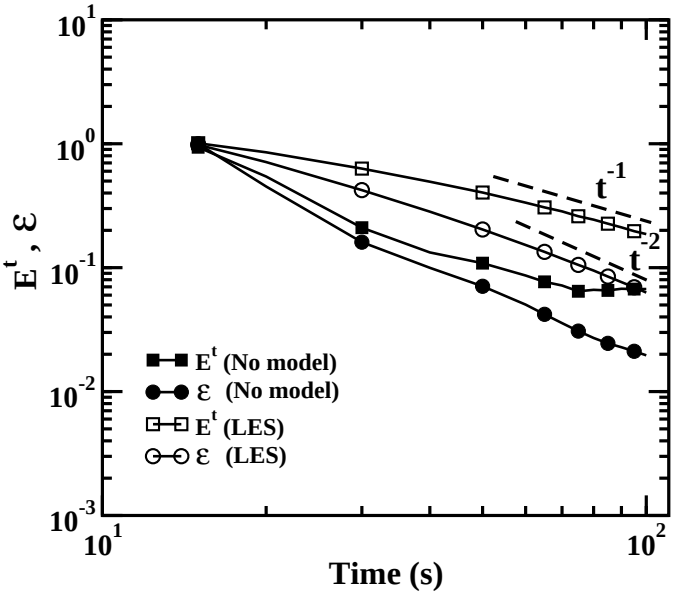

Figure 17: Comparison of no model and LES results for the time histories of kinetic and magnetic energy for *Case 3*. The grid resolution is 32^3 for both cases.

($E^t \sim t^{-2/3}$). Biskamp derived $E^t \sim t^{-2/3}$ theoretically by assuming that H_m was invariant during the energy decay (10). However, this assumption is not always satisfied in 3D MHD turbulence. Also, his calculation shows $E^t \sim t^{-1}$ for small H_m. Even though Biskamp attributes these different decay rates to the difference of initial H_m, our calculation shows that H_c also plays a significant role in energy decay. The back-scatter of kinetic energy for *Case 2* can be seen in Fig. 16 (b). Compared to the *Case 1*, *Case 2* has relatively large amount of kinetic energy remaining during energy decay.

Finally, large R_m cases (*Cases 3* and *4*) are investigated. For this range of R_m, the two-way coupling between the velocity and the magnetic field occurs both in the small-scale and in the large-scale. For example, the disturbance of velocity field generates magnetic field perturbations, propagating through $Alf\grave{v}en$ wave. This oscillation survives much longer than in the case of low R_m, where such perturbations quickly diffuse away. Moreover, the α-effect that promotes back-scatter of magnetic energy plays an important role in this range of high R_m so that the treatment of $\tau_{i,j}^{sgs,b}$ directly influences the accuracy of turbulent model.

Figure 17 compares the time histories of kinetic energy and dissipation rate ϵ with and

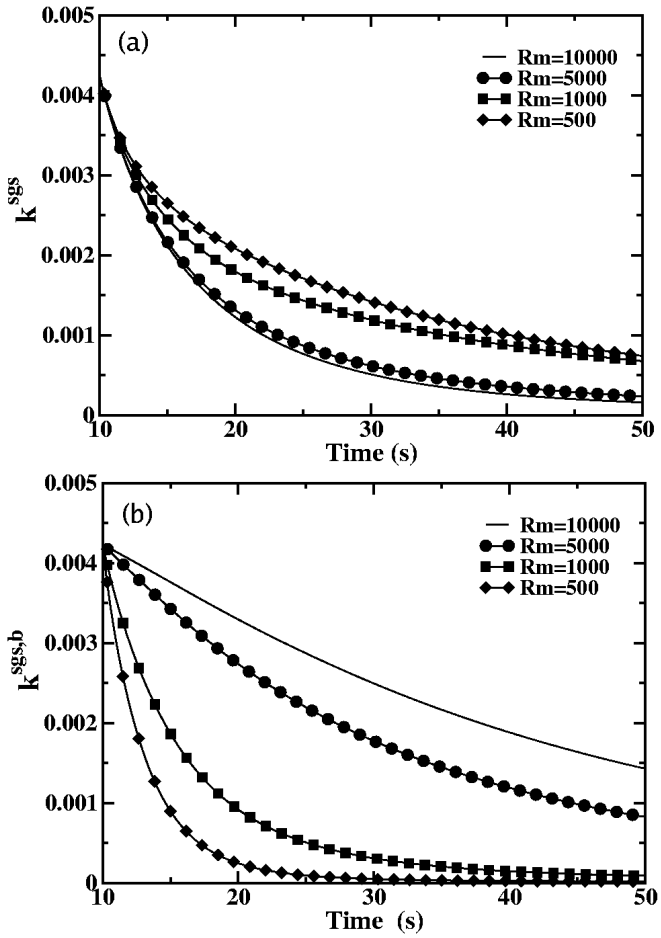

Figure 18: Time evolution of (a) k^{sgs} and (b) $k^{sgs,b}$ with various magnetic Reynold's number for *Case 4*.

without the subgrid model. LES exhibits the power-law behavior $E \sim t^{-n}$ and $\epsilon \sim t^{-(n+1)}$ ($n = 1$ for *Case 3*). On the other hand, no-model case does not follow the power-law behavior, and unphysical increase of kinetic energy is observed. This suggests that the current dynamic subgrid closure is behaving properly in producing the necessary dissipation at the grid scale.

Figures 18 (a)-(b) show the time evolution of subgrid kinetic and magnetic energy for various $R_m = 500 \sim 10000$ (*Case 4*). In this case, $\bar{\sigma}$ varies. As R_m increases (i.e, $\bar{\sigma}$ decreases), the characteristic time scale related to Joule dissipation $\tau_m = \bar{\rho}/(\bar{\sigma}\bar{B}^2)$ decreases compared with the eddy turnover time $\tau_e = l/\tilde{u}$. Therefore, the time ratio, called the interaction number $N = \tau_e/\tau_m$ drops. Consequently, rapid kinetic energy decay is observed.

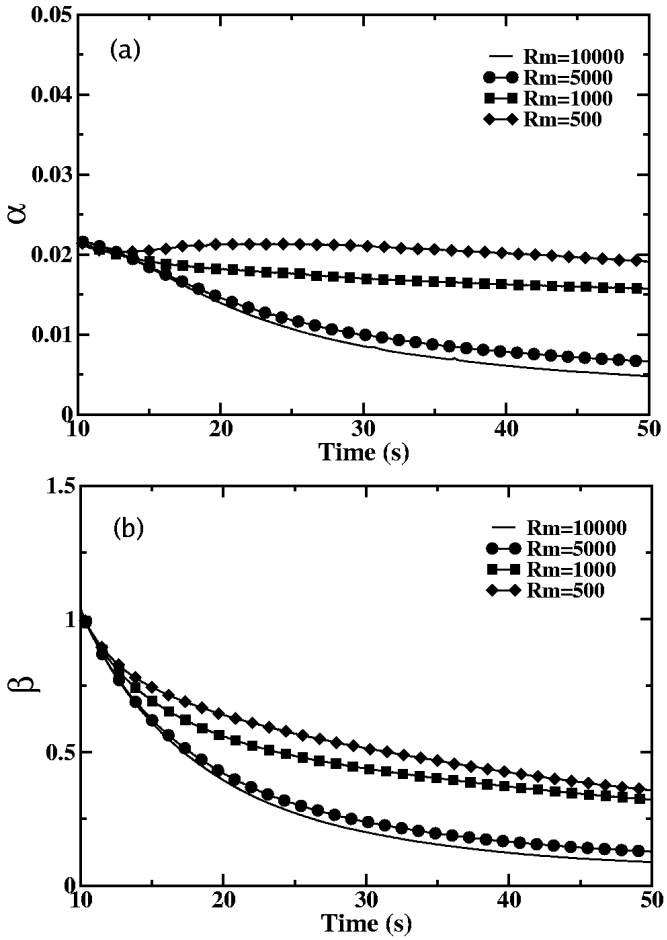

Figure 19: Time evolution of (a) α and (b) β with various magnetic Reynold's number for *Case 4*.

On the other hand, increase of R_m has slower decay rate of magnetic energy due to smaller diffusion since $\bar{\lambda}$ is inversely proportional to $\bar{\sigma}$.

Finally, the evolution of α and β are shown in Figs. 19 (a)-(b), respectively for *Case 4*. It is observed that α increases as R_m decreases. This inverse dependence of α on R_m is also reported by Cattaneo and Hughes (18) for MHD turbulence with a mean magnetic field. Another interesting observation is that α remains finite even after magnetic energy become very small. This indicates that α is not a function of only the magnetic field strength. Earlier studies also reported that α is related to the turbulent residual helicity (159). Comparing the difference between $\alpha_{R_m=10000}$ and $\alpha_{R_m=5000}$ with the difference between $\alpha_{R_m=1000}$ and $\alpha_{R_m=500}$, we can see α is less sensitive to R_m when R_m is large. This is because diffusion

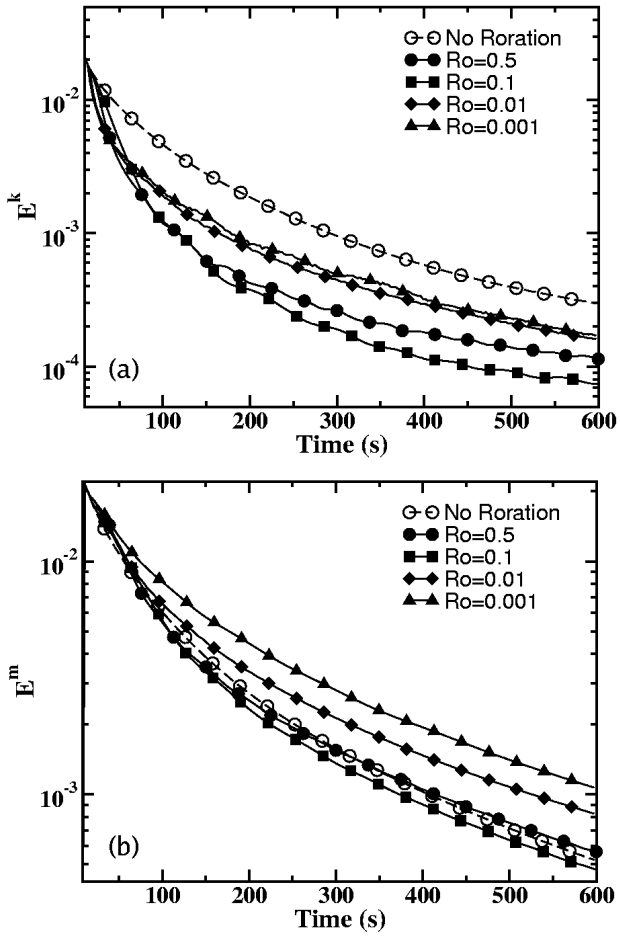

Figure 20: Time evolution of (a) E^k and (b) E^m with various Rossby number for *Case 3*.

is not that important when R_m is large. The parameter β also has the same behavior with respect to R_m but continuously decays. Since β is related to the enhancement of magnetic diffusivity by turbulence transport mechanism (157), it can be understood that β becomes smaller as the turbulence decays.

5.2.2 Rotational case

For non-MHD rotating turbulence case, the nonlinear effect through Coriolis force and viscous effect are important and can be characterized by the Rossby number:

$$R_o = \epsilon/(2E^k\omega) \tag{125}$$

When R_o is larger than unity, the effect of rotation does not play an important role. On

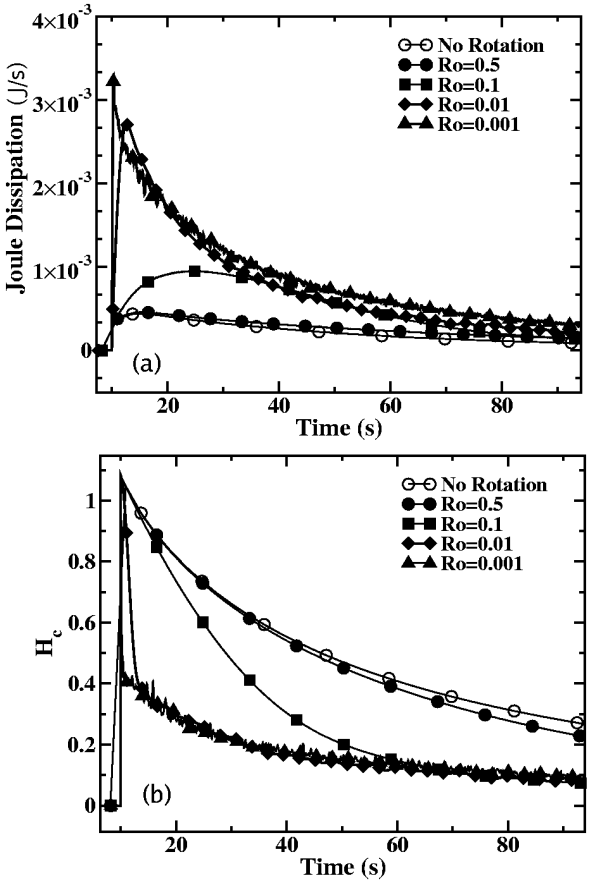

Figure 21: Time history of (a) Joule dissipation and (b) H_c for *Case 3*.

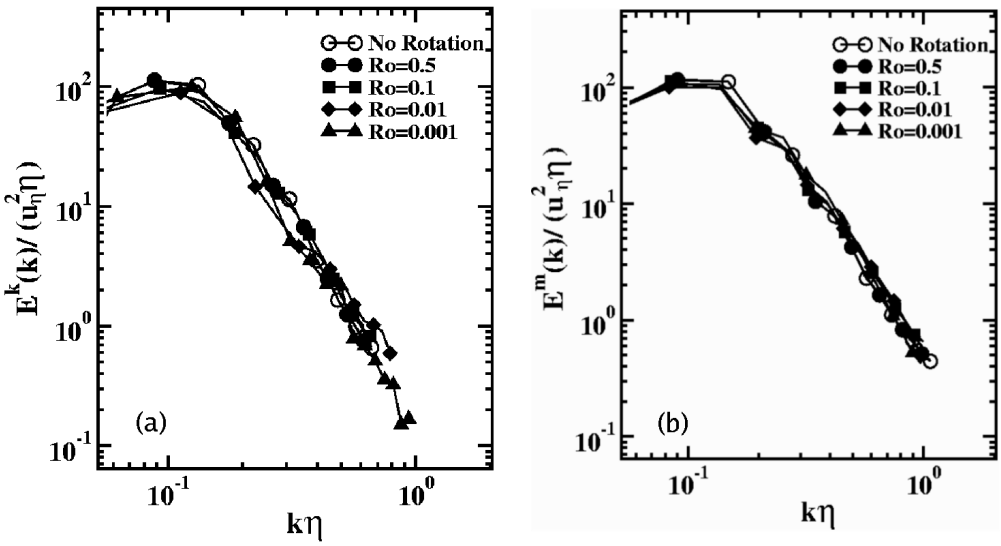

Figure 22: The normalized (a) kinetic energy spectra and (b) magnetic energy spectra with various Robby Number for *Case 3*.

the other hand, when R_o is less than unity, the non-linear effect causes the flow to become anisotropic and the integral length scale in the vertical direction to grow. Past studies have shown that in non-MHD rotating turbulence the energy transfer from the large-scale to the small-scale is prevented due to phase scrambling by the Coriolis force (104; 156), and that the inertial range of rotating turbulence has a steeper slope ($k^{-2} \sim k^{-3}$) than the Kolmogoroff spectrum (164; 166; 155). The flow features also changes prominently, departing from 3D isotropic turbulence to 2D anisotropic turbulence (63).

When MHD effect is included, rotational effect on turbulence is further complicated by the nonlinear interaction due to the Lorentz force. However, the only modification of the governing equation for the rotating MHD turbulence is simply to introduce a Coriolis force term defined by $2\epsilon_{i,j,l}\omega_j\tilde{u}_l$ in the momentum equation, and no new term appears in the other equations (145). An initially homogeneous isotropic turbulence (*Case 3*) being subjected to a frame rotation at a rate $\omega_i = \omega\delta_{i3}$ (where ω is a constant value.) is considered here.

Figures 20 (a)-(b) show the time-history of kinetic and magnetic energy decay, respectively. Compared with non-MHD rotating turbulence case, some significant differences are observed such as the rapid decay of kinetic energy in MHD rotating case. The decay rate

attenuates with decrease of R_o, and when R_o becomes less than 0.1, the decay rate approaches the no rotation case. This gives an indication of the presence of a critical value of R_o (for this calculation, $R_{o,c} \approx 0.1$). We can explain this attenuation with the decrease of R_o by considering the phase scrambling effect introduced in non-MHD case. However, to understand the strong decay at the initial stage, it is necessary to investigate the rotation effect on Joule dissipation. Figure 21 (a) shows the time history of Joule dissipation. It can be seen that the increase of the rotation rate significantly enhances Joule dissipation immediately right after frame rotation is turned on. Since the Coriolis force directly effects on the velocity field, the velocity field that is initially aligned with the magnetic field starts to deviate at later time. This motion promotes Joule dissipation. This is consistent with the result of the cross helicity H_c evolution shown in Fig. 21 (b).

The evolution of magnetic energy has the same trend even though the initial strong decay seen in the kinetic energy related to Joule dissipation is not as dominating. Figures 22 (a)-(b) show the normalized kinetic and magnetic energy spectra at $t = 50\ s$, respectively. Unlike non-MHD case (164; 166; 155), the rotation has minor effects on the spectra in MHD case. Since energy decay is steeper than the non-MHD rotation case, it is reasonable that there is not relatively large energy accumulation in the large-scale eddies.

5.3 Summary of MHD LDKM Model

A new dynamic subgrid model for LES of MHD turbulence is developed and demonstrated. The unique feature of this approach is that the six model coefficients are computed dynamically, and thus, there are no *ad hoc* model parameters to adjust. To determine the performance of this model, several simulations are carried out. The structure of MHD turbulence is examined by comparing DNS and LES results for energy and dissipation spectra. Also, the time variation of ideal invariants is also investigated. For the case with frame rotation, the energy decay rate is steeper than in non-MHD case because frame rotation enhances Joule dissipation. The current study also suggests that there exists a critical R_o beyond which the phase scrambling effect due to the Coriolis force dominates the enhancement of Joule dissipation by rotation. Finally, it is shown that the new dynamic subgrid

model is capable of capturing accurately the MHD turbulence within the LES context. Since there is no requirement of low magnetic Reynolds number assumption to simplify the formulation of this model, this model can be adapted to study a wide variety of physical problems.

CHAPTER VI

FREE-BURING EQUILIBRIUM ARGON ARC

In this chapter, the numerical implementation used in modeling the free-buring equilibrium argon arc is presented.

6.1 Background of Equilibrium Plasma discharge

The experimental combustion group at Georgia Institute of Technology demonstrated the capability of a plasma discharge to sustain methane/air combustion (148). Their experimental results show that very lean and high velocity combustion is possible with plasma-assistance.

To gain further insight an accurate numerical model able to simulate the physics of plasma-assisted combustion is desirable, most importantly a simulation of the plasma-arc physics. There have been several notable efforts to develop numerical models for high-intensity free-burning arcs (9; 45; 61; 65; 68; 80; 52; 81; 126; 127; 128; 136; 152). The most fundamental work was done by Hsu *et al.* (61). They solve the set of conservation equations of mass, momentum, energy and current assuming that the arc is in local thermodynamic equilibrium (LTE), steady, rotationally symmetric, and optically thin. Their simplified numerical results capture many important features of a free-burning arc. The MHD pumping action near the cathode tip is observed, and the results agree well with spectroscopic measurements of the temperature for two different electrode gap sizes and three different current inputs (100, 200, and $300A$). These temperature measurements are used in this paper as a part of code validation.

Kelkar *et al.* model an atmospheric argon arc in a cross flow under assumptions similar to Hsu's model, but additionally, the time-dependent terms are neglected (no turbulent effects are considered) (68). The results show higher temperatures and velocities near the cathode as a result of the larger current densities occurring when there is a cross-flow. Also, Westhoff and Szekely use a two-dimensional, laminar, steady state code to investigate the

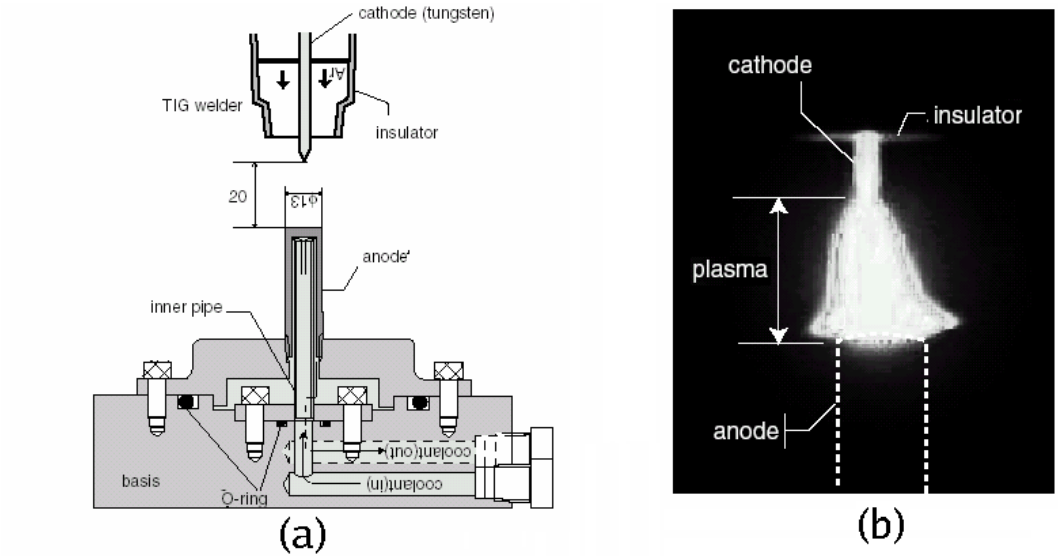

Figure 23: (a) The experimental set-up which is used for the Tungsten Inert gas welder, and (b) plasma picture (65)

nontransferred arc argon plasma torch in which the arc was assumed to be inside the touch all time. To calculate the induced magnetic field, Ampere's law was directly integrated. It was shown that electromagnetic forces play a significant role in affecting the velocity profiles as well as the temperature profiles. Swirl formed inside the discharge region was significantly modified by these forces and had a large effect on the character of the arc by changing the arc attachment point.

Most recently, Bini *et al.* (9) proposed a thermionic emission mechanism in order to eliminate the dependence of boundary conditions on the empirical distribution of the current density near the electrode tips. The electrode sheaths were considered in evaluating the current density and heat flux. In their model, the assumptions of LTE, laminar flow, and steady-state were made. Anode evaporation was neglected. Detailed investigations of the heat fluxes show that larger electrode gaps result in a reduction of overall efficiency as a result of losses toward the chamber.

The magnetically deflected arc has attracted researchers since in welding processes, arcs are frequently exposed to external fields and deflection in an uncontrolled manner occurs (126). With strong external fields, both experimental and numerical investigations show a

detached arc column resulting from the interaction between the self-induced current and the external fields (136). This behavior is used for the design of circuit breakers and contractors (11). As an extension of the modeling a free-burning arc, the magnetically deflected arc has been numerically investigated by many authors (80; 126; 136). These models assume a three-dimensional laminar flow in LTE. Schmidt *et al.* (136) compare their numerical results with experimental data and show that arc interruption occurs with an external magnetic field strength of 3.5 mT. They claim, however, that near the cathode the assumption of LTE fails. Schmidt *et al.* include gas ablation effects to model the sublimation of the walls to see if this cooling affects interruption. Gonzalez *et al.* (80) develop a comprehensive model in which they calculate the energy balance at the interface between the plasma and the material instead of a "zero" heat flux condition at the anode surface. In comparison with the cases without the anode model, they observe a significant difference in the arc root deviation, especially with the higher current intensity case ($\approx 150\ A$).

Previous studies of the effects of turbulence on a DC plasma torch were done by Bauchire *et al.* (4). In their model, Prandtl's mixing length model and a $k-\epsilon$ model were used for the calculation of the turbulent viscosity, which enhances the mixing. They assumed there were no turbulent fluctuations in the density and used prescribed model coefficients for closure. This overestimates the turbulence effects. However, qualitatively, it shows that turbulent enhancement of the entrainment of ambient gas results in an increase of MHD pumping.

For our study, a detailed model for the electrical discharge using the current LES model has been developed, and, in this section, the focus is on the validation of this model and its extension of applicability to modeling and evaluating the effects of external field, cross flow and turbulence on free-burning arc profiles.

6.2 Problem Setup and Boundary Condition

The conservation equations of mass, momentum, energy for an electrically conducting flow, and the magnetic induction equation and the state equation are already given in Section 2. A simplified geometry is adapted (see Fig. 24(a)) to model Hsu's experiments (61). The grid resolution is $145 \times 69 \times 145$. The rectangular solid (D) on the top surface represents the

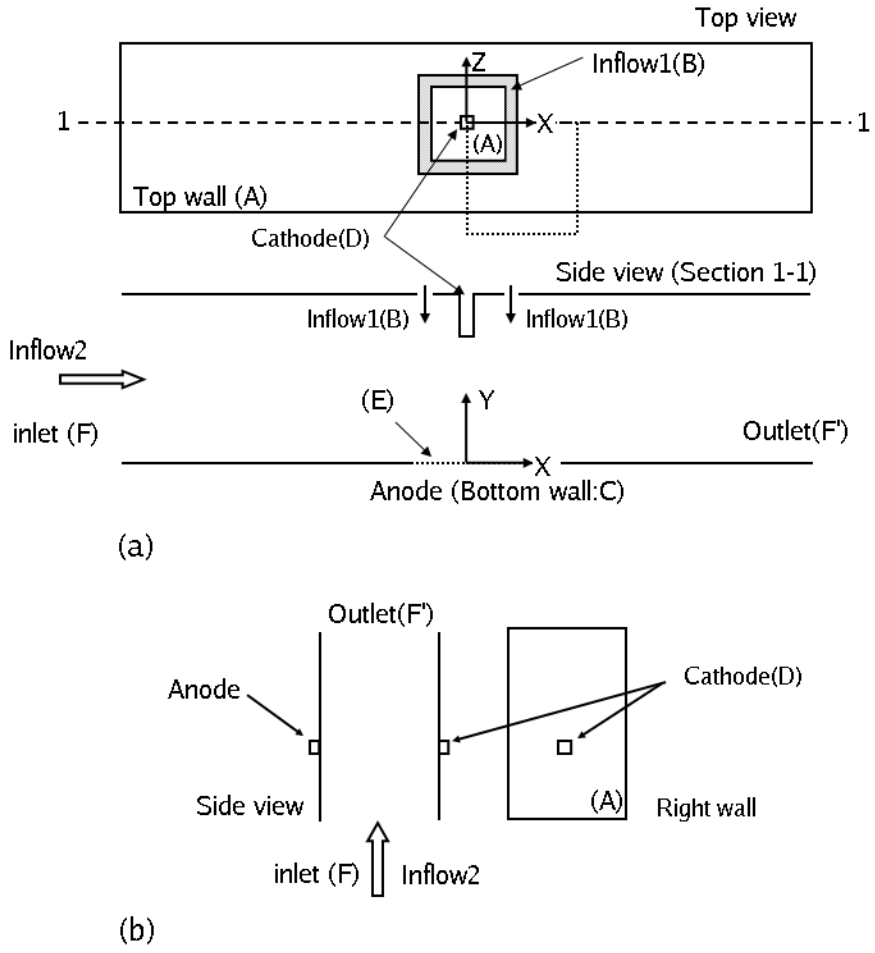

Figure 24: Three dimensional geometry of the arc setup simulated here. (a) Cases 1-3 and Cases 5-9, and (b) Case 4. The dotted box shown in (a) describes the computational domain for Cases 1-3Three dimensional geometry of the arc setup simulated here. (a) Cases 1-3 and Cases 5-9, and (b) Case 4. The dotted box shown in (a) describes the computational domain for Cases 1-3.

Table 3: Boundary Condition for $\bar{\mathbf{A}}_\mathbf{i}, \bar{\phi}, \bar{\mathbf{T}}, \bar{\mathbf{U}}, \bar{\mathbf{V}}, \bar{\mathbf{W}}$. For Case 1-3, we introduce pure argon flow from the surface (B). $\vec{n}$ is the surface-normal vector.(C) and (D) denote the vertical surface of the anode and cathode, respectively. The adiabatic condition is used at the circle (E) with the radius $13mm$ (45). (F) and (F') are inlet and outlet when we introduce the cross flow.

Surface	$\bar{\mathbf{A}}_\mathbf{i}$	$\bar{\phi}$	$\bar{\mathbf{T}}$	$\bar{\mathbf{U}}$	$\bar{\mathbf{V}}$	$\bar{\mathbf{W}}$
A	$\frac{\partial A_i}{\partial n} = 0$	$\frac{\partial \phi}{\partial n} = 0$	$\frac{\partial \bar{T}}{\partial n} = 0$	0	0	0
B	$\frac{\partial A_i}{\partial n} = 0$	$\frac{\partial \phi}{\partial n} = 0$	$\bar{T} = 1000$	0	-10	0
C	$\frac{\partial A_i}{\partial n} = 0$	$\frac{\partial \phi}{\partial n} = 0$	$\bar{T} = 1000$	0	0	0
D	$\frac{\partial A_i}{\partial n} = 0$	$Eq.126$	$\bar{T} = 3500$	0	0	0
E	$\frac{\partial A_i}{\partial n} = 0$	$\bar{\phi} = 0$	$\frac{\partial \bar{T}}{\partial n} = 0$	0	0	0
F	$A_i = 0$	$\frac{\partial \bar{\phi}}{\partial n} = 0$	$\bar{T} = 300$	$-$	$-$	$-$

cathode and has a square bottom surface with 1 mm width. The field distributions around the tip are not modeled. Freton *et al.* (45) claim that a difference between a tipped cathode and a blunt cathode leads to a negligible difference in the temperature distribution because the temperature distribution is largely controlled by the Lorentz forces. A more detailed discussion is given later. The gap between the cathode (D) and anode (C) is 10 mm for all cases expect Case 4. The length of cathode is 10 mm. The incoming flow has an uniform velocity of 10 m/s and temperature of 1000 K and is introduced from the side labeled (B).

The boundary conditions for the incoming flow of a free-burning arc are always problematic because there is no analytical solution for the flow affected by MHD pumping. Hsu uses an extended boundary condition (61), and Freton *et al.* set inlet injections on the top wall. The advantage of introducing injections is to generate a recirculation zone above the cathode which allows the flow to automatically adjust to the conditions of the electrical discharge. The dependence of the arc column on the inlet flow velocity will be discussed later.

In this configuration, cold argon (inflow 1) is supplied from the top boundary (B) and the hot gas is exhausted from surface (F) and (F') for cases 1-3. When cross flow is introduced in cases 5-8, the cold argon (inflow 2) enters only through inlet (F) and leaves the domain at outlet (F'). Other boundary conditions for $\bar{\mathbf{A}}_\mathbf{i}, \bar{\phi}, \bar{\mathbf{T}}, \bar{\mathbf{U}}, \bar{\mathbf{V}}$, and $\bar{\mathbf{W}}$ are given in Table

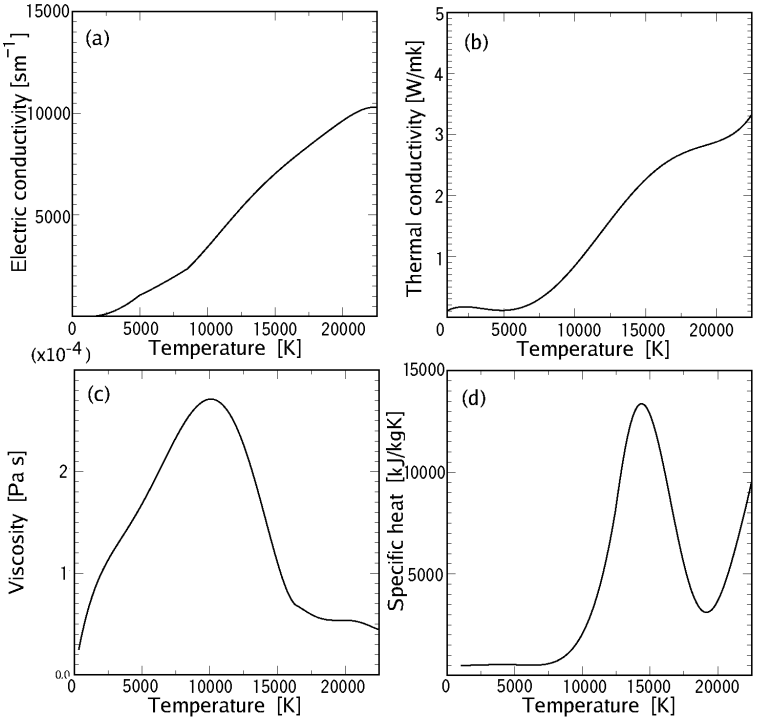

Figure 25: Thermal properties of argon at atmospheric pressure: (a) electric conductivity, (b) thermal conductivity, (c) viscosity, and (d) specific heat (11).

3. The no-slip condition is used for all solid surfaces. An analytical form for the electric potential,$\bar{\phi}$, at the cathode surface is specified as:

$$\bar{J}_{0,y}(r) = J_{max} exp(-br) \tag{126}$$

Here, J_{max} and b are the constant and r is the distance from the center of cathode (45; 61). For the 200 A case, $J_{max} = 1.4 \times 10^8\ Am^{-2}$ and b is 2000. The total input current is calculated by integrating the surface current density so that $I = 2\pi \int_0^R \bar{J}_{0,y}(r) r dr$, where $R = 3\ mm$ and represents the estimated radius of circle inside which the intense current exists (45; 61). The model assumes that the time-varying self-induced magnetic field tends to zero at surface (F) since there is no strong imposed magnetic field related to the arc at this surface. Moreover, the temperature is low enough for the magnetic field to diffuse immediately. At all surfaces, the normal gradient inside the insulator is assumed to be zero and inside the conductor, the magnetic field is assumed to be everywhere zero. Also, in this

Table 4: Arc configurations, the external field and cross flow conditions. Reference is used for the comparison of our current LES results with the experimental data.

Case	Input$[A]$	Ref.	Gap $[mm]$	External Field $[mT]$	Inflow 2 $[m/s]$
1	100	(61)	10	0	0
2	200	(61)	10	0	0
3	300	(61)	10	0	0
4	34	(7)	6.65	0	0.5
5	200	(52)	10	0	$2, 5, 10$
6	200	–	10	$Bz_{ex} = 2, 5, 10$	2
7	200	–	10	$By_{ex} = 6$	2
8	400	–	10	0	100

current model, the sheath has been omitted. The simple model proposed by Lowke (88) solve electron continuity equation considering the ambipolar diffusion, thermal ionization and recombination. They showed that there is a noticeable difference of electron density profiles between LTE model and their model within 5×10^{-5} m in the vicinity of the cathode surface. As a result, the profiles of the electric conductivity near the cathode are different, and a few thousands temperature difference in the vicinity of the cathode was observed compared with LTE model. (So I would like to address necessity to implement a sheath model as a future work.)

The presence of a small concentration of metal vapor in the arc caused by ablation at the anode surface has significant impact on the gas properties such as the electrical conductivity and the radiative emission coefficient. This influence is limited near the anode and does not significantly affect the overall arc features (95). Thus for simplicity, anode ablation is neglected and the classic "zero" heat flux condition is used at the anode surface. The anode surface temperature is specified (45).

In this study, for estimation of the radiation loss R_d, empirical data for high-temperature argon at atmospheric pressure is used (37). The temperature dependence of all thermal properties of argon at 1 atm are shown in Fig. 25 (11).

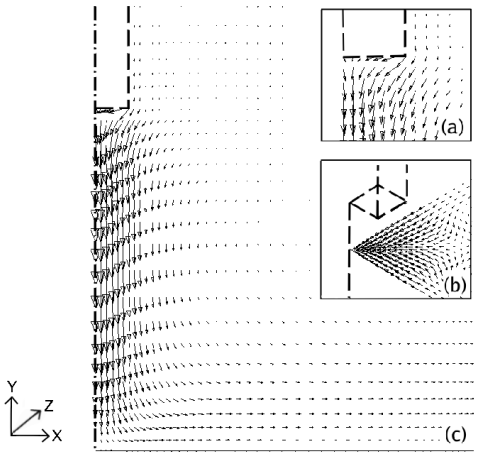

Figure 26: Flow field vector near the cathode for case 2.

6.3 Numerical results

To test the validity of the current code, we compare the numerical results with the experimental results (61; 7) for the Case 1-4. Also, the effects of cross flow (Case 5) and external fields case (Case 6-7) are investigated. The speed of incoming flow for these cases is small, and the flow is essentially laminar. Therefore, all subgrid terms in LES equations are neglected. For Case 8, in order to capture turbulent motions, subgrid terms are turned on, and turbulent effects are investigated.

6.3.1 Comparison with Hsu's Experimental Results, Case 1-3

The free-burning argon arc without cross flow or external field is studied first. The computational domain is a quarter of the whole simulation domain (inside the dotted box in Fig. 24(a)) and the grid resolution is $73 \times 69 \times 73$. Figures 26 (a)-(c) show the flow field for Case 2 around the cathode region. The flow is significantly squeezed inward at the cathode surface and accelerated downward by Lorentz force. The stagnation point exists below the cathode where the flow is decelerated due to the high pressure and turns in the radial direction. The maximum velocity is around 280 m/s in the middle of the gap. Figures 27 (a)-(b) show contours of the magnitude of the magnetic field, current density and

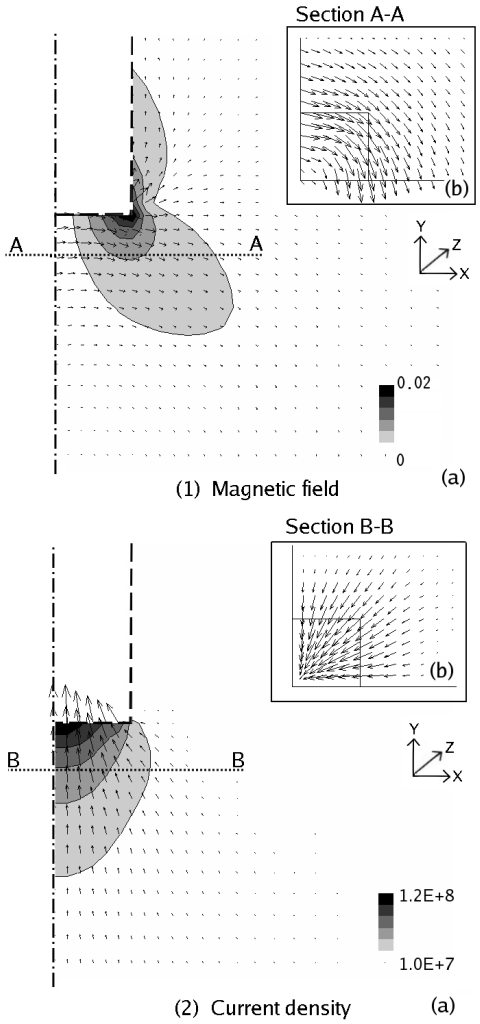

Figure 27: Contours of (1) the magnetic field and (2) the current density and the relevant vector fields.

the relevant vector fields. Despite simplified modeling of the electrodes as squares, both fields become axisymmetric right below the cathode surface (see Figs. 27 (1) inset). These features are strongly dependent on the current profile at the cathode surface (given by Eq. (126)), and this profile ensures axial symmetry regardless of the shape of the cathode. The axial symmetric self-induced magnetic field and the vertically directed current field results in the generation of a strong Lorentz force ($\vec{J} \times \vec{B}$) that constricts the surrounding flow inward (the so-called pinch force). This effect contributes to the bell-shape of the arc. The arc voltage drops and enhances the convective heat flux toward the anode.

Figures 28 (a)-(c) show a comparison of the current LES model results (right half of these

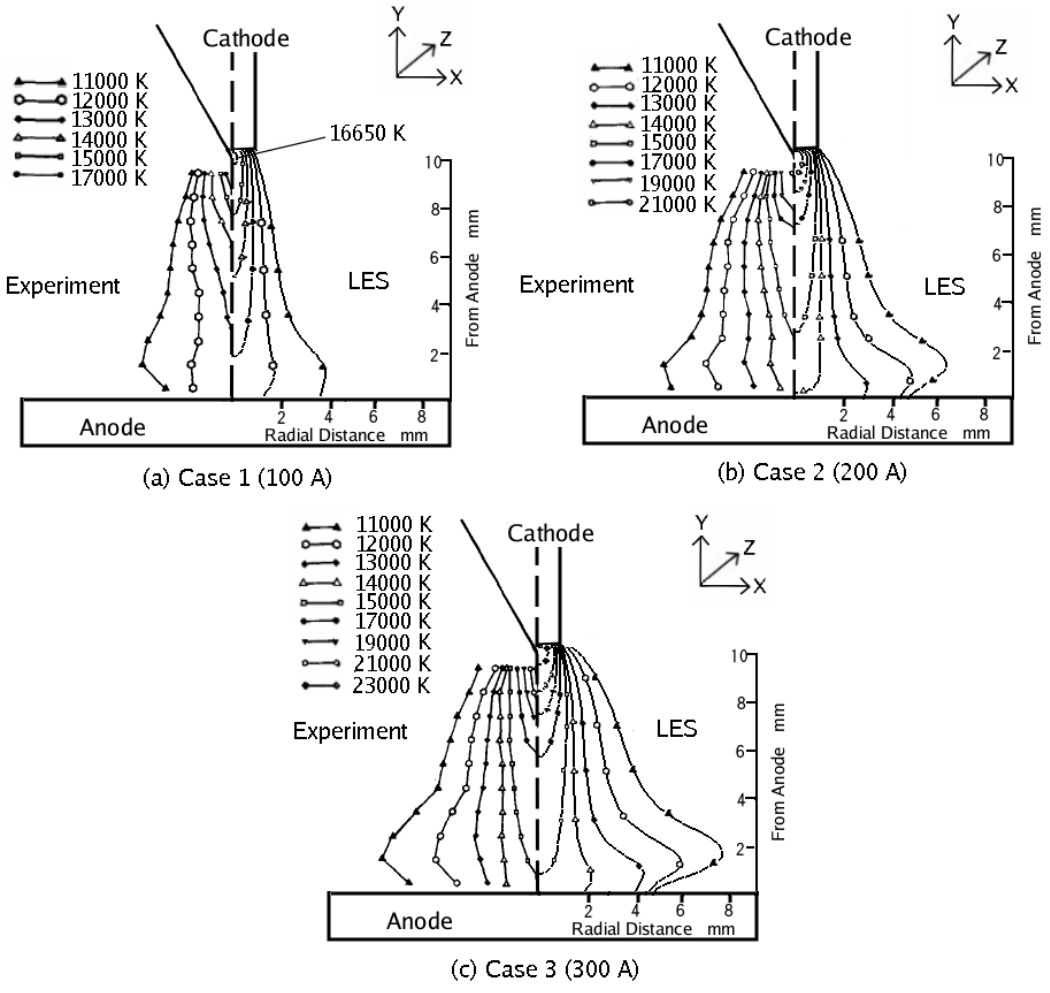

Figure 28: Comparison of the temperature profiles for the numerical and experimental data for (a) Case 1, (b) Case 2, and (c) Case 3.

figures) with the spectrometric measurements of Hsu (61) for $100A$ (Case 1), $200A$ (Case 2), and $300A$ (Case 3). In the experiment, the temperature of the atmospheric argon arc was measured based on absolute line and continuum intensities. The arc was established between a thoriated tungsten cathode and a plane water-cooled copper anode. The gap between the cathode and the anode is fixed 10 mm. As the input current increases, the maximum temperature rises from 17000 K to 22000 K, and the high-temperature region near the cathode extends. The radius of the arc column also increases noticeably near the anode region resulting from the enhanced convective heat flux. The radial heat diffusive flux is significant near the cathode where the maximum temperature is achieved, and the width of the arc increases noticeably at this location. Overall agreement between the experimental data and numerical results are good. The excellent agreement of temperature profile along the center line implies that the current model predicts the velocity field well. For 100 A case (Fig.28(a)), the calculated maximum temperature is slightly lower than the experimental data. This is attributed to the uncertainly of choice of maximum current density (J_{max}). Also, the difference might be due to the evaporation of cathode material in the arc, resulting in a change of thermal properties and the failure of the assumption of LTE (61; 136).

Figures 29 (a) and (b) show the profiles along the center line from Hsu's model and our current model for the temperature and the axial velocity, and the electric potential and the current density profiles. The comparison is for Case 2. In the earlier model, it was assumed that the arc was steady and rotationally symmetric. Another difference between these two models are that they specified the flow field on the top boundaries based on mass conservation rather than using injections. According to these results, the differences are not significant. However, there is a noticeable difference in the axial velocity profile near the anode. Hus's model predicts a steeper gradient, and this might be a result of the different choice in symmetry assumptions (rotationally symmetric).

Figure 30 shows the dependence of the axial temperature profile on the boundary injection velocity. The right half of these figures show isothermal lines of 11000 K with the different velocities. As the velocity increases, the arc column becomes slightly wider, but the maximum temperature remains same. Thus in conclusion, the arc column is relatively

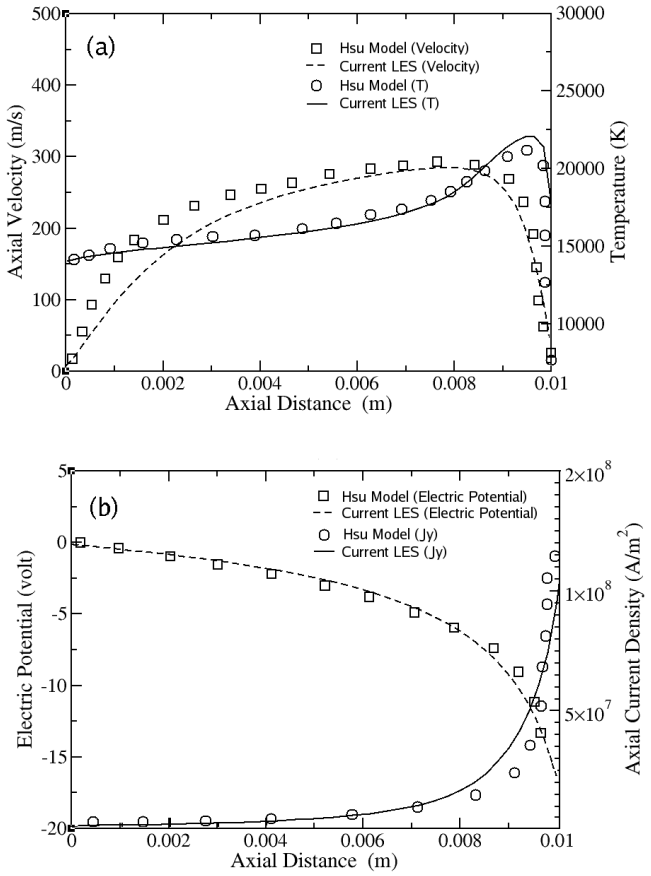

Figure 29: Comparison of (a) axial velocity, temperature, and (b) electric potential and current density with Hsu's model.

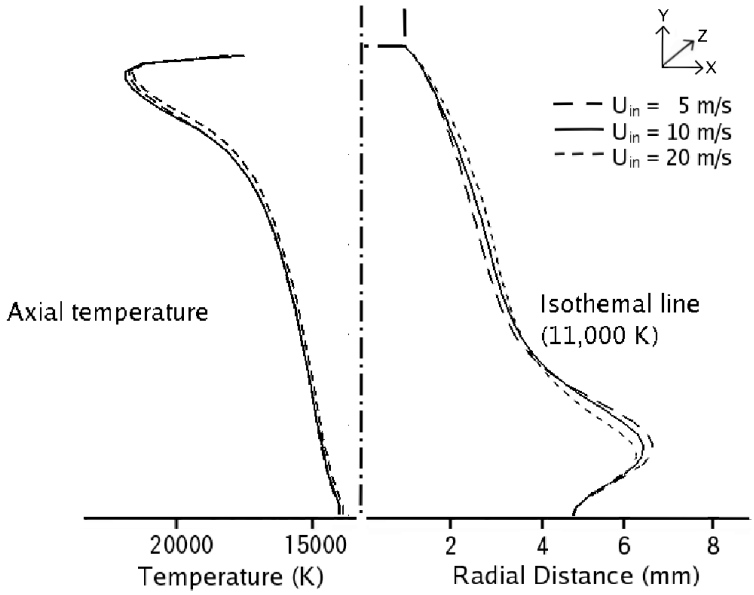

Figure 30: Dependence of temperature profile on the top boundary injection velocity. Left half: axial temperature profile, and right half: isothermal lines of $11,000\ K$.

insensitive to the injection velocity, and a velocity of 10 m/s is used throughout for the rest of calculations. Figures 31 (a)-(b) show the temperature and axial velocity profiles for the three different input current intensities (100 A, 200 A, and 300 A). As the current intensity increases both temperature and velocity increase. This is consistent with past studies (61). The velocity increase rate from 200 A to 300 A is relatively smaller than the rate from 100 A to 200 A, since the maximum velocity is a function of not only the input power, but the gap between two electrodes. Since the gap remains constants, the maximum velocity has to be limited. Hsu's numerical model achieved a much higher velocity for the 300 A case ($\approx$ 395 m/s). Freton and *et.al* also reported that their maximum velocity difference from Hsu's model for 200 A is about 70 m/s and claimed that this difference was due to the different treatment of the shape of the cathode (45). This could be a likely explanation for the difference observed in Figure 31.

Figures 32 (a)-(c) show the energy balance for the 200 A case at the three different locations: (a) 1 mm below the cathode, (b) at the middle of gap, and (c) 1 mm above the anode. In this figure, the radial direction and the axial direction correspond to x-direction and y-direction, respectively. For all cases, the energy transport related to the electron is

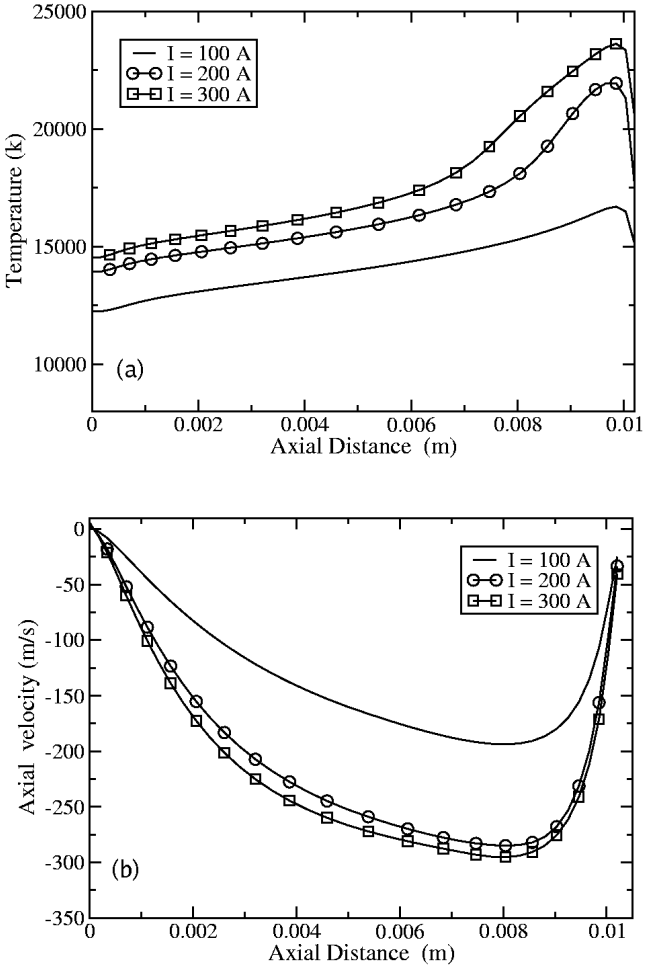

Figure 31: (a) Temperature and (b) axial velocity for Case 1, 2, and 3

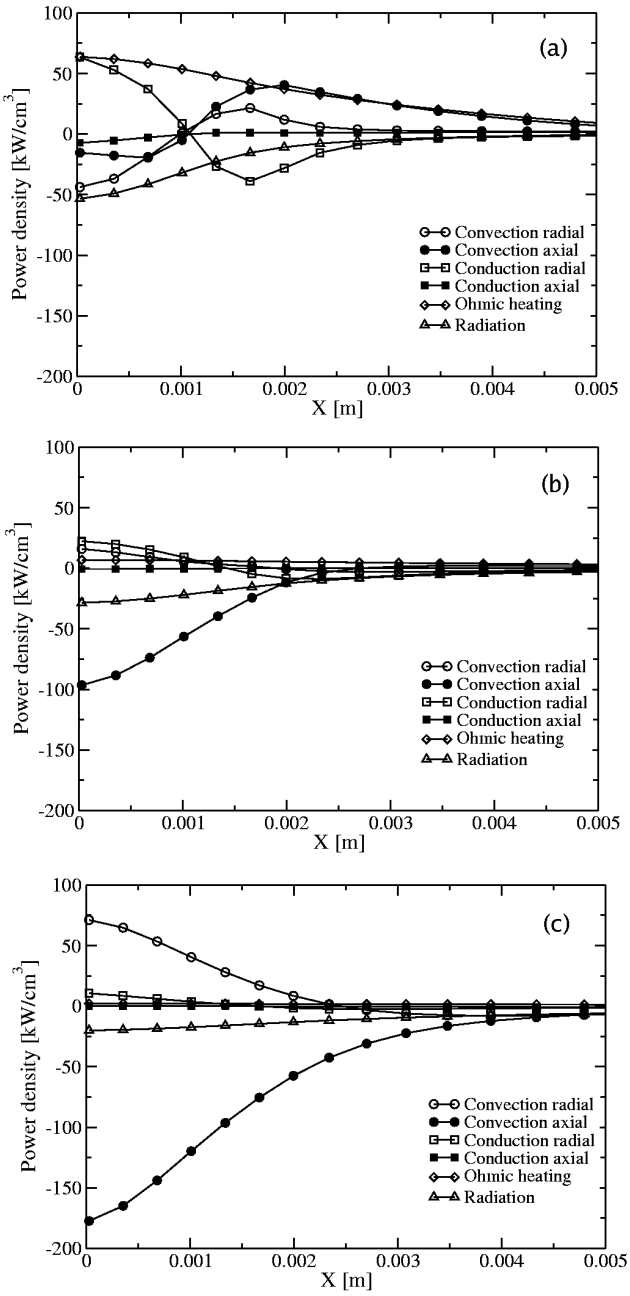

Figure 32: Energy budget (a) near cathode, (b) midgap, and (c) near anode for Case 2

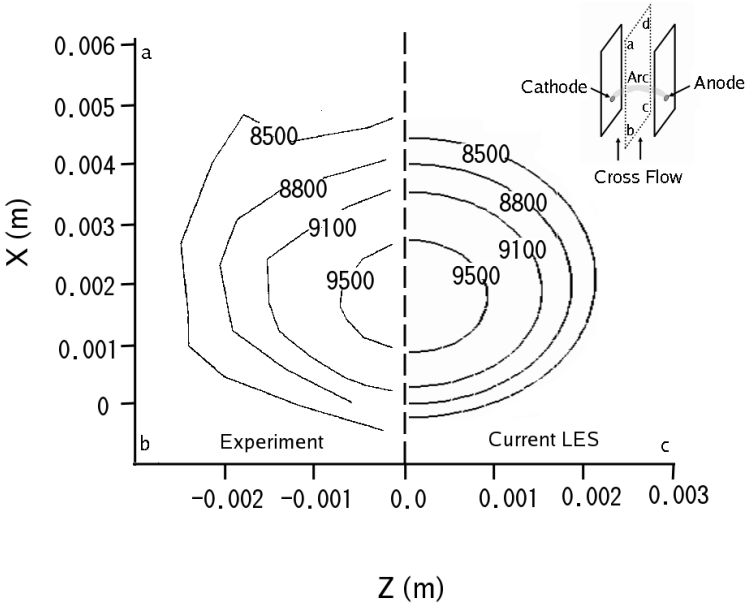

Figure 33: Comparison with the experimental of Benenson *et al.* (7). The input is $J_{max} = 34$, and the cross flow velocity is 0.5 ms^{-1}. $Y = 0$ and $X = 0$ is corresponded to the center of the anode/cathode.

relatively small and is not shown. Near the cathode, the ohmic heating balances with the radiation heat loss and the radial conduction due to the large radial temperature gradient. Also, the negative radial convection is related to the MHD pumping that squeezes the flow inward. At this location, the axial conduction/convection is not significant comparatively. On the other hand, in the middle of the gap, the axial conduction starts to dominate other, and radial conduction also increases. At this point, the temperature inside the arc core reduces, resulting in lower radiation losses and ohmic heating. Near the anode, the convective motion primarily controls the energy balance. Since the temperature gradient is smoothed out, the relevant conductive flux becomes less significant. Note that the axial conductive heat flux might be underestimated due to the isothermal boundary condition.

6.3.2 Influence of Cross Flow, External Fields, and Turbulence

In this section, the effects of laminar and turbulent cross-flows and external fields on an arc column are investigated. It is observed that both an imposed uniform magnetic field

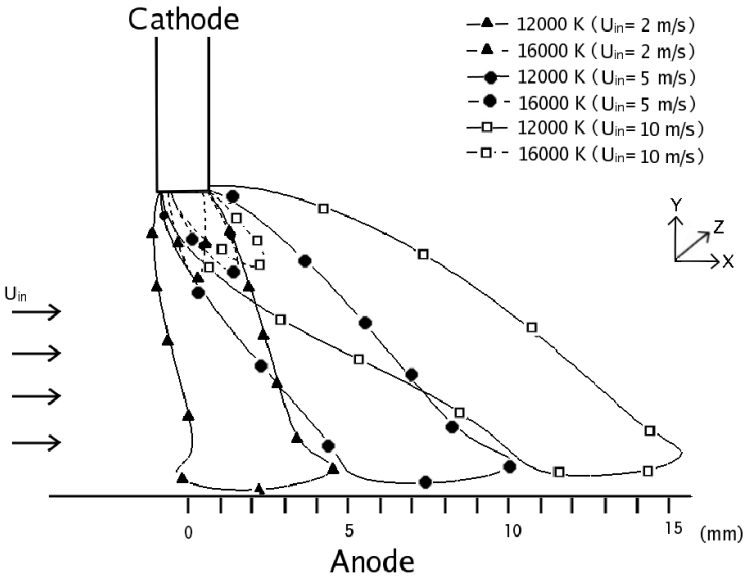

Figure 34: Isothermal lines for 12000 K (solid line) and 16000 K (dotted line) with the different cross flow velocity $U_{in} = 2, 5, 10\ ms^{-1}$.

in z-direction (Bz_{ex}) and a cross flow deflect the arc column downstream. The former is related to an unbalanced Lorentz force, and the latter is purely a convective effect. When we increase the magnitude of the external uniform magnetic field or the cross flow velocity, the arc becomes unstable and results in a "run-away " situation in which the the arc breaks away from the electrodes and distinguishes (136; 126).

Therefore, there are limiting values of the field (Bx_{ex}) and cross flow (U_c) that cause "run-away " for a given the arc intensity. The influence of an external field (By_{ex}) is studied as well. Lastly, the effects of turbulence on the arc structure are investigated. For further validation, the free-burning arc with the cross flow (Case 4) is modeled under the same setup as the experimental work done by Benenson *et al.* (7). They used an integrated line emission coefficient method to measure the temperature profile in the plane perpendicular to the arc column in the middle of the electrodes gap. The experimental setup had an electrode spacing is 6.65 mm, a current intensity of 34 A, a cross flow velocity of 0.5 ms^{-1}, and no external field. The anode and cathode had dimensions of 3 $mm \times 3$ mm. The current numerical setup is based on the previous work by Kelkar and Heberlein (68). The

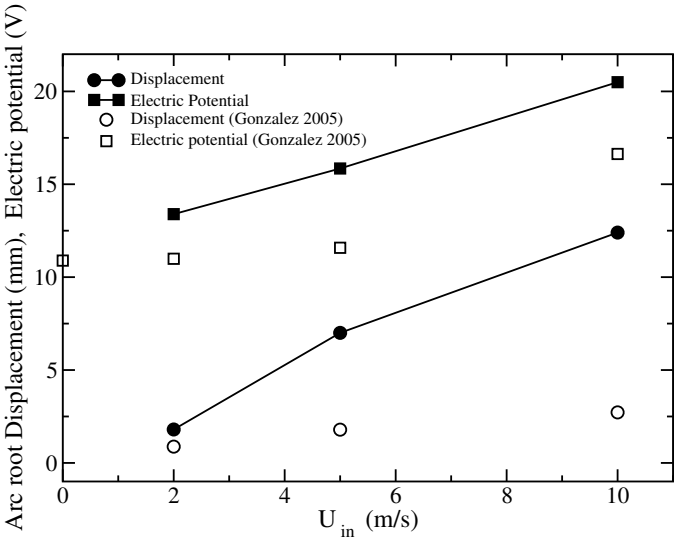

Figure 35: Comparison of the arc root displacement and electric potential drop with the previous work done by Gonzalez *et al.* (52).

grid resolution of the computational domain shown in Fig. 24 (b) is $182 \times 43 \times 59$ in which the electrodes are resolved by 10 points. The comparison with the experimental data is shown in Fig. 33. In this figure, the location at $Z = 0$ and $X = 0$ represents the point where the line passing the centre of the anode/cathode intersects the x-y plane at the mid-gap. Therefore, both the experimental measurement and current numerical results show that the arc column is deflected about 2 mm downstream. The predicted isotherms are slightly smaller than the measurement. This is attributed to uncertainty in the incoming flow condition. However, the overall agreement is qualitatively and quantitatively good. In the following subsection, cross-flow velocity and arc intensity are studied parametrically and compared with other works (52; 81).

6.3.2.1 Cross Flow Effect, Case 5

We investigate the dependence of the arc structure on laminar cross flow velocity in the channel configuration shown in Fig. 24 (a) for Case 5. The grid resolution for this study is $145 \times 69 \times 145$. Figure 34 shows the isothermal lines for 12000 K (solid line) and 16000 K (dotted line) with different cross flow velocities ($U_{in} = 2, 5, 10\ ms^{-1}$). It is observed that the high-temperature region corresponding to the arc core is swept downstream by the flow,

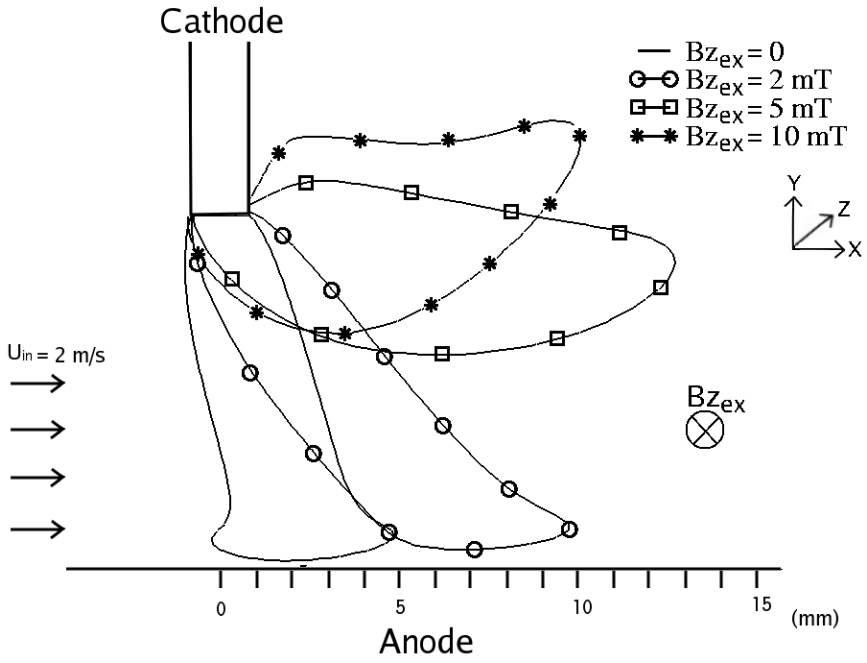

Figure 36: Isothermal lines for 12000 K with different imposed magnetic field, $Bz_{ex} = 0$, 2, 5, and 10 mT.

but still remains localized around the cathode due to the pre-determined current density profile at the electrode surface given by Eq. (126). In addition to the convective effect of the cross flow, the arc is bent by the deformation of the current profiles swept downstream resulting in an unbalanced Lorentz force distribution. This effect is analogous to the case where the external field is imposed. Discussed in the next section.

Figure 35 shows the dependence of the arc root displacement and electric potential on the cross flow velocities. The effect of the cross flow results in the elongation of arc column length due to the convection of the high-temperature region, and thus, the electric potential increases. Therefore, the displacement and electric potential are positively correlated as observed in Fig. 35. Compared with previous work done by Gonzalez *et al.* (52), the results presented here qualitatively have the same trend, but show more pronounced effects. This can be explained by the difference of boundary conditions. In the model, a constant temperature profile ($T_{exit} = 1000\ K$) is imposed at the boundary of the simulation domain which is only 15 mm away from the original arc root. This may contribute to an

underestimation. The model used here does not prescribe a boundary temperature, and the simulation domain is adequately large (the arc sits 60 mm away from the boundary) to ensure the boundary conditions do not adversely affected by the arc structure.

Further increases in the cross-flow velocity should result in the detachment of arc from the cathode surface and thus the arc can not sustain itself. The current model can not predict this mechanism due to the lack of a detailed cathode model and further studies are still needed to fully investigate the cross flow effect on the arc detachment.

6.3.2.2 External Field Effect, Case 6-7

In this section, we investigate the dependence of the arc structure on the different external field strengths, (Bz_{ex} = 2, 5, and 10 mT) in the same channel configuration as Case 5. The cross-flow velocity is kept constant ($U_{in} = 2\ ms^{-1}$).

Figure 36 shows the isothermal lines for 12000 K. With an increase in the imposed field, the bell-shape of the arc column is swept downstream, and the cold incoming flow penetrates through the column near the anode. Figures 37 (a)-(d) show the corresponding flow field vectors. In Fig. 37 (c), it is seen that the negative axial velocity caused by the MHD-pumping is diminishing and an increase of streamwise velocity is seen, which convects the hot gas toward the top wall. This is not seen in the case of a strong cross-flow velocity, since this effect is due to the unbalanced Lorentz forces near the cathode (the x-component of the Lorentz force). Also, with further increase of the external field, the y-component of the Lorentz force accelerates the flow downward at the upstream side of the cathode (not the typical MHD pumping effect) which enhances the overall convection of the hot gas in the x-direction. These results mirror those observed in previous works (80; 126; 136).

Figure 38 shows the x component of the Lorentz force ($J_yB_z - J_zB_y$) 1 mm away from the cathode surface. Without the external field, the Lorentz force is nearly symmetrical about the center point and thus, the flow equally squeezed inward and "MHD pumping" is observed. On the other hand, when an external field is applied, a decrease in the Lorentz force directing the flow in the negative x-direction occurs resulting in the attenuation of MHD pumping and the enhancement of convection in the x-direction.

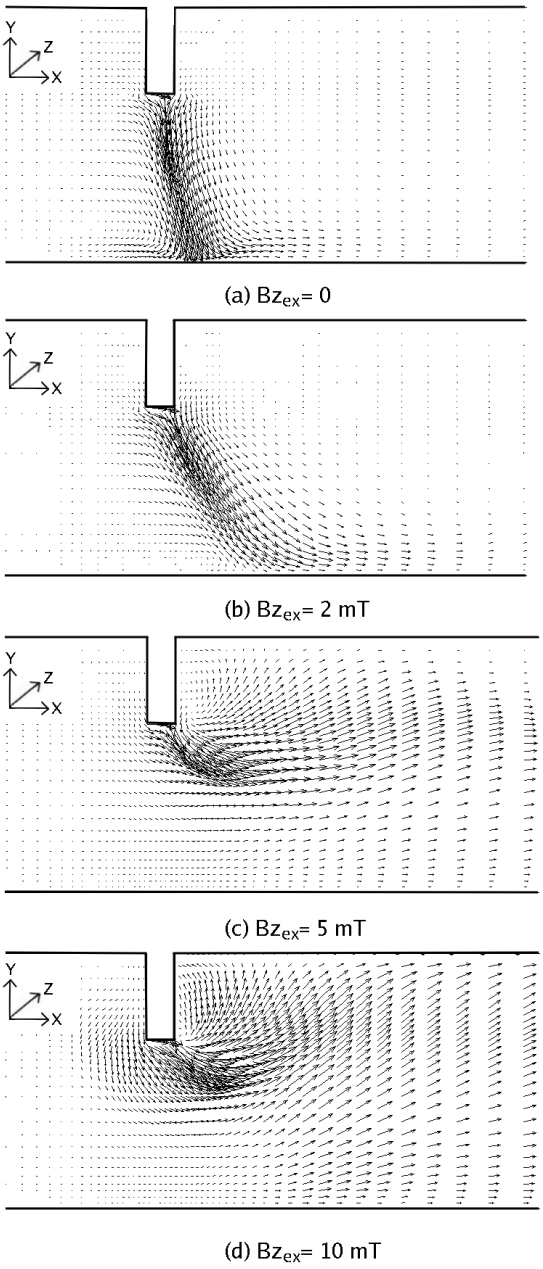

Figure 37: Calculated plasma velocity fields for the different imposed magnetic field (a) $Bz_{ex} = 0\ mT$, (b) $Bz_{ex} = 2\ mT$, (c) $Bz_{ex} = 5\ mT$, and (d) $Bz_{ex} = 10\ mT$.

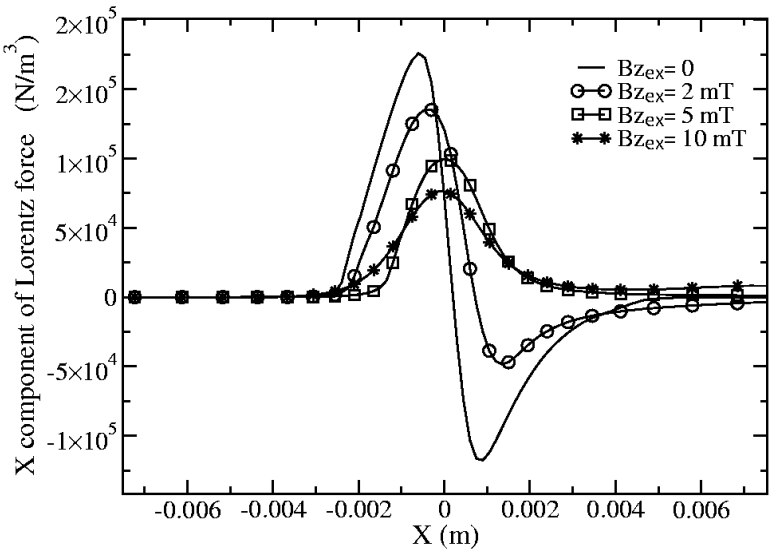

Figure 38: Lorentz force in the cross stream direction for Case 6.

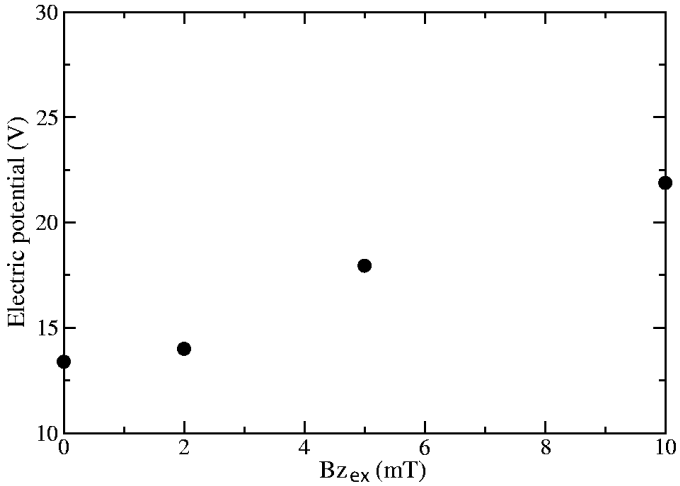

Figure 39: Electric potential variation with the different external fields intensities for Case 6.

Figure 39 shows the calculated voltage drops. Generally, an imposed magnetic field results in an increase in the voltage drop at the anode. It is worth noting that the drops do not vary linearly with increasing external magnetic field. This non-linearity can be explained by the arc detachment from the anode when the external magnetic field is sufficiently strong (over 5 mT for this case). Also, experimental studies show that the arc detaches for values greater than $Bz_{ex} = 7\ mT$ for a pressure 1 MPa, a current intensity of 100 A and a 3 mm electrode gap (136).

Unlike the cross flow effect acting on the entire arc column through convective forces, the external magnetic field interacts with the localized current field near the cathode and effectively bends the base of the arc column downstream resulting in the interruption of the arc. This capability to terminate an undesirable discharge is applied to the design of circuit breakers the contractors.

Figure 40 shows temperature contour surfaces (9000, 11000, and 12000 K) and velocity field vectors at the iso-contour of the temperature 12000 K for Case 5 and Case 7. When the external magnetic field is imposed in the transverse direction (y-direction), the arc column straightens, and the flow starts to rotate around the y axis. This appreciable change is related to the unique interaction between the external field and the self-induced current field by which circumferential stresses generated by the Lorentz force cause the flow to rotate. Because of this spiral motion, the arc column remains parallel to the y axis. These motions are clearly seen in the flow field vector distributions shown at Figs. 41.

In summary, the effect of external fields (in the spanwise and transverse direction) on the arc column are discussed. The direction of external field has a positive (Case 6) or negative (Case 7) impact on the arc root detachment from the anode. For the purpose of stabilization of the arc, the external field being parallel to the arc axis is preferred.

6.3.2.3 Turbulent Effect, Case 8

Finally, the turbulent effect on the arc structure is investigated with the channel configuration (Case 8). Realistic turbulent flow that has separatedly calculated without the arc is introduced from surface (F) with a mean velocity of $U_{in} \sim 100\ m/s$. The grid resolution

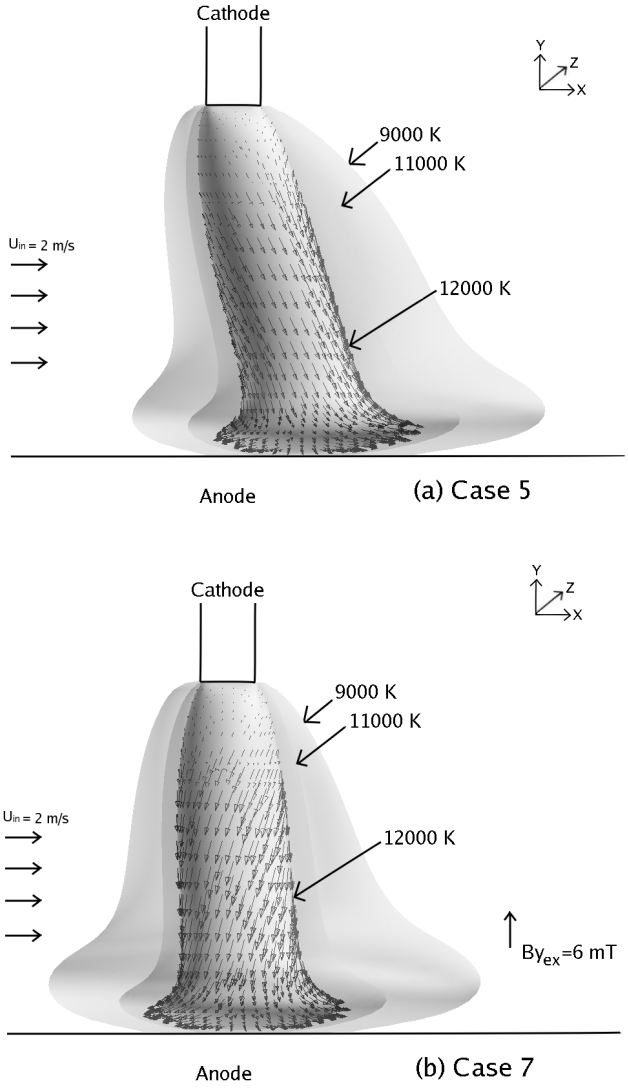

Figure 40: Temperature contours and velocity vectors (a) Case 5 and (b) Case 7.

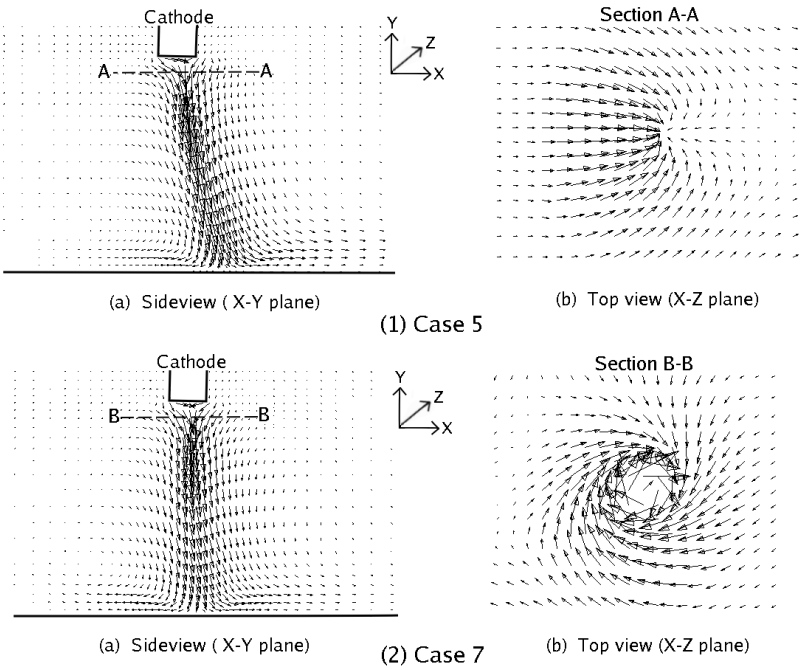

Figure 41: Velocity vectors in x-y, and x-z planes for (1) Case 5 and (2) Case 7.

for this study is $227 \times 103 \times 139$, and the minimum grid spacing used near the cathode surface is $5 \times 10^{-5}\ m$. Since viscosity increases with temperature near the cathode, the grid is adequate to resolve the turbulent effects. (For this resolution, the minimum grid spacing near the cathode in y-direction, $\triangle y^+$, is 5.)

Figure 42 shows the time-averaged streamlines (dark lines) and temperature contours. The data are averaged over $1 \times 10^4\ s$, which corresponds to one flow time based on the channel height and U_{in}. It is observed that there is a wake region behind the cathode, and vortices are formed. Due to the MHD pumping, the flow is vertically redirected downward at the cathode surface as observed in previous results. The corresponding time-averaged subgrid kinetic energy normalized by the kinetic energy is shown in Fig. 43. It has a maximum value behind the cathode where vortices are formed and the kinetic energy is relatively small. Also, localized maximum value is observed below the cathode surface. This corresponds to the left side of the arc column faced with the cross flow. The formation of the localized maximum value can be attributed to the effect of MHD pumping and the large temperature gradient between incoming cold flow and the arc column, since the large

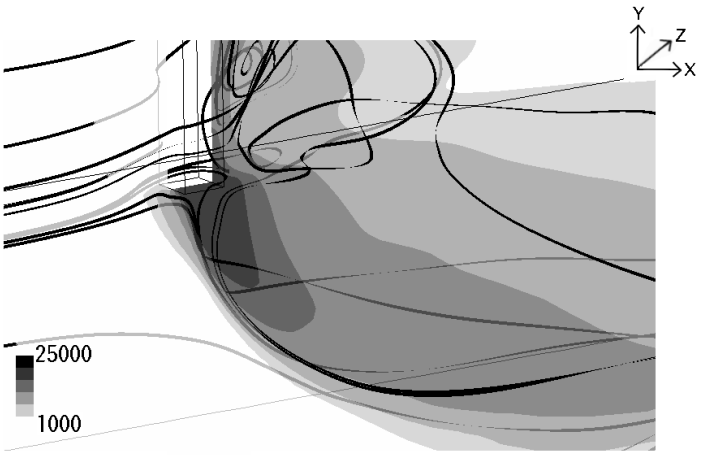

Figure 42: Time-averaged temperature profile and streamline (black lines) for Case 8.

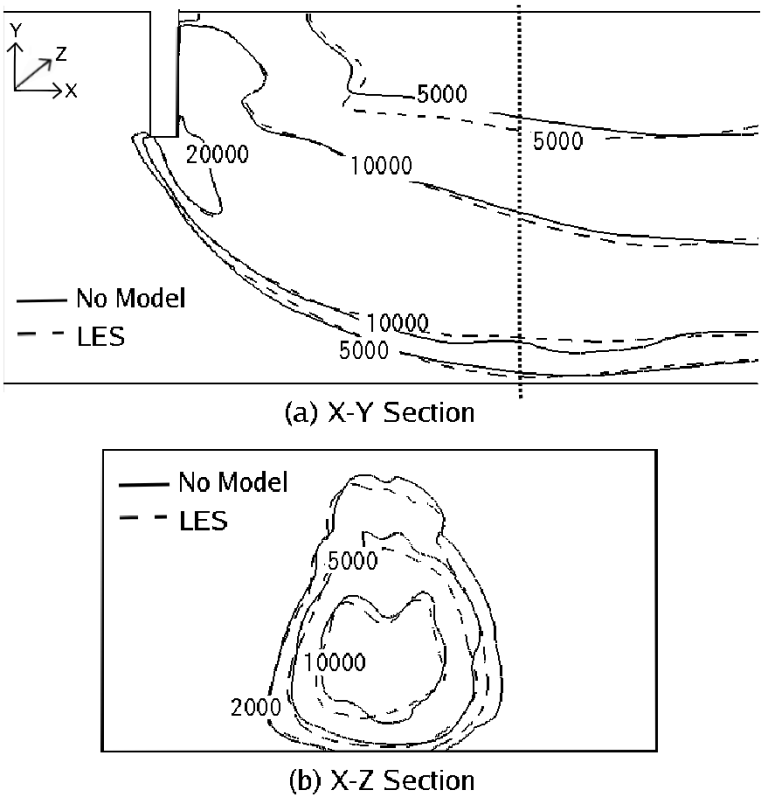

Figure 43: Time-averaged subgrid kinetic energy normalized by kinetic energy

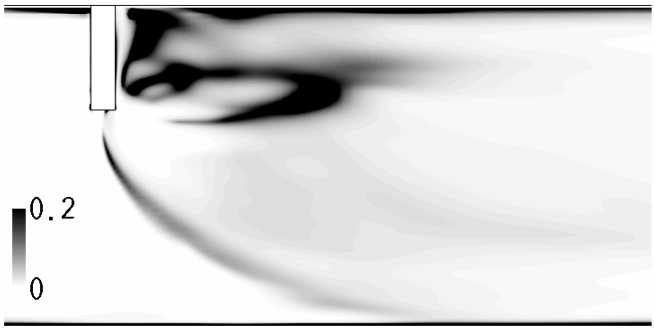

Figure 44: Time-averaged temperature profiles from the current LES and without turbulent model. The dotted line indicates the location of x-z cross section.

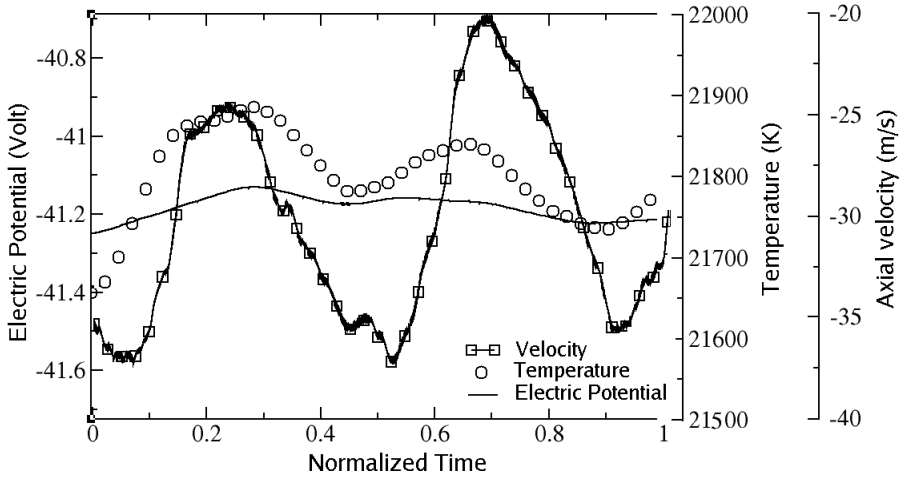

Figure 45: Time variation of the electric potential, the temperature and the axial velocity 10^{-4} m away from the cathode surface. Time scale is normalized by the flow time (10^{-4} s).

temperature gradient enhances Baroclinic torque ($\frac{1}{\rho^3}\nabla\rho \times \nabla p$) that is related to turbulent production. Except in these regions, the subgrid kinetic energy is small implying that the level of turbulence is low. This may be due to the thermal expansion effect.

Figures 44(a) and (b) show a comparison of the time-averaged temperature contour (a) x-y cross section and (b) x-z cross section from the current LES and one without a subgrid model. As expected, large differences are not expected near the cathode because the turbulence is attenuated due to thermal expansion. However, some noticeable differences are observed downstream in both profiles. Nevertheless, for the condition of this study,

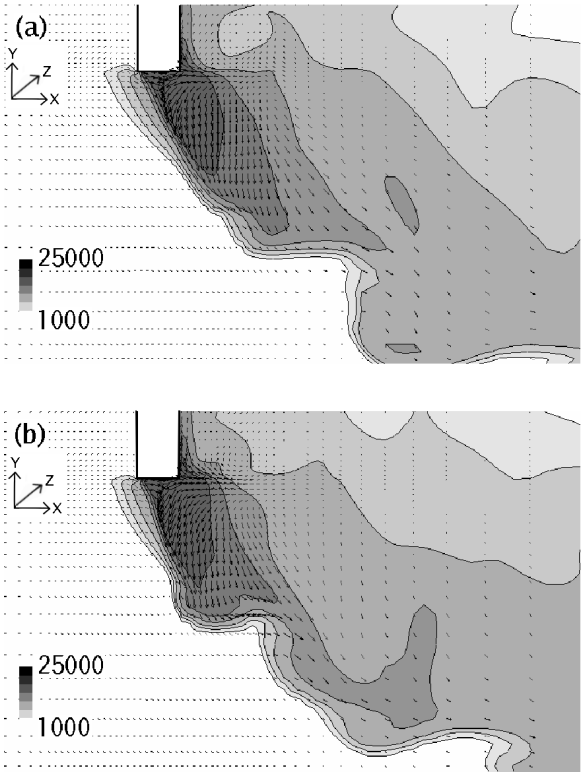

Figure 46: Instantaneous temperature profile with velocity vectors (a) $T' = 0.5$, and (b) $T' = 0.7$.

subgrid closure effect is not very pronounced but may be important when turbulence level is high.

The incoming velocity fluctuations do cause perturbations in the arc column. Figure 45 show time histories of the electric potential, the temperature and the axial velocity 10^4 m below the cathode surface. The time scale, T', is normalized by the flow time. It is observed that the axial velocity oscillates by 30 %, but the electric potential remains constant. In order to understand this, instantaneous profiles of the temperature contour and the flow field vectors at $T' = 0.5$ and $T' = 0.7$ are shown in Figs. 46 (a) and (b), respectively. At $T' = 0.5$, the axial velocity reaches $37m/s$ and it is observed that the arc column is smoothly stretched downward. Also in the vicinity of the cathode surface, negative and positive streamwise velocity produced by MHD pumping is balanced. However, at $T' = 0.7$, strong counter flow below the cathode is induced, and the arc column becomes straightened. This is caused by the cold incoming flow entering from the left edge of the cathode, which

weakens the Lorentz force. As a result, a large eddy is formed at the left side of the arc column. On the other hand, the electric potential is strongly dependent on total arc column length, which remains relatively constant. Therefore, the time variation of electric potential is small. However, the temperature profile is influenced by the current profile (e.g., electric potential profile) as well as velocity profile related to the convective transfer (see Fig. 32 (a)). This explains why both the velocity profile and the temperature profile have local maximum at the same time.

CHAPTER VII

SUPERSONIC FLOW OVER THE BACKWARD FACING STEP WITH EQUILIBRIUM / NON-EQUILIBRIUM PLASMA

This chapter addresses the application of the equilibrium/non-equilibrium plasma in supersonic reacting flow over a backward facing step. First, the code has been carefully validated for reacting/non-reacting flow without an electrical discharge by comparing with the available experimental data. The plasma effects on the flow fields as well as combustion enhancement are discussed.

7.1 Code validation

The base code without the plasma discharge (Case 1) has been validated for the same geometry as the available experimental data (92) for the supersonic flow over the rearward-facing step. Figures 47 (a)-(a') show the experimental and CFD results of the pressure contour, respectively. It is seen that the angle of expansion waves and the magnitude of pressure behind the step also agree well for two cases. The same agreement is also found in the comparison of the temperature contours shown in Figures 47 (b)-(b'). However, the some discrepancy is seen at the bottom wall where the computed temperature is slightly higher than the experimental data. This is attributed to our adiabatic wall condition and the lack of proper subgrid mixing closure that enhances thermal diffusivity. For the more quantitative validation, we compare the distribution of the pressure, the temperature, the U velocity component and the V velocity component in the y-direction at the three various locations

Table 5: Free-stream flow conditions.

Case	Ma	Gas	$T_{in}[K]$	$P_{in}[kPa]$	Arc [A]	$Bz_0[T]$
1	2.0	N_2	167	35	-	-
2	2.0	N_2	167	35	-	-
3	1.4	$21\%O_2/Ar$	2200	40	-	-

Table 6: Jet flow conditions. For all cases, $Ma_{jet} = 1$.

Case	Fuel	$T_{in}[K]$	$P_{in}[kPa]$
1	no injection		
2	O_2, two jets	250	139
3	$1\%NO, 19\%CO/H_2$	221	162

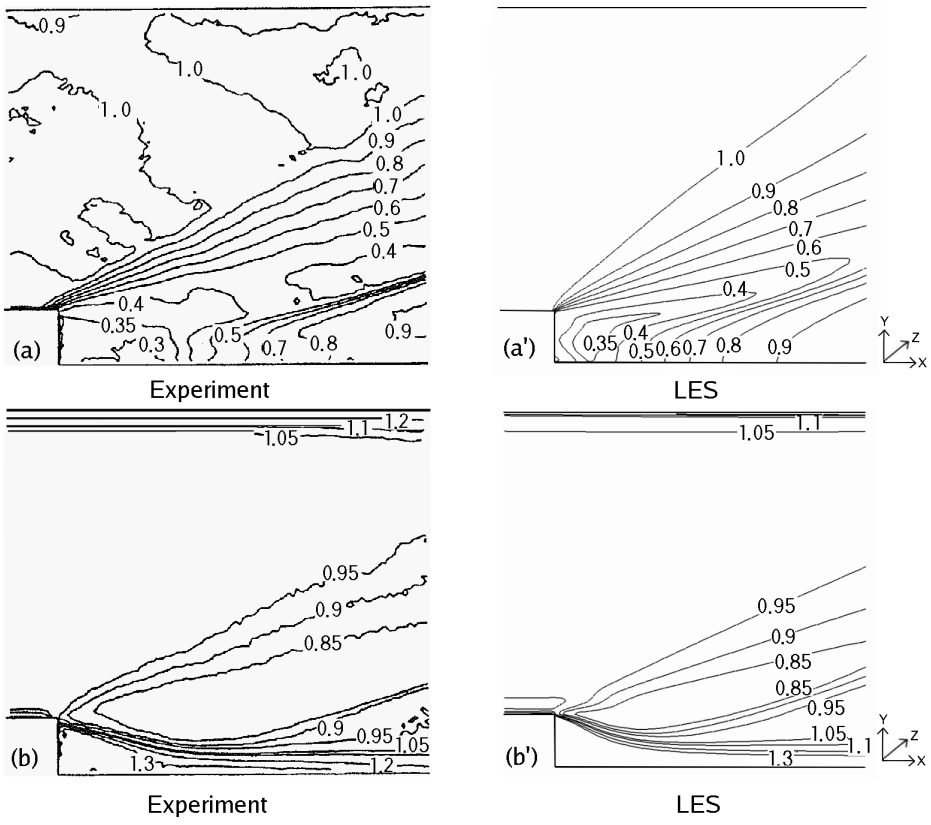

Figure 47: Comparison of experimental data (93) and LES predictions of (a)-(a'): normalized pressure profiles and (b)-(b'):normalized temperature profiles for non-reacting Case 1.

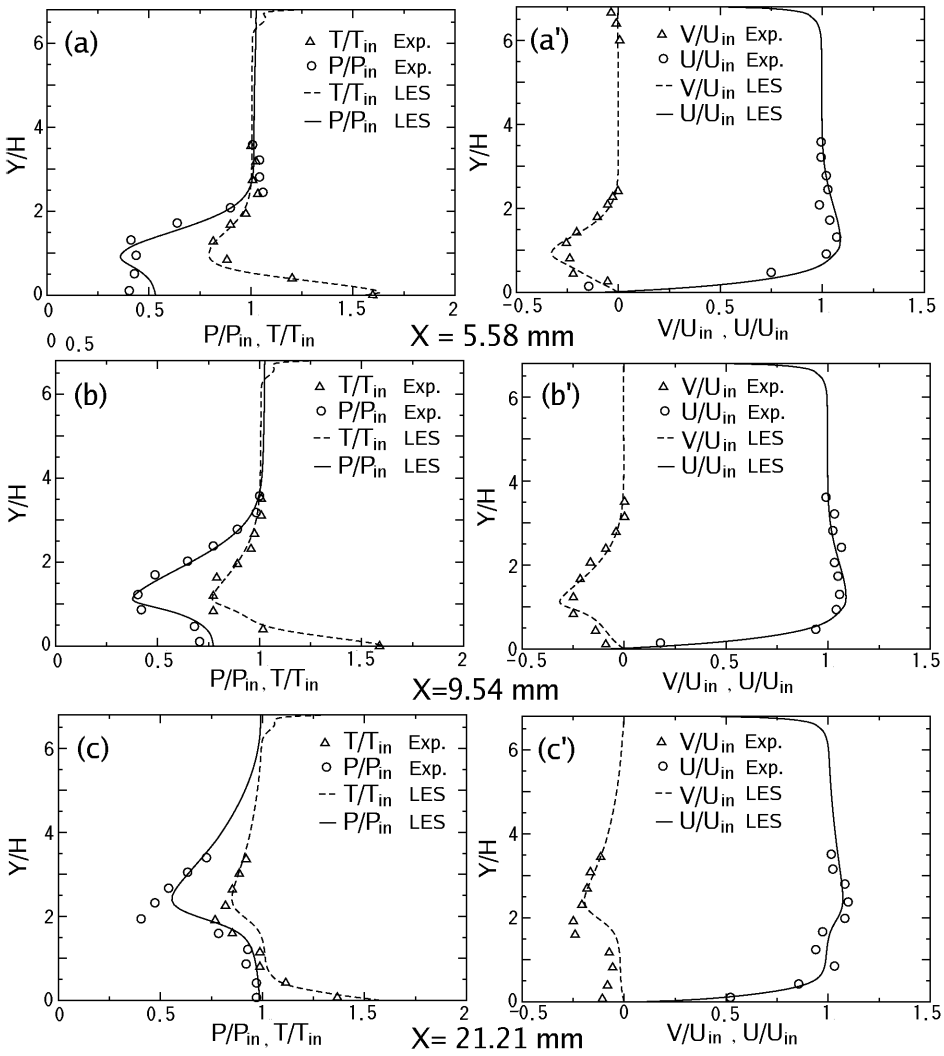

Figure 48: Comparison of experimental data (93) and LES predictions of flow properties for non-reacting Case 1. All quantities are normalized by the inflow condition of the free-stream. (a)-(a'): $x = 5.58\ mm$, (b)-(b'): $x = 9.54\ mm$ and (c)-(c'): $x = 21.21\ mm$

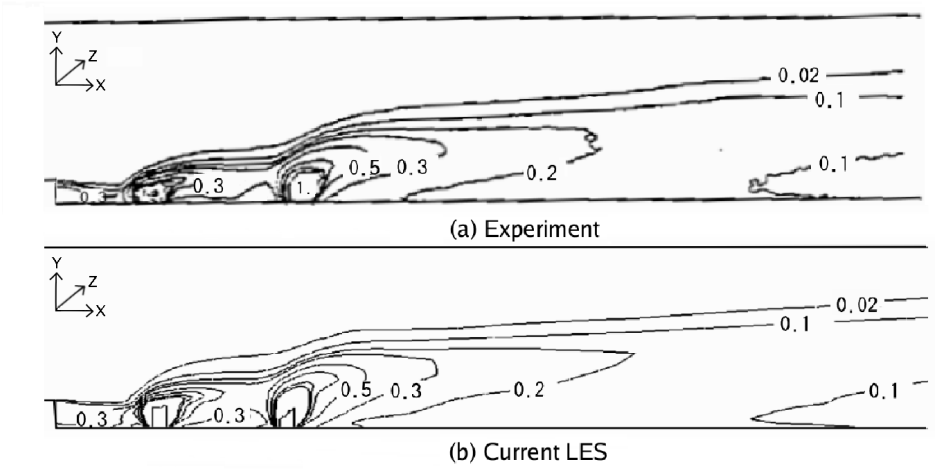

Figure 49: Comparison of experimental data (92) and LES prediction of mole fraction of O_2 for Case 2.

downstream. The distances from the step where the data are taken are $X = 5.58mm$ (Figs. 48 (a)-(a')) , $9.54mm$ (Figs. 48 (b)-(b')) and $21.21mm$ (Figs. 48 (c)-(c')). At $X = 5.58mm$, even though there are some discrepancies of the pressure near the bottom wall, it can be seen that the LES can reproduce the experimental results well. The increase of the pressure at the bottom wall is corresponded to the stagnation point the end of the step. The lack of this pressure increase in the experimental data is uncertain. At $X = 9.54mm$ where the recompression shocks are originated, the agreement is overall excellent. This ensure that the LES can correctly obtain the bending angle of the shear layer. At the further downstream ($X = 21.21mm$), we can see some noticeable discrepancies in the pressure profile and the V velocity profile. The LES slightly overestimates the strength of an oblique shocks, however, all the detailed quantitative comparison show good agreement with data.

Figure 49 shows Case 2 with two non-reacting injectors. The over-expanded fuel jets create shock bubbles that becomes bent by the oncoming flow. Multiple recirculation regions are formed behind the step and in the wake of the jets, and they result in a relatively high fuel mass fractions near the bottom wall. The fuel penetration distance is in good agreement with experiment, and thus the structure of the shock bubble and turbulent mixing of the flow are assumed to be captured accurately by the current LES.

The reacting case (Case 3) McMillin *et al.* obtained temperature data using NO and

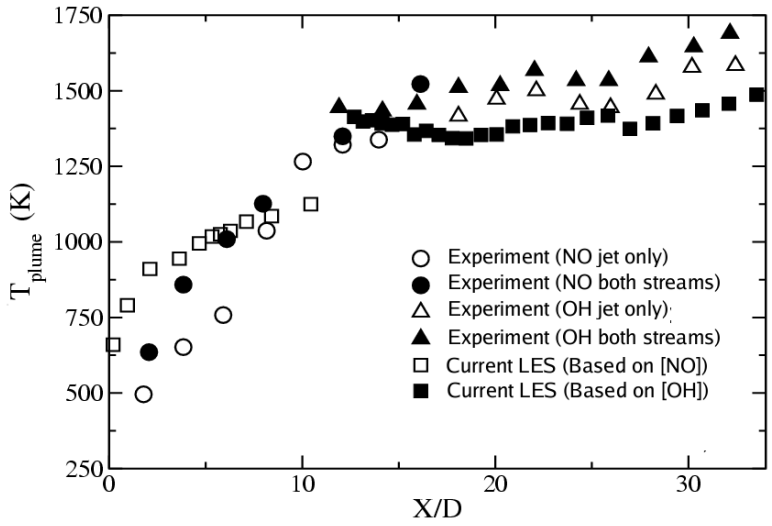

Figure 50: Time-averaged temperature variation in the wake of the dual injector (93) for Case 3. For the experimental NO measurement (in the near-field of the injector), the shot-noise temperature uncertainty ranges from $\sim 4-20$ % over the temperature range 300-1500 K. For OH, the temperature uncertainty range is $\sim 13-30$ %. For the numerical results, the temperature is averaged in the regions of the x-y plane where the concentration of NO and OH is more than 0.01 % and 0.1 % in the plume region, respectively.

OH as the temperature tracers. Figure 50 compares this data with the numerically predicted time-averaged plume temperature. The agreement is acceptable considering that the measurements were reported to have a large degree of uncertainty (see figure caption).

These non-reacting and reacting supersonic flows serve to establish additional validity of the LES solver to simulate non-MHD supersonic combustion. Earlier validation efforts (99) for non-reacting MHD turbulent flows and the earlier well established accuracy of the LES solver for both non-reacting and reacting flows serve to complete the validation of the solver for these various applications. In the following, we discuss plasma-assisted combustion in supersonic flow.

7.2 No reacting Plasma flow with/without Plasma

7.2.1 Problem Setup

Schematic of the two dimensional geometry is show in Fig. 51. The purpose of this calculation is to investigate how the location of the plasma source effects on the flow fields. In addition, the uniform magnetic field is imposed in the vertical direction, and the effect of

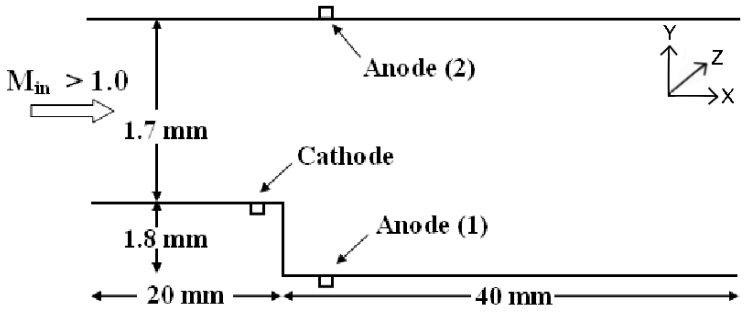

Figure 51: Schematic of two demensional dump combustor. The physical size is similar to the experimental set up by Hartfield (1993). The location of the cathode and two locations for the anode (called Configuration 1 and 2) are also shown. Each electric node (5 mm) is resolved by 14 points.

Lorentz force on the flow field and the pressure fields at the bottom wall are investigated. These studies are mirror of computational work done by Khan (69). He has investigated the effects of MHD in low magnetic Reynolds number limit by which Maxwell equation is decoupled with Navier-Stokes equations and showed that an applied magnetic field near the step increases the distance from the step where reattachment occurs as a result of increased pressure in the recirculation region. For this current study, Navier-Stokes equations are fully coupled with Maxwell equation, and low magnetic Reynolds number assumption has been relaxed.

About the boundary condition, on all solid surfaces, the no-slip, adiabatic conditions are imposed, except at the cathode and the anode surfaces, which are held at a constant temperature of $T_{wall} = 3500\ K$ (Freton *et al.*, 2000). At the solid surfaces, and at the inlet and the outlet, the scalar potential, $\bar{\phi}$ and the vector potential, $\bar{\mathbf{A}}$ are required to have zero normal gradients. This translates to requiring $\frac{\partial \bar{\phi}}{\partial n_i} = 0$ and $\frac{\partial \bar{A}_i}{\partial n_i} = 0$, where n_i is the surface normal unit vector. At the anode and the cathode surfaces an analytical form, commonly used in the literature (Hsu *et al.*, 1982; Freton *et al.*, 2000), is used to specify the current density distribution as shown before, and is given by: $\bar{J}_{ex,y}(l) = J_{max} exp(-bl)$, where J_{max} and b are the constant, and l is the distance from the center of cathode. In this model, $J_{max} = 1.4 \times 10^8\ Am^{-2}$ for the 200 A case, and b is set to 2000 by calculating the total current. The estimated size of electric nodes is $\approx 0.5\ mm$.

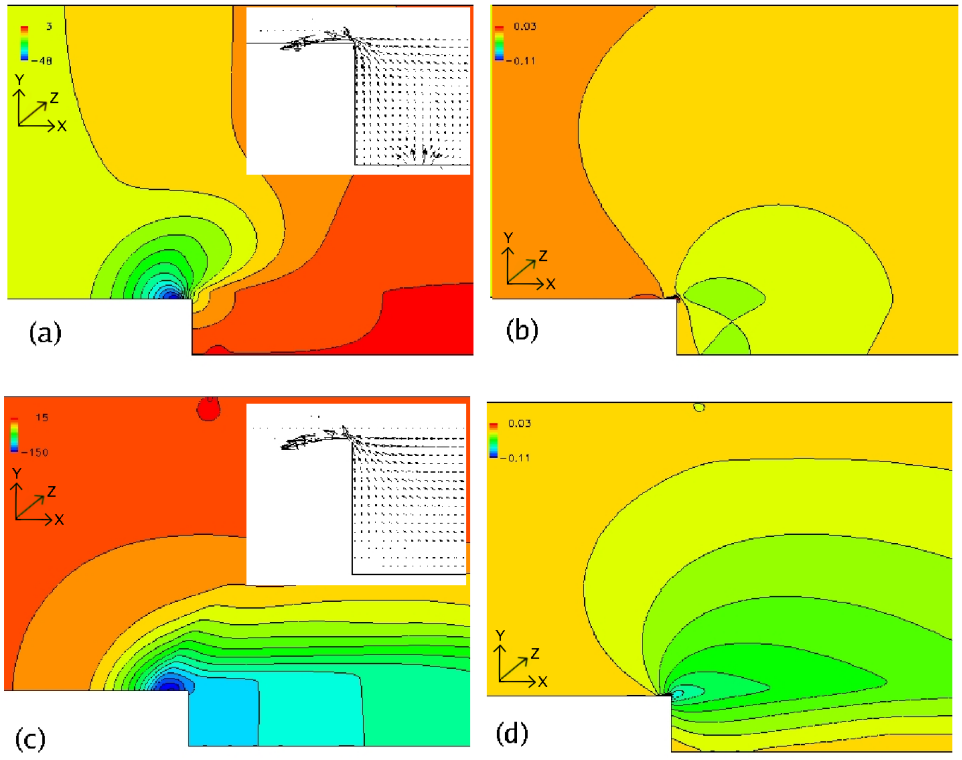

Figure 52: (a) Electric potential contours [V] for configuration (1) and (b) magnetic contours [T] for configuration (1). Similarly, configuration (2) is shown in (c) and (d). The inset figures show the corresponding fields vectors.

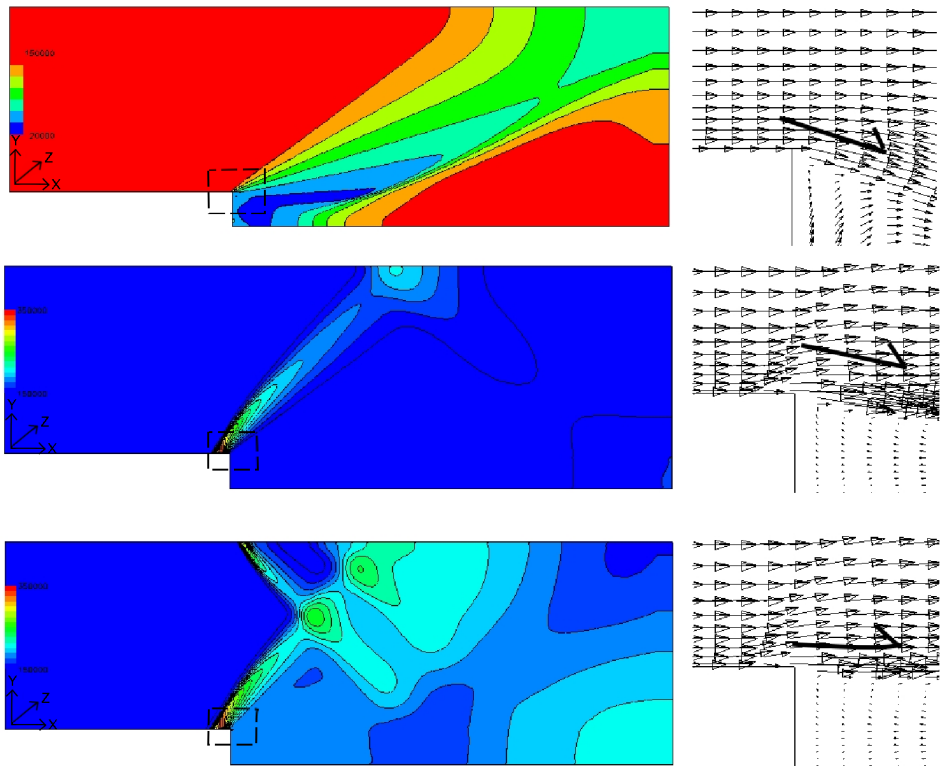

Figure 53: Pressure distribution [Pa] (a) No electrical field, (b) Anode at the bottom wall, and (c) Anode at the top wall. The right figures show the flow fields near the step corner.

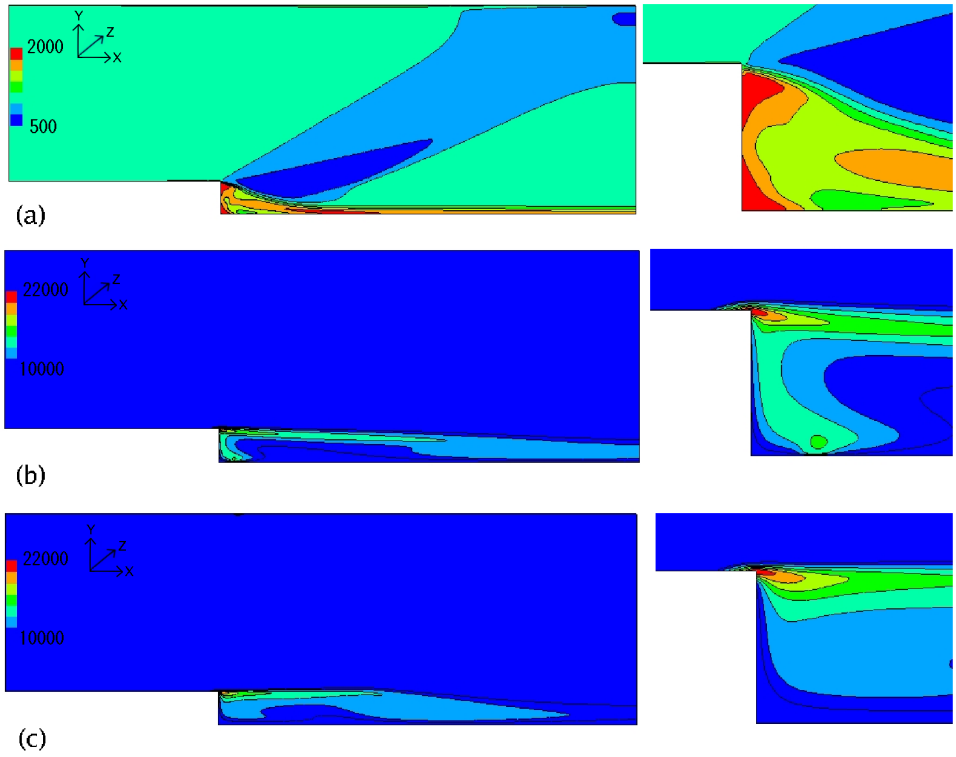

Figure 54: Temperature distribution [K] (a) No electric field, (b) Anode at the bottom wall, (c) Anode at the top wall. The right figures show the temperature distribution near the step corner.

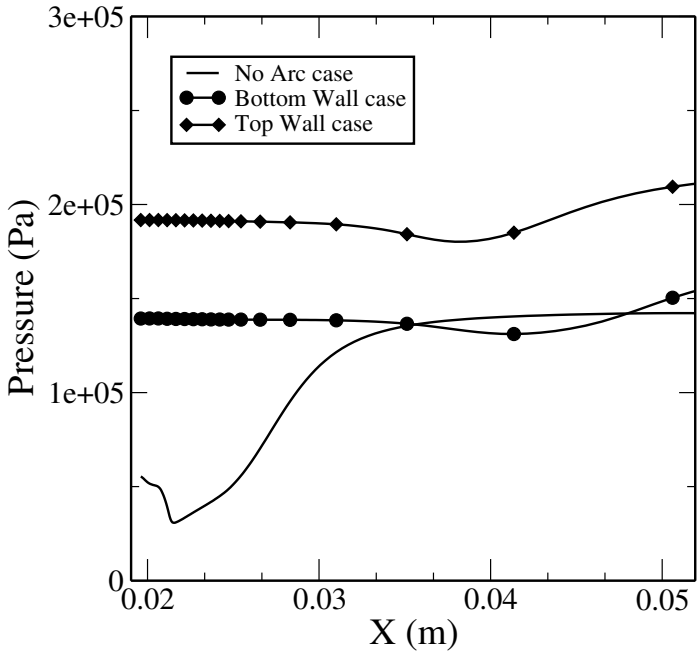

Figure 55: Pressure profile along the bottom wall behind the step.

For current study, the gas is assumed to be pure argon since the transport coefficients, such as the electrical conductivity, the viscosity, and the thermal conductivity are all well known values. The thermal properties such as the specific heat are easily calculated, and the radiation loss terms can be approximated. Curve-fits for these quantities can be found in literature (37).

For all cases, the following incoming flow conditions are used: $U_{in} = 1000\ ms^{-1}$ ($M_{in} = 1.7$), $P_{in} = 1.4 \times 10^5\ Pa$, and $T_{in} = 1000\ K$. In the cases investigated below, either the applied magnetic field or the applied current is held constant throughout the simulation time.

7.2.2 Applied Electric Field

An electric field is applied in the rearward-facing step by prescribing a potential difference between two conducting surfaces (the cathode and the anode). Two different configurations are investigated. The cathode is mounted on the bottom wall just before the step in both configurations, and only the location of the anode is varied; for the first configuration, the anode is located on the bottom wall aft of the step, and for the second configuration, the

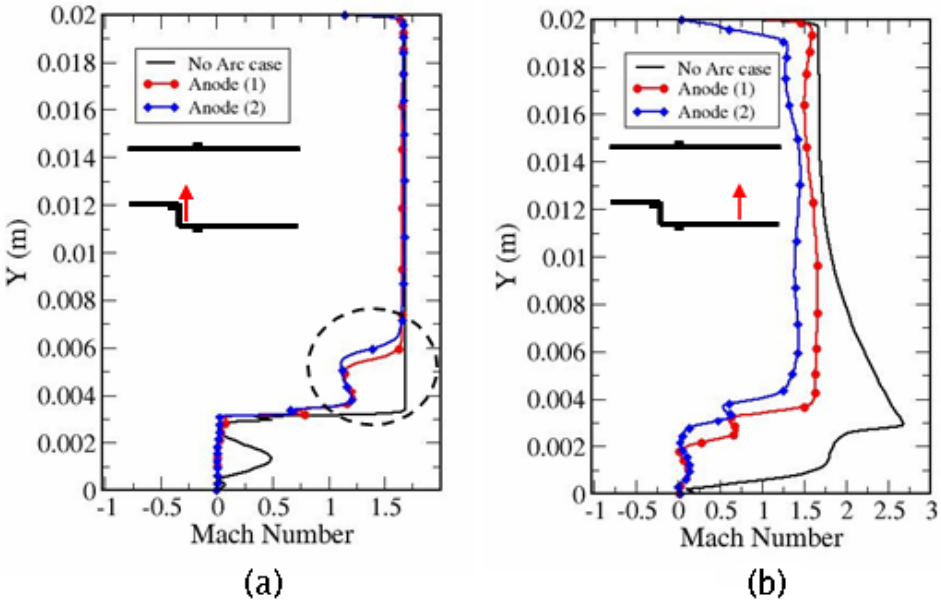

Figure 56: Mach number profile (a) near the step corner and (b) in the Y-direction (10 mm from the step).

anode is located on the top wall. Figures 52(a)-(d) show the distributions of the electric field, the current lines, and the magnetic field for these two configurations.

Figures 53(a) and 54(a) show the pressure and the temperature distributions, respectively, for the nominal case with no applied external fields. Several well known features are captured here, including the expansion fan at the corner which creates a low pressure recirculating region just aft of the step. The temperature also decreases and reaches a minimum of approximately 500 K. The inlet boundary layer on the wall separates at the corner and the resulting free shear layer bends downward as a result of the low pressure recirculating region, eventually reattaching at the lower wall further downstream. A recompression shock is seen as the shear layer attaches to the wall.

When an electric field is applied in either of the configurations, the most noticeable difference is that no expansion fan forms at the corner of the step. This is obvious from the pressure distribution profiles for these two cases given in Fig. 53(b) and Fig. 53(c). Instead, a strong shock is formed just prior to the electrical discharge surfaces. In configuration (1), (Fig. 53(b)), only one shock is formed, since the anode is located in the recirculation

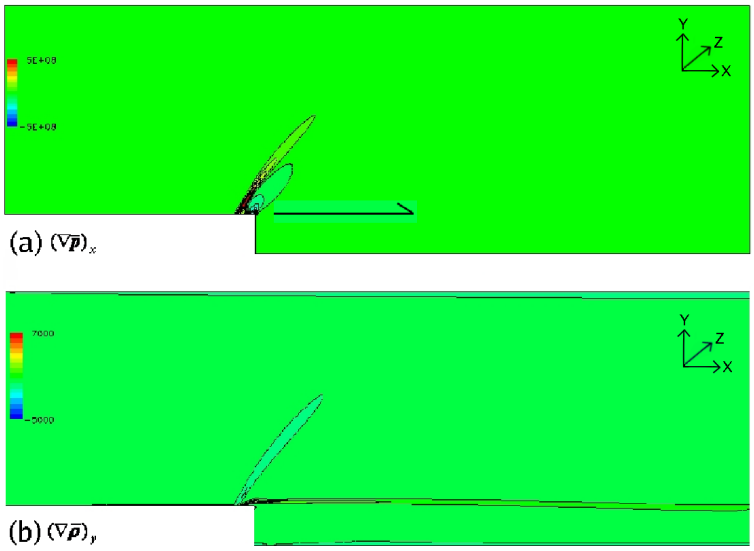

Figure 57: Pressure gradients for configuration (1) (a) x component and (b) y component.

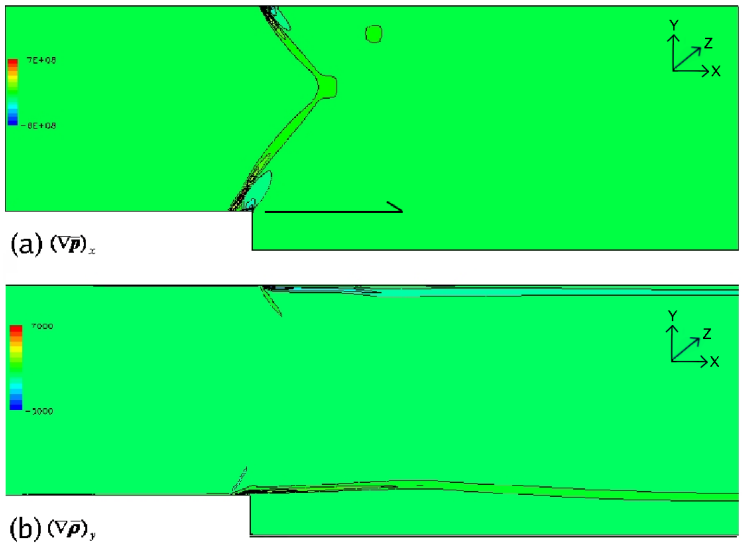

Figure 58: Pressure gradients for configuration (2) (a) x component and (b) y component.

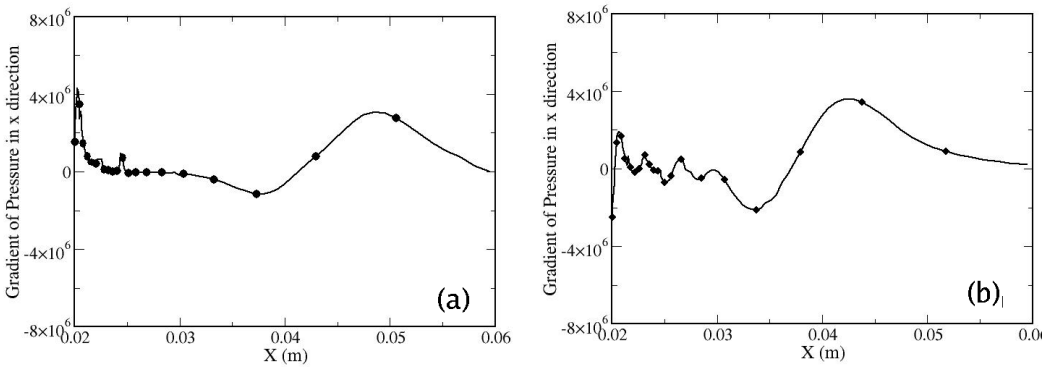

Figure 59: Pressure gradient profiles $Y = 0.003\ m$ at the mid plane (a) configuration (1) and (b) configuration (2).

zone. However, in configuration (2), (Fig. 53(c)), two oblique shocks are created, which merge together in the center of the flow. The reason these shocks develop is that the high temperature region near the electrical discharge surfaces act as bluff bodies. The large thermal gradient in these regions promote boundary layer separation and the formation of the oblique shocks. As a result of the shock waves, the downstream velocity is reduced, especially for configuration (2) as a result of the formation of two oblique shocks.

Figure 55 represents pressure distribution along the bottom wall. In comparison with the non-arc case, the two cases with the arc have flat profiles and there is no gradual pressure increase seen for the non-arc case, which occurs due to recompression shock. It is clear that there is no reattachment of shear layer. For configuration (2), the pressure is twice as large as the other configurations because of the merging of the two shock waves. Furthermore, it can be seen that the pressure gradually increases downstream when an electric field is applied. This is related to the approach of the shear layer to the bottom wall.

Figures 56 (a)-(b) show the Mach number profiles near the corner and downstream. Near the step corner, there is significant reduction of Mach number related to the electrical discharge. There are mainly two reasons associated with this. First, the electrical discharge greatly increases the gas temperature resulting in the increase of the sound of speed. Secondly, it blocks the flow like a bluff body. These effects remains further downstream (see

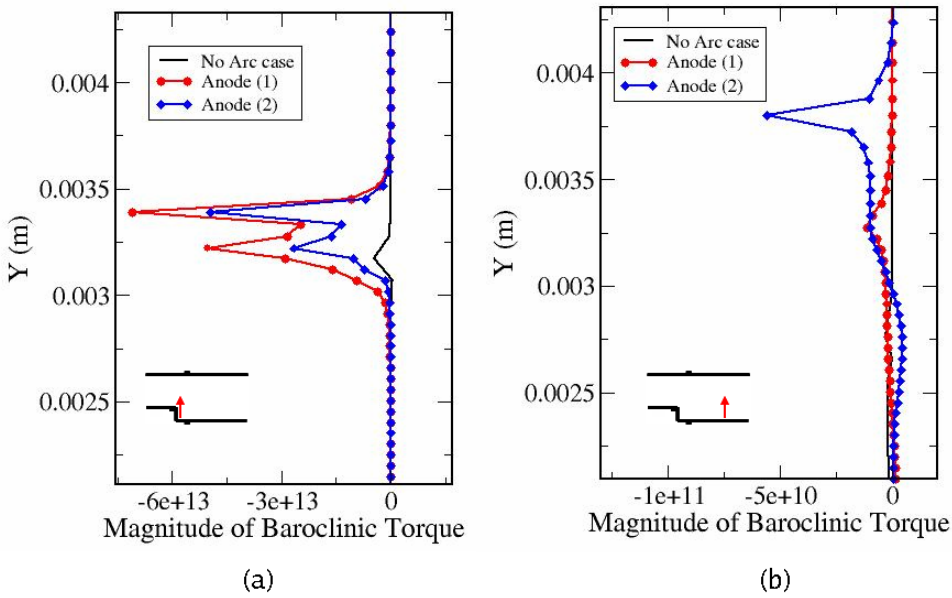

Figure 60: Magnitude of baroclinic torque profile (a) near the step corner and (b) in the y-direction (10 mm from the step).

Fig. 56(b)). Also, for the case without the electrical discharge, there is some increase of Mach number around $Y = 0.003$ m related to the reattachment of the shear layer. However, we can not see the corresponding acceleration for the cases with the electrical discharge due to the delay of of the shear layer reattachment.

Figures 57 (a)-(b) and Figures 58 (a)-(b) represent the x and y components of the pressure gradients for configuration (1) and configuration (2), respectively. It is clearly see that the large gradients related to the electrical discharge are seen for both cases. Corresponding x component of pressure gradient for both cases are shown in Figs 59 (a)-(b). This type of electrical discharge may significantly increase the baroclinic torque seen in the vorticity equation.

Figures 60 (a)-(b) show the magnitude of baroclinic torque near the step corner and in the Y-direction $10mm$ from the step. Compared with the case without the electrical discharge, the large magnitude of baroclinic torque are observed near the shear layer region. Since the baroclinic torque term acts as a production term for turbulence, the flow is expected to be highly turbulent within the shear layer. This may aid in the enhancement

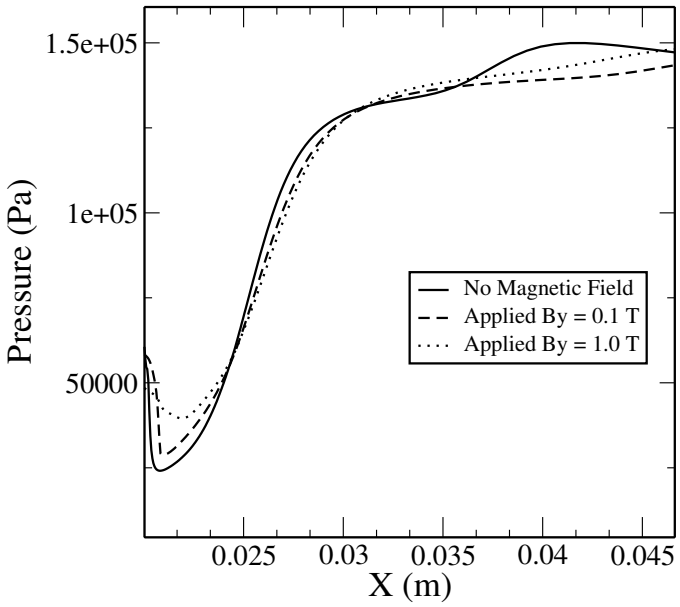

Figure 61: Pressure distribution along the bottom surface for different strengths of the external magnetic field, $\bar{B}_{ex,y} = 0.0,\ 0.1\ Tesla,\ 1.0\ Tesla.$

of supersonic mixing process if fuel is appropriately injected into these regions.

7.2.3 Applied Magnetic Field

An external magnetic field is applied in the positive $y-$direction. Figure 61 shows the pressure at the wall just aft of the step for various magnitudes of the applied field. The magnetic field increases the pressure in the recirculation region, which affects the development of the shear layer. The pressure here is the sum of the thermal pressure and the magnetic pressure given by the trace of the magnetic stress tensor. The magnetic pressure is essentially a component of the Lorentz force that acts to increase the pressure and the temperature in the recirculation zone. This result agrees with previous work (Khan and Hoffmann) (69). It is noticed that the application of an applied magnetic field does not create any shock waves prior to the step, and thus an expansion fan is still seen at the corner.

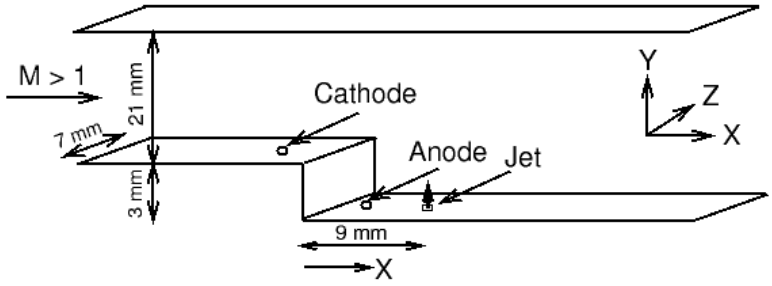

Figure 62: Three dimensional geometry and electric node locations. The step height $H = 3.1\ mm$. The transverse sonic injection is set at the bottom surface ($3H \sim 9\ mm$ downstream from the step). The second injection for Case 2 is $7H \sim 22\ mm$ downstream. The grid resolution is $229 \times 69 \times 65$ and clustered around the step and the fuel injector. Each electric node ($5\ mm \times 5\ mm$) are resolved by 14 points.

7.3 Reacting flow with/without equilibrium Plasma

In this section, the capability of a equilibrium plasma to sustain premixed hydrogen/air combustion over a backward facing step are investigated.

7.3.1 Boundary condition and inflow/plasma parameters

Figure 62 shows the computational domain and other reference parameters. The cathode is located upstream of the step, and the anode is positioned on the bottom wall aft of the step. Fuel is injected perpendicularly upwards from the bottom wall. The top wall is a slip wall, and no-slip wall boundary conditions are used elsewhere. Adiabatic wall conditions are used everywhere except at the anode and cathode where the wall temperature is held at a constant temperature ($T_{wall} = 3500\ K$) (45). At the cathode and the anode surfaces, the electric potential, ϕ, is determined by specifying the current in the normal direction as Eg. (126) where $J_{max} = 1.4 \times 10^8\ Am^{-2}$, $b = 2000$ for an input current of 200 A. The current density in the tangential direction is set to zero at the conducting surfaces. Everywhere else the scalar electric potential and vector magnetic potential are required to have zero normal gradients (see Table 7.3.1).

The inflow conditions for the supersonic air is summarized in Table 7.3.1. Cases 1-5

Table 7: Boundary Condition for $\bar{\mathbf{A}}_\mathbf{i}, \bar{\phi}, \bar{\mathbf{T}}, \bar{\mathbf{U}}, \bar{\mathbf{V}}, \bar{\mathbf{W}}$.($n$ is the normal direction.)

Surface	$\bar{\mathbf{A}}_\mathbf{i}[\mathbf{Tm}]$	$\bar{\phi}[volt]$	$\bar{\mathbf{T}}[K]$	$\bar{\mathbf{U}}[m/s]$	$\bar{\mathbf{V}}[m/s]$	$\bar{\mathbf{W}}[m/s]$
AHLI	$A_i = 0$	$\frac{\partial \phi}{\partial x} = 0$	1000	$Ma > 1$	0	0
ABGH	$\frac{\partial A_i}{\partial y} = 0$	$\frac{\partial \phi}{\partial y} = 0$	$\frac{\partial \bar{T}}{\partial y} = 0$	0	0	0
BCFG	$\frac{\partial A_i}{\partial x} = 0$	$\frac{\partial \phi}{\partial x} = 0$	$\frac{\partial \bar{T}}{\partial x} = 0$	0	0	0
CDEF	$\frac{\partial A_i}{\partial y} = 0$	$\frac{\partial \phi}{\partial y} = 0$	$\frac{\partial \bar{T}}{\partial y} = 0$	0	0	0
DEKJ	$A_i = 0$	$\frac{\partial \phi}{\partial x} = 0$	$\frac{\partial \bar{T}}{\partial x} = 0$	–	–	–
IJKL	$\frac{\partial A_i}{\partial y} = 0$	$\frac{\partial \phi}{\partial y} = 0$	$\frac{\partial \bar{T}}{\partial y} = 0$	0	0	0
Cathode	$\frac{\partial A_i}{\partial y} = 0$	$Eq.10$	3500	0	0	0
Anode	$\frac{\partial A_i}{\partial y} = 0$	$Eq.10$	3500	0	0	0

Table 8: Free-stream flow conditions. For Case (3)-(5), an uniform magnetic field of 3 Telsa is applied in the z-direction. For all cases, the $Ma = 1$ pure hydrogen fuel jet is introduced from the bottom wall with $P_{in} = 162\ kPa$ and $T_{in} = 221\ kPa$.

Case	Ma	Gas	$T_{in}[K]$	$P_{in}[kPa]$	Arc [A]	$Bz_0[T]$
1	3.5	Air	1300	32	-	-
2	3.5	Air	1300	32	200	-
3	3.5	Air	1300	32	200	3
4	3.5	Air	1300	32	200	-3
5	3.5	Air	1300	32	200	$3sin(2\pi\omega t)$

study plasma-assisted combustion at $Ma = 3.5$. In Case 3 and 4, an uniform external magnetic field ($B_{0,z}$) are applied in the z-direction with a strength of $B_{0,z} = 3T and - 3T$, which is thought to be practical with current technology. For Case 5, the oscillating uniform external magnetic field is introduced. The frequency is $250KHz$ that is roughly same as $\sim 1/T_{eddy}$ where T_{eddy} is the eddy turnover time inside the recirculation zone. To explain the importance of introducing the external field, Fig. 63 shows a schematic of the various processes and forces (albeit in a time-averaged sense) based on the interpretation of the current results in order to emphasize the MHD flow control. The detail effect of MHD flow control will be discussed in the result section.

The grid is chosen based on past experience and a limited number of grid refinement studies for this configuration. The current $229 \times 69 \times 65$ resolution gives around 10-15 points in the separating shear layer region, which is considered adequate. The grid dependence study and the ability of capturing the turbulence using this grid resolution is shown in the

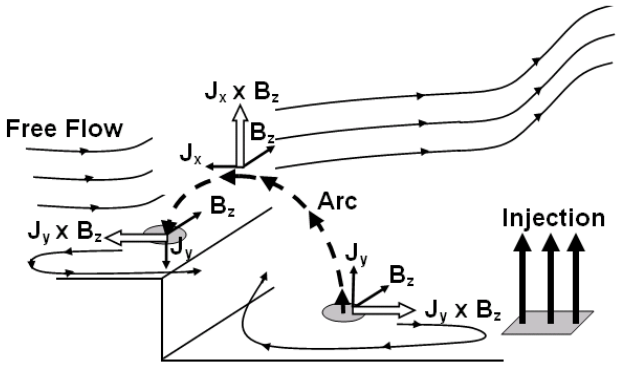

Figure 63: Schematic of the flow around the step corner with an applied magnetic field and electrical discharge with the resulting Lorentz forces.

following section.

7.3.2 Chemical kinetics

A 16 species ($H_2O, H_2, O_2, N_2, H, O, N, OH, NO, H_2^+, N_2^+, H^+, O^+, N^+, NO^+, e^-$), 74 reactions kinetics hydrogen-air combustion and high temperature air dissociation model is employed. The hydrogen combustion kinetics are based on a 7-step and 7-species mechanism (32). The remaining species and reactions are based on a high-temperature dissociation mechanism (109). These reactions are summarized in Tables 1, 2, and 3. The hydrogen mechanism is only used for temperatures up to $5,000K$, and the high-temperature air mechanism is only used above $3,000K$. At present, the plasma is assumed to be in local thermodynamic equilibrium, therefore, it is not necessary to solve the electron energy equation, and because of quasi-neutrality, the electron density n_e is given by $n_e = \sum_{m=1}^{6} Z_m n_m$, where Z_m is charge number, and 6 denotes the number of positive ions ($H_2^+, N_2^+, H^+, O^+, N^+, NO^+$). In the current model, a subgrid eddy breakup model called EBU-LES (97) is used to obtained the filtered reaction rates. Such a closure is considered simplistic but computationally efficient and is used here as an initial effort. However, in the future a more comprehensive subgrid scalar closure (97; 122) will be considered. For estimation of the radiation loss R_d , empirical data for high-temperature air at atmospheric pressure is used (105).

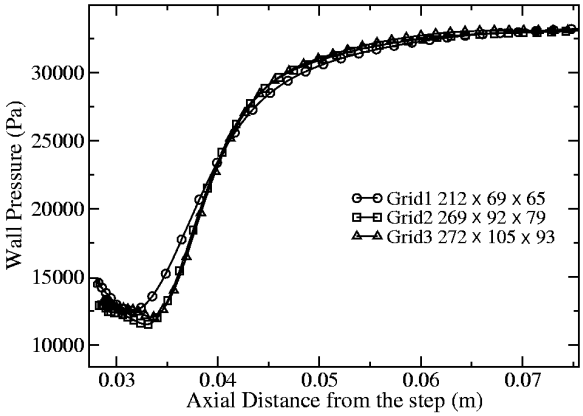

Figure 64: Grid independence study for Ma = 3.5 non-reacting flow.

7.3.3 Numerical results and discussion

The grid dependence study for $Ma = 3.5$ non-reacting flow is performed with the three different grid resolutions, Grid 1: $229 \times 69 \times 65$, Grid 2: $269 \times 92 \times 79$, and (Grid 3) $272 \times 105 \times 93$. Figure 64 show the pressure distribution at the bottom wall. Even though some disparities is seen near the step wall, the location of reattachment of the shear layer and the pressure after the recompression are same. Also, the turbulent kinetic energy spectra using Grid 1 is shown in Fig. 65 inside the shear layer at X = 2H downstream and is overlaid with the solid line indicating $-5/3$ slope. Due to these results, we confirm that current LES-LDKM model has a capability to capture turbulent motion with Grid 1 and use it for the rest of studies.

For comparison with the high Mach number flow case what we concern, Figs 66 show the characteristic flow fields of $Ma = 1.4$ flow. For such a low Mach number supersonic flow, the flame can be hold by the hot products which stays in the recirculation zone, and there is no necessary to use the plasma. Also, the fuel penetration depth is relatively long.

Figures 67 (a) and (b) show two representative snapshots of the density field for the case with/without an arc (Case 1 and 2). Compared with low Ma (shown in previous section), the flow in the recirculation zone between the fuel injector and the step changes in magnitude, the leading shock angle (in front of the injector) is reduced and fuel penetration is decreased. The corresponding cases with the arc show qualitatively similar overall features,

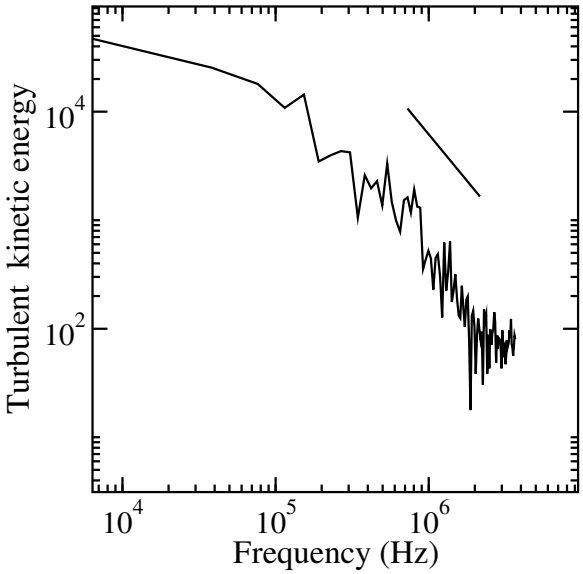

Figure 65: FFT of the turbulent kinetic energy spectra with Grid 1 for Ma = 3.5 non-reacting flow. The data is taken in the shear layer at the $X = 2H$ downstream. The solid line indicates $-5/3$ slope.

with some significant near-field differences that are discussed further below.

Figures 68(a) and (b) show the snapshots of corresponding temperature profiles. The high temperature ($\sim 13,000K$) can be seen in the temperature in Fig. 68(b). It is seen that there is a significant increase of temperature gradient when we turn on the arc, and it manifests itself as a strong local baroclinic torque ($\nabla p \times \nabla\rho/\rho^2$) in the near field shear layer, as shown by the time-averaged profiles of its magnitude in Figs. 69 (a)-(b) for case 1 and case 2. It is well known that this force effect can increase vorticity strength and hence can impact turbulent mixing.

Figures 91 shows the mole fractions of minor species along the centerline at the step height for the case with an arc (Case 2). The large concentration of electrons indicates the location of the plasma source. An increase in charged species is seen, which recombine instantly downstream. The region of zero H species corresponds to the location of the fuel injection. The non-zero NO radical mole fractions located behind the fuel injector is a result of spanwise entrainment of hot products.

Figure 71(a) shows the iso-contour of the magnitude of the current density, $|\vec{J}|$, and the current vector lines for Case 2. It is observed that the current density is swept downstream

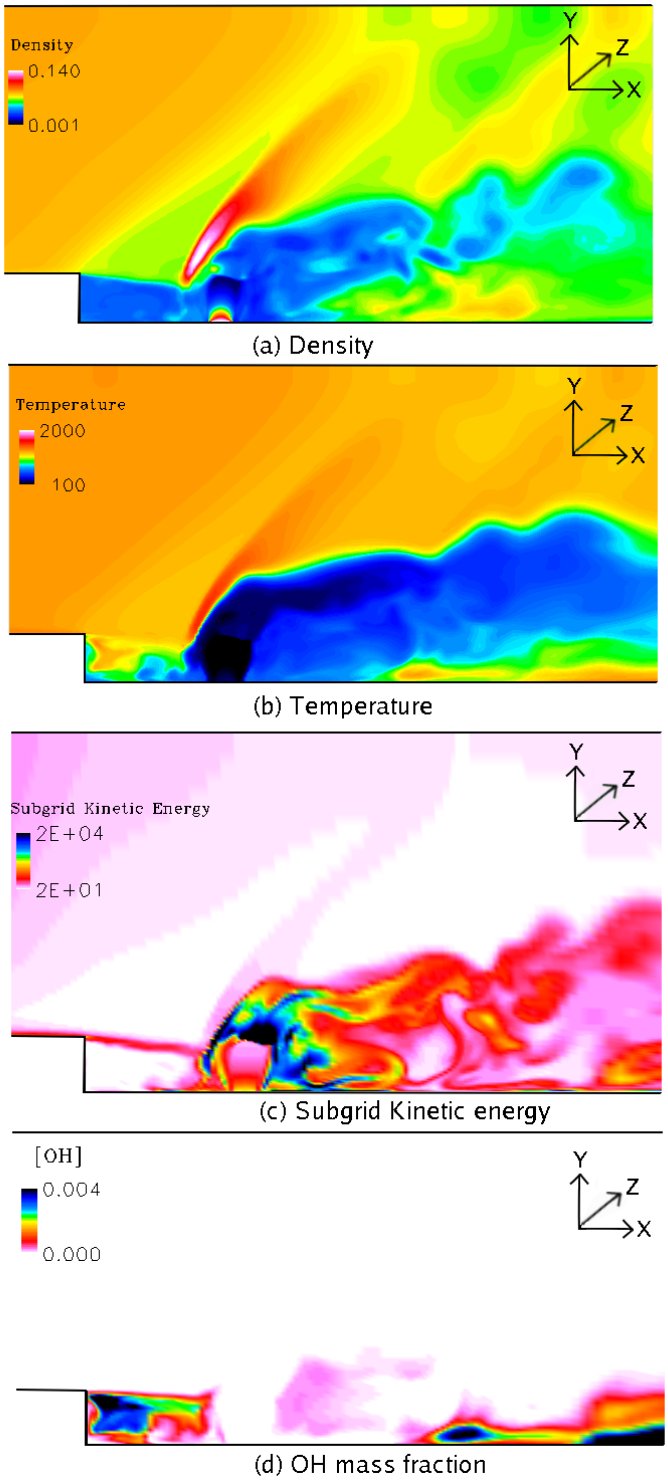

Figure 66: Characteristic of Mach 14 flow (a) density, (b) temperature, (c) subgrid kinetic energy, and (d) OH mass fraction.

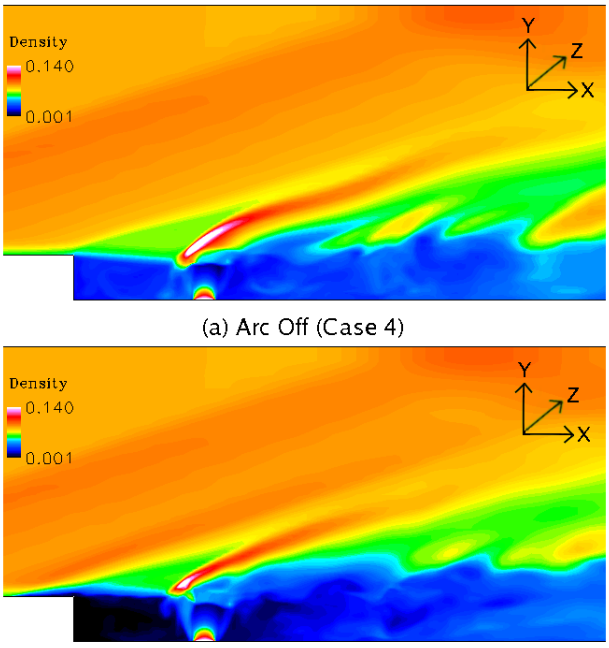

Figure 67: Comparison of density contours for (a) Arc-Off (Case 1) and (b) Arc-On (Case 2).

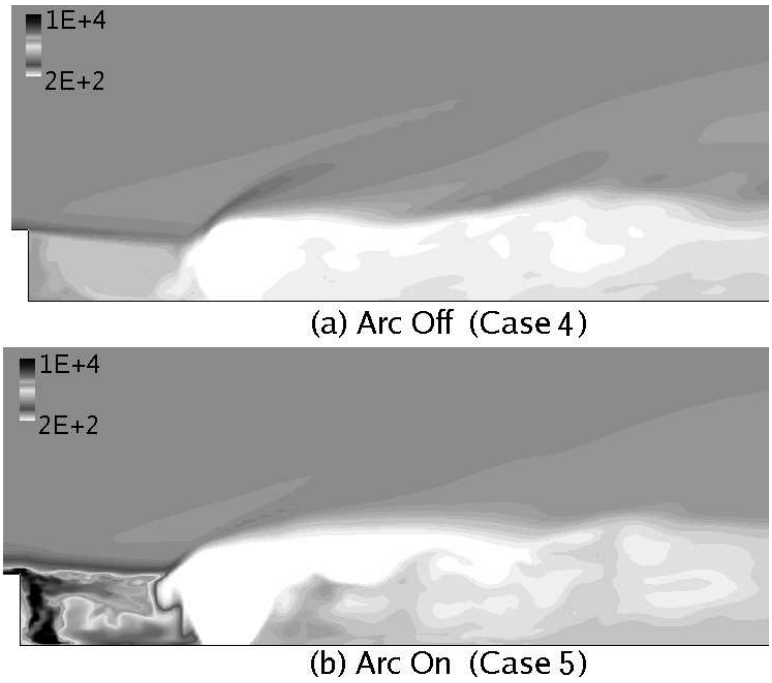

Figure 68: Comparison of temperature contours for (a) Arc-Off (Case 1) and (b) Arc-On (Case 2).

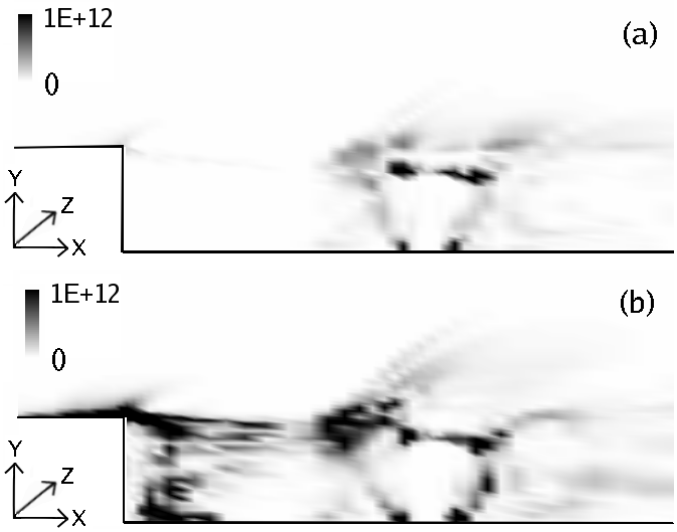

Figure 69: Comparison of the contour of the magnitude of baroclinic torque for (a) Arc-off (Case 1) and Arc-On (Case 2).

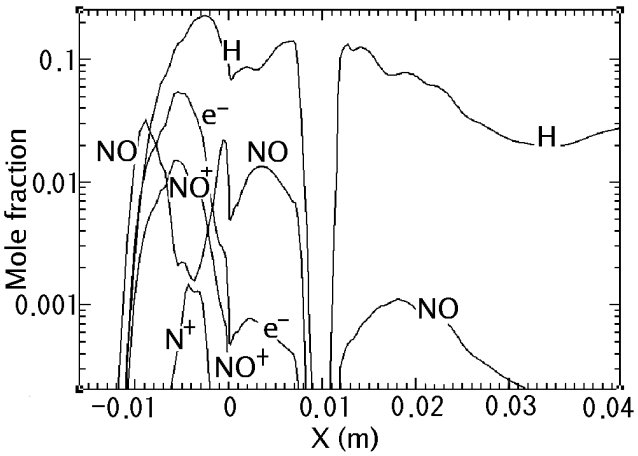

Figure 70: Mole fractions of minor species along the centerline at $Y/H = 1.0$ for Case 2.

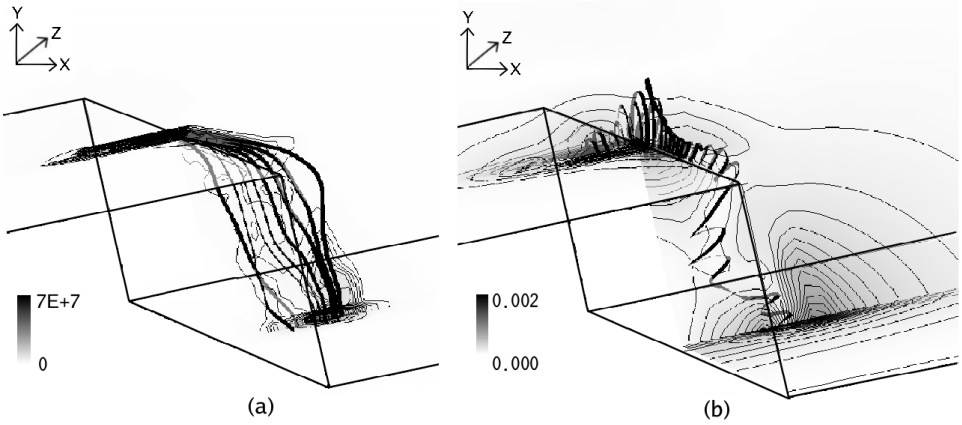

Figure 71: Simulated electromagnetic fields for Case 2 with an input current of 200 A (a) current density ($|\vec{J}|$) contours and vector field (dark lines), and (b) magnetic field magnitude contours ($|\vec{B}|$) and its vector field (dark lines).

by the flow, but still remains localized around the electrical nodes due to the high temperature dependence of the electrical conductivity σ. These results mirror those observed in experiments (84). Figure 71(b) shows the corresponding iso-contours of the magnetic field, $|\vec{B}|$, and the magnetic vector lines. The magnetic field achieves a maximum strength ($0.002\ T$) near the step. The induced magnetic field for all cases is more than four orders of magnitude smaller than the magnetic field associated with the arc current due to the large magnetic diffusivity, λ. This observation is consistent with the fact the magnetic Reynolds number based on the channel height and the inflow velocity is much less than unity. By shifting the shear layer, the fuel penetration depth increases by approximately 20% for Case 3, and more of the free-stream air is mixed with the fuel leading to increased combustion and heat release (see Fig. 75). Also, inside the recirculation zone. there is a strong force that push the stagnant flow there and results in further mixing. This is a critical factor to achieve spread the effect of the arc as a wide-range flame-holder.

Figures 72(a)-(d) show that flow fields for Case 1-4. Compared with the case without the arc (Fig. 72(a)), the flow field is not significantly affected (Fig. 72(b)). However, when a uniform magnetic field is applied (Case 3 and 4), it creates a significant body force effect that changes the flow field . When we impose the positive constant magnetic field (Case 3), it appears that the shock strength is weakened and therefore, fuel penetration and fuel-air

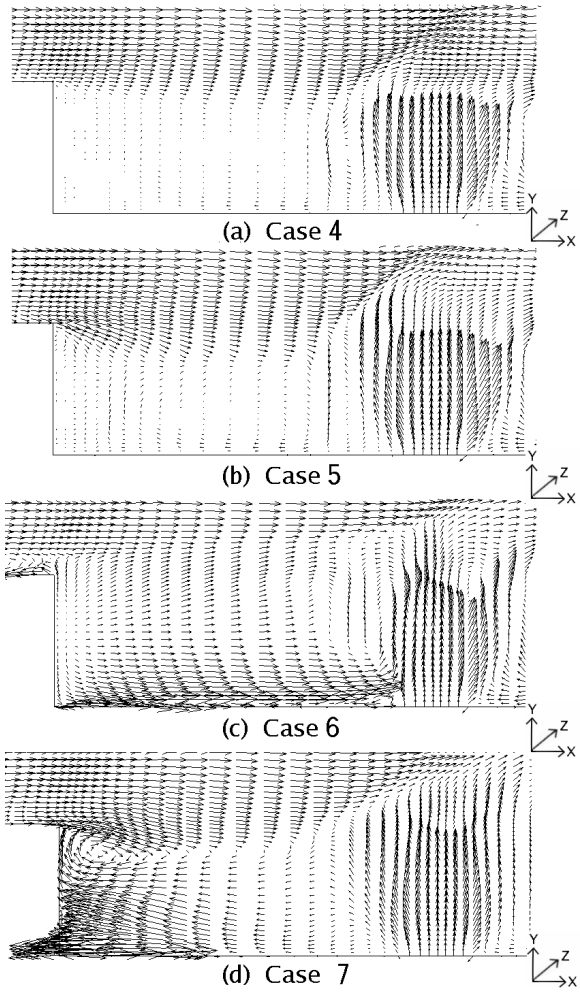

Figure 72: Velocity vector fields around the step for case 1-4.

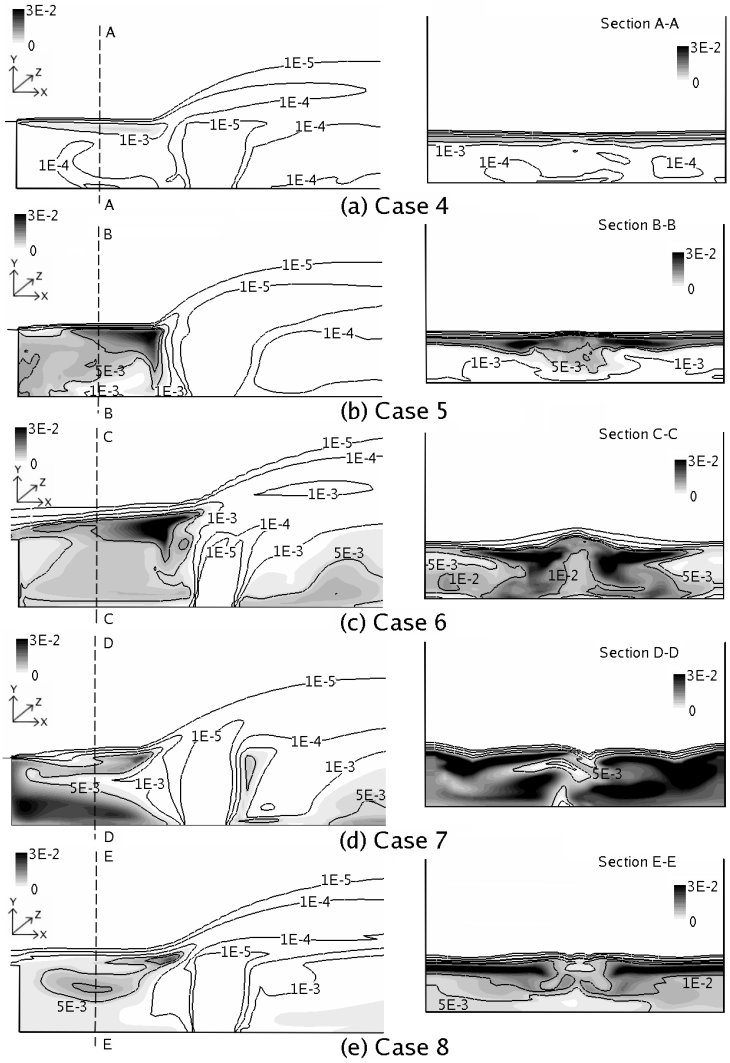

Figure 73: Comparison of time-averaged OH mass fraction contours in the x-y cross section (left) and the y-z cross section for (a) Case 1, (b) Case 2, (c) Case 3, (d) Case 4, and (e) Case 5.

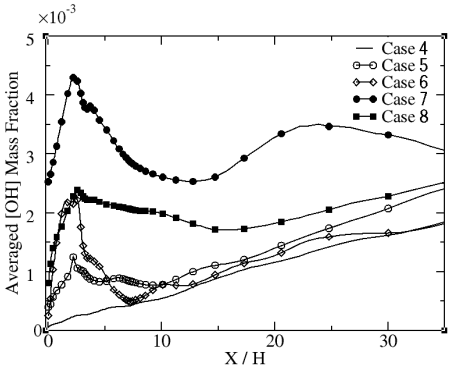

Figure 74: Comparison of [OH] mass fraction for Cases 1-5. The data is averaged on the y-z cross section.

mixing increases. On the other hand, when the negative magnetic field is applied (Case 4), the strong eddy is formed around the step due to the flow curved downward from the shear layer and the flow induced the Lorentz force from the bottom wall. Even though this does not effectively increase the penetration depth, this results in creating a radical pool (a hot temperature region) in the widerange in the spanwaise (z-direction).

Figure 74 shows the OH mass fraction averaged on the y-z cross section for cases 1-5. For all the plasma assisted combustion case, OH concentration greatly exceed the case without the plasma (Case 1). It is seen that OH concentration has a local peak behind the step due to the plasma and drops slightly resulting from the cold fuel injection. The steady increase behind the fuel injection seen for all cases is due to the ignition delay. However, for the plasma assisted cases, much higher OH concentration is overall achieved especially for Case 5 in which the Lorentz force impacts mixing hot products inside the recirculation zone effectively.

Figure 76 shows the shear layer thickness at the mid plane ($Z = 0$) for cases 1-5. All data are normalized by the case without the arc (Case 1). It is seen that Case 4 has a maximum value due to the Lorentz force that makes the shear layer bend downward. On the other hand, Case 3 has almost same value as Case 4 even though the plasma is turned on. It is caused by lifting the shear layer by the Lorentz force.

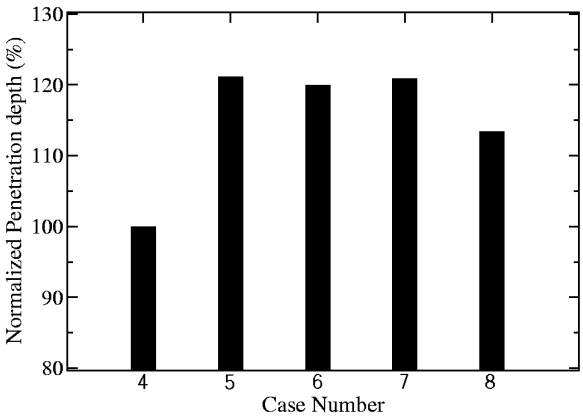

Figure 75: Comparison of penetration depth of fuel injection for Cases 1-5. The penetration depth is measured by 10% of the original concentration of the injection exit and are normalized by Case 1.

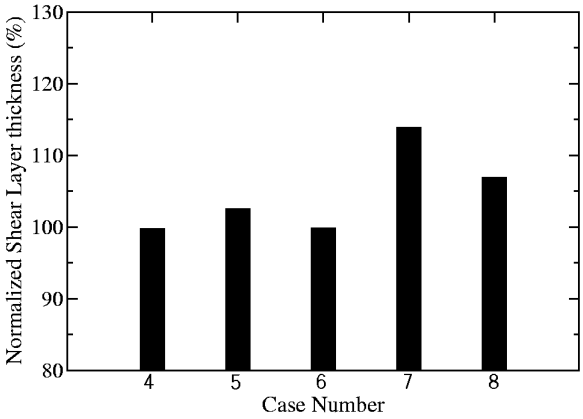

Figure 76: Comparison of the shear layer thickness for Cases 1-5. The thickness is measured from $10\% \sim 90\%$ of the free-stream velocity. The data are normalized by Case 1.

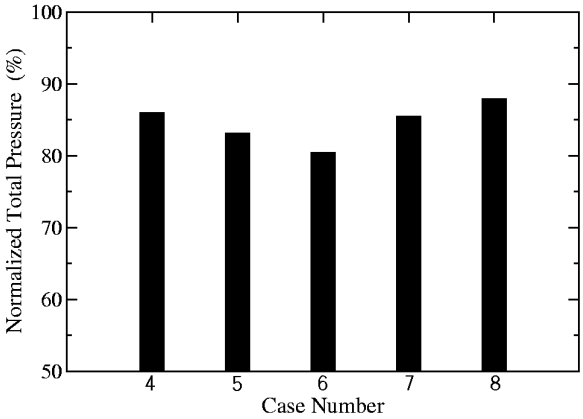

Figure 77: Comparison of the total pressure at exit for Case 1-5. All the data are normalized by the total pressure of the inflow.

Finally, Fig. 77 shows the total pressure normalized by the inflow condition. Overall, all cases has the same values ($\sim 85\% \pm 3\%$). The reduction is due to the dissipative nature of the scramjet combustor environment where the numerous compression waves are formed. However, there is no significant reduction by introducing the arc, and it shows that the aerodynamic negative impact of the plasma introduction on the combustor performance is limited.

From these simulations, an insight into equilibrium plasma-assisted mixing and combustion can be obtained. Overall, the effect of the equilibrium plasma (as simulated here) is limited to the near-field of the plasma source with significant impact on fuel-air mixing and combustion. Further studies are still needed to fully investigate the plasma effect for a range of Ma and is deferred to a future effort. Studies are also required with improved subgrid closure for the reaction kinetics to confirm these observations. This is a part of future works.

7.4 Reacting flow with/without Non-equilibrium Plasma

In this section, we investigates the capability of a non-equilibrium plasma to enhance flame stability and possibly reduce ignition delay in a SCRAMJET geometry. Unlike the thermal plasma discussed in the previous section, the non-equilibrium plasma that requires relatively low input power to generate is implemented at the vertical wall of the step. The power for the non-equilibrium is about $2 \sim 3$ order less the required input power for the thermal plasma ($1 \sim 100$ kW (111)). Since electrons with higher mobility effectively pull electrical energy from the electric field and it takes time to shear it with the heavy particle through binary collisions, the electron temperature is much higher than the heavy particle temperature resulting in thermally non-equilibrium state. In such a system, the high-temperature electrons can easily dissociate molecules such as O_2, N_2 and H_2 and generates radical atoms that potentially accelerate the chemical reaction and has attracted to SCRAMJET applications.

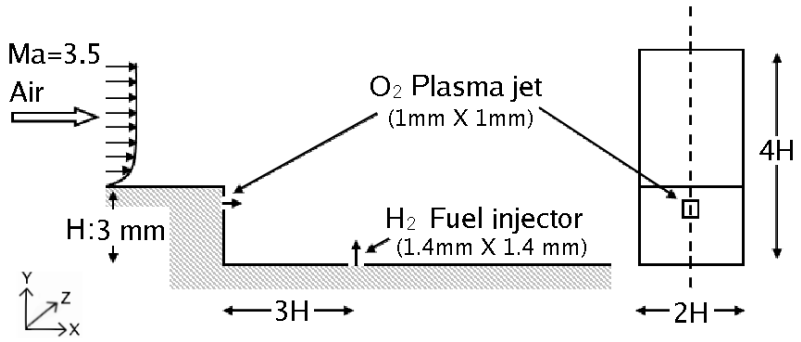

Figure 78: Schematic of the dump combustor. The grid resolution is $346 \times 217 \times 55$ and clustered around the step and the fuel/plasma jets.

Table 9: Plasma jet conditions. For all cases, U_{jet} is set to 535 m/s and P_{jet} is the same as the inflow pressure ($P_{in} = 32$ $[kPa]$). The gas is O_2 and the positive ions is only O_2^+. The electron temperature is set to 2 eV for all cases.

Case	$T_{h,jet}[K]$	Mode	$n_{e,jet}[m^{-3}]$	$\vec{E}_{ex}[V/m], \vec{B}_{ex}[T]$
1	-	-	-	-
2	3500 K	Const.	10^{17}	-
3	3500 K	250KHz	10^{17}	-
4	3500 K	Const.	10^{20}	-
5	3500 K	Const.	10^{20}	$Ez_{ex} = 10^3$,$By_{ex} = -10$

7.4.1 Problem Setup

Figure 78 shows the schematic of a typical SCRAMJET geometry, the locations of the plasma jet, and the fuel injection port. On all solid surfaces, no-slip, adiabatic wall boundary conditions are imposed. Like the previous calculation, Mach 3.5 air enters at the left boundary with the following temperature, pressure and velocity: $T_{in} = 1300\ [K]$, $P_{in} = 32\ [kPa]$, and $U_{in} = 2420\ [m/s]$. Pure hydrogen is injected as fuel from the bottom wall at sonic speed with the following temperature, pressure and velocity: $T_f = 221\ [K]$, $P_f = 162\ [kPa]$, and $U_f = 815\ [m/s]$. The shape of the fuel injection port is square with each side measuring $1.4mm$. The parameters for the plasma jet are summarized in Table 1, and discussed briefly below.

For Case 1, pure O_2 with a temperature of $T_{jet} = 3500\ [K]$ and a pressure of $P_{jet} = 32\ [kPa]$ is used instead of a plasma for a baseline comparison. For Cases 2-5, a non-equilibrium plasma is used with an electron temperature of 2 eV ($\sim 23200\ K$) and a heavy particle temperature, T_h of 3500 $[K]$. The electron number density, n_e, is set two different values $\sim 10^{17}\ [m^{-3}]$ and $\sim 10^{20}\ [m^{-3}]$. Cases 2 and 4, respectively, are used to investigate how different ionization levels in the plasma jet effect combustion. For Case 5, external fields are imposed: $\vec{B}_{ex} = (0, -10\ T, 0)$ and $\vec{E}_{ex} = (0, 0, 1000\ V/m)$. The resulting Lorentz force acts as a damping force in x-direction and is used to to see if MHD flow control can help aid in combustion efficiency through mixing.

A grid of $346 \times 217 \times 55$ is used here with around 20 points in the shear layer region. This grid is chosen based on past studies (97; 122) for similar non-MHD Reynolds number flow. Future studies of the grid resolution sensitivity are planned for MHD flows.

7.4.2 Results and Discussion

In this subsection, the numerical results are presented. For the validation of our non-equilibrium code, a shock tube test case is first modeled. Other validations for the current model have been performed in the previous section.

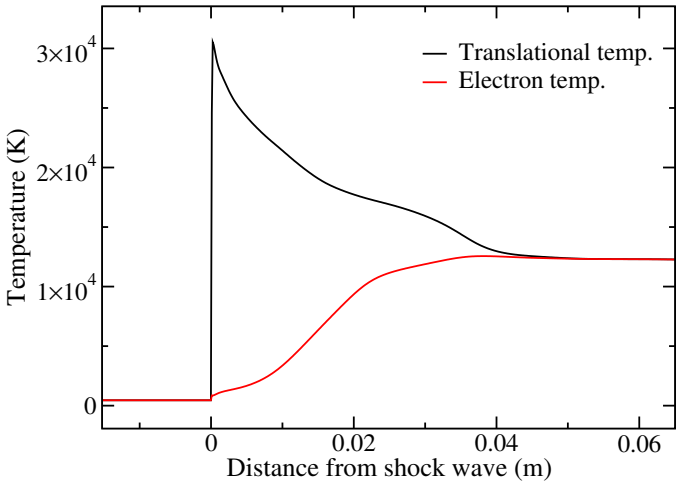

Figure 79: $\tilde{T}_h$ behind the shock.

7.4.2.1 Shock tube studies

In order to qualitatively test the non-equilibrium code, a strong shock is simulated in one-dimension. The domain was $0.1m$ and 800 grid points were used. The validation is only qualitative and in the future a more rigorous validation of the chemical kinetics needs to be conducted. However, at present, the results show that the model is capturing the correct trends and that the data is of the proper order of magnitude. A shock strength of Mach 15 is simulated and modeled in the moving-shock frame-of-reference by adjusting the boundary conditions. It is assumed that the gas is calorically perfect for simplification, but still chemically reacting. Thus, the heavy particle temperature reduces behind the shock as a result of chemical reactions (i.e., dissociation of N_2 and O_2) and energy exchange with the free electrons. The initial conditions were determined from the Hugoniot relationships.

Park (109) provides several validations for the two-temperature chemical kinetic mechanism that is used in this paper. However, the model presented in this paper does not include vibrational or electronic non-equilibrium energy modes. In this respect, our model is different from Park's model, which will be referred to as the Park93 model. Thus, the assumption in our model is that the free-electron temperature can be used for chemical rate control instead of the vibrational-electronic temperature. Therefore, only qualitative comparisons can be made to this data. Future planned studies will revisit this issue.

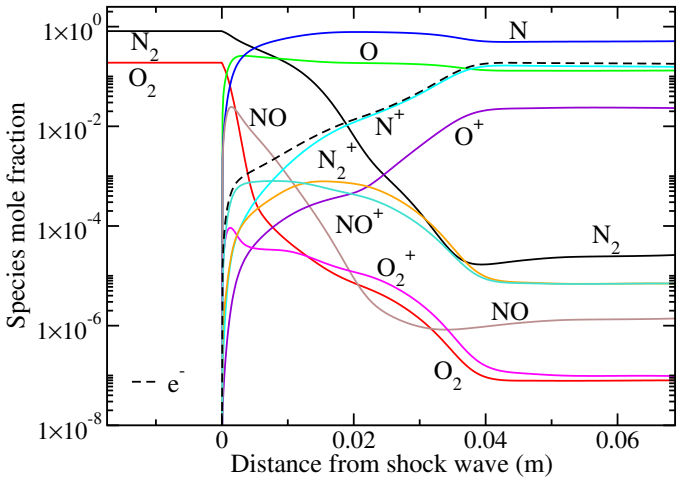

Figure 80: Mole fractions of each species behind the shock.

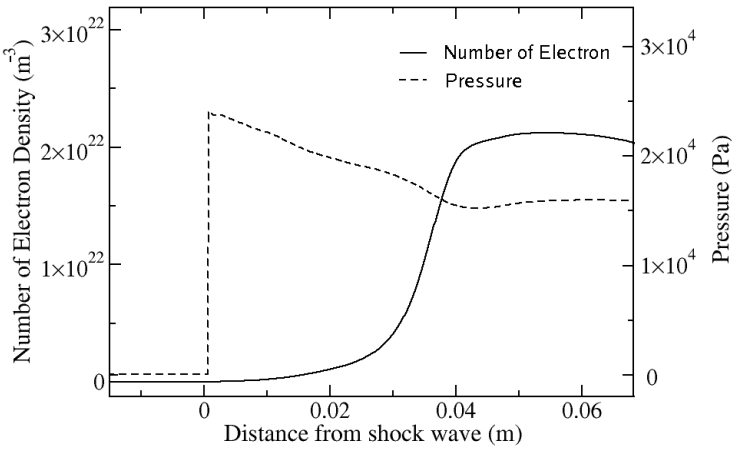

Figure 81: $\bar{n}_e$ and $\bar{p}$ profiles behind the shock.

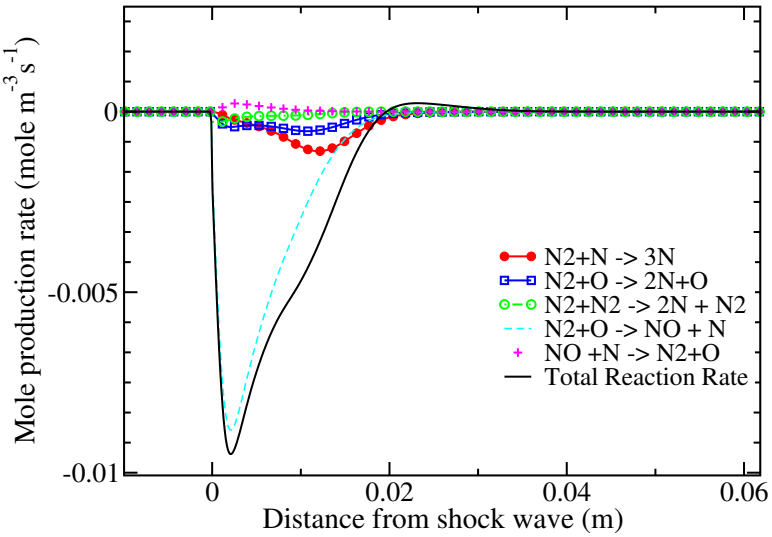

Figure 82: Mole production rate for N_2 near the shock front.

Figure 79 shows the heavy particle and electron temperatures. Park (109) provides a computation of a re-entry bow shock for a free-stream velocity of 12 km/s and density of 10^{-4} kg/m^3, which produces a shock stronger than the Mach 15 shock simulated here, but with a post-shock pressure of similar magnitude. The relaxation distances for both cases are of the order of centimeters, but our model seems to over-predict the relaxation distance at least from a qualitative stand-point. The relaxation distance for the stronger shock should be longer as a result of a higher degree of non-equilibrium. Since our model does not include vibrational or electronic energy sinks, the transfer of energy between heavy particles and electrons may occur at a slower rate than what is physical.

From Fig.80, it is observed that immediately after the shock large concentrations in O and N are produced. Through associative ionization reactions, electrons are created as well as the by-products N_2^+, O_2^+, and NO^+. Charge-exchange reactions occur, and then electrons impact ionization. These later reactions account for the growing population of N^+ and O^+ concentrations. This matches the results observed in Park (109). Moreover, the order of magnitudes for the equilibrium mole fractions and the relationships of all the species mole fractions with respect to each other follow the observed trends. In both our and the Park 93 models, the mole fraction of electrons is approximately equal to the equilibrium

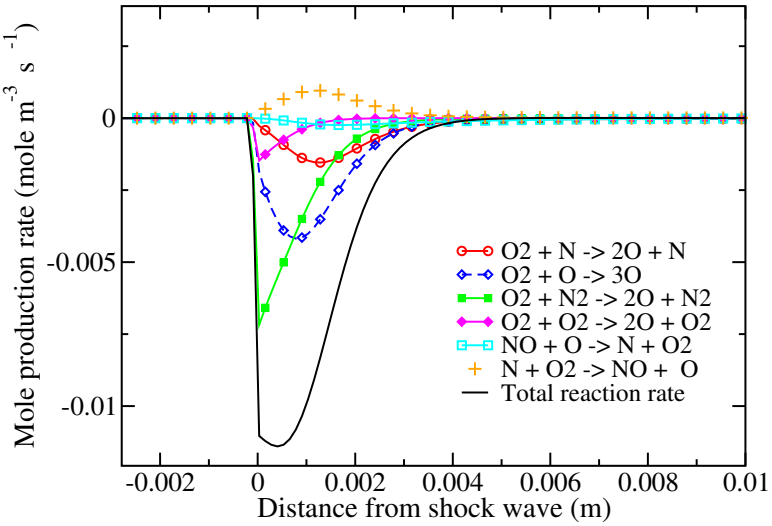

Figure 83: Mole production rate for O_2 near the shock front.

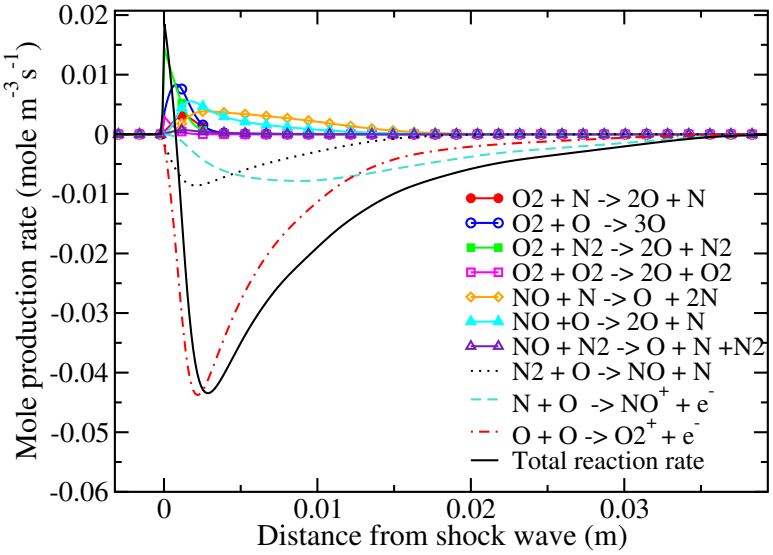

Figure 84: Mole production rate for O near the shock front.

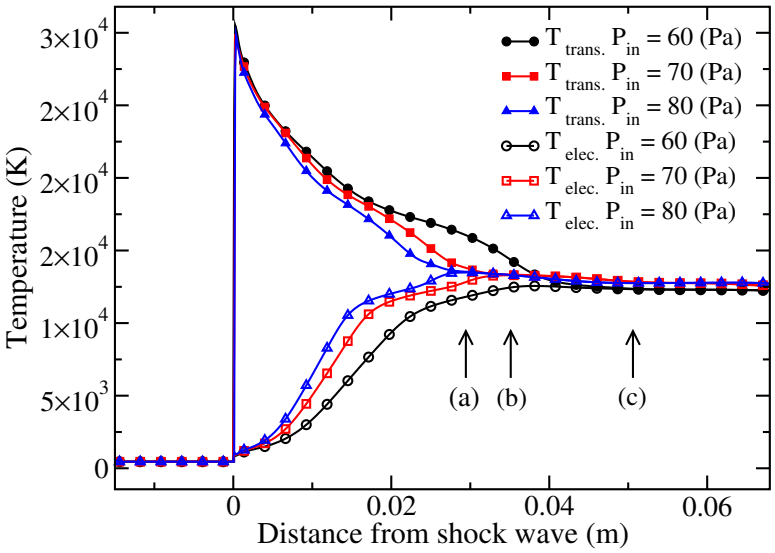

Figure 85: Pressure dependence of relaxation distance. Locations (a), (b) and (c) indicate the locations where the two temperatures equilibrate.

mole fraction of N^+, with O^+ having the next largest mole fraction, and NO^+ and N_2^+ mole fractions falling below the N_2 mole fraction. The number density of electrons and their corresponding pressures are shown in Fig. 81. To further understand the chemical kinetics occurring in the post-shock region, the reaction rates for O_2 and N_2 dissociation are plotted in Figs. 82 and 83, respectively. It is observed that in Fig. 83 that the $N_2 + O_2 \rightarrow O + O + N_2$ is very important in creating a large O atom concentration. The large O atom concentration is what triggers N_2 dissociation, and eventually creates large NO concentration and ionization of NO^+. The NO molecule ionizes relatively easily (also the O_2 molecule) as seen in Fig. 84. It is observed that the modeling of O_2 dissociation and ionization is very high important for non-equilibrium plasma generation.

Figure 85 shows the dependence of the pre-shock pressure on the relaxation distance. For each case, the shock strength is kept constant and only the pre-shock conditions are varied. The resulting post-shock pressures increase monotonically with the increase in pre-shock pressure. As expected, as the pressure is increased, the relaxation distance decreases as a result of high collision frequencies between electrons and other species. This result gives further confidence that proper trends are being captured.

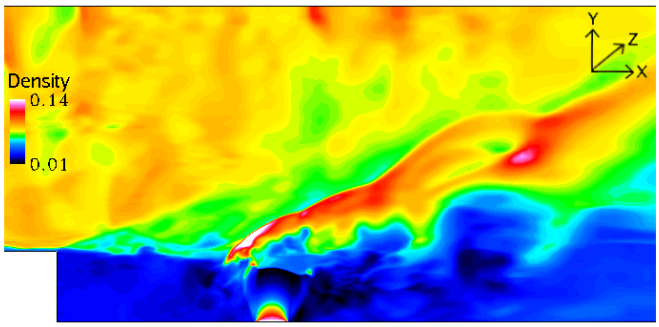

(a)

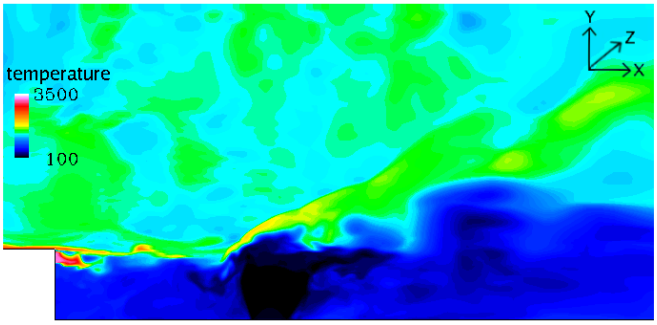

(b)

Figure 86: Instantaneous flow field for Case 2 (a) density contour and (b) temperature contours.

7.4.2.2 Scramjet combustor

Figures 86 (a)-(b) show representative snapshots of the density and temperature fields for Case 1. Part of the jet shock structure, the barrel shock and the Mach disk are seen, as well as the jet/freestream interface following behind the bow shock. There are two types of recirculation zones formed by the fuel injector: one is between the fuel injector and the step, and the other one is in the wake region of the fuel injector. The first recirculation plays an important role in holding the flame by maintaining a zone of hot products and has a positive impact on SCRAMJET combustion since it pushes the shear-layer upward resulting in an increase in the fuel penetration distance. The eddies formed there cause an

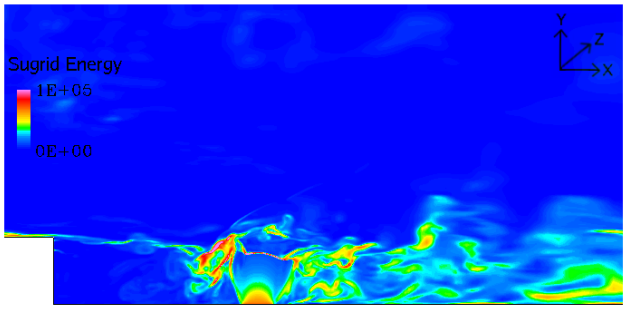

(a)

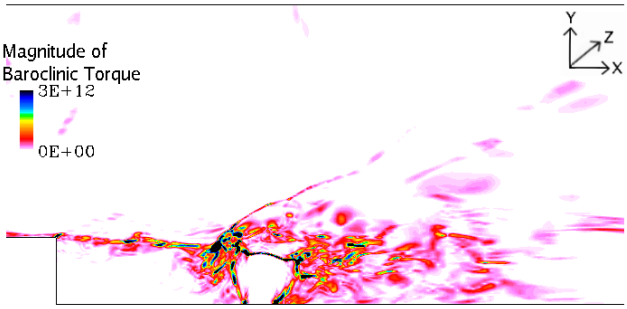

(b)

Figure 87: Contours of (a) subgrid kinetic energy and (b) magnitude of baroclinic torque for Case 2.

unsteady feature in the shear-layer and may cause additional total pressure loss. It is seen in Fig. 86(b) that the hot jet from the vertical wall is partially entrained by these eddies into the recirculation region. These hot products are expected to be entrained downstream and initiate combustion. The other recirculation zone remains unburnt due to low the temperatures in this region. The high density region seen in Fig. 86 (a) is formed above the Mach disk due to the compression waves where the vertical velocity of fuel injector is attenuated by the interaction with the shear-layer. Behind these compression waves, strong turbulent motions are seen. The corresponding cases with plasma injection (Cases 2-5) show qualitatively similar overall features (not shown). There is, however, a significant difference in the distribution of radical species, and this is discussed further below.

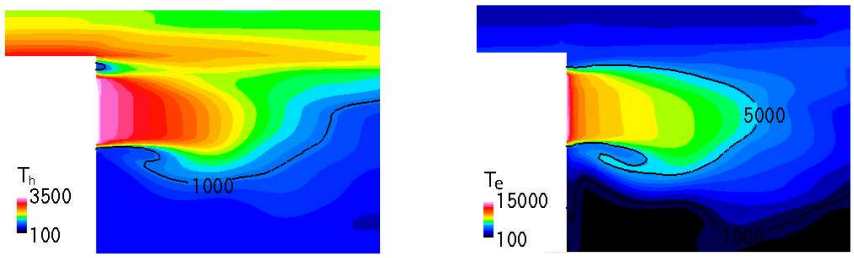

(a) (b)

Figure 88: Contours of (a) the heavy particle temperature and (b) electron temperature near the plasma injector for Case 2.

Figures 87 (a)-(b) show respectively, the representative instantaneous snapshots of the subgrid kinetic energy, k^{sgs} and magnitude of baroclinic torque for Case 3. Here, the baroclinic torque is defined as $\frac{1}{\bar{\rho}^2}\nabla\rho \times \nabla p$. The k^{sgs} contour in Fig. 87(a) show the level of subgrid turbulence in the domain. Also, since k^{sgs} is used for closure of the the reaction rate in the EBU-LES model, it gives some insights about how turbulent mixing occur affects the chemical kinetics. As seen in Fig. 87(a), compared to the large value of k^{sgs} behind the bow shock, k^{sgs} remains small inside the recirculation region. An additional force may be required to enhance mixing (98) in this area. The contour of baroclinic torque shown in Fig. 87(b) is a mirror of the k^{sgs} profile because both are related to the turbulent motion. The only difference is that the profile of baroclinic torque has a more localized feature than the k^{sgs} profile. Since this torque carries additional vorticity, this can effectively enhance mixing in the small scales, but unlike the previous studies with the equilibrium plasma arc (98), the non-equilibrium plasma jet does not significantly contribute to the enhancement of baroclinic torque. This is an important difference.

Figures 88(a)-(b) show $\tilde{T}_h$ and $\tilde{T}_e$ near the plasma injector for Case 2, respectively. It is seen that $\tilde{T}_e$ immediately drops below $10,000\ K$ after the plasma is injected due to the energy transfer through binary collisions and by dissociation of O_2, N_2 and H_2 and ionization reactions. Below $10,000\ K$, $\tilde{T}_e$ gradually drops mainly due to the binary collisions since inelastic collision cross sections significantly fall off at low electron temperatures. On the

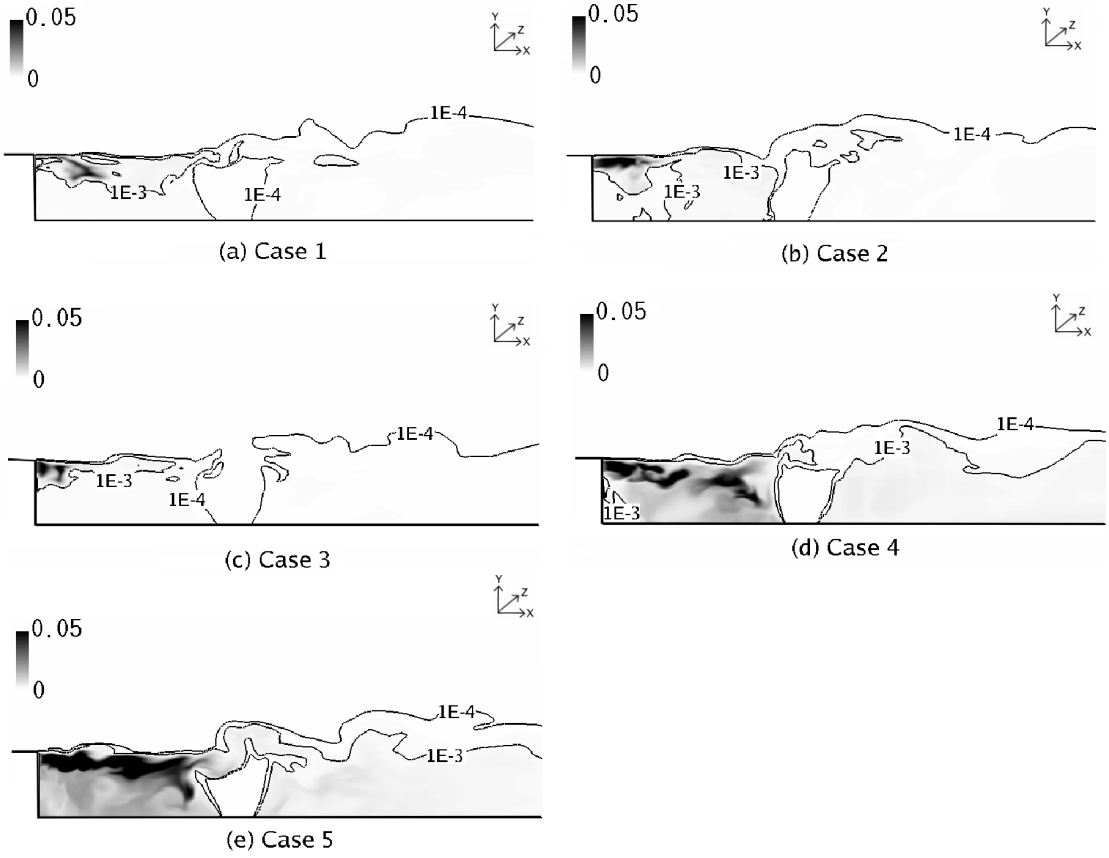

Figure 89: O mass fraction fields for Case 1-5.

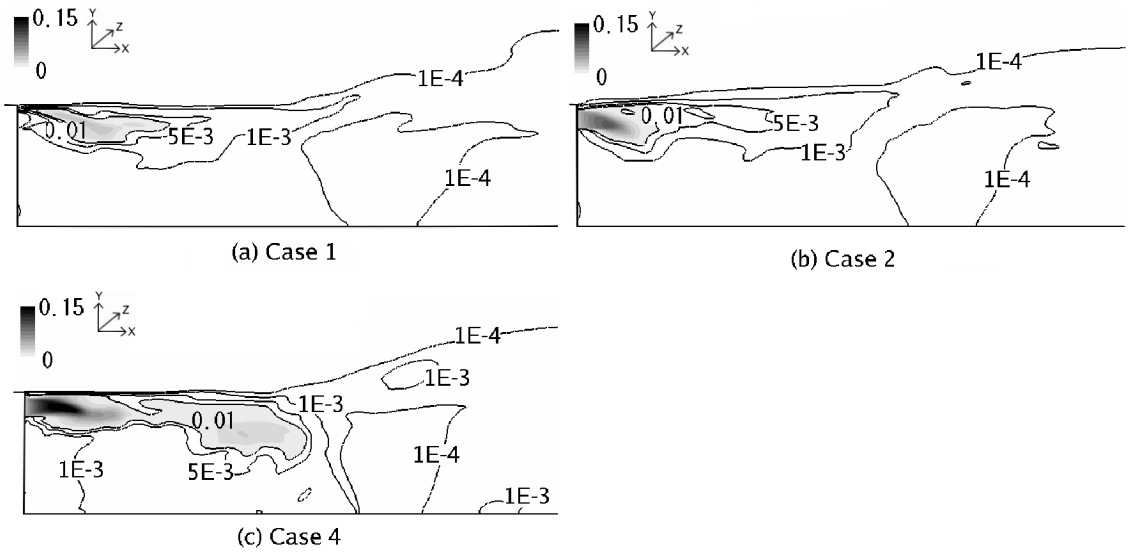

Figure 90: OH mole fraction fields for different electron density in the plasma injection: (a) Case 1 (no plasma jet), (b) Case 2 and (c) Case 4.

other hand, $\tilde{T}_h$ decreases slowly and merges into the hot shear-layer downstream. However, a rapid drop in $\tilde{T}_h$ from $3,500\ K$ to $3,000\ K$ near the plasma injector is seen. This is associated with the chemical non-equilibrium effect. The relaxation distance for the heavy particle and electron temperatures is of the order of millimeters. This is reasonable considering the low pressures inside the recirculation zone.

Figures 89(a)-(e) show mass fraction contours of O for Cases 1-5. Compared to the case with no plasma injection (Case 1), all cases with plasma injection show an increase in O concentration except Case 3. In this case even though it was expected that the oscillating injector would cause the shear layer to be perturbed resulting in the enhancement of mixing, the effect is limited to the near field of the injector, and therefore, the overall result is similar to Case 1. The influence of the injector becomes significant when the electron density is raised (Cases 4 and 5), which is as expected. The relatively high O ($\sim 10^{-3}$) observed in the wake region of the fuel injector is due to the entrainment from the radical pool formed between the step and the fuel injector. With the applied external fields (Case 5), the Ohmic heating keeps $\tilde{T}_e$ high and additional production of radicals occur. The Lorentz force is not noticeable because the electrical conductivity is only appreciable near the injector and is

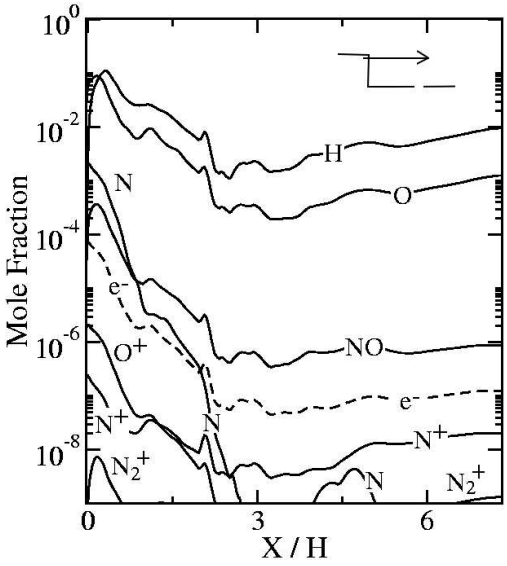

Figure 91: Mole fraction of minor species along the centerline at Y/H = 2.5 where the center of the plasma injector is located.(see inset)

orders smaller inside the shear-layer. This observation suggests that it is necessary to increase the ionization fraction of the flow in order to have appreciable MHD control. Also, because of the low electrical conductivity (e.g., large magnetic diffusivity), the induced magnetic field is more than five orders of magnitude smaller than the imposed magnetic field. This observation is consistent with the fact the magnetic Reynolds number based on the channel height and the inflow velocity is much less than unity.

In order to see the dependence of OH concentration on the electron densities, representative time-averaged snapshots of OH for Case 1, Case 2 and Case 4 are shown in Figs. 90 (a)-(c), respectively. In hydrogen combustion kinetics (32), there are three reactions to produce OH: (1) $O_2+H_2 \rightarrow OH+OH$, (2) $O+H_2 \rightarrow OH+H$, and (3) $H+O_2 \rightarrow OH+O$. Without the plasma injector, the OH concentration starts to rise at some distance away from the hot injector, since O and H concentration is not sufficient. Therefore, the main reaction mechanism to produce OH is seemingly the reaction (1). At the bottom part of the recirculation region, OH concentration is quite low. Therefore, the rise in OH is due to the high-temperature injection gas, and is limited inside the shear layer. With plasma injection, a high concentration of OH is observed near the injector resulting from reactions

(2) and (3), in addition to (1). In fact, large amount of H and O species created through electron dissociation is observed in Fig. 91 (see Table 2). For Case 2, high OH concentration is seen only near the shear layer region similar to Case 1, and the effect of the plasma jet is limited. Overall, profiles for Case 1 and Case 2 are similar downstream. On the other hand, relatively uniform distribution is achieved for Case 4 between the step and the fuel injector. Considering the O profile (see Fig. 89 (d)), this uniform distribution of OH is significantly due to the large radicals concentration created by the plasma jet.

Finally, Fig. 91 shows the mole fractions of minor species along the centerline at the injector height for Case 2. The large concentration of electrons indicate the location of the plasma injector at $X/H = 0$. At the plasma injector, large amount of H and O resulting from the H_2 and O_2 dissociation reactions are seen as well as other radicals including ions (O^+, N^+, and N_2^+). These charged species recombine instantly downstream. Also, N drops significantly since the electronic dissociation reaction of N_2 has a strong electron temperature dependency (See Fig. 88(b)). On the other hand, relatively large amount of H and O species remain downstream. These long-lived radicals can possibly contribute to reduce ignition delay in a SCRAMJET.

CHAPTER VIII

CONCLUSIONS

The main accomplishment of this thesis was to develop a LES model for MHD turbulence that is easily implemented to a well-established non-MHD solver. The unique feature of this model is that the six model coefficients are computed dynamically, and thus, are not *ad hoc* adjustable model parameters. To determine the performance of this model, several simulations are carried out. The structure of MHD turbulence is examined by comparing DNS and LES results for energy and dissipation spectra. Also, the time variation of ideal invariants is also investigated. For the case with frame rotation, the energy decay rate in the presence of magnetic field is steeper because frame rotation enhances Joule dissipation. The current study also suggests that there exists a critical R_o beyond which phase scrambling due to the Coriolis force dominates the enhancement of Joule dissipation by rotation. Finally, it is shown that the new dynamic subgrid model is capable of accurately capturing the MHD turbulence within the LES context. Since there is no requirement of low magnetic Reynolds number assumption in the formulation of this model, the model can be adapted to study a wide variety of physical problems.

This MHD LES model is first used to model an equilibrium argon plasma. To capture/model electrical discharges is essential for accurately modeling a plasma assisted combustion. Therefore, a large portion of the thesis is also devoted to investigate electrical discharge modeling and its validation. The effect of cross flow, external field and turbulent inflow are investigated. Important observations from these studies are following. The effects of cross flow and external fields significantly effect the arc structure. Since MHD pumping results from a balance of Lorentz force around the cathode, these effects readily cause a disturbance in the balancing of the forces and alter the structure of the arc column. If an external field is applied in y-direction, a component of the Lorentz force in the azimuthal direction appears and confines the arc thus straightening the distorted arc caused

by the cross-flow velocity. When turbulence is introduced into the cross-flow velocity, it is observed that the turbulent structures are smoothed out near the arc due to thermal expansion laminarizes the downstream flow. However, the fluctuations of the incoming flow results in an unbalance of the Lorentz force near the cathode and causes the arc to swing back and forth. As a result of this change in arc column length, the electric potential varies significantly. Turbulent mixing effects are not appreciable at the low turbulent incoming velocities modeled here.

Finally, this model is used to model plasma-assisted combustion in a SCRAMJET. To consider high temperature chemical kinetics, a detailed kinetic model containing 16 species and 76 reactions are solved using a two-temperature approach. As a validation. the LES conservation equations for heavy particles with an electron energy equation is initially evaluated in a shock tube test case. Reasonable chemical non-equilibrium effects were obtained. Using this H_2/Air chemistry, two types of plasmas, an equilibrium plasma (arc) and non-equilibrium plasma jet, are investigated in SCRAMJET configuration. For the case with an equilibrium plasma, the plasma source in the recirculating zone is shown to control and enhance fuel-air mixing. It is observed that an electrical discharge creates a high temperature and a radical rich concentration region in the recirculation zone that aids in ignition and flame-holding. When an uniform magnetic field is applied, mixing is significantly enhanced since the shock structure ahead of the fuel jet is weakened and fuel penetration into the air cross flow is increased. Moreover, the distribution of the radical species inside the recirculation zone is highly uniform, and the reduction of ignition delay is observed. The total pressure loss from introducing the arc is not significant.

For the non-equilibrium plasma injector case, the results indicate that the non-equilibrium plasma jet produces radicals such as O and H in sufficient amount resulting in an increase in OH concentration. This is a strong indication for this type of the plasma to have the ability to reduce ignition delay time. However, the mixing in the recirculation zone is no enough to see uniform distributions of such radicals, and as a result, the recirculation region remains unburnt. Overall this newly developed MHD-LES approach has provided a well-validated numerical code to aid in the development of plasma and discharge application in

aerospace sciences. This thesis highlights a few of these applications, but the approach of this MHD-LES model could be adequately used to study a wide range of MHD phenomena such as MHD electrical thruster, astrophysical, and fusion plasmas.

CHAPTER IX

FUTURE RECOMMENDATIONS

The comprehensive model developed in this study has been carefully validated in each module and has demonstrated the ability of this code to describe the physics of plasma-assisted combustion in a SCRAMJET giving us insight into such a complicated system. However, there is some room for modification. In this section, drawbacks of the current code are addressed and further studies to improve this model are proposed.

9.1 MHD LDKM

Even though the formulation of this LES model for MHD turbulence is for compressible flow applications, there is no test done in this studies to show its capability to capture compressibility. The governing equation of the subgrid magnetic energy equation contains a term related to the compressibility:

$$k^{sgs,b}\frac{\partial \tilde{u}_j}{\partial x_j} \tag{127}$$

Therefore, if compression (ρ increases) locally occurs, $k^{sgs,b}$ increases. It would be interesting to introduce the following relationship. Along a field line (131), $\rho|dr| = |B|$ is hold where dr is the element of a line of moving fluid particles. Even though this simple relationship is derived from the incompressible formulation, it gives a hint to understand MHD turbulence. For compressible flow, density increases, and as a result the magnetic field is intensified. Therefore, it is reasonable the relevant subgrid kinetic energy also increases. On the other hand, for incompressible flow, $|dr| \propto |B|$ is always true. This is a stretching effect of a motion and is similar to the stretching effect caused by vorticity. These effects should be successfully modeled in this current model, and thus, it is worthy of testing this model in predicting a system where compressibility dominates such as shock interaction with magnetic fields in an ionized flow.

9.2 High temperature chemical kinetics

The main drawback of this current model is coming from the use of experimental data related to the thermal properties of gas (air, H_2 and argon). For the case with mono-atomic gas, it is relatively simple to evaluate all thermal properties based on basic thermodynamics and quantum physics by introducing a partition function. However, when a system of combustion takes place, it becomes rather complicated to describe all species information with theoretical expressions. Since in a high temperature system, it is necessary to determine intermediate energy states of all species and obtain accurate distribution of energy over the available energy state.

9.3 Discharge model

The current model solves the Poisson equation to obtain the current field related to the arc discharge. This is based on the assumption that there is no spatial charge separation. However, in reality, it is known that the sheath region is formed near the electrodes count for the mobility difference between an electron and a heavy ion. Due to the presence of the sheath region where a substantial electric potential exits, the actual gradient of electric potential along an arc column is smaller than what this current code calculates. This implies that the calculated temperature near electrodes is probably under-estimated. This assumption may be acceptable in a relatively high-pressure discharge case where the sheath region becomes negligibly thin. Also, an ignition part is ignored by assuming that a cold gas has finite electrical conductivity. Note that a gas starts to have finite electrical conductivity after the actual ignition occurs. Ignorance of modeling the ignition phenomena does not have a significant influence on the final structure of arc column, however, the current code does not have a capability to model a high-frequency unsteady electrical discharge that may be interesting for our future applications.

9.4 Computational cost/Performance

Computational expense is another main drawback of the current code. This is coming from the following reasons, (1) implicit calculation of diffusion term in MHD equations,

(2) solving the Poisson equations of a magnetic vector potential and an electrical potential, (3) many species required for detail high-temperature chemistry and (4) additionally solving the induction equation using a finite element method. In the current effort, a three-dimensional parallel multigrid scheme has been implemented, and it has drastically reduced the computational cost resulting from (1) and (2). However, (3) and (4) still remain issues to be resolved. In modeling a SCRAMJET combustor, it is not necessary to solve the induction equation since the induced magnetic field is smaller in several orders magnitude than the imposed external fields. Therefore, it must be adequate to solve induction equations only in the region where the electrical conductivity is finite. (Where it is very small, a diffusion process of magnetic field is significant, and as a result, the induced magnetic field smooths out immediately.) In addition to necessity of detail chemistry, it may be required to track information of energy distribution over energy modes (kinetic, rotation, vibration, electric excitation) for each species in a non-equilibrium plasma calculation. This brings in additional computational load.

9.5 Recommended future work

Considering the aforementioned drawbacks of the current code, I recommend some future works. First of all, it is really interesting to see the capability of the MHD LDKM solver to capture the dynamo effect by which small turbulent motions effect large scale motions. Therefore, to use the code to the large Reynolds/magnetic Reynolds number plasma flow typically seen in astrophysical applications is preferable. Note in such applications, an implicit calculation of diffusion term in MHD equation is not necessary due to the small magnetic diffusivity. Typical such applications include solar/earth dynamo, alpha-effect quenching *et al.*

To improve the discharge model, simple sheath model should be implemented by solving the continuity equations for electron, ions, and metastables like (121). In such a formulation, the spatial charge difference can be captured by considering each species flux at the top boundary of the sheath, and the electric field inside the sheath region is calculated by solving the Poisson equation there. With such a sheath model, an ignition process is automatically

included.

For further investigation of SCRAMJET with equilibrium/non-equilibrium plasma, I recommend the use of other types of plasma such as laser spark, nanosecond pulse discharge, corona *et al.* As mentioned in the introduction, each method has advantages and disadvantages and contribute to the SCRAMJET performance differently. To clarify which plasmas do best and how plasmas are introduced for optimizing the performance can provide variable information for designing next generation SCRAMJET engines. For this purpose, we need a solid understanding of mechanisms of plasmas in atmospheric pressure. In the current model, the step height is set to be 3^{mm} based on the experimental setup. However, from the practical viewpoint, this is too small. With a larger step height, it is not feasible to generate arc between the top wall and the bottom wall of the SCRAMJET configuration studied here. Therefore, it is recommened to consider the same geometry with the larger scale being comparable to actual applications. One of our interests in this study is how to enhance fuel/air mixing by the barocliniq torque. It has been shown that the magnitude of the barocliniq torque is greatly enhanced by the introduction of equilibrium plasma. But it is recommened to perform quantitative analyses of the efficiency of the mixing related to the barocliniq torque and to clarify the effect of this torque.

9.6 Code limitations and critical assumptions

For future users of this code, I would like to address the critical assumptions to be used in the current model and wish them to be relaxed as a part of future work.

9.6.1 MHD LDKM

• Electric conductivity is treated as a scaler. It can be a tensor for some cases where there is a strong magnetic fields.

• Some subgrid terms such as $\sigma_i^{sgs,v}$, $S^{sgs,b}$, and $d_{ij}^{sgs,b}$ are neglected.

• The case with strong compressibility effect is not studied.

• Only periodic boundary conditions are used.

• Because of usage of constrained transport scheme, only Cartesian grid can be used.

9.6.2 Discharge model

• Rectangular shape is used to represent a cathode tip.

• No sheath model is implemented.

• Evaporation of electrodes material are neglected.

• Ignition is not modeled. Finite electric conductivity is initially assumed.

• Simple radiation model based on experimental data is used.

• Constant temperature is assumed at electrodes and solid surfaces.

9.6.3 High temperature chemistry and non-equilibrium plasma

• No intermediate species

• Thermal properties are calculated based on experimental data for air/argon.

• It is questionable to use two-temperature model for low temperature (below 3000 K). In the current model, we use 7 step mechanisms.

• Only 76 reactions and 16 species are considered.

• We assume that translational temperature is same as rotational temperature, and that vibrational temperature and electron temperature.

• Electric excitation state of an electron is not considered.

• Collision rates of ions are assumed to be the same as its atoms/molecules.

APPENDIX A CHEMICAL KINETICS

Table 10: Reaction rate coefficients for high-temperature air for $k_f = CT_x^n \exp(-T_d/T_x)$ and $T_a = \sqrt{TT_e}$

Reaction	M	T_x	C	n	T_d
Dissociation Reactions					
$N_2 + M \rightarrow N + N + M$	N	T_a	3.0×10^{22}	-1.60	$113,200$
	0		3.0×10^{22}		
	H		3.0×10^{22}		
	N_2		7.0×10^{21}		
	O_2		7.0×10^{21}		
	H_2		7.0×10^{21}		
	NO		3.0×10^{22}		
	N^+		3.0×10^{22}		
	O^+		3.0×10^{22}		
	H^+		3.0×10^{22}		
	N_2^+		7.0×10^{21}		
	O_2^+		7.0×10^{21}		
	H_2^+		7.0×10^{21}		
	NO^+		7.0×10^{21}		
	e^-	T_e	1.2×10^{25}		
$O_2 + M \rightarrow O + O + M$	N	T_a	1.0×10^{22}	-1.50	$59,500$
	0		1.0×10^{22}		
	H		1.0×10^{22}		
	N_2		2.0×10^{21}		
	O_2		2.0×10^{21}		
	H_2		2.0×10^{21}		
	NO		2.0×10^{22}		
	N^+		1.0×10^{22}		
	O^+		1.0×10^{22}		
	H^+		1.0×10^{22}		
	N_2^+		2.0×10^{21}		
	O_2^+		2.0×10^{21}		
	H_2^+		2.0×10^{21}		
	NO^+		2.0×10^{21}		
$H_2 + M \rightarrow H + H + M$	N	T_a	2.2×10^{14}	0.00	$48,300$
	0		2.2×10^{14}		
	H		2.2×10^{14}		
	N_2		2.2×10^{14}		
	O_2		2.2×10^{14}		
	H_2		5.5×10^{14}		

continued from above ...

Reaction	M	T_x	C	n	T_d
Dissociation Reactions					
$H_2 + M \rightarrow H + H + M$	NO	T_a	2.2×10^{14}	0.00	$48,300$
	N^+		2.2×10^{14}		
	O^+		2.2×10^{14}		
	H^+		2.2×10^{14}		
	N_2^+		2.2×10^{14}		
	O_2^+		2.2×10^{14}		
	H_2^+		2.2×10^{14}		
	NO^+		2.2×10^{14}		
$NO + M \rightarrow N + O + M$	N	T_a	1.1×10^{17}	0.00	$75,500$
	0		1.1×10^{17}		
	H		1.1×10^{17}		
	N_2		5.0×10^{15}		
	O_2		5.0×10^{15}		
	H_2		5.0×10^{15}		
	NO		1.1×10^{17}		
	N^+		1.1×10^{17}		
	O^+		1.1×10^{17}		
	H^+		1.1×10^{17}		
	N_2^+		5.0×10^{15}		
	O_2^+		5.0×10^{15}		
	H_2^+		5.0×10^{15}		
	NO^+		5.0×10^{15}		
Recombination Reactions					
$O_2^+ + e^- \rightarrow O + O$	–	T	1.9×10^{17}	-0.70	0.00
$N + O + M \rightarrow NO + M$	N	T_a	1.1×10^{-7}	-0.50	0.00
	0		1.1×10^{-7}		
	H		1.1×10^{-7}		
	N_2		1.1×10^{-7}		
	O_2		1.1×10^{-7}		
	H_2		1.1×10^{-7}		
	NO		1.1×10^{-7}		
	N^+		1.1×10^{-7}		
	O^+		1.1×10^{-7}		
	H^+		1.1×10^{-7}		
	N_2^+		1.1×10^{-7}		
	O_2^+		1.1×10^{-7}		
	H_2^+		1.1×10^{-7}		
	NO^+		1.1×10^{-7}		

continued from above ...

Reaction	M	T_x	C	n	T_d
NO Exchange Reactions					
$NO + O \rightarrow N + O_2$	–	T	8.4×10^{12}	0.00	19,450
$N_2 + O \rightarrow NO + N$	–	T	6.4×10^{17}	−1.00	38,400
Associative Ionization Reactions					
$N + O \rightarrow NO^+ + e^-$	–	T	8.8×10^{8}	1.00	31,900
$O + O \rightarrow O_2^+ + e^-$	–	T	8.4×10^{2}	2.70	80,600
$N + N \rightarrow N_2^+ + e^-$	–	T	8.4×10^{7}	1.50	67,500
Charge Exchange Reactions					
$NO^+ + O \rightarrow N^+ + O_2$	–	T	1.0×10^{12}	0.50	77,200
$N^+ + N_2 \rightarrow N_2^+ + N$	–	T	1.0×10^{12}	0.50	12,200
$O_2^+ + N \rightarrow N^+ + O_2$	–	T	8.7×10^{13}	0.14	28,600
$O^+ + NO \rightarrow N^+ + O_2$	–	T	1.4×10^{5}	1.90	26,600
$O_2^+ + N_2 \rightarrow N_2^+ + O_2$	–	T	9.9×10^{12}	0.00	40,700
$O_2^+ + O \rightarrow O^+ + O_2$	–	T	4.0×10^{12}	−0.09	18,000
$NO^+ + N \rightarrow O + +N_2$	–	T	3.4×10^{13}	−1.08	12,800
$NO^+ + O_2 \rightarrow O_2^+ + NO$	–	T	2.4×10^{13}	0.41	32,600
$NO^+ + O \rightarrow O_2^+ + N$	–	T	7.2×10^{12}	0.29	48,600
$O^+ + N_2 \rightarrow N_2^+ + O$	–	T	9.1×10^{11}	0.36	22,800
$NO^+ + N \rightarrow N_2^+ + O$	–	T	7.2×10^{13}	0.00	35,9500
Electron-Impact Ionization Reactions					
$O + e^- \rightarrow O^+ + e^- + e^-$	–	T_e	3.9×10^{33}	−3.78	158,500
$N + e^- \rightarrow N^+ + e^- + e^-$	–	T_e	2.5×10^{34}	−3.82	168600
$H + e^- \rightarrow H^+ + e^- + e^-$	–	T_e	2.2×10^{30}	−2.80	157800

Table 11: Parameters for equilibrium constants for high-temperature air of $k_e = \exp\left[A_1/Z + A_2 + A_3 \ln(Z) + A_4 Z + A_5 Z^2\right]$, where $Z = 10000/T$

Reaction	A_1	A_2	A_3	A_4	A_5
$N_2 + M = N + N + M$	−3.292682	0.998998	−8.237028	−5.526183	−0.582174
$O_2 + M = O + O + M$	1.578640	2.688744	4.215573	−8.091354	0.174260
$H_2 + M = H + H + M$	1.817328	1.202335	4.427498	−7.574115	0.185211
$N_2 + e^- = N + N + e^-$	−3.292682	0.998998	−8.237028	−5.526183	−0.582174
$O + e^- = O^+ + e^-$	0.614124	−6.755241	−0.774319	−16.003456	0.005502
$N + e^- = N^+ + e^-$	0.200588	−3.965871	−0.041731	−18.063001	0.125939
$H + e^- = H^+ + e^-$	−0.192097	−6.276289	−1.903784	−15.510915	−0.025936
$N_2 + O = NO + N$	−3.032189	0.078468	−7.693047	1.153872	−0.238985
$NO + O = O_2 + N$	−1.840133	−1.768215	−4.759554	1.153872	−0.268345
$O + N = NO^+ + e^-$	3.429239	−7.431449	6.012721	−8.276563	0.503539
$N + N = N_2^+ + e^-$	−0.062523	−5.822935	−0.924052	−8.136642	0.188105

Table 12: Reaction rate coefficients for hydrogen-air mechanism of $k_f = CT^n \exp T_d/T$ with $M_1 = 2.5H_2 + 12.0H_2O + O_2 + N_2$ and $M_2 = H_2 + 6.5H_2O + 0.4O_2 + 0.4N_2$.

Reaction	C	n	T_d
$H_2 + O_2 \rightarrow OH + OH$	1.70×10^{13}	0.0	24245
$H + O_2 \rightarrow OH + O$	1.42×10^{14}	0.0	8258
$OH + H_2 \rightarrow H_2O + H$	3.16×10^{7}	1.8	1525
$O + H_2 \rightarrow OH + H$	2.07×10^{14}	0.0	6923
$OH + OH \rightarrow H_2O + O$	5.50×10^{13}	0.0	3524
$H + OH \rightarrow H_2O + M_1$	2.21×10^{22}	-2.0	0.0
$H + H \rightarrow H_2 + M_2$	6.53×10^{17}	-1.0	0.0

Bibliography

[1] Agullo, O., Müller, W.-C., Knaepen, B., and Carati, D., "large eddy simulation of decaying magnetohydrodynamics turbulence with dynamic subgrid-modeling," *Physics of Plasma*, vol. 8, pp. 3502–3505, 2001.

[2] Andrews, E. H. and Mackley, E. A., "Review of nasa's hypersonic research engine project," *AIAA Paper 93-2323*, 1994.

[3] Anikin, N. B., Mintoussov, E. I., Pancheshnyi, S., Roupassov, D., Sych, V. E., and Starikovskii, A. Y., "Nonequilibrium plasmas and its applications for combustion and hypersonic flow control," *AIAA-2003-1053: 41th AIAA Aerospace Sciences Meeting and Exhibit, January 9-12, Reno, NV*, vol. 5, pp. 23–38, 2003.

[4] Bauchire, J. M., Gonzalez, J. J., and Gleizes, A., "Modeling of a dc plasma torch in laminar and turbulent flow," *Plasma Chemistry and Plasma Processing*, vol. 17, pp. 409–432, 1997.

[5] Becker, R., *Electromagnetic fields and interactions*. Dover Publications Inc, New York, 1964.

[6] Ben-Yakar, A. and Hanson, R. K., "Supersonic combustion of cross-flow jets and influence of cavity flame-holdings.," *AIAA-1999-0484: 37th AIAA Aerospace Sciences Meeting and Exhibit, January 11-14, Reno, NV*, 1999.

[7] Benenson, D. M., Baker, A., and Cenkner, A. A., "Diagnostics on steady-state cross-flow arcs," *IEEE Transactions on Power Apparatus and Systems*, vol. 88, pp. 513–521, 1969.

[8] Billing, F. and Jacobsen, L., "Comparison of planar and axisymmetric flowpaths for hydrogen fueled space access vehicles.," *AIAA Paper 03-4407*, 2003.

[9] Bini, R., Monno, M., and Boulos, M. I., "Numerical and experimental study of transferred arcs in argon," *Journal of Physics D*, vol. 39, pp. 3253–3266, 2006.

[10] Biskamp, D. and Müller, W.-C., "Scaling properties of three-dimensional isotropic magnetohydrodynamic turbulence," *Physics of Plasmas*, vol. 7, pp. 4889–4900, 2000.

[11] Boulos, M. I., Faucchais, P., and Pfender, E., *Thermal plasma: Fundamentals and Applications, Vol.1*. Plenum Publishing Corporation,New York, Cambridge, 1994.

[12] Bozhenkov, S., Starikovskaia, S., and Starikovskii, A, Y., "Nanosecond gas discharge ignition of h2 and ch4-constaining mixtures.," *Combustion and Flame*, vol. 133, pp. 133–146, 2003.

[13] Brackbill, J. U. and Barnes, D., "The effect of nonzero $\bigtriangledown \cdot b = 0$ on the numerical solution of the magnetohydrodynamic equations," *Journal of Computational Physics*, vol. 35, pp. 426–, 1980.

[14] Brandt, A., "Multi-level adaptive solutions to boundary value problems," *Mathematics of Computation*, vol. 31, pp. 333–390, 1977.

[15] Brovkin, V. G. and Kolesnichenko, Y., "Structure and dynamics of stimulated microwave gas discharge in wave beams," *Journal of the Moscow Physical Society*, vol. 5, pp. 23–38, 1995.

[16] Calcote, H. and Berman, C., "Increased methane-air stability limits by a dc electric field," *in Fossil Fuel Combustion symposium, Huston, TX*, vol. 25, pp. 25–31, 1989.

[17] Carleton, F. and Vince, I.M.and Weinberg, F., "Energy and radical losses from plasma jet igniters to solid surfaces.," *19th Symposium on Combustion/The Combustion Institute.*, pp. 1523–1531, 1983.

[18] Cattaneo, Y. and Vainshtein, S., "Suppression of turbulent transport by a weak magnetic field," *Astrophysical Journal Letter*, vol. 376, pp. 21–24, 1991.

[19] Caunt, S. E. and Korpi, M. J., "A 3d mhd model of astrophysical flows: Algorithms, test and parallelisation," *Astronomy and Astrophysics*, vol. 369, pp. 706–728, 2001.

[20] Chase, R. L. and Tang, M. H., "A history of the nasp program from the formation of the joint program office to the termination of the hystp scramjet performance demonstration program," *AIAA Paper 95-5173*, 1994.

[21] Chids, R.E. and. Caruso, S. C., "On the accuracy of turbulent base flow prediction," *AIAA Paper 87-1939*, 1987.

[22] Chintala, N., Bao, A., Lou, G., and Admovich, I., "Measurements of combustion efficiency in nonequilibrium rf plasma-ignited flows.," *Combustion and Flame*, vol. 144, pp. 744–756, 2006.

[23] Correa, S. M. and Warren, R., "Supersonic suddenexpansion flow with fluid interaction: an experimental and computational study," *AIAA Paper 89-0389*, 1989.

[24] Cuuran, E. T., Heiser, W. H., and Pratt, D. T., "Fluid phenomena in scramjet combustion system," *Annual Review of Fluid MechanicsJournal of Fluid Mechanics*, vol. 28, pp. 323–360, 1996.

[25] Cuuran, E. T. and Murthy, S. N., *Scramjet Propulsion*. Progress in Astronoutics and Aeronautics, AIAA, Washington, DC, 2001.

[26] Davidson, P. A., *An introduction to magnetohydrodynamics*. Cambridge University Press, Cambridge, 2001.

[27] Drayna, T., Nompelis, I., and Candler, G., "Hypersonic inward turning inlet:design and optimization.," *AIAA Paper 2006-297*, 2006.

[28] Dutton, J., Herrin, J. L., Molezzi, T., and Smith, K. M., "Recent progress on high speed separated base flows," *AIAA Paper 93-0472*, 1993.

[29] Ebrahimi, H., "Cfd validation and evaluation for reacting flow," *AIAA Paper 95-0735*, 1995.

[30] Ebrahimi, H., Gaitode, D. V., and Malo-Molina, F., "Simulations of hydrocarbon-based scramjet combustors with integrated inward-turning inlets.," *AIAA-2008-1063: 46th AIAA Aerospace Sciences Meeting and Exhibit, January 7-10, Reno, NV*, 2008.

[31] Eklund, D. R., Baurle, R. A., and Gruber, M. R., "Numerical study of a scramjet combustor fueld by an aerodyanmic ramp injector in dual-mode combustion.," *AIAA Paper 01-0379*, 2001.

[32] Eklund, D.R.and Drummond, J., Philip, J., and Hassan, H. A., "Calculation of supersonic turbulent reacting coaxial jets," *AIAA Journal*, vol. 28, pp. 1633–1641, 1990.

[33] El-Asrag, H. and Menon, S., "Large eddy simulation of bluff-body stabilized swirling non-premixed flames.," *Proceedings of the Combustion Institute*, vol. 31, pp. 1747–1754, 2007.

[34] Erkebacher, M., Hussaini, C., Spezial, G., and Zang, T., "Toward the large-eddy simulation of compressible turbulent flow," *Journal of Fluid Mechanics*, vol. 238, pp. 155–185, 1992.

[35] Erlebacher, G., Hussaini, M. Y., Speziale, C. G., and Zang, T. A., "Toward the large-eddy simulation of compressibleturbulent flows," *Journal of Fluid Mechanics*, vol. 238, pp. 155–185, 1992.

[36] Evans, C. and Hawley, J., "Simulation of magnetohydrodynamic flows: A constrained transport method," *Astrophyical Journal*, vol. 332, pp. 659–677, 1988.

[37] Evans, D. and Tankin, R. S., "Measurement of emission and absorbtion of radiation by an argon plasma.," *Physics of Fluids.*, vol. 10, pp. 1137–1144, 1967.

[38] Faulkner, R. F. and Weber, J, W., "Hydrocarbon scramjet propulsion system development, demonstration and application.," *AIAA Paper 99-4922*, 1999.

[39] Ferri, A., "Review of problems in application of supersonic combustion," *Journal of the Royal Aeronautical Society*, vol. 68, pp. 575–597, 1964.

[40] Ferri, A., "Mxing controlled supersonic combustion," *Annual Review of Fluid Mechanics*, vol. 5, pp. 301–338, 1973.

[41] Ferri, A. and Fox, H., "Analysis of fluid dynamics of supersonic combustion process controlled by miing," *Proceddings of the Twelfth International Symposium on Combustion, Combustion Inst., Pittsburgh,*, pp. 1105–1113, 1968.

[42] Fletcher, D. G. and McDaniel, J. C., "Quantitative measurement of transverse injector and free stream interaction in a nonreacting scramjet combustor using laser induced fluorescence," *AIAA Paper 87-0087*, 1987.

[43] Forsythe, J. R. and Hoffman, K. A.and Dietiker, J., "Detached-eddy simulation of a supersonic axisymmetric base flow with an unstructured solver," *AIAA Paper 00-2410*, 2000.

[44] Forsythe, J. R. and Hoffman, K. A.and Squires, K., "Detached-eddy simulation with compressibility correction applied to a supersonic axisymmetric base flow," *AIAA Paper 02-0586*, 2002.

[45] Freton, P., Gonzalez, J., and Gleizes, A., "Comparison between a two- and a three-dimentional arc plasma configuration," *Journal of Applied Physics D*, vol. 33, pp. 2442–2452, 2000.

[46] Frisch, U., Pouquet, A., Leorat, J., and Mazure, A., "Relaxation processes in a low-order three -dimensional magnetohydrodynamics model," *Journal of Fluid Mechanics*, vol. 68, pp. 769–778, 1975.

[47] Fureby, C. and Müller, S.-I., "Large-eddy simulation of reacting flows applied to bluff body stabilized flames," *AIAA journal*, vol. 33, pp. 2339–2347, 1995.

[48] Galley, D. Pilla, G., lacoste, D., Ducruix, S., Lacas, F., and Veynante, D.and Laux, C., "Plasma-enhanced combustion of a lean premixed air-propane turbulent flame using a nanosecond repetitively pulsed plasma," *AIAA-2005-0616: 44th AIAA Aerospace Sciences Meeting and Exhibit, January 10-13 , Reno, NV*, 2005.

[49] Gaston, M. J., Mudford, N., and Houwing, F., "A comparison of two hypermixing fuel injectors in a supersonic combustor," *AIAA Paper 98-0964*, 1998.

[50] Gerlinger, P., Schneider, F., and Aigner, M., "Numerical investigation of mixing enhancement by streamwise vorticity in supersonic combustion," *Proceddings of the 14th International Symposium on Air Breathing Engines, ISABE Paper 2005-1019*, pp. 453–477, 2005.

[51] Germano, M., Piomelli, P., Moin, U., and Cabot, W., "A dynamic subgrid scale eddy viscosity model.," *Center for turbulencd reseach, Proceedings of the Summer Programs*, pp. 5–17, 1990.

[52] Gonzalez, J. J., Lago, F., Freton, P., Masquere, M., and Franceries, X., "A numerical modelling of an electric arc and its interaction with the anode: part1. the three-dimensional model-influence of external forces on the arc column," *Journal of Applied Physics D*, vol. 38, pp. 306–318, 2005.

[53] Gruzinov, A. V. and Diamond, P. H., "Self-consistent mean field electrodynamics of turbulent dynamos," *Physics of plasmas*, vol. 2, pp. 1941–1946, 1995.

[54] Gupta, S., Tannehill, C., and Mehta, B., "Simulation of 3-d nonequilibrium seeded airflow in the nasa ames mhd channel," *Journal of Thermophysics and Heat Transfer.*, vol. 21, pp. 276–283, 2007.

[55] Haag, D., Auweter-Kurtz, M., Fertig, M., and Kurtz, H., "Numerical and experimental investigations of magnetoplasmadynamic thrusters with coaxial applied magnetic field," *AIAA-2006-5015, 42nd AIAA/ASME/SAE/ASEE Joint Propulsion Conference and Exhibit, Sacramento, California, July 9-12, 2006*, 2006.

[56] Halupovich, Y., Natan, B., and Rom, J., "Numerical solution of the turbulent supersonic flow over a backward facing step," *Fluid Dynamics Research*, vol. 24, pp. 251–273, 1999.

[57] Hamba, F., "One dimensional calculation of a turbulent dynamo model for reversed field pinches," *Physics of Fluids B*, vol. 2, pp. 3064–3073, 1990.

[58] Hartfield, R. J., Hollo, S. D., and McDaniel, J. C., "Planar measurement technique for compressible flow using laser induced fluorescence," *AIAA Journal*, vol. 31, pp. 483–490, 1993.

[59] Heirrmann, J. and Kurtz, M., "Numerical and experimental investiogation of the current distribution in self-field mhd thrusters," *Journal of Propulsion and Power*, vol. 21, pp. 119–127, 2005.

[60] Heller, H. H. and Bliss, D. B., "The physical mechanism of flow induced pressure fluctuations in cavities and concepts for their supression.," *AIAA paper 75-491*, 1975.

[61] Hsu, K. C., Etemadi, K., and Pfender, E., "Study of the free-bourning high-intensity argon arc," *Journal of Applied Physics*, vol. 54, pp. 1293–1301, 1982.

[62] Hueter, U., "Rocket-based combined-cycle propulsion technology for access to space applications," *AIAA paper 99-4925*, 1999.

[63] Jacquin, L., Leuchter, O., Cambon, C., and Mathieu, J., "Homogeneous turbulence in the presence of rotation," *Journal of Fluid Mechanics*, vol. 220, pp. 1–52, 1990.

[64] Katta, V. R. and Roquemore, W., "Study on trapped-vortex after bodies.," *Journal of Propulsion and Power*, vol. 14, pp. 273–281, 1998.

[65] Kawachi, T. and Watanabe, T., "The computational analysis of the anode using numerical method of thermal plasma," *Fifth world congress on Computational Mechanics, July7-12,2002,Vienna, Austria*, 2002.

[66] Keinigs, "A new interpretation of the alpha effect," *Physics of Fluids*, vol. 26, pp. 2558–2560, 1983.

[67] Keith, S. M. and Jack, R. E., "Simulation of thermal choking in a model scramjet combustor," *AIAA Paper 1999-3411*, 1999.

[68] Kelkar, M. and Heberlein, J., "Physics of an arc in cross flow," *Journal of Physics D*, vol. 33, pp. 2172–2182, 2000.

[69] Khan, O. U. and Hoffmann, K. A., "The effect of applied magnetic field on back step flows," *37th Plasmadynamics and Lasers Conference,San Francisco, CA, AIAA-2006-3237*, 2006.

[70] Kim, E., Hahm, T. S., and Diamond, P. H., "Eddy viscosity and laminarization of sheared flow in three dimensional reduced magnetohydrodynamics turbulence," *Physics of Plasmas*, vol. 8, pp. 3576–3582, 2001.

[71] Kim, W.-W. and Menon, S., "A new dynamic one-equation subgrid model for large-eddy simulation.," *AIAA-95-0356*, 1995.

[72] Kim, W.-W. and Menon, S., "An unsteady incompressible navier-stokes solver for large-eddy simulation of turbulent flows," *Int. J. Numer. Meth. Fluid*, vol. 31, pp. 983–1017, 1999.

[73] Kim, W.-W., Menon, S., and Mongia, H. C., "Large-eddy simulation of a gas turbine combustor flow," *Combust. Sci. Tech.*, vol. 143, pp. 25–62, 1999.

[74] Knaepen, B. and Moin, P., "Large-eddy simulation of conductive flows at low magnetic reynolds number," *Center for Turbulence Reserach Annual Reserach Briefs*, pp. 297–306, 2003.

[75] Kobayashi, H., "Large eddy simulation of magnetohydrodynamics turbulent channel flows with local subgrid scale model based on coherent structure," *Physics of Fluids B*, vol. 18, p. 045107, 2006.

[76] Kobayashi, H., "Large eddy simulation of magnetohydrodynamic turbulent duct flows," *Physics of Fluids B*, vol. 20, p. 015102, 2008.

[77] Kodera, M., Sunami, T., and Scheel, F., "Numerical study on the supersonic mixing enhancement using streamwise vortices.," *AIAA 2002-5117, 11th AIAA/AAAF International Conference Space Planes and Hypersonic Systems and Technologies, Orleans, France*, 2002.

[78] Krause, F. and Rädler, K.-H., *Mean-field magnetohydrodynamics and dynamo theory*. Oxford Press, Oxford, UK, 1980, 1980.

[79] Kuratani, N., Ikeda, Y., Nakajima, T., Tomioka, S., and Mitani, T., "Mixing characteristics of normal injection into supersonic backward-facing step flow measured with piv," *AIAA Paper 02-0237*, 2002.

[80] Lago, F., Gonzalez, J. J., Freton, P., and Gleizes, A., "A numerical modelling of an electric arc and its interaction with the anode: part1. the two-dimensional model," *Journal of Applied Physics D*, vol. 37, pp. 883–897, 2004.

[81] Lago, F., Gonzalez, J. J., Freton, P., Uhlig, F., Lucius, N., and Piau, G. P., "A numerical modelling of an electric arc and its interaction with the anode: part3. application to the interaction of a lightning strike and an aircraft in flight," *Journal of Applied Physics D*, vol. 39, pp. 2294–2310, 2006.

[82] Leer, B., "Towards the ultimate conservative difference scheme, v. a second order sequel to godunov's method," *Journal of Computational Physics*, vol. 32, pp. 101–136, 1979.

[83] Lenzner, S., Kurtz, M., and Heirrmann, J., "Energy partition in inductively heated plasma source for reentry simulation," *Journal of Thermophysics and Heat Transfer*, vol. 14, pp. 388–395, 2000.

[84] Leonov, S. B. and D.A.Yarantsev, "Plasma-assisted iginition and flameholding in high-speed flow," *44th AIAA Aerospace Science Meeting, AIAA-2006-0563, AIAA, Reno, NV, 2006*, 2006.

[85] Lilly, D. K., "A proposed modification of the germano subgrid-scale closure method," *Physics of Fluids A*, vol. 4, pp. 633–635, 1992.

[86] Liu, S., Meneveau, C., and Katz, J., "On the properties of similarity subgrid scale models as deduced from measurements in a turbulent jet," *Journal of Fluid Mechanics*, vol. 275, pp. 83–119, 1994.

[87] Lou, G., Bao, M., Nishihara, M., Keshav, S., Utkin, Y., and Admovich, I., "Ignition in premixed hydrocarbon-air flows by repetitively pulsed, nanosecond pulse duration plasma," *AIAA-2006-1215: 44th AIAA Aerospace Sciences Meeting and Exhibit, January 9-12 , Reno, NV*, 2006.

[88] Lowke, J. J., Morrow, R., and Haidar, J., "A simplified unified theory of arcs and their electrodes," *Journal of Physics D: Applied Physics*, vol. 30, pp. 2033–2042, 1997.

[89] Maclatchy, C. S., Clements, R. M., and Smy, P., "An experimental investigation of microwave. radiation on a propane-air flame.," *Combustion and Flame*, vol. 45, pp. 161–169, 1982.

[90] Malo-Molina, F., Gaitonde, D., and Kutschenreuter, P., "Numerical investigation of an innovative inward turning inlet.," *AIAA Paper 05-4871*, 2005.

[91] Matthaeus, W. H., Goldstein, M. L., and Montgomery, D. C., "turbulent generation of outward-traveling interplanetary alfvenic fluctuations," *Physical Review Letters*, vol. 51, pp. 1484–1487, 1983.

[92] McDaniel, J., Fletcher, D., Hartfield Jr, R., and Hollo, S., "Staged transverse injection into mach. 2 flow behind a rearward-facing step: A 3-d compressible test case for hypersonic combustor. code validation.," *3rd AIAA International Aerospace Planes Conference, AIAA-1991-5071*, 1991.

[93] McMillin, B. K., Seitzman, J., and Hanson, R., "Comparison of no and oh planar fluorescence temperature measurements in scramjet model flowfields," *AIAA Journal*, vol. 32, pp. 1945–1952, 1994.

[94] Müller, W.-C. and Carati, D., "Dynamic gradient-diffusion subgrid models for incompressible magnetohydrodynamics turbulence," *Physics of Plasma*, vol. 9, pp. 824–834, 2002.

[95] Menart, J. and Lin, L., "Numerical study of a free-buring argon arc with copper contamination from the anode," *Plasma Chemistry and Plasma Processing*, vol. 19, pp. 153–170, 1999.

[96] Menon, S., "Active combustion control in a ramjet using large-eddy simulations.," *Combustion Science and Technology.*, vol. 84, pp. 51–79, 1992.

[97] Menon, S. and Patel, N., "Subgrid modeling for simulation of spray combustion in large-scale combustors.," *AIAA Journal*, vol. 44, pp. 709–723, 2006.

[98] Miki, K. Schulz, J. and Menon, S., "Large eddy simulation of equilibrium plasma-assisted combustion in supersonic flow," *Proceedings of the Combustion Institute*, vol. 32, 2008. (to appear).

[99] Miki, K., Schulz, J., and Menon, S., "Large-eddy simulation of a supersonic plasma flow over a backward facing step," *Turbulence and Shear Flow Phenomena 5*, pp. 985–990, 2007.

[100] Miki, K., Schulz, J., and Menon, S., "Large-eddy simulation of non-equilibrium plasma-assisted combustion in supersonic flow," *44th AIAA/ASME/SAE/ASEE Joint Propulsion Conference, AIAA-2008-5072, 20-23 July 2008, Hartford, CT*, 2008.

[101] Moffatt, H. K., "Magnetic field generation in electrically conducting fluids," *Cambridge University Press, Cambridge, 1978*, 1978.

[102] Moin, U., Squires, W., Cabot, W., and Lee, S., "A dynamics sub-grid model for compressible turbulence and scalar transport.," *Physics of Fluids*, vol. 3, pp. 2746–2757, 1991.

[103] Montgomery, D., Turner, L., and Vahala, G., "Three-dimensional magnetohydrodynamics turbulence in cylindrical geometry," *Physics of fluids*, vol. 21, pp. 757–764, 1978.

[104] Morinishi, Y., Nakabayashi, K., and Ren, S. Q., "A new dns algorithm for homogeneous decaying rotating turbulence," *International Journal of Heat and Fluid Flow*, vol. 22, pp. 30–38, 2001.

[105] Naghizadeh-Kashani, Y., Cressault, Y., and Gleizes, A., "Net emission coefficient of air thermal plasmas.," *Journal of Physics D*, vol. 35, pp. 2925–2934, 2002.

[106] Ombrello, T., Qin, X., Ju, Y., Gustol, A., Fridmann, A., and Carter, C., "Combustion enhancement via stabilized piecewise nonequilibrium gliding arc plasma discharge," *AIAA Journal*, vol. 44, pp. 142–150, 2006.

[107] Pancheshnyi, S., Lacoste, D. A., Bourdon, A., and Laux, C. O., "Ignition of propan-air mixtures by reoetitively pulsed nanosecond gas discharges," *Proceedings of 17th international Symposium on Plasma Chemistry (Toronto, Canada, 7-12 August,2005)*, 2005.

[108] Papamoschou, D. and Roshko, A., "The compressible turbulent shear layer: an experimental study," *Journal of Fluid Mechanics*, vol. 197, pp. 453–477, 1988.

[109] Park, C., "Review of chemical-kinetic problems of future nasa mission," *Journal of Thermophysics and Heat Transfer*, vol. 7, pp. 385–398, 1993.

[110] Park, C., "Chemical-kinetic parameters of hyperbolic earth entry," *AIAA-2000-0210: 38th AIAA Aerospace Sciences Meeting and Exhibit, January 10-13 , Reno, NV*, 2000.

[111] Park, J., Henins, I., Herrmann, H., and Selwyn, G., "Discharge phenomena of an atmospheric pressure radio-frequency capacities plasma source.," *Journal of Applied Physics*, vol. 89, pp. 20–28, 2001.

[112] Patel, N. and Menon, S., "Structure of flow separation and reattachment behind an axisymmetric hill," *Journal of Turbulence*, vol. 8, 2007. *DOI* : 10.1080/14685240701534484.

[113] Paul, A., Stalker, R. J., and Mee, D. J., "Experiments on supersonic combustion ramjet propulsion in a shock tunnel," *Journal of Fluid Mechanics*, vol. 296, pp. 156–183, 1995.

[114] Peaceman, D. C. and Rachford, H. H., "The numerical solution of parabploc and elliptic differential equations," *Society for Industrial and Applied Mathematics*, vol. 3, pp. 28–41, 1955.

[115] Pope, S. B., *Turbulent Flows*. Cambridge University Press, Cambridge, 2000.

[116] Powell, K., "Large-eddy simulation of reacting flows applied to bluff body stabilized flames," *ICASE Report No.9-24,Langley,VA*, 1994.

[117] Rausch, V. and McClinton, C. and. Sitz, J., "Hyper-x program overview," *Proceddings of the 14th International Symposium on Air Breathing Engines, ISABE Paper 99-7213*, 1999.

[118] Rusch, D., Pfau.A. and. Schlienger, J. and.Kalfas, A., and Abhari, R., "Deterministic unsteady vorticity field in a driven axisymmetric cavity flow," *Journal of Computational and Applied Mechanics*, vol. 5, pp. 353–365, 2004.

[119] Ryu, D., Miniati, F., Jones, T. W., and Frank, A., "A divergence-free upwind code for multidimensional magnetohydrodynamics flows," *Astrophyical Journal*, vol. 509, pp. 244–255, 1998.

[120] Sahu, J. L., "Numerical computation of supersonic base flow with special emphasis on turbulence modeling," *AIAA Journal*, vol. 32, pp. 1547–1549, 1994.

[121] Sakiyama, Y. and Graves, D., "Corona-glow transition in the atmospheric pressure rf-excited plasma needle," *Journal of Physics D: Applied Physics*, vol. 39, pp. 3644–3652, 2006.

[122] Sankaran, V. and Menon, S., "Subgrid combustion modelling of 3-d premixed flames in the thin-reaction-zone regime," *Proceedings of the Combustion Institute*, vol. 30, pp. 575–582, 2004.

[123] Sankaran, V. and Menon, S., "Subgrid combustion modeling of 3-d premixed. flames in the thin-reaction-zone regime.," *Proceedings of the Combustion Institute*, vol. 30, pp. 575–582, 2005.

[124] Sasse, S. and Koschel, W., "Turbulent chemical reacting supersonic flow calculation using the finite element methode on unstructured grids," *7th Space planes and Hpersonic Systems and technologies Conference, AIAA-1996-4558, Nov 18-22, Norfolk, VA*, 1996.

[125] Sato, N., Imamura, A. Shiba, S., Takahashi, S., Tsue, M., and Kono, M., "Advanced mixing control in supersonic airstream with a wall mounted cavity," *AIAA Paper 96-4510*, 1996.

[126] Schlitz, L. Z., Garimella, S., and Chan, S. H., "Gas dynamics and electromagnetic processes in high-current arc plasma: part 1. effects of external magnetic fields and gassing materials," *Journal of Applied Physics*, vol. 85, pp. 2546–2547, 1999.

[127] Schlitz, L. Z., Garimella, S., and Chan, S. H., "Gas dynamics and electromagnetic processes in high-current arc plasma: part 1. model formulation and steady-state solutions," *Journal of Applied Physics*, vol. 85, pp. 2540–2546, 1999.

[128] Schmidt, H.-P., "Experimental and theoretical investigation of high-pressure arcs - part1: The cylindrical arc column (two-dimensional modeling)," *IEEE Transactions on Plasma Science*, vol. 24, pp. 1229–1238, 1996.

[129] Schulz, J., Miki, K., and Menon, S., "Simulation of mhd turbulence-chemistry interaction in supersonic flow," *37th Plasmadynamics and Lasers Conference, AIAA-2006-2894,June 5-8, San Fransicso, CA*, 2006.

[130] Seehafer, N., "Nature of the α effect in magnetohydrodynamics," *Physical review E*, vol. 53, pp. 1283–1286, 1996.

[131] Shercliff, J., *A Textbook of magnetohydrodynamics*. Pergamon press, Oxford, UK, 1965, 1965.

[132] Shimomura, Y., "Large eddy simulation of magnetohydrodynamics turbulent channel flows under a uniform magnetic field," *Physics of fluids A*, vol. 3, pp. 3098–3106, 1991.

[133] Smagorinsky, J., "general circulation experiments with the primitive equations. the basic experiment.," *Monthly weather review*, vol. 91, pp. 99–164, 1963.

[134] Smith, K. M. and Dutton, J., "Investigation of large scale simulation in supersonic planar base flows," *AIAA Journal*, vol. 34, pp. 1146–1152, 1996.

[135] Sosounov, V., "Research and development of ram/scramjet and tubojets in russia," *AGARD Lecture ser, 194, AGARD*, 1993.

[136] Speckhofer, G. and Schmidt, H., "Experimental and theoretical investigation of high-pressure arcs - part2: The magnetically deflected arc (three-dimensional modeling)," *IEEE Transactions on Plasma Science*, vol. 24, pp. 1239–1248, 1996.

[137] Starikovskaia, S. M., "Plasma assisted ignition and combustion.," *Journal of Physics D: Applied Physics*, vol. 39, pp. 265–299, 2006.

[138] Starikovskaia, S., Anikin, I., Kosarev, N., Popv, A., and Yu, A., "Analysis of ignition by nonequilibrium sources. ignition of homological series of hydrocarbons by volume nanosecond discharge.," *AIAA-2006-616: 44th AIAA Aerospace Sciences Meeting and Exhibit, January 9-12 , Reno, NV*, 2006.

[139] Stribling, T. and Matthaeus, W. H., "Relaxation processes in a low-order three -dimensional magnetohydrodynamics model," *Physics of Fluids,B*, vol. 3, pp. 1848–1864, 1991.

[140] Tewari, G. P. and Wilson, J. R., "On experimental study of the effects of high frequency. electric fields on laser-induced flame propagation," *Combustion and Flame*, vol. 24, pp. 159–167, 1975.

[141] Theobald, M. L., Fox, P. A., and Sofia, S., "A subgrid-scale resistivity for magnetohydrodynamics," *Physics of Plasma*, vol. 1, pp. 3016–3032, 1994.

[142] Tobias, S., Jaechul, C., and Jens von, W., "Experimental investigations of scramjet combustor characteristics.," *AIAA Paper 08-2552*, 2008.

[143] Toth, G., "The $\bigtriangledown \cdot b = 0$ constraint in shock-capturing magnetohydrodynamic code," *Journal of Computational Physics*, vol. 161, pp. 605–652, 2000.

[144] Tretyakov, P. K., *The study of supersonic combustion for a scramjet.* Experimental, Modeling and Combustion in Flow, Turbulence, and Combustion, Wiley, New York, 1996.

[145] Trocheris, M. G., "Electrodynamics in a rotating frame of reference," *Philosophical Magazine*, vol. 40, pp. 1143–1154, 1949.

[146] Uenishi, K., Rogers, R., and Northam, G., "Numerical predictions of a rearward-facing step in a supersonic combustor," *Journal of Propulsion and Power*, vol. 5, pp. 158–164, 1989.

[147] Varvill, R. and Bond, A., "A comparison of propulsion concepts for ssto reusable launchers.," *Journal of the British Interplanetary Society*, vol. 56, pp. 108–117, 2003.

[148] W.-S. Choi, W.-S., Neumeier, Y., and Jagoda, J., "Stabilization of a combustion process near lean blow off by an electric discharge.," *AIAA-2004-982: 42th AIAA Aerospace Sciences Meeting and Exhibit, January 5-8 , Reno, NV*, 2004.

[149] Waltrup, P., Stull, F., and Anderson, G., "Supersonic combustion ramjet (scramjet) engine development in the united states," *Proceddings of the 3rd International Symposium on Air Breathing Engines, Deutsche Gesellschaft, germany. March*, pp. 835–862, 1976.

[150] Wang, F., Liu, J. B. Sinibaldi, J., Brophy, C., Kuthi, A., Jiang, C., Ronney, P., and Gundersen, M. A., "Transient plasma ignition of quiescent and flowinig air/fuel mixtures.," *IEEE Transactions on Plasma Science*, vol. 33, pp. 326–327, 2005.

[151] Weber, R. J. and MacKay, J. S., "An analysis of ramjet engines using supersonic combustion," *NACA TN 4386, Sep.*, 1958.

[152] Westhoff, R. and Szekely, J., "A model of fluid, heat flow, and electromagnetic phenomena in a nontransferred arc plasma torch," *Journal of Applied Physics D*, vol. 70, pp. 3455–3466, 1991.

[153] Won, S. H., Cha, M., Park, C., and Chung, S., "Effect of electric fields on reattachment and propagation speed of tribrachial flames in laminar coflow jets.," *Proceedings of the Combustion Institute*, vol. 31, pp. 963–970, 2007.

[154] Yang, S. Y., "Adaptive refinement of a supersonic flow over a backward-facing step," *AIAA Paper 01-3741*, 2001.

[155] Yang, X. and Domaradzki, J. A., "Large eddy simulation of decaying rotating turbulence," *Phys. Fluids*, vol. 16, pp. 4088–4104, 2004.

[156] Yeung, P. K. and Zhou, Y., "Numerical study of rotating turbulence with external forcing," *Physics of Fluids*, vol. 10, pp. 2895–2909, 1998.

[157] Yokoi, N., "Magnetic-field generation and turbulence suppression due to cross-helicity effects," *Physics of Fluids*, vol. 11, pp. 2307–2316, 1999.

[158] Yoshizawa, A., "Subgrid modeling for magnetohydrodynamic turbulent shear flows," *Physics of plasmas*, vol. 30, pp. 1089–1095, 1987.

[159] Yoshizawa, A., "Self-consistent turbulent dynamo modeling of reversed field pinches and planetary magnetic fields," *Physics of Plasmas B*, vol. 2, pp. 1589–1599, 1990.

[160] Yoshizawa, A., "Compressibility and rotation effects on transport supression in magnetohydrodynamic turbulence," *Physics of plasmas*, vol. 3, pp. 889–900, 1995.

[161] Yoshizawa, A. and Hamba, F., "A turbulent dynamo model for the reversed field pinches of plasma," *Physics of plasmas*, vol. 31, pp. 2276–2284, 1988.

[162] Yoshizawa, A. and Yokoi, N., "Stationary large-scale magnetic field generated by turbulent motion in a spherical region," *Physics of plasmas*, vol. 3, pp. 3604–3613, 1996.

[163] Yu, K. H. and Shadow, K. C., "Cavity-actuated supersonic mixing and combustion control.," *Combustion and Flame*, vol. 99, pp. 295–301, 1994.

[164] Zeman, O., "A note on the spectra and decay of rotating homogeneous turbulence," *Physics of Fluids*, vol. 6, pp. 3221–3223, 1994.

[165] Zhang, X. and Edwards, J., "An flows driven by thick shear layers.," *Aeronautical Journal*, pp. 355–364, 1990.

[166] Zhou, Y., "A phenomenological treatment of rotating turbulence," *Physics of Fluids*, vol. 7, pp. 2092–2094, 1995.

[167] Zhou, Y. and Matthaeus, W. H., "Phenomenology treatment of magnetohydrodynamic turbulence with nonequipartition and anisotropy," *Physics of plasmas*, vol. 12, pp. 056503–1 – 056503–8, 2005.

VITA

On October 13th, 1976, Kenji Miki was born as the second son to Minoru Miki and Yoshiko Miki in Akashi City facing the beautiful Akashi Srraits in Japan. He placed first on the entrance examination for Akashi junior high school under the direction of the faculty of Human Development at Kobe University where both my brother Tadakazu Miki and my sister Mari Miki attended. In 2000, he graduated with a Bachelor degree in Aeronautical and Astronautical Engineering at Kyoto University in Japan under the instruction of Prof. Kouichi Ono who inspired him to go to the US. Continuing at Kyoto University for his Master degree in Aeronautical and Astronautical Engineering, he had the opportunity to study as an intern at University of California, San Diego (2000-2001). He received his Master in 2002. He then attended the University of Texas at Austin (2002-2003), but transfered to Georgia Institute of Technology in August of 2003 to pursue his doctoral degree under the instruction of Prof. Suresh Menon. At Georgia Institute of Technology, he has been involved in the development and modeling of MHD applications.